Monitoring Heart and Lung Function Using In-line Laser Spectroscopy



Nicholas M. J. Smith
Worcester College
University of Oxford

A thesis submitted for the degree of
Doctor of Philosophy

Michaelmas 2019

Monitoring Heart and Lung Function Using In-line Laser Spectroscopy

Nicholas M. J. Smith

Worcester College

University of Oxford

A thesis submitted for the degree of

Doctor of Philosophy

Michaelmas 2019

Abstract

Current techniques of assessing respiratory health and cardiovascular function have inherent limitations. Commonly used methods of assessing lung function are generally insensitive to early stage respiratory disease, while techniques for evaluating cardiac output are highly invasive. The aim of this thesis is to demonstrate new techniques for assessing respiratory function and cardiac output that exploit the information encoded within breathing profiles, and which can address these shortcomings.

A molecular flow sensor (MFS) has been developed that utilises laser absorption spectroscopy to measure the number densities of O_2, CO_2, and H_2O every 10 ms in the main airway. Respiratory flow is measured using a custom pneumotachograph. The highly-accurate respiratory profiles recorded by this device during a nitrogen washout procedure are fit to a computational model of lung to provide estimates of lung inhomogeneity. This thesis presents the first applications of this technique in clinical settings, describing a series of studies that evaluated lung inhomogeneity in patients with asthma, chronic obstructive pulmonary disease, and pneumothorax.

A compact Herriott cell was integrated into the MFS, facilitating the measurement of CH_4 and C_2H_2 in addition to the pre-existing spectroscopic systems. C_2H_2 is soluble in blood, whereas CH_4 is relatively insoluble. Thus, analysis of the relative uptake rates of these gases by the body, when small amounts are included in the inspiratory gas, can provide insight into an individual's cardiac output. This strategy was utilised, with cardiac output assessed by fitting a model of CH_4 and C_2H_2 uptake to MFS recorded data. This method was validated in a study that evaluated healthy volunteers at rest and during moderate exercise on five consecutive days.

Acknowledgements

First and foremost I would like to thank Grant for all of his support and guidance throughout the duration of my studies at Oxford. He has been a dedicated tutor, supervisor and mentor and this commitment is hugely appreciated. Peter and Gus have also made massive contributions; their wisdom and enthusiasm have been invaluable. I feel incredibly lucky to have been able to learn from John and Graham, two endless sources of knowledge and technical expertise, thank you.

I am very grateful to have had the opportunity to meet so many fantastic people as part of the Ritchie group. In particular, I'd like to thank Katherine and Luca for being brilliant mentors without whom I think it is unlikely I would have pursued this DPhil, James for coffee mornings to wake me up and for providing a lovely dog to cuddle, Sam for ensuring I know more about Salisbury now than I ever intended to, Dáire for her tolerance of my attempts to teach her about cricket, Pev, who proved himself to be really quite good at squash, Lorenzo for lively debate, rucksack reviews and Patagonia passion, and finally to all members of the Ritchie Group Mölkky Club.

Thank you to all of the members of the Robbins group, particularly Snapper for keeping Wednesday mornings entertaining, and Nick and Nayia whose tireless efforts ensured the work at the hospital ran smoothly.

Thank you to all of my friends and family. To Lucy, a constant source of kindness and positivity in my life. You keep the tough times manageable and the good times a whole lot of fun, thank you!

Finally to my parents, for their love, support and encouragement throughout my life.

Contents

Abstract ii

Acknowledgements iii

1 Introduction 1

1.1 Motivation for the Research . . . 1

1.2 Introduction to Respiratory Physiology . . . 2

1.3 Respiratory Disease . . . 4

1.3.1 Chronic Obstructive Pulmonary Disease . . . 4

1.3.2 Asthma . . . 5

1.3.3 Pneumothorax . . . 6

1.4 Respiratory Assessment Techniques . . . 6

1.4.1 Spirometry . . . 6

1.4.2 Body Plethysmography . . . 7

1.4.3 Measuring Lung Inhomogeneity . . . 8

1.4.3.1 Multiple Inert Gas Elimination Technique . . . 9

1.4.3.2 Hyperpolarised Gas MRI . . . 9

1.4.3.3 Multiple Breath Nitrogen Washout and Lung Clearance Index . . . 10

1.5 Techniques for Assessing Cardiac Output . . . 11

1.5.1 Invasive Techniques . . . 12

1.5.2 Non-invasive Techniques . . . 13

1.5.2.1 Bioimpedance and Bioreactance . . . 14

1.5.2.2 Partial Carbon Dioxide Rebreathing . . . 14

1.5.2.3 The Rebreathing Method . . . 15

1.5.2.4 The Open Circuit Method 17
1.6 Summary 19
1.7 Outline of Thesis 20

2 Molecular Flow Sensing and Assessment of Lung Inhomogeneity 22
2.1 Existing Methodology in Breath Diagnostics 23
2.2 Laser Absorption Spectroscopy 25
2.3 Molecular Flow Sensing 29
2.3.1 Water and Carbon Dioxide Spectroscopy 30
2.3.2 Oxygen Spectroscopy 43
2.3.3 Temperature and Pressure Sensors 50
2.3.4 Respiratory Flow Measurement 51
2.3.5 Validation by Air and High Oxygen Breathing 57
2.4 Lognormal Lung Model 61
2.4.1 Parameterisation of Inhomogeneity 61
2.4.2 Experimental Protocol 64
2.4.3 Model Fit to MFS Data 65
2.5 Summary 68

3 Investigation of Chronic Obstructive Pulmonary Disease Patient Group 70
3.1 Cross-sectional Investigation of Lung Inhomogeneity in COPD 73
3.1.1 Methods 73
3.1.2 Results 75
3.1.3 Discussion 81
3.1.4 Conclusions and Future Work 84
3.2 Cross-sectional Study Evaluating Patients Following Primary Spontaneous Pneumothorax 86
3.2.1 Methods 86
3.2.2 Results 87
3.2.3 Discussion 89
3.3 Validation of Inhomogeneity Assessment by Comparison with MIGET 91

3.3.1 Methods . . . 92
3.3.1.1 Subjects . . . 92
3.3.1.2 Experimental Setup . . . 92
3.3.1.3 Lognormal Lung Experimental Setup . . . 93
3.3.2 Results . . . 93
3.3.2.1 MIGET Results . . . 94
3.3.2.2 Lognormal Lung Results . . . 96
3.3.3 Discussion . . . 98
3.4 Conclusions . . . 106

4 Investigating Lung Inhomogeneity in Asthma 108
4.1 Cross-sectional Study of Lung Inhomogeneity in Asthma . . . 112
4.1.1 Methods . . . 112
4.1.2 Results . . . 115
4.1.3 Discussion . . . 117
4.2 Longitudinal Study of Patients with Asthma . . . 121
4.2.1 Methods . . . 122
4.2.2 Results . . . 123
4.2.2.1 Asthma Treatment Pathway . . . 123
4.2.2.2 Mepolizumab Treatment . . . 128
4.2.3 Discussion . . . 133
4.3 Summary . . . 141

5 Development of a Non-invasive Technique for Determination of Cardiac Output 142
5.1 Development of 5-gas Molecular Flow Sensor . . . 143
5.1.1 Design and Implementation of Herriott Cell . . . 146
5.1.2 Integration into 5-gas Analyser . . . 153
5.2 Determination of Cardiac Output . . . 158
5.2.1 Cardiac Output Modelling . . . 159
5.2.2 Experimental Procedure . . . 163
5.2.3 Model Fitting Methods . . . 163

5.3 Cardiac Output Reproducibility at Rest and Exercise 165
5.3.1 Methods 166
5.3.2 Results 166
5.3.2.1 Evaluation of Tissue Volume Multiplier 170
5.3.2.2 Maximal Bias of $\dot{Q}$ Measurement 173
5.3.2.3 Estimation of Error 176
5.3.3 Discussion 177
5.4 Future Developments and Applications 181
5.5 Summary 183

6 Conclusions and Future Work **185**

Bibliography **189**

Chapter 1

Introduction

1.1 Motivation for the Research

There are significant issues associated with current techniques for assessing respiratory health and cardiovascular function. Techniques for assessing respiratory disease lack the sensitivity required to allow clinicians to diagnose early stage lung disease. The most common method for assessing lung function is spirometry.[1] Spirometry is cheap, rapid, and simple to perform for all but patients with severe lung disease. It is, however, a blunt assessment of lung function, assessing the volume of gas that can be forcefully exhaled from the lungs and the speed with which this can be achieved. There is clinical desire for assessment techniques with indicators that are more sensitive to minor changes in respiratory health. Such techniques would present clinicians with opportunities to identify early lung disease. There would be downstream benefits from the application of a highly sensitive technique, providing accurate assessment of disease progression and response to treatment.

Methods of assessing cardiac output, a parameter that describes the volume of blood pumped by the heart per unit time, are currently unsatisfactory for widespread clinical use. Techniques are either highly invasive, or represent substantial compromises to accuracy and reliability. Clinical management of critically ill patients would benefit significantly from a technique providing accurate, non-invasive cardiac output assessment. Cardiac output measurement could provide a valuable parameter in goal-directed resuscitation of patient cardiovascular systems.[2]

This thesis explores the hypothesis that there is significant information about respiratory and cardiac function encoded within inspiratory and expiratory gas profiles that is, as yet, unused by existing methodologies. In order to quantify this information, the gas profiles must be measured with very high precision, and then computational models fitted to these profiles. This thesis demonstrates

a device capable of measuring respiratory profiles, principally gas compositions and flows, with the necessary level of precision. Data measured with this device are combined with a computational model of lung inhomogeneity to provide an assessment of lung function. The measurement device is extended, and combined with a model of the body's tracer gas uptake, to provide a method of assessing cardiac function via the physiological parameter of cardiac output.

This chapter provides an introduction to this work, briefly describing respiratory physiology and disease, followed by the currently used clinical techniques of assessing lung function. The current methods of assessing cardiac output are described and critically evaluated. The chapter ends with an outline of the work presented in this thesis.

1.2 Introduction to Respiratory Physiology

The heart and lungs play crucial roles in the physiological processes that occur within the human body. Blood provides a means of transporting gases around the body, either as physically dissolved species or as reversibly reacted compounds. The heart provides the mechanism by which the blood is transported around the cardiovascular system. The cardiovascular system works alongside the respiratory system, with the lungs at its core, to provide the body with oxygen (O_2) for metabolism and to excrete the carbon dioxide (CO_2) produced by metabolism.[3] Pulmonary gas exchange, which takes place within the lungs, provides the link between the respiratory and cardiovascular systems.

The body's respiratory system consists of the lungs and the airways that connect them to the external environment. The primary function of the respiratory system is to facilitate the exchange of O_2 and CO_2 between the body and air. The secondary functions include regulation of body temperature, and immunological and mechanical protection. Contraction of the diaphragm and the intercostal muscles during inhalation expands the lungs, reducing the pleural pressure and hence the pressure of the alveolar gas, drawing in air. After passing through the bronchial tubes, the air enters the alveoli, small sacs within the lung with thin walls and large surface area. Gas exchange occurs by diffusion across the thin blood-gas barrier in the alveoli, termed the alveolar capillary membrane. O_2 diffuses into the blood within pulmonary capillaries, where it binds reversibly to the haemoglobin of the red blood cells. Conversely, CO_2 is carried to the lung by the venous system, both physically dissolved within the blood and present as reversibly formed bicarbonate and carbamino-haemoglobin.[4] CO_2 diffuses back into the lungs before it is released by exhalation.

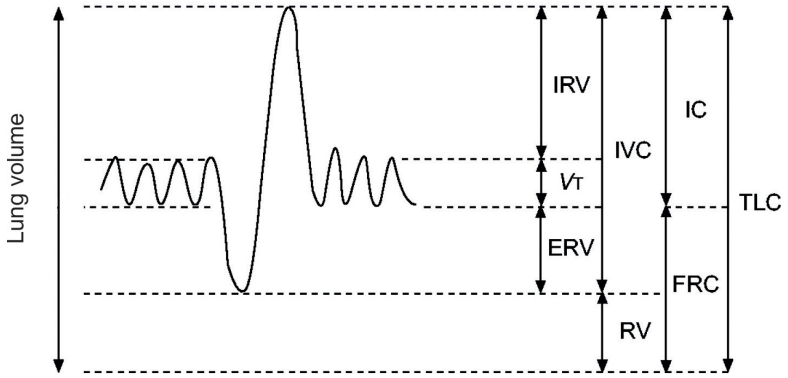


Figure 1.1: The definition of static lung volumes based on a volume-time spirogram. Inspiratory Reserve Volume (IRV): volume of gas that can be further inspired from the end of inspiration in conventional tidal breathing. Tidal Volume (V_T): volume of gas expired/inspired during normal tidal breathing. Expiratory Reserve Volume (ERV): volume of gas that can be further expired from the end of expiration during normal tidal breathing. Inspiratory Vital Capacity (IVC): maximum volume of gas that can be inspired after a maximal expiration. Residual Volume (RV): volume of gas remaining in the lungs after a maximal expiration. Inspiratory Capacity (IC): volume of gas that can be maximally inspired from the end of tidal expiration. Functional Residual Capacity (FRC): volume of gas remaining in the lungs at the end of tidal expiration. Total Lung Capacity (TLC): total volume of gas in the lungs at the end of a maximal inspiration. Figure from Wagner *et al.*.[5]

The volume of the lung changes considerably throughout a breathing cycle. As a result, there is a series of different lung volumes that can be defined and measured, and these are illustrated in Figure 1.1 with the aid of a spirogram.[5] The volume of gas inspired and expired during normal breathing is defined as the tidal volume, V_T. The function residual capacity, FRC, is the volume of gas that remains in the lung following passive expiration. Deadspace within the lung is defined as the lung volume that does not take part in gas exchange. This volume can be split into two categories: anatomical and alveolar.[3] Anatomic deadspace is the volume of gas that remains within the conducting airways between the end of inhalation and the start of exhalation. The gas filling the volume between the nose or mouth and the terminal bronchioles will not be exposed to pulmonary blood supply, and thus will be exhaled unchanged.[6] Alveolar deadspace consists of the alveolar volume in which gas exchange does not occur, usually due to an absence of blood supply to these regions.[7] In healthy individuals, the alveolar deadspace is negligible, but increases significantly with certain respiratory disease types.[3]

The capacity of a region within the lung to participate in gas exchange can be evaluated by considering the relative supplies of newly inspired gas, alveolar ventilation ($\dot{V}$) with units of gas volume per minute, and pulmonary blood, perfusion ($\dot{Q}$) with units of blood volume per minute.

This is quantified using the ratio of ventilation to perfusion in a given lung volume, $\dot{V}/\dot{Q}$.[3] The largest contributions to gas exchange will occur in lung regions with comparable supplies of these quantities, i.e. where $\dot{V}/\dot{Q}$ is close to unity. In regions where $\dot{V}/\dot{Q}$ falls below this, gas exchange will become ventilation limited and inefficient as a result. Pulmonary shunt describes the fraction of total perfusion to regions without sufficient ventilation to allow meaningful gas exchange to take place ($\dot{V}/\dot{Q} = 0$). Conversely, regions with $\dot{V}/\dot{Q}$ greater than unity will have perfusion limited gas exchange. When perfusion drops to zero ($\dot{V}/\dot{Q} = \infty$) the result is alveolar deadspace. In a healthy lung, the majority of lung volume will exhibit a $\dot{V}/\dot{Q}$ ratio close to one. Deviations from this are associated with a range of respiratory disease states.

1.3 Respiratory Disease

This section provides an introduction to a series of respiratory conditions, chronic obstructive pulmonary disease, asthma and pneumothorax, that provide the basis for the motivation of the work described in this thesis. The underlying pathophysiology of these conditions is varied, but all are characterised by high morbidity and/or mortality.[8]

1.3.1 Chronic Obstructive Pulmonary Disease

Chronic obstructive pulmonary disease (COPD) is among the five leading causes of death in the developed world, and is a rapidly rising cause of death in most other countries.[9] In the UK, COPD accounts for 1/8th of acute hospital admissions and more than one million bed days per annum.[10] Current strategies for tackling COPD focus on both primary prevention, aiming to reduce risk factors such as exposure to tobacco smoke, and tertiary prevention, reducing symptoms in patients where the disease is fully developed.[11]

COPD is a highly heterogeneous disease, characterised by two clinical phenotypes.[12] A clinical phenotype describes the presentation of disease within a patient, for example observable traits or characteristics. The first phenotype of COPD is chronic bronchitis, a narrowing of the small airways that leads to their increased resistance to gas flow.[13] The result of this is poorly ventilated volumes within the lung and inefficient gas exchange resulting from low $\dot{V}/\dot{Q}$. The second phenotype is emphysema, characterised by destruction of alveoli which leads to the creation of large, poorly perfused cavities.[14] The $\dot{V}/\dot{Q}$ ratio is elevated this case, again with inefficient gas exchange being

the result. Both of these phenotypes contribute to the persistent airflow limitation that is defined as COPD. The heterogeneous nature of the disease and lack of effective screening options make treatment difficult. Only one new class of medication for COPD, roflumilast,[15] has been approved in the last 25 years.[16] This is, in part, due to the difficulty of tracking COPD progression, meaning that large, and therefore expensive, clinical trials are necessary. It is also due to the fact that without an effective method of stratifying patients into subgroups with different COPD phenotypes, new treatments must be shown to be effective for all COPD in order to be approved.

1.3.2 Asthma

Asthma is a respiratory disease characterised by lower airway inflammation and episodic airflow obstruction. When uncontrolled, asthma can place severe limits on daily life and can be fatal. Around 300 million people are affected by asthma, placing a huge burden on global healthcare.[8] The airway obstruction in asthma is reversible, meaning that it can usually be resolved with treatment. The chronic inflammation is associated with airway hyperresponsiveness that leads to recurrent episodes of wheezing, breathlessness, chest tightness, and coughing.[17] In a large population of asthma patients the disease can be well controlled with appropriate treatment, meaning symptom recurrence is occasional and severe exacerbations are rare.[18] Disease control is established via an iterative cycle of assessment and treatment adjustment. The factors that influence the risk associated with asthma can be divided into those that lead to the development of asthma, primarily genetic, and those that trigger asthma symptoms, usually environmental.

The heterogeneity of asthma is becoming increasing well understood, the disease represented by several distinct underlying mechanistic pathways (endotypes) and variable clinical presentations (phenotypes). The clinical result of asthma heterogeneity is patients with similar symptoms responding very differently to the same therapeutic interventions. Asthma patients can be divided into two endotype groups, eosinophilic and non-eosinophilic.[19] The phenotypes and disease severity profiles are broadly similar for these two groups. Roughly half of asthma patients fall into each of these endotype groups.[20] Eosinophilic asthma is better understood, with a clear mechanistic inflammation pathway elucidated and a series of valuable biomarkers assessed. Non-eosinophilic asthma is characterised by neutrophilic inflammation, the mechanism for which is as yet unknown.[21]

1.3.3 Pneumothorax

The term pneumothorax refers to a condition whereby a collapsed lung results in air in the pleural cavity between the lung and the chest wall. Primary spontaneous pneumothoraces (PSP) occur in healthy individuals and are a significant global health problem, with a reported incidence of around 25/100 000 cases per annum for men and around 20 % of this figure for women.[22] Patients suffering a pneumothorax report a sudden ipsilateral chest pain, which usually resolves without treatment within 24 hours.[23] The precipitating cause(s) of a pneumothorax cannot usually be identified, but there are risk factors associated with smoking, age and height. Atmospheric pressure changes and even exposure to loud music have been linked to pneumothoraces.[24,25] Most primary spontaneous pneumothorax episodes occur at rest. Recently, anatomical abnormalities have been demonstrated in pneumothorax patients. Subpleural blebs have been identified, using a combination of thoracoscopy and CT scanning, in 90 % of investigated cases of PSP, and are thought to play a role in instigating the condition, however, this role has not yet been elucidated.[26,27]

1.4 Respiratory Assessment Techniques

The challenges for the techniques used to assess respiratory health focus particularly on early diagnosis of disease. Methods capable of sensitive assessment of early stage disease would provide significant opportunities for early therapy, for example with inhaled corticosteroids in eosinophilic asthma,[28] or secondary prevention, including smoking cessation.[11,29] Beyond the desire for earlier disease diagnosis, the limitations of currently used techniques include the inability to identify specific phenotypes in patients with established disease and a lack of sensitivity to symptom or disease activity responses to treatment. Conventional methods of assessing respiratory health are described below, with the benefits and limitations of each technique summarised.

1.4.1 Spirometry

Spirometry is the most routinely used method for airway disease diagnosis and progression monitoring.[30] Patients are asked to forcefully exhale from the mouth into a flow sensor following maximal inhalation. The quantities assessed are exhaled gas volumes, the forced expiratory volume in the first second (FEV_1), and the forced vital capacity over the entire duration of the breath (FVC). The FVC is the maximum volume of gas forcefully expired from the total lung capacity to residual

volume, illustrated in Figure 1.1. FEV_1 decreases as airway disease severity increases, but evaluation of the absolute volume is not clinically useful as this value is affected not only by disease, but also by sex, age, height, and ethnicity.[31] A more clinically valuable assessment takes these patient characteristics into account and compares the measured volume with a predicted one, quantifying FEV_1 as the percentage of the predicted value. The FEV_1/FVC ratio is used to diagnose airflow obstruction, with obstruction illustrated by this ratio falling below 0.7.[32] Patients are asked to perform at least three spirometric manoeuvres, the best two of which must fufill the reproducibility criteria, FEV_1 and FVC should be within 5% or 150 ml of each other, whichever is greater.[33]

The advantages associated with spirometry stem from its simplicity. Spirometers are widely available and inexpensive, and measurements are standardised with well-defined normal ranges of FEV_1 and FVC volumes. The clinical value of spirometry, however, is limited by the nature of the parameters being measured. The expired volumes are partly effort and technique dependent, and so despite the requirement to produce reproducible measurements, incorrect clinical conclusions can be drawn due to incomplete expiration. Spirometry provides a single global measure of lung function, and thus is an effective evaluation of average function across the lung. This makes spirometry relatively insensitive to early disease and small airways dysfunction, both of which are likely to manifest in localised regions in the lung. The forced nature of expiration and the effort that is required makes spirometry difficult to perform for patients with severe airways disease, particularly those exhibiting airflow obstruction.[34]

1.4.2 Body Plethysmography

Body plethysmography provides indices representing a series of static lung volumes such as total lung capacity (TLC), residual volume (RV), functional residual capacity (FRC), and airway resistance (R_{aw}). Patients perform a series of unforced breathing manoeuvres in a sealed chamber via a closed airway.[35] A pressure transducer is used to measure the pressure difference between the chamber and atmosphere, with another placed close to the mouth to measure pressure during breathing. Respiratory flow is recorded using conventional apparatus, such as a pneumotachograph.[36] The principle of plethysmography relies on detecting changes in chamber pressure in combination with a pressure change at the mouth, or with flow rate. Briefly, to measure lung volume, the patient breathes in and the resulting slight increase in volume of the lung reduces the free volume of air in

the sealed chamber, thereby increasing its pressure. At the same time, the increase in volume of the lung results in a reduction of pressure in at the mouth; from the changes in the two pressures and the volume of the box, the volume of the lung can be derived.[37] If defined breathing manoeuvres are followed, the series of lung volumes, defined in Figure 1.1, can be evaluated in this way.

Interpretation of the lung volumes determined by body plethysmography is generally, like spirometry, performed using comparison with normative data.[38] Hyperinflation of the lung in COPD patients is known to lead to increases in TLC and RV, and increases in the ratio RV/TLC.[39] This hyperinflation is caused by either airway narrowing, or a loss of elastic recoil due to emphysema, leading to airway closure and gas trapping. Body plethysmography provides sufficient sensitivity to detect these changes, and monitor disease progression as the abnormality of each of these parameters increase with disease severity.[40] Body plethysmography has been shown to inaccurately overestimate lung volumes in asthma patients,[41] although there is also evidence that measures such as the RV and the RV/TLC ratio may correlate with small airways disease.[42] Compared to spirometry, body plethysmography is time consuming, and displays greater within-subject variability.

1.4.3 Measuring Lung Inhomogeneity

One descriptor of lung physiology that could be used to evaluate lung disease is the degree of inhomogeneity within the lungs. In a homogeneous lung, each unit volume would receive the same amount of fresh gas, ventilation, and fraction of the lung's blood flow, perfusion. Inhomogeneity in the lungs generally refers to a mismatch between either ventilation and perfusion, or ventilation and alveolar volume. Healthy lungs will have a degree of inhomogeneity, the lower lung is both better perfused and ventilated than the upper lung, but the differing vertical distributions of these quantities lead to $\dot{V}/\dot{Q}$ variation within the lung.[3] It is well established that the degree of inhomogeneity increases with disease.[43,44] As an indicator of mild COPD, it has been suggested that inhomogeneity shows abnormality earlier than spirometry.[45]

A number of experimental methods have been used to investigate inhomogeneity in the lungs. Despite the potential clinical value of a technique which measures inhomogeneity, no 'gold standard' method for assessing lung inhomogeneity has been established. Three methods for assessing lung inhomogeneity are discussed below: the Multiple Inert Gas Elimination Technique, Hyperpolarised Gas Magnetic Resonance Imaging, and the Nitrogen Washout.

1.4.3.1 Multiple Inert Gas Elimination Technique

The multiple inert gas elimination technique (MIGET) has been used to investigate the inhomogeneity of ventilation-perfusion matching in the lung. The technique is complicated to perform, with six inert gases with differing solubilities dissolved into a saline solution and intravenously infused into a patient.[46] After 20 minutes, retention values for each of the gases are calculated based on measured arterial and expired gas partial pressures. Equations are then derived which relate gas retention to local ventilation-perfusion ratios. From these equations, a ventilation-perfusion distribution of the lungs is estimated. Healthy subjects appear to have narrow unimodal distributions, older subjects broader unimodal distributions, and subjects with COPD may have multi-modal distributions, illustrating the increased inhomogeneity caused by the disease.[47] The MIGET technique appears to facilitate sensitive indication of early stage airway disease, with significant ventilation-perfusion abnormalities reported in both early stage asthma and COPD.[45,48] The central issues with this technique as a clinical tool are its complexity and the questions regarding the information content of this estimation procedure.[49] As a result, this technique is only available in a handful of expert research centres. A validation study of the technique developed in this work, by way of comparison with MIGET, is described in Section 3.3.

1.4.3.2 Hyperpolarised Gas MRI

Hyperpolarised gas magnetic resonance imaging (MRI) has also been used to investigate lung inhomogeneity. One of the primary applications of this technique is ventilation imaging, in which a series of 2D images are acquired during a breath hold following the inspiration of a hyperpolarised gas, usually ^{3}He or ^{129}Xe.[50] Regions of high signal intensity in the images correspond to normally ventilated areas, and regions of low intensity indicate ventilation defects.[51] A second application of hyperpolarised gas MRI stems from the fact that the relaxation rate of a hyperpolarised gas is directly proportional to the local oxygen concentration.[52] This allows the partial pressures of oxygen in the lung to be mapped which, combined with a measurement of the composition of mixed venous blood, enables a ventilation-perfusion distribution to be estimated. The most significant issue with this technique is the cost associated with hyperpolarised gases; supplies of the gases are often regulated by governments due to their use in security scanners.[53]

1.4.3.3 Multiple Breath Nitrogen Washout and Lung Clearance Index

Multiple breath nitrogen washout (MBNW) data can provide an index of ventilation inhomogeneity with the potential to perform sensitive detection of early lung disease.[54] During this procedure, the patient is switched from breathing room air to pure oxygen. The concentration of nitrogen in the expired gas is measured as it washes out of the lungs.[55] In adults, a fixed tidal volume is typically used to minimise changes in the deadspace-to-tidal volume ratio. In children, normal tidal breathing is used, this technique being easier to perform than forced manoeuvres for spirometry. Originally, mass spectrometry was used to measure N_2 concentration data, but recent advances in mainstream gas analysers have led to a resurgence of interest in this technique.[56]

An exemplar dataset collected during a multiple breath nitrogen washout is shown in Figure 1.2. This data can be analysed in a variety of ways, deriving a series of ventilation distribution indices.[57] The most commonly reported MBNW index is the the lung clearance index (LCI), defined as the number of lung turnovers (total litres of ventilation/FRC) required to reduce the alveolar nitrogen concentration to 1/40th of its starting concentration.[58] Despite variability of end-tidal points, the nitrogen concentration at these points is used to evaluate alveolar concentrations.[59] The LCI provides a global measure of ventilation inhomogeneity. Importantly, this measurement has been found to be more sensitive than FEV_1 for measuring lung abnormalities in adult and paediatric cystic fibrosis patients.[60]

Further analysis of MBNW data attempts to differentiate the contributions to ventilation inhomogeneity due to the conductive airways and the acinar airways. These parameters are evaluated from normalised nitrogen phase III slope analysis (the gradient of N_2 fraction against expired volume for the final 30 % of tidal volume) for each exhalation during the MBNW.[61,62] In smokers, abnormalities in these parameters predated abnormalities in spirometry.[63] In asthma, inhomogeneity indices have been found to correlate with airway inflammation, disease severity, and control of disease.[64,65]

Despite the potential of MBNW, there remain limitations associated with this technique. Perhaps the primary issue is the lack of standardisation or specification of equipment, procedures and analytical algorithms.[66,67] There also remains a lack of consensus regarding standard parameter ranges. Furthermore, MBNW is unable to differentiate between structural damage within the lung and airway narrowing by other mechanisms, for example mucus secretion. These limitations have,

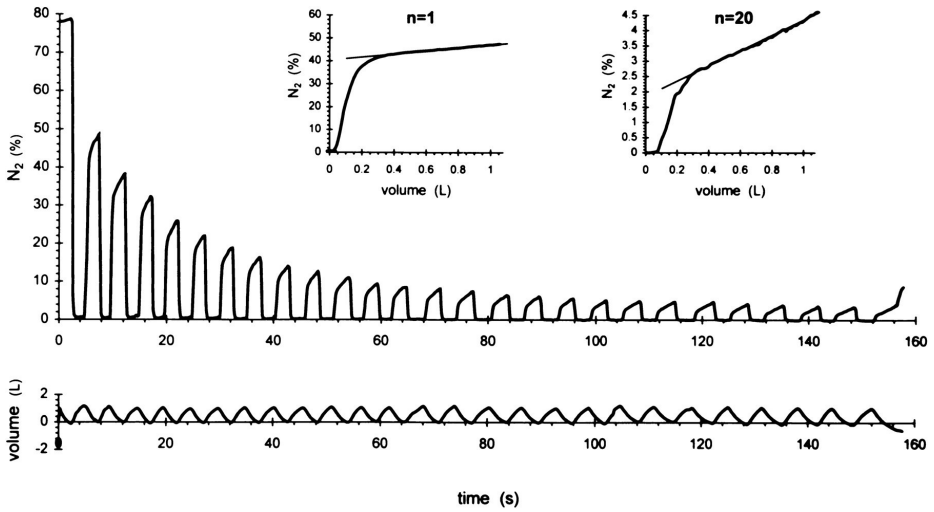


Figure 1.2: N_2 concentration and volume profiles during a multiple breath nitrogen washout (MBNW). The lung clearance index (LCI) is the number of lung turnovers required to produce a fall in nitrogen concentration to 1/40th of the starting value. The inset shows the phase III nitrogen gradients against expired volume for breaths 1 and 20 of the washout. Figure reproduced from Verbanck *et al.*.[61]

to this point, prevented widespread employment of MBNW in clinical practice.

1.5 Techniques for Assessing Cardiac Output

The cardiovascular system consists of the heart, the blood vessels and the blood. This system is responsible for the transportation of oxygen, nutrients, hormones and cellular waste throughout the body. The heart, the body's muscular pumping organ, is formed of two atria and two ventricles. Strongly muscled ventricles pump blood to the entire body, whilst the atria receive blood returning to the heart. Oxygen rich blood is pumped to the body tissue from the left ventricle and oxygen deficient blood, rich in carbon dioxide, is pumped to the lungs by the right ventricle.

Heart function is typically quantified by a cardiac output, $\dot{Q}$, defined as the volume of blood pumped by either of the heart's ventricles in a given time period, usually expressed in litres min^{-1}.[68] Cardiac output varies depending on the supply of oxygen required by the body's muscular system. At rest, $\dot{Q}$ will typically be around $5\,\text{l}\,\text{min}^{-1}$, rising to up to five times this during exercise as an increasing heart rate increases the rate of blood transportation.[69] The significance of $\dot{Q}$ as a diagnostic indicator is a result of the number of physical conditions that cause a change in physiological behaviour of the heart. For example, a change in $\dot{Q}$ can be used to indicate trauma during surgery, sepsis,

hypothermia and other critical illnesses.[70,71] Repeated measurements of $\dot{Q}$ can also be used to assess fitness, valuable for sportsmen and women.[72]

Many of the current methods of evaluating cardiac output are invasive in nature or inaccurate. The limitations of these diagnostic methods provide the motivation for part of the work presented in this thesis. The development of an ideal device - non-invasive, compact, accurate, fast responding, operator-independent, cheap and safe - would allow the examination of $\dot{Q}$ in intensive care units as well as general clinic settings.

1.5.1 Invasive Techniques

A series of invasive techniques exist for assessing cardiac output. These techniques require catheterisation procedures to obtain information about heart function, either directly or indirectly.[73] The concept of $\dot{Q}$ measurement stretches as far back as the nineteenth century with the direct Fick method. Fick's Principle forms the basis of this measurement method, describing the relationship of cardiac output, oxygen uptake ($\dot{V}_{\mathrm{O}_2}$) and the difference between the arterial ($C_{a\mathrm{O}_2}$) and mixed venous blood oxygen content ($C_{v\mathrm{O}_2}$):[74]

$$\dot{Q} = \frac{\dot{V}_{\mathrm{O}_2}}{(C_{a\mathrm{O}_2} - C_{v\mathrm{O}_2})} \,. \tag{1.1}$$

Oxygen uptake is measured using exhaled gases, whilst the mixed venous oxygen content must be measured using a pulmonary artery catheter (PAC).

Conventional methods for obtaining $\dot{Q}$ values, the dye dilution and thermodilution methods, continue to rely on Fick's Principle, but utilise indicators to indirectly quantify blood flow. The dye dilution method, the development of which started roughly fifty years ago, achieved greater accuracy than the direct Fick method.[75] In this case, a known mass of an indicator compound, M_I, either coloured or radioactive, is injected into a vein in the arm. Serial blood samples are then removed via the PAC. An average indicator concentration during one circulation of the blood, $[I]_{art}$, is then derived from these samples. The cardiac output is then determined from the measured dilution of the indicator as follows:[76]

$$\dot{Q} = \frac{M_I}{\int_{t_0}^{t_f} [I]_{art} \, \mathrm{d}t} \,. \tag{1.2}$$

Limitations of this method, other than the overriding issue of its invasive nature, include the assumption that indicator injection is instantaneous. This assumption is only valid in situations where the mean transit time through the cardiovascular system is long relative to the injection time.[77] There is also the issue of recirculation to consider; detectable levels of indicator will remain within the cardiovascular system beyond the measurement time.

Currently, the practical 'gold-standard' method for determining $\dot{Q}$ is the thermodilution method. This technique, similar to the dye dilution method, relies upon heat as the indicator to be measured within the blood. A certain amount of cold fluid is injected into the blood stream near the right atrium of the heart and the resulting dilution curve is measured using a PAC equipped with a thermistor.[78] This dilution curve is evaluated using the following relationship:

$$\dot{Q} = \kappa \, \frac{T_{body} - T_{injectate}}{\int \Delta T_b(t) \mathrm{d}t} \quad , \tag{1.3}$$

where T refers to temperature, $\int \Delta T_b(t) \mathrm{d}t$ is the area under the thermodilution curve and κ is a computational constant, which contains corrections for the specific masses and heats of the injectate and blood, injected volume and loss of indicator in the catheter. This method carries the advantage over dye dilution that recirculation does not have to be considered, making the method appropriate for a series of repeated measurements. A series of large studies have, however, questioned the safety and accuracy of the PAC used within all of these techniques.[79–81] The results of studies such as these have suggested that the decision to assess cardiac output by techniques requiring catheterisation leads to no improvement in patient morbidity or mortality. These conclusions have led to declines in PAC use[82,83] and an increased emphasis on less invasive techniques.[78]

1.5.2 Non-invasive Techniques

Non-invasive monitoring of cardiac output presents the obvious advantage of being associated with fewer clinical complications, but currently this advantage comes at the expense of accuracy and precision. Even the current National Institute for Health and Care Excellence (NICE) approved technology, the CardioQ-ODM (Deltex Medical),[84] an oesophageal doppler monitor, is associated with large measurement errors and significantly reduced precision when compared with the thermodilution technique.[85] A series of non-invasive assessment techniques are briefly described and critically evaluated below.

1.5.2.1 Bioimpedance and Bioreactance

Thoracic electrical bioimpedance (TEB) is based on the assumption that the electrical resistance of the thorax is related to the blood volume within it. Changes in resistance are assumed to be exclusively a function of changes in intrathoracic blood volume. A low-amplitude, high frequency electrical current (I) is applied across the thorax with received voltage (V) measured by electrodes.[86] Thoracic impedance (Z) is defined by the ratio V/I. Hemodynamic variables, including the cardiac output, are derived from the temporal fluctuation of Z. The precision and accuracy of this method is questionable, with determined values that are highly sensitive to electrode positioning, pulmonary oedema, and electrical noise.[87]

The bioreactance technique was developed in an effort to decrease the errors associated with electrode positioning, body size, temperature and humidity that are typically encountered with the bioimpedance technique. Bioreactance systems use frequency modulation of the applied current, as opposed to the amplitude modulation used in bioimpedance.[88] The theoretical basis for this is the improved noise filtering possible with a frequency modulated signal.[89] Literature assessing the accuracy and effectiveness of the bioreactance is contradictory. In two examples, Ravel *et al.* found bioreactance to have "acceptable accuracy in challenging clinical environments"[90], whereas Kupersztych-Hagege *et al.* stated that bioreactance "cannot accurately estimate the cardiac output in critically ill patients".[91] The clinical consensus is that the accuracy of the bioreactance technique is currently insufficient, meaning that this technique has not been widely adopted.

1.5.2.2 Partial Carbon Dioxide Rebreathing

Fick's Principle, described in Equation 1.1, can be modified to consider the behaviour of carbon dioxide instead of oxygen. This is the basis of the non-invasive partial CO_2 rebreathing technique. In this case the gradient of the product of the CO_2 dissociation curve (S) and the end-tidal CO_2 concentration (et_{CO_2}) is used to derive an estimated value of the arterial blood CO_2 content. To prevent the need to estimate the CO_2 content of venous blood, two time periods, one of normal respiration n, and one of rebreathing r, are used. The assumption is made that both the venous blood CO_2 content and $\dot{Q}$ are unchanged during these periods of time, allowing the cardiac output to be calculated from the CO_2 production and the difference in arterial CO_2 content surrogate during these two periods:

$$\dot{Q} = \frac{\Delta \dot{V}_{CO_2}}{\Delta(S\,et_{CO_2})}\ . \tag{1.4}$$

There are several limitations associated with this technique. First, the accuracy of the technique is related to the tidal volume, requiring patient respiratory states to be steady; this is often not the case in intensive care.[92,93] Secondly, differences in the CO_2 production and end-tidal concentrations only account for ventilated regions of the lung, meaning that there is significant error associated with this technique in patients with significant intrapulmonary shunts.[94] Finally, validation studies of this method by comparison with the thermodilution method have failed to prove equivalence between these two methods.[95]

1.5.2.3 The Rebreathing Method

The rebreathing method evaluates the rate of uptake of two foreign gases in the body, one soluble in blood and one insoluble.[96] Patients inhale through a mouthpiece from a non-diffusing gas bag containing a reservoir of gas mixture containing 0.3% acetylene (soluble in blood), 0.3% methane (insoluble), and 35% oxygen balanced in nitrogen. A single inhalation is made from this gas mixture, followed by exhalation into a 'rebreathing bag', as shown in figure 1.3. This rebreathing bag is then the source of the inhaled gas for the remaining duration of the experiment. The path of the gas flow is controlled by a sliding three way valve, switching from room air at the start of the experiment, to the bag containing the gas mixture, and finally to the rebreathing bag. The gas flow, and concentrations of the three diagnostic gases, are measured by the spectrometer positioned in-line at the mouth. The inspired volume is measured using either a spirometer or flow data at the spectrometer. This method requires a degree of patient participation, although there is no need for breath holding or precise, regular breathing. Patients are required to wear nose clips to prevent breathing through the nose.

The relative concentrations of the gases in up to ten exhalations, along with pressure, temperature and inhaled volume, are used to determine $\dot{Q}$. Analysis centres on the disappearance profiles of the acetylene relative to methane. Methane, which is insoluble in blood, will remain in the alveolar volume, whilst soluble acetylene is taken up by the blood. Analysis is undertaken starting with the following standard equation:[97]

$$\text{CH}_4 \text{ dilution} \quad = \quad \frac{F_{ET_{CH_4}}}{F_{I_{CH_4}}} \tag{1.5}$$

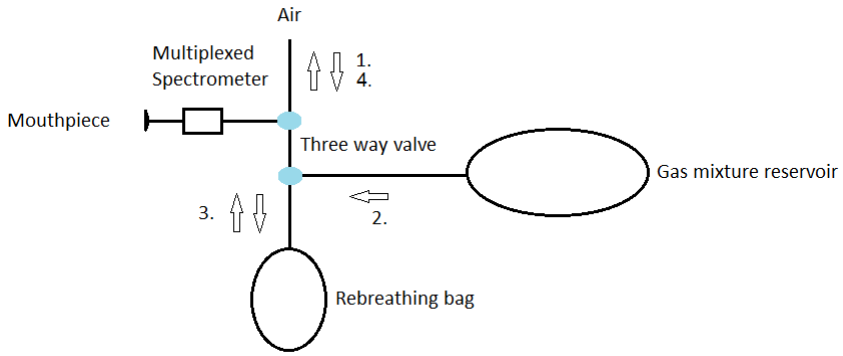


Figure 1.3: Schematic of rebreathing experimental setup. Numbered arrows represent sequence of experimental protocol. 1: subject initially breathes room air, 2: subject inhales from gas mixture, 3: subject exhales into and inhales from the rebreathing bag for up to ten breaths, 4: subject returns to breathing room air.

where, 'CH_4 dilution' is the ratio of the end-tidal (end of expiration) methane concentration, $F_{ET_{\mathrm{CH_4}}}$, to the inspired concentration, $F_{I_{\mathrm{CH_4}}}$. Once good mixing has been achieved, this ratio should remain roughly constant due to the insolubility of methane in blood. The maximum lung volume, V_{MAX}, is found by:

$$V_{MAX} = \left(\frac{V_I}{\mathrm{CH_4\ dilution}}\right)\left(\frac{P_B\ (273 + T_b)}{(P_B - 47)\ (273 + T_r)}\right) \tag{1.6}$$

where P_B is barometric pressure in units of Torr, T_b and T_r are the temperatures of the body and room respectively, and V_I is the volume of gas inspired from the gas mixture reservoir for the first breath. The number 47 is included as the saturated partial pressure of water under conditions of body temperature and pressure. The cardiac output can then be determined:

$$\dot{Q} = \frac{-60\ V_{MAX}}{\beta_{bl}\ e^{(F_{ET_{\mathrm{C_2H_2}}})_0}}\ \frac{760}{(P_B - 47)}\ \frac{\Delta \ln\left(\frac{F_{ET_{\mathrm{C_2H_2}}}\ /\ F_{I_{\mathrm{C_2H_2}}}}{F_{ET_{\mathrm{CH_4}}}\ /\ F_{I_{\mathrm{CH_4}}}}\right)}{\Delta t}\ . \tag{1.7}$$

The $\Delta \ln / \Delta t$ term above represents the gradient of the logarithmic disappearance of end-tidal acetylene with respect to methane. These gradients have units of s^{-1}, with the factor of 60 simply accounting for the fact that the physiological parameters are quoted in units of min^{-1}. The solubility coefficient of acetylene in blood is represented by β_{bl} and the exponential term in the denominator of equation 1.7 is the extrapolated time zero intercept of the acetylene disappearance profile; this is non-zero due to the rapid uptake of the gas by tissue. In addition, the lung tissue volume, V_{ti}, can be determined using the equation:

$$V_{ti} = \left(\frac{V_{SYS}}{\beta_{bl}} \right) \left(\frac{1}{e^{(F_{ET_{C_2H_2}})_0}} - 1 \right) \quad . \tag{1.8}$$

Data from the first few breaths are discarded to allow good mixing between the inspired gas and the resident alveolar air, while breaths late in the experiment, after ~ 15 s, are also discarded to remove the possibility of foreign gas recirculation back into the alveolar volume.[98] Similar breath-selection criteria are used in the work presented in Chapter 5 of this thesis. End-tidal data points are required for both methane and acetylene. These data points are then used to determine the logarithmic disappearance profile for acetylene, with the gradient and intercept evaluated.

While the rebreathing method is an effective technique for measuring cardiac output, it does have limitations. Patient participation is required, so despite this technique being non-invasive, its potential for use within critical care or surgery remains limited. The second issue is associated with the build-up of carbon dioxide during the experiment. Carbon dioxide in the sealed rebreathing bag builds up over time as a result of respiration, leading to dyspnoea, shortness of breath. This effect can reduce the accuracy of the determined parameters due to unpredictable changes in the breath volumes.[98] There are two further limitations that apply to all foreign gas uptake experiments. The more soluble gas, in this case C_2H_2, will dissolve into the plasma within the blood of pulmonary capillaries, meaning that any shunted blood flow cannot be measured by this technique.[99] Finally, this experiment can only be repeated once the concentrations of the foreign gases have fallen back to normal levels – around 10 mins in the case of this technique.[100]

1.5.2.4 The Open Circuit Method

The open circuit method for determining cardiac output is built on the same foundations as the rebreathing method, requiring the evaluation and analysis of the concentrations of two inhaled foreign gases, one soluble and one insoluble in the blood. This technique has the advantage of not requiring patient participation; breathing can remain spontaneous, giving the open circuit method potential for use with unconscious patients. Exhalation into the room rather than a rebreathing bag also prevents a build up of carbon dioxide. This method is, however, more computationally involved than the rebreathing experiment.

Patients inspire a gas mixture containing 0.3% acetylene, 0.3% methane and 21% oxygen in nitrogen and this is followed by exhalation into the room air.[100] This procedure is followed for up

to ten breaths, using the setup shown in figure 1.4. Breathing through the nose is again prevented by a nose clip and the spectrometer is again placed in-line as close as possible to the mouthpiece.

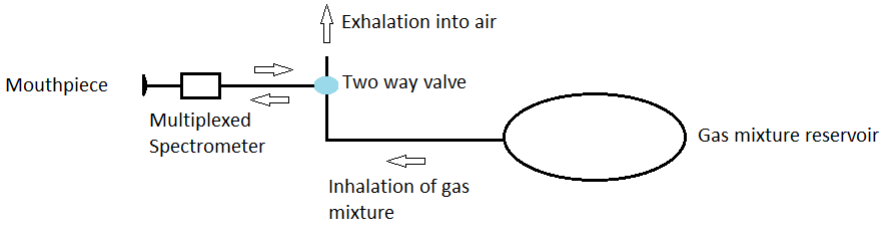


Figure 1.4: Schematic of the open circuit experiment. Arrows represent direction of flow of gas.

The determination of $\dot{Q}$ using the open circuit method involves the construction of equations with two unknown parameters representing the lung tissue volume and cardiac output:[101]

$$z_k \;=\; V_{ti}\, u_{1k} \;+\; \dot{Q}\, u_{2k} \tag{1.9}$$

where k is the breath number, and:

$$z_k \;=\; \frac{V_{(\mathrm{C_2H_2})}(k) \;-\; K_{EE}(k)\, V_{(\mathrm{CH_4})}(k)}{T_k} \tag{1.10}$$

$$u_{1k} \;=\; \beta_{t(\mathrm{C_2H_2})}\,(P_B \;-\; 47)\left(\frac{F_{E(\mathrm{C_2H_2})}(k) \;-\; F_{E(\mathrm{C_2H_2})}(k-1)}{T_k}\right) \tag{1.11}$$

$$u_{2k} \;=\; (P_B \;-\; 47)\big(\beta_{bl(\mathrm{C_2H_2})}\, F_{A(\mathrm{C_2H_2})}(k) - K_{EE}(k)\, \beta_{bl(\mathrm{CH_4})}\, F_{A(\mathrm{CH_4})}(k)\big)\;. \tag{1.12}$$

In the above equations $\beta_{t(i)}$ and $\beta_{bl(i)}$ are the solubilities of gas in lung tissue and blood respectively, $V_{(i)}$ refers to the inspired volume of each gas, F_E and F_A refer to end-tidal and alveolar concentrations of gas respectively, T_k is the time taken for each breath, and $K_{EE}(k)$ is defined as:

$$K_{EE}(k) \;=\; \frac{F_{E(C_2H_2)}(k) \;-\; F_{E(C_2H_2)}(k-1)}{F_{E(CH_4)}(k) - F_{E(CH_4)}(k-1)}\;. \tag{1.13}$$

These simultaneous equations are solved for pairs of breaths to find a solution for V_{ti} and $\dot{Q}$ for each pair, producing $n \times (n-1)$ solutions, where n is the total number of breaths. For each parameter, an initial average is found, outlying solutions (>98th percentile) are removed, and then a final result is found by averaging the remaining solutions.[100]

The open circuit technique is highly attractive due to the fact that it is non-invasive and requires no patient participation. To this point, however, utilisation of this technique has been limited by the availability of an accurate, fast responding gas analyser capable of making simultaneous measurements of methane and acetylene concentrations in the main airway. Chapter 5 describes the development of a device capable of meeting these demands and reports initial application of a modified open-circuit method for measuring cardiac output.

1.6 Summary

This chapter has described the current methods for assessing respiratory and cardiovascular function. In respiratory medicine, there is a range of techniques for quantifying different aspects of lung function. While some are non-invasive and relatively simple to undertake, for example spirometry and body plethysmography, these techniques give single, global measures of lung function, lacking the desired level of sensitivity. Sensitivity improvements would provide clinicians with the capability to both diagnose respiratory disease earlier, and to better monitor disease progression and response to treatment. Other techniques seek to quantify inhomogeneity within the lung, a more sensitive marker of the presence of disease. At present, these techniques remain complex to perform, MIGET, or lack the required accuracy and reproducibility, MBNW, preventing their widespread clinical use.

There are a range of methods for assessing cardiac output, but none of these have been deemed acceptable for widespread adoption in clinical settings. The techniques are limited, in some cases by their fundamentally highly invasive nature, for example the dye dilution and thermodilution method. For other methods, the limitations are associated with accuracy and reproducibility in clinical settings, for example the bioreactance and partial carbon dioxide rebreathing methods. Determination of cardiac output via breath analysis has shown clinical potential, but the short comings in current gas analysers have prevented developments towards a technique with the necessary accuracy and precision.

There is great clinical potential for techniques capable of meeting the challenges of elucidating respiratory and cardiac function. A method of determining respiratory and/or cardiac function that is safe, accurate, easy to perform, and non-invasive could provide clinicians with the ability to improve patient outcomes.

1.7 Outline of Thesis

This thesis describes non-invasive methods for assessing lung and heart function. Specifically, gas exchange at the mouth is measured using in-line laser absorption spectroscopy and the underlying physiology is then modelled.

In Chapter 2, the novel in-line molecular flow sensor (MFS) is described. The device evaluates concentrations of O_2, CO_2, and H_2O in the main airway utilising laser spectroscopy. The spectroscopic measurement systems are embedded within a flow sensor based on a pneumotachograph. Gas composition and flow, along with sample temperature and pressure are evaluated every 10 ms. Also described is a computational model which parametrises the level of inhomogeneity within the lung. This is termed the Lognormal Lung model. These two innovations are combined to provide a new technique for assessing lung function that is based on underlying respiratory physiology.

The third chapter describes a series of small scale clinical trials conducted to evaluate the measured lung inhomogeneity parameters in COPD patients. First, a cross-sectional study of COPD patients was performed, demonstrating abnormal inhomogeneity in patients with mild disease. Secondly, a method validation was undertaken, comparing derived parameters of ventilation and perfusion inhomogeneity with those from the well-established but highly invasive multiple gas elimination technique. Good correlation between the two techniques was reported for the airway parameters, ventilation inhomogeneity and fractional deadspace ventilation, but measures describing the perfusion inhomogeneity and fraction of shunt were more discordant. Finally, a cross-sectional study of recovered pneumothorax patients is presented. The hypothesis that the Lognormal Lung method would have the sensitivity to elucidate subtle abnormalities in the underlying lung physiology of these patients proved to be a null result. The new technique, however, was shown to be more sensitive than spirometry as a descriptor of the changes that occur as a result of smoking.

Investigating the lung inhomogeneity of patients with asthma is the focus of the fourth chapter. In the initial study, the indices determined by this new technique were evaluated as measures of disease activity in the lungs of asthmatic patients. Unlike spirometry in these patients, the inhomogeneity parameters were found to reflect disease control rather well. A longitudinal study of patients with severe eosinophilic asthma was carried out in parallel with clinical interventions to further establish the potential of these indices as measures of disease control. To ascertain optimal therapy for these

patients, a range of treatment options are prescribed for a short duration and the responses to each are evaluated within an asthma treatment pathway. Lung inhomogeneity responses to inhaled and injected steroid therapies were measured and compared with clinical measures including well-established biomarkers of airway inflammation. Responses to biologic therapy were also evaluated.

The final experimental chapter describes the development of a molecular flow sensor capable of contemporaneously evaluating the fluxes of five gas species. The design of a miniaturised Herriott cell is described, facilitating the sensitive measurement of trace amounts methane and acetylene. This optical system was integrated into an existing three-gas MFS, and the performance of the resulting five-gas analyser was evaluated. A computational model of methane and acetylene uptake was written, allowing cardiac output to be estimated from data measured during tracer gas washin. A proof of principle study is described, evaluating the cardiac output repeatability at rest and exercise in eight healthy volunteers. The reproducibility was found to be good, and good agreement of cardiac output determined by this non-invasive method with literature was established. Finally, the conclusions of this work are summarised and potential avenues of future work are discussed.

Chapter 2

Molecular Flow Sensing and Assessment of Lung Inhomogeneity

The sampling and analysis of exhaled breath has attracted significant interest in the areas of medical diagnosis and disease monitoring. This interest is a reflection of the fundamentally non-invasive nature of breath analysis and the unlimited sample supply. This chapter starts by describing the existing methodologies in the field of breath diagnostics, discussing the potentials and limitations of currently employed techniques.

A recently developed technology for accurate measurement of gas exchange is then introduced. This molecular flow sensor (MFS) utilises highly accurate laser absorption spectroscopy to evaluate the concentrations of oxygen, carbon dioxide, and water within the main airway every 10 ms. The spectroscopic systems are embedded within a precision flow meter based on the principles associated with pneumotachograph-type devices. Gas exchange can be directly calculated as the integral of the product of the measured respiratory flows and gas concentrations. The theoretical bases behind the measurement techniques employed within this device are discussed, along with a detailed description of the device's structural design, calibration, and an assessment of performance.

In the final part of this chapter, a computational model of the lung is described. This model makes the assumption that, if measured with sufficient accuracy, there is enough information contained within the way that expiratory gases emerge from the lungs during steady breathing and during a subsequent period of inert gas washout to infer much of the form and degree of inhomogeneity present within the lung. Lung inhomogeneity is known to increase with respiratory disease.[43,44] A non-invasive quantitative assessment of lung inhomogeneity that is accurate, reliable and easy

to perform, both from the point of view of patients and operators, has potential to provide a step change improvement in the diagnosis of early stage respiratory disease.

2.1 Existing Methodology in Breath Diagnostics

The most common strategies for concentration analysis in the field of breath diagnostics are based upon mass spectrometry and non-dispersive infrared sensors. Analysis in breath diagnostics can be divided into two basic types: mainstream analysis, also called in-line or non-divergent, and sidestream analysis.[102] A sidestream system will transport a portion of breath, either inspired or expired, along a tube to be analysed by a sensor away from the principal path of gas flow. In contrast, mainstream devices feature concentration analysis by a sensor that is placed directly in the gas flow's principal path.

Sidestream sensors have the advantage of being more robust and sensitive due to the remote location of the sensing apparatus. There are, however, disadvantages associated with sidestream devices that relate to transportation of the gas. There is a time lapse associated with the gas transportation, causing a delay between the patient's breathing and the analysis. The validity of gas concentration measured via sidestream analysis is potentially drawn into question by several effects of the gas transportation to the sensor: mixing of the sample, changes in the water vapour pressure and a pressure drop along the sampling tube. There will also be a different pressure, temperature and humidity at the sensor compared to the body. These effects, when considered together, could contribute to incorrect concentration outputs from the analyser, potentially leading to incorrect or inaccurate diagnoses. Furthermore, sidestream analysis cannot provide accurate measurements of flux. These fundamental limitations of sidestream systems can be overcome by mainstream devices, facilitating more accurate concentration analysis, provided they are designed in a robust and compact fashion.

Mass spectrometry is currently the most commonly used method of concentration analysis in breath diagnostics. In this technique, the gaseous sample is ionised, often by direct electron impact, and an electric field used to separate ions according to their mass-to-charge ratio (m/z), producing a characteristic mass spectrum.[103] The intensity of the m/z peaks is used to infer concentrations of the constituents of breath. The respired gas is continuously sampled, and fast acquisition rates such as 20 Hz are achievable. Mass spectroscopy is primarily used for 'trace gas' sensing in respiratory gas

analysis. For example, there is significant interest associated with the analysis of volatile organic compounds (VOCs), gas phase biomarkers the production of which in the body is modulated by a variety of diseases.[104] These compounds are typically present in breath at the 1-100 ppb range. Fragmentation of these samples during ionisation by direct electron impact can be suppressed by utilising proton transfer reaction mass spectrometry (PTR-MS), where positive ions are introduced to act as ion source reagents.[105] Hydronium ions (H_3O^+) have been used for this purpose, achieving low ppb sensitivities for detection of VOCs.[106] The applicability of this technique, however, is limited to species with a greater proton affinity than water or else proton transfer will not occur. To extend this technique to a wider range of breath compounds, chemical ionisation mass spectrometry (CIMS) has been developed, with ionised species such as NO^+, Kr^+, and Xe^+ serving as ion source reagents.[107] Both PTR-MS and CIMS offer good detection sensitivities, a few ppb or better, but maximum detectable concentrations are limited by the ion source reagent number densities. Instrument responses will generally become non-linear at concentrations exceeding 10 ppm.[105] Field asymmetric ion mobility spectrometry (FAIMS) has also shown potential for VOC sensing, using a rapidly time-varying electric field to separate ionised species based not on mass, but on species mobility in an electric field, providing a wider range of detectable concentrations and/or species.[108] One major limitation with this emerging technology, however, has been the difficulty to achieve reproducibility and cross-calibration between different instruments.[109] Mass spectrometry is only used in sidestream gas analysis, due to the modification of the sample that is required. In addition to the disadvantages of sidestream analysis, the issues with mass spectrometry include high power consumption, large cost, bulky nature (although they are getting smaller), sensitivity to mechanical vibration and shock and complexity of the frequent recalibration.[73]

Non-dispersive infrared (NDIR) sensors make use of IR lamps emitting radiation across a broad range of frequencies. Prior to detection, an optical filter is used to eliminate all light except that at the specific wavelengths at which the target gas molecules absorb. The gas concentrations are determined following the subtracting of thermal background signals. Thermal offset is calibrated using a rapidly rotating mechanical chopper. NDIR sensors are principally used as sidestream devices due to the vulnerability of moving parts such as the mechanical chopper, to mechanical vibrations and mishandling.[102]

2.2 Laser Absorption Spectroscopy

Laser absorption spectroscopy is a powerful analytic tool which combines generality, all atoms and molecules absorb electromagnetic (EM) radiation at some frequency, and specificity, all atoms and molecules have unique frequency-dependent absorption profiles. Lasers provide tunable monochromatic radiation making them ideal for high resolution spectroscopy. The concentration of individual species can be quantitatively determined using relatively straightforward analysis, with the measurements performed in a non-destructive way.[110] Absorption spectroscopy measures the attenuation of electromagnetic radiation as it passes through an absorbing medium. Attenuation occurs when radiation of an appropriate resonant frequency interacts with the transition dipole moment of a molecule as it oscillates through a specific vibration, rotation or combination of the two. The Beer-Lambert Law describes the attenuation of radiation when it passes through a homogeneous, weakly absorbing medium:[111]

$$I(\nu) = I_0(\nu)e^{-\alpha(\nu)l} \quad , \tag{2.1}$$

where $I(\nu)$ is the light intensity transmitted through the absorbing medium, $I_0(\nu)$ is the incident light intensity, l is the path length through the medium, $\alpha(\nu)$ is the frequency dependent absorption coefficient and ν is the frequency of the radiation, typically quoted in wavenumbers, cm^{-1}. The product $\alpha(\nu)l$ is traditionally referred to as absorbance. The absorption coefficient is described by $\alpha(\nu) = \sigma(\nu)c$, where c is the absorbing species' concentration and $\sigma(\nu)$ is the absorption cross-section, an effective area that a photon needs to traverse in order to be absorbed.

The frequency dependence of the absorption cross-section will be unique, making absorption spectroscopy a highly selective technique. Selectivity coupled with the return of absolute concentrations makes it a powerful and attractive technique for gas measurement. The lineshapes for individual transitions vary with experimental conditions, and as such, it is common to report absorption cross-sections for a given transition as its integrated value, $\sigma_{INT} = \int \sigma(\nu)\mathrm{d}\nu$. Measurements of the absolute concentration of a specific gas can be determined by fitting an absorption spectrum to a lineshape model in order to find the integrated area of a sample's absorption, then applying the Beer-Lambert Law. The factors affecting the width of a spectral lineshape can be broadly split into two classes, known as homogeneous and inhomogeneous broadening mechanisms. Homogeneous broadening refers to factors that equally affect all molecules.[112] One example is natural broadening,

a fundamental quantum mechanical broadening contribution which arises from the non-zero uncertainty in the transition energy, ΔE, introduced by the finite lifetime, τ, that the upper and lower quantum states experience. By analogy with the Heisenberg uncertainty principle:

$$\tau \Delta E \geq \hbar \quad , \tag{2.2}$$

For typical gas sensing applications at room temperature and within the mid-infrared spectral region, this contribution to the linewidth ($\sim$ kHz) is orders of magnitude smaller than other broadening mechanisms and can be neglected.

Pressure broadening, also called collisional broadening, is another case of homogeneous broadening. Collisions between neighbouring gas molecules reduce the lifetime of both the upper and lower quantum states involved in a spectroscopic transition and as a result there is a consequent increase in the energy uncertainty associated with the transition. Broadening will be more significant for greater collision rates, and so this effect is more marked at high pressures. Pressure broadening results in a Lorentzian lineshape, $L(\nu)$, analytically described by

$$L(\nu) = \frac{2}{\pi} \frac{\Delta\nu_L}{\Delta\nu_L^2 + 4(\nu - \nu_0)^2} \quad , \tag{2.3}$$

where $\Delta\nu_L$ is the full-width half-maximum (FWHM) Lorentzian component, often expressed as

$$\Delta\nu_L = 2 \sum_i \gamma_i \, p_i \quad , \tag{2.4}$$

with γ being the broadening coefficient of a given transition for the target molecules' collisions with molecules of species i, and p_i being the partial pressure of species i in the sample. Broadening coefficients in air, γ_{air}, are typically ca. $0.05\,\mathrm{cm^{-1}atm^{-1}}$, although self broadening, γ_{self}, can be several times larger in polar molecules. As well as broadening spectral transitions, collisions also shift the frequency of the transition line centre.[113] This pressure shifting is typically linear with pressure and can be expressed in wavenumber units by:[114]

$$\nu^* = \nu_0 + \sum_i \delta_i \, p_i \quad , \tag{2.5}$$

where ν^* and ν_0 are the pressure shifted and vacuum transition energies at line centre, respectively, δ_i is the shift coefficient for the given transition by species i, and p_i is the partial pressure of species i. The pressure shift coefficients have the same units as the pressure broadening coefficients, but are

typically an order of magnitude smaller. Pressure line shifts have been confirmed to be negligible in this work.

The most common example of an inhomogeneous broadening mechanism is Doppler broadening. There is a shift in the frequency of absorbed radiation caused by the relative motion of an absorbing molecule with respect to the propagation direction of the radiation. The distribution of thermal velocities within a gas sample is Maxwellian in nature, leading to a distribution of absorbed frequencies that is described by a Gaussian lineshape.[112]

$$G(\nu) = \frac{2}{\Delta\nu_G}\sqrt{\frac{\ln 2}{\pi}}\ \exp\left[-\frac{4\ln 2(\nu-\nu_0)^2}{\Delta\nu_G^2}\right] \quad , \tag{2.6}$$

where the linewidth-dependence on the sample temperature, $\Delta\nu_G(T)$, is described by

$$\Delta\nu_G = 2\nu_0\sqrt{\frac{2k_BT\ln 2}{mc^2}} \quad , \tag{2.7}$$

for a molecule of mass m. As this highlights, the FWHM of a Doppler lineshape, $\Delta\nu_G$, is dependent on the transition frequency, and thus ranges from ten of MHz in the mid-infrared up to a few GHz in the UV for a light molecule such as O_2. At low pressures, a few Torr or less, spectral lineshapes are dominated by the Gaussian contribution that arises from the Doppler broadening mechanism.

The Voigt profile, shown in fig. 2.1, describes the lineshape that is observed when there are significant contributions from both collisional and Doppler broadening.[115] This lineshape results from the convolution of Equations 2.3 and 2.6, and takes the following form:

$$V(\nu) = \frac{2}{\Delta\nu_G}\sqrt{\frac{\ln 2}{\pi}}\frac{y}{\pi}\int_{-\infty}^{+\infty}\frac{e^{-t^2}}{y^2+(x-t)^2}\,\mathrm{d}t \quad , \tag{2.8}$$

where x and y are the detuning and Lorenztian width, respectively, both normalised to the Doppler width

$$x = \sqrt{\ln 2}\,\frac{2(\nu-\nu_0)}{\Delta\nu_G} \quad , \tag{2.9}$$

$$y = \sqrt{\ln 2}\,\frac{\Delta\nu_L}{\Delta\nu_G} \quad . \tag{2.10}$$

A Voigt profile is the most appropriate to describe the spectra shown in this work, all of which are evaluated at atmospheric pressure where the contributions to broadening are comparable in magnitude.

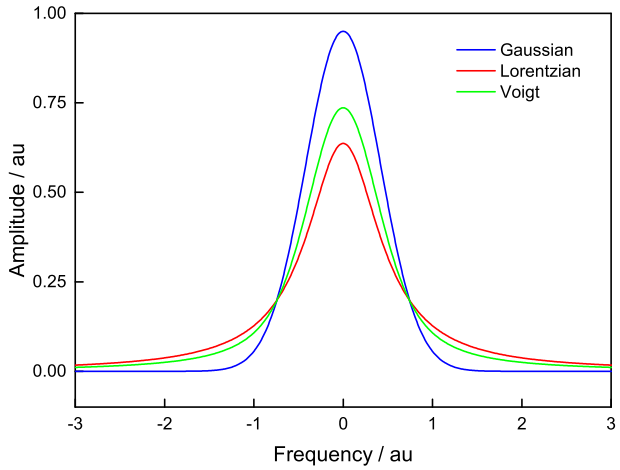


Figure 2.1: Comparison of Gaussian, Lorentzian and Voigt lineshapes, each of which have a total area of 1 and a full-width-half-maximum of 1. The Voigt lineshape displayed here has equal contributions from the Gaussian and Lorentzian components.

The sensitivity of laser absorption spectrometers for trace gas measurements can be limited by the requirement to measure small intensity changes relative to a large baseline intensity.[111] This issue can be addressed using optical cavities,[116] which increase optical path length, and modulation techniques, such as frequency modulation,[117] which increase the signal-to-noise ratio by moving detection to higher frequencies where the acoustic noise, for example, is reduced. The sensitivity of the spectrometers utilised in this thesis will principally be quantified by a minimum detectable concentration (c_{min}) for the gas species in question, determined from the residual of a fit of a modelled lineshape profile to an experimental spectrum. The standard deviation of the residual (σ_{res}) is used to determine c_{min}:

$$c_{min} = \frac{1}{l\,\sigma_{max}} \ln\left(\frac{I_0}{I_0 - \sigma_{res}}\right) \quad , \tag{2.11}$$

where σ_{max} is calculated from the integrated absorption coefficient data using:

$$\sigma_{max} = \frac{2\,\sigma_{INT}}{\pi\,FWHM} \quad . \tag{2.12}$$

The pressure broadening coefficients, γ can be used to determine the FWHM. The HITRAN spectroscopic database provides numerical values for broadening and absorption coefficients required for these calculations.[118]

2.3 Molecular Flow Sensing

A new technology for measuring gas exchange has been developed, utilising laser absorption spectroscopy to evaluate the concentrations of physiologically significant molecules within breath. [119] This novel *molecular flow sensor* (MFS) combines gas composition data with measurements of temperature, pressure and flow. Volunteers breathe into the device's measurement head via a mouthpiece and bacterial filter, as shown in Figure 2.2. The measurement head is connected to the MFS electronics module by a pair of hybrid cables. The device is controlled from a laptop connected to the electronics module via a USB lead. When the device is running, the measured data are streamed to this laptop, with analysis software written to provide real time reporting of gas concentrations. The respired gas is analysed for oxygen, carbon dioxide and water vapour within the main gas stream every 10 ms. The principal advantage of analysing the gas within the airway, as opposed to more traditional sidestream technology, is that it provides measurements that can be precisely aligned in time with measurements of respiratory flow, which are made under the same physiochemical conditions. [102] The precise time alignment offered by the system allows integration of the product of respiratory flow and concentration in a manner that is sufficiently accurate to calculate gas exchange. The motivation to facilitate these measurements is the potential positive impact of monitoring a patient's gas exchange in a range of clinical settings (e.g. anaesthesia, intensive care units), where current side-stream technology is not wholly applicable. [120,121] The challenges underlying the development of the MFS originate in ensuring volunteer comfort whilst using the device. The volume of gas within the measurement cell, known as the device deadspace, must be limited to ensure that additional volunteer effort is not required to prevent rebreathing of previously exhaled gas. Measures to reduce the deadspace risk increasing the equipment's resistance to respiratory flow, altering breathing patterns and respiratory mechanics as a result. [122] The result of these competing factors is a compact device, contributing only 55 ml of deadspace to the airway, with a relatively low resistance and a flow axis bore size that is compatible with customarily used respiratory tubing.

The MFS directly measures respiratory gas concentrations in the main airway. Within the measurement cell carbon dioxide and water vapour concentrations are measured by direct laser absorption spectroscopy. The oxygen concentration is contemporaneously evaluated using the technique of cavity enhanced absorption spectroscopy (CEAS). Given concentrations of O_2, CO_2 and H_2O,



Figure 2.2: Photo of volunteer breathing into molecular flow sensor via a mouthpiece and bacterial filter. The spectroscopic and sensor systems are built into a measurement cell housed within the measurement head. The subject provided consent for the reproduction of this photograph.

the balance gas (primarily N_2) concentration can be calculated by subtraction. Schematics of the device's measurement cell are shown in figure 2.3.[119] The gas analysis system is embedded within a precision flow meter based on the principles associated with pneumotachograph-type devices.[123] This highly accurate system operates by measuring the pressure drop across a pair of mesh screens and then calculating the associated flow rate. The gas composition analysis within the flow meter allows for accurate calculation of the instantaneous viscosity and density of the respired gas which is used to enhance the accuracy of the measurement of respiratory flow.

The following sections describe the measurement systems used within the MFS, several of which have been improved during the course of this research. The spectroscopic systems are described, initially for evaluation of CO_2 and H_2O concentrations and then for O_2 concentration determination. The temperature, pressure and flow measurement systems are then described.

2.3.1 Water and Carbon Dioxide Spectroscopy

In order to evaluate concentrations of H_2O and CO_2 within the MFS, direct laser absorption spectroscopy is utilised. Distributed feedback (DFB) diode lasers operating in the near-IR region of the electromagnetic spectrum were chosen as light sources for this application. Diode lasers are photon-emitting semiconductor *p-n* junction diodes. Lasing action is based upon radiative recombination of electron-hole pairs across the material bandgap which separates the conduction and valence energy bands. Direct-bandgap semiconductor material is typically confined within an optical resonator, where population inversion and amplified stimulated emission efficiently take place. The emitted

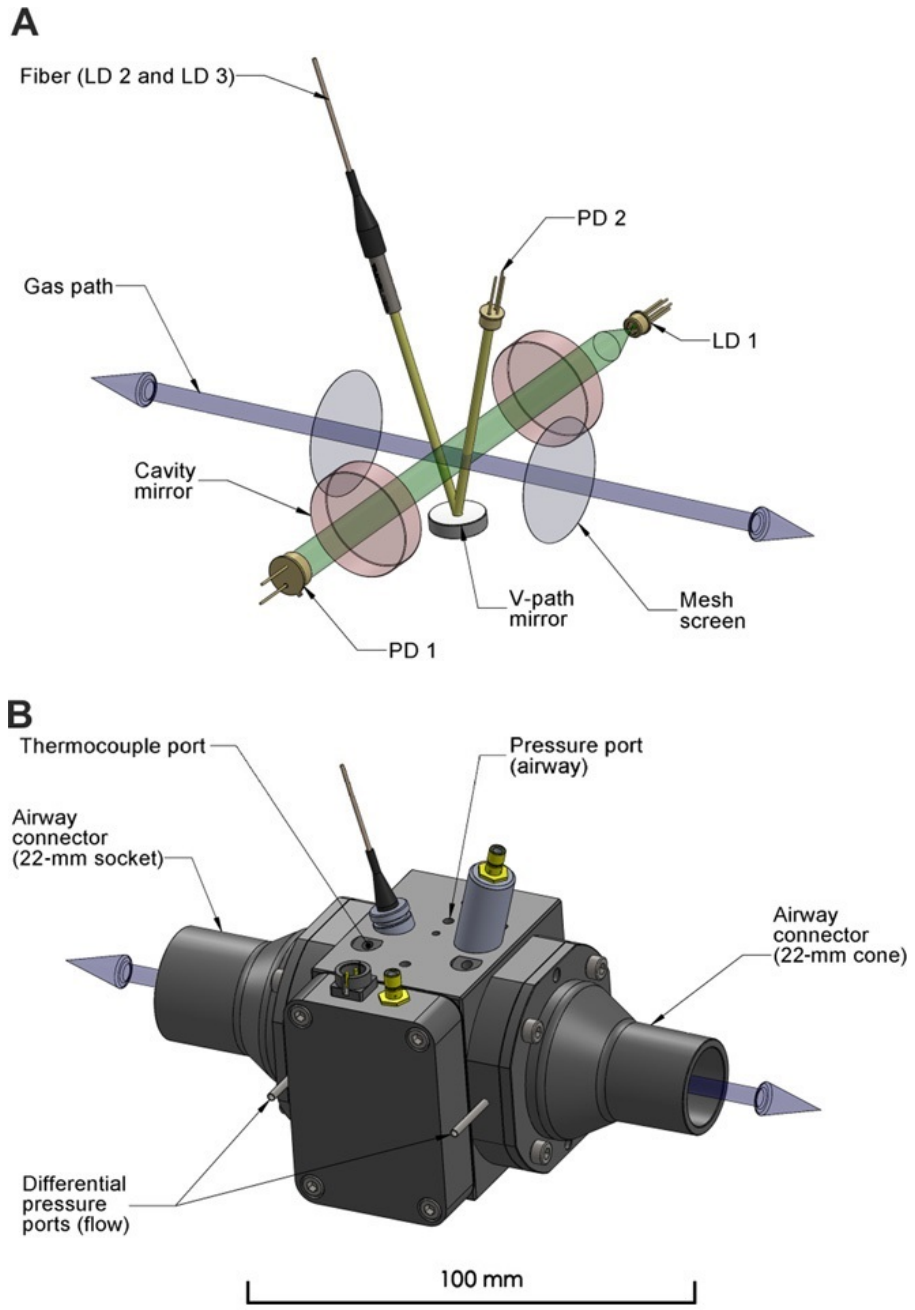


Figure 2.3: (**A**) simplified diagram of the multichannel absorption spectrometer and pneumotachograph within the measurement head. The bidirectional gas path (blue) is shown along with the two mesh screens (grey), across which pressure drop is measured. Radiation used for probing oxygen is injected into an optical cavity constructed from a pair of highly reflective mirrors (red) and collected by a photodiode (PD 1) positioned along the optical axis (green). Radiation probing carbon dioxide and water vapour is launched into the V path (yellow), reflected by a concave mirror, and collected by the photodiode (PD 2). (**B**) Three-dimensional CAD model of the measurement cell. Differential pressure ports located on the outer sides of the mesh screens are shown, together with the ports for the thermocouple probe and airway pressure sensor.

wavelength is determined by the chemical nature of the active material, and is generally tuned by altering the refractive index of the active material via temperature or injection current tuning. DFB diode lasers incorporate an optical feedback element, in the form of a Bragg grating lithographically engraved on a confining layer, and this optical feedback enables efficient selection and stabilisation of the laser wavelength. Development of DFB diode lasers has been driven by the telecommunications industry over the past decades, such that nowadays these lasers offer compact sources of single-mode, tunable radiation at relatively high powers (up to tens of mW). While commercial devices are commonly marketed as being available across the 0.4-2.7 μm spectral range, it should be noted that lasers are not available at all wavelengths within this range and costs escalate significantly towards the upper wavelength limit. Furthermore, only relatively weakly absorbing molecular features, resulting from rovibrational overtone or combination bands, can be accessed in the visible and near-infrared regions, limiting the maximum attainable sensitivities and hence minimum detectable concentrations of spectrometers based on such light sources.

The spectrometers for detecting these species needed to be able to provide good sensitivities over a reasonably broad range of concentrations; concentrations of CO_2 and H_2O in exhaled breath rise to 6 and 2 % of the total expired number density respectively. Transitions were sought within the operating range of DFB diode lasers that would provide sufficient absorption to ensure sensitive concentration determination via direct absorption, and that were free from interference resulting from transitions arising from other major components of breath. The chosen transitions are shown in Table 2.1.

Table 2.1: Spectroscopic data of carbon dioxide and water transitions from HITRAN database.[118] The rotational assignment is reported as $\Delta J(J")$ for CO_2 and as $(J_{K_aK_c})' \leftarrow (J_{K_aK_c})"$ for H_2O vapour. The double prime (") and single prime (') symbols denote the lower and upper rotational energy states of the molecules, respectively.

Molecule	ν_0/cm^{-1}	σ_{INT}/cm^{2}cm^{-1}	γ_{air}/cm^{-1}atm^{-1}	γ_{self}/cm^{-1}atm^{-1}	Assignment
CO_2	4989.97	1.287×10^{-21}	0.075	0.102	$2\nu_1 + \nu_3$ R(16)
H_2O	7306.75	1.795×10^{-20}	0.093	0.51	$\nu_1 + \nu_3$ ($3_{12} \leftarrow 2_{12}$)

The spectral feature of CO_2 at 2004 nm, the R(16) transition within the $\nu_1 + \nu_3$ combination band, was targeted. This transition was probed using a commercially available 3 mW DFB diode laser (Nanoplus S/N:1862/15-14). The laser was housed within the MFS electronics module, along

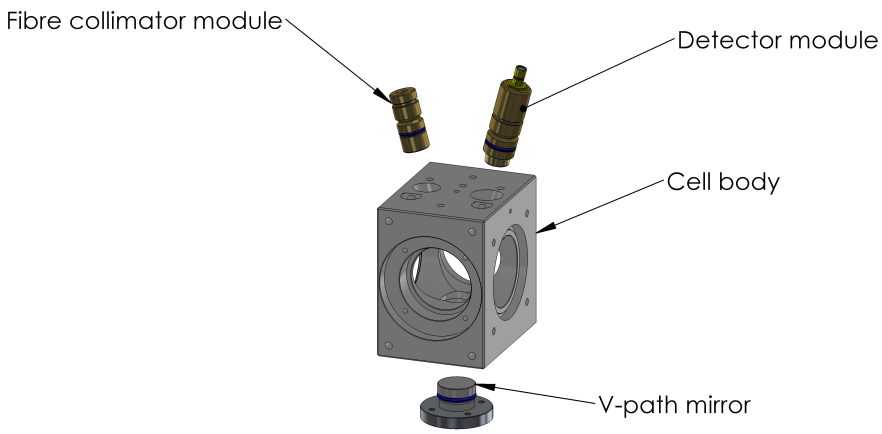


Figure 2.4: Schematic of v-path components. Radiation is injected by a collimating lens, reflected by the v-path mirror, and detected by a InGaAs photodiode housed within the detector module.

with the control circuits governing the temperature and current applied to the laser chip. The detector used with this laser was an InGaAs photodiode (Hamamatsu G12182-020K). The peak photosensitivity of this detector was at 1.95 μm, with a circular photosensitive area with a 2 mm diameter. The detector is housed in a sealed package. The laser was scanned over the spectral range of interest at a frequency of 200 Hz, with two 200 data point spectra averaged so that a transmission spectrum was reported every 10 ms. A 5.4 cm optical v-path through the gas sample was probed, the light injected and detected on the upper surface of the body of the measurement cell, as shown in Figure 2.4. The mirror used within the v-path is a concave spherical mirror with a protected aluminium surface (Thorlabs CM127-025-G01). The mirror has a half inch diameter and a focal length of 25 mm, ensuring that the optical beam is focussed close to the surface of the detector module.

Quantitative analysis of the absorbance signals through a sample requires knowledge of the spectral range across which the laser is tuned. This is achieved by assessing the laser's emission wavelength at each time point within a spectrum by injecting the radiation onto an optical spectrum analyser. The features of the detected light intensity profile as the laser frequency is scanned provides information on the time-to-wavenumber calibration during each laser ramp. Periodic maxima in the signal are observed at the resonant frequencies, where the light exhibits constructive interference, which are equally spaced in the optical frequency domain by a quantity know as the free spectral

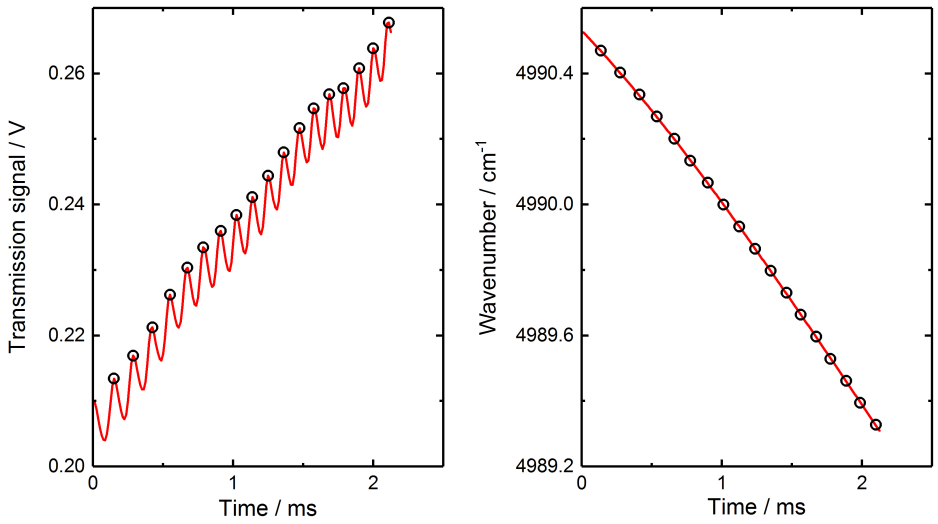


Figure 2.5: Spectral calibration for quantitative CO_2 analysis. The left plot shows the transmission spectrum detected within the spectral analyser in red, with identified transmission local maxima shown with open black circles. The resulting calibration is shown in red on the right, a third order polynomial fitted to the data shown by open circles.

range (FSR). In the case of the 2004 nm laser, a calibration was achieved using a spectral analyser (Melles Griot) with a free spectral range of 0.067 cm^{-1}. The output from the spectral analyser is averaged over 20 seconds and the calibration established by fitting a third order polynomial to the data representing the absolute wavenumber points (integer multiples of the FSR offset by the central spectral frequency) versus the time stamps of the maxima in the transmission signal. An example transmission signal and resulting time-to-wavenumber calibration from a free spectral analyser is shown in Figure 2.5.

Software was written in LabVIEW to determine target gas concentrations from measured spectra in real time. To evaluate number density from measured absorption spectra, a theoretically predicted Voigt lineshape is regressed onto the measured data. For direct absorption spectroscopy as is used here, the Beer-Lambert law stated in Equation 2.1 can be directly applied, giving:

$$c_n \sigma l = \ln\left(\frac{I_0 - I_{off}}{I_n - I_{off}}\right) \quad . \tag{2.13}$$

where I_n is the measured spectrum, I_0 is the baseline spectrum in the absence of absorbing species, and I_{off} is the offset signal recorded in the absence of radiation from the laser. One complication associated with determining concentrations in real time is that the baseline, I_0, cannot be measured

either preceding or simultaneously with each experimental spectrum. The solution is to measure baseline data prior to system use, under conditions of flowing pure nitrogen. During use, however, the form of the baseline will subtly change due to drift, within the laser or associated electronics, and/or due to changes in the performance of the optical components. It is assumed that the real time absorbance function can be related to that calculated from the baseline recorded in nitrogen through a relatively low degree of translation.

$$\ln\left(\frac{I_0 - I_{off}}{I_n - I_{off}}\right) = \ln\left(\frac{I_{0,N_2} - I_{off}}{I_n - I_{off}}\right) + q_1 \tag{2.14}$$

where I_{0,N_2} is the baseline signal recorded whilst flushing the system with nitrogen. The parameter q_1 allows the baseline variation during data collection to be accounted for and quantified. The concentration determined from a measured spectrum, c_n, is then related to an arbitrary reference concentration, c_{ref}, by the parameter q_2

$$c_n = q_2 \; c_{ref} \quad . \tag{2.15}$$

The definitions of parameters q_1 and q_2 can be combined with the Beer-Lambert law to give

$$q_2 \, c_{ref} \, \sigma \, l = \ln\left(\frac{I_{0,N_2} - I_{off}}{I_n - I_{off}}\right) + q_1 \quad . \tag{2.16}$$

In this expression, the measured spectrum, recorded baseline and offset data take the form of data arrays, as does the absorption cross-section σ. The form of σ is the result of a modelled Voigt lineshape evaluated using a method similar in nature to that proposed by Humlicek.[124] Inputs into this model include the target transition's pressure broadening parameters and integrated absorption cross-section taken from the literature. The laser's periodic time-to-wavenumber calibration is also required. The temperature and pressure of the sample, measured contemporaneously with the experimental spectrum, as well as the gas composition determined for the previous 10 ms window, are used to calculate appropriate Gaussian and Lorentzian broadening contributions to the lineshape model. The product of σ, c_{ref} and l is an absorbance signal simulated for the reference concentration and measured optical path length. The multiple linear regression module in LabVIEW is then used to evaluate Equation 2.16 for each data point within an experimental spectrum to identify best fit regression parameters q_1 and q_2. The latter parameter relates directly to the reported gas concentration evaluated for a given spectrum. In order to assess the success of this method, the

quality of fit can be determined by constructing the modelled spectrum, $I_{n,fit}$ produced by the determined parameters:

$$I_{n,fit} = e^{-(q_2\, c_n\, \sigma\, l\, -\, q_1)}(I_{0,N_2} - I_{off}) + I_{off} \quad . \tag{2.17}$$

The calibration procedure required in order to evaluate CO_2 concentrations by this method is to measure a baseline spectrum in the absence of the target species. This is achieved by flowing pure N_2 through the measurement cell at a rate of around $5\,\mathrm{l\,min^{-1}}$. The photodiode offset is measured initially, with the CO_2 laser turned off, and then a transmission baseline signal is measured with the laser turned on and the current to the laser chip ramping periodically. Both calibration steps are 30 sec in duration, with the final 5 sec of each averaged to give the spectra used within the analysis software.

Figure 2.6 illustrates an example measured CO_2 spectrum and the associated absorbance spectrum for a gas mixture with 5% CO_2 composition (BOC Industrial Gases). In both cases, the modelled best fit data is overlaid, illustrating the quality of the fit to the data. Despite the presence of a degree of structure in the residual profiles shown, particularly at line centre, the Voigt profile was determined to be the optimal lineshape for this application. The sums of squared residuals, and measurement sensitivity as a result, were evaluated for two further lineshapes, the Galatry [125] and Rautian [126] profiles. These profiles extend the Voigt profile to consider collisional narrowing, by hard- and soft-collision models for the Rautian and Galatry profiles, respectively. [127] This effect, however, describing collision-induced reduction of the Doppler width, is insignificant at atmospheric pressures due collisional broadening dominating the lineshape. Accordingly, neither the Galatry profile nor the Rautian profile improved measurement sensitivity (i.e. decreased the residuals), despite increased computational complexity. Thus, simulated Voigt lineshapes were fit to the measured spectra throughout this work.

The data analysis method described above allows CO_2 concentrations to be evaluated in real time, at a frequency of 100 Hz, with a calculated minimum detectable concentration of 0.047% of total number density at atmospheric pressure and room temperature. This value is only marginally higher than current atmospheric CO_2 levels (just above 400 ppm). An example of the concentration data determined by this analysis is shown in Figure 2.7 for a volunteer breathing. The determined concentration is close to zero during inspiration of air, rises rapidly early in expiration and then

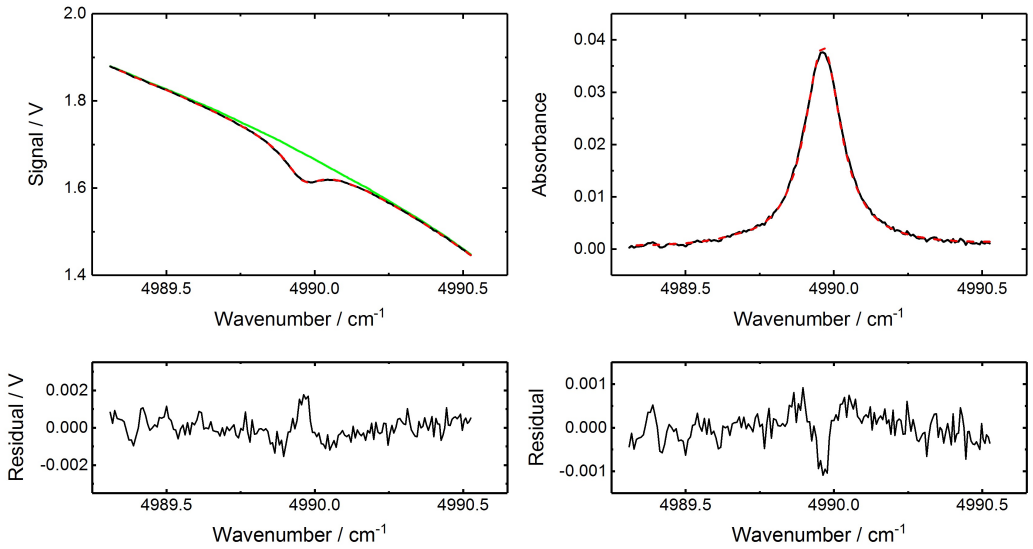


Figure 2.6: An example transmission (left) and absorbance (right) spectrum from CO_2 spectrometer. In the upper plots, detected signals are shown in black and best fit Voigt simulations are shown as dashed red lines. The optimised modelled transmission baseline (following application of q_1 adjustment) is shown in green. The lower plots show the residual spectra for the fits to the data.

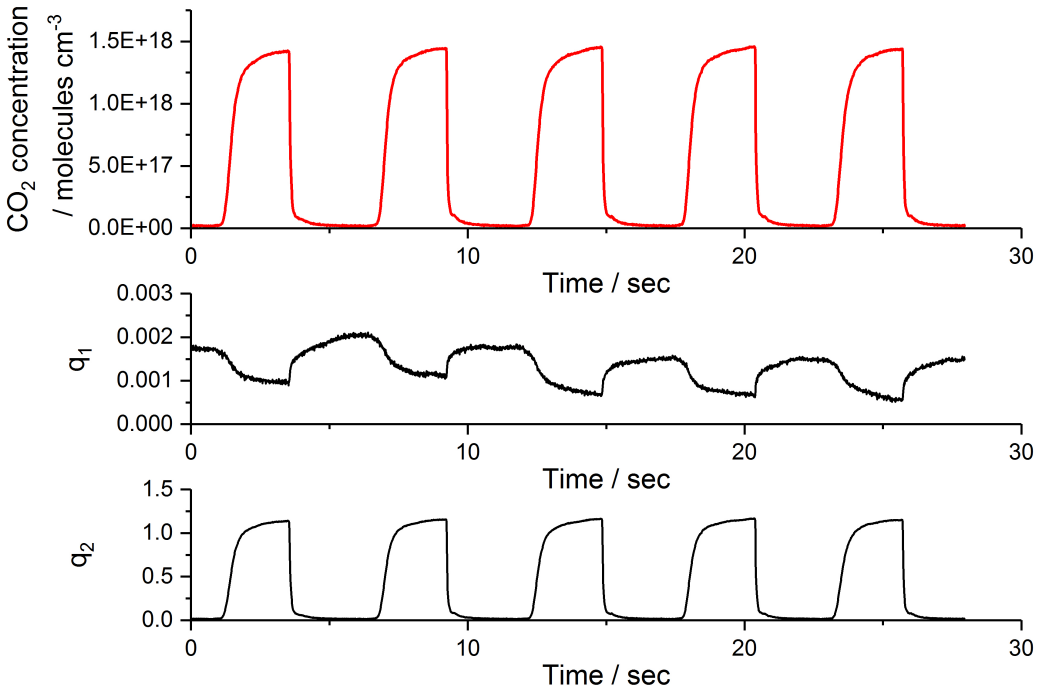


Figure 2.7: CO_2 profile during volunteer breathing for 5 breaths. The upper plot shows the CO_2 concentration profiles determined in real time from recorded transmission spectra. The middle and lower plots show the variation in Voigt simulation model for parameters q_1 and q_2 respectively.

reaches an end-expiratory value of ca. 1.45×10^{18} molecules cm^{-3}, a gas fraction of around 6%. The average q_1 parameter value during this time is 0.0013, representing a relatively low correction, around 3% of the maximum absorbance at the line centre. The profile is periodic in nature, illustrating the variation from measured baseline as the temperature and water content in the sample varies. The q_2 parameter is proportional to the determined CO_2 concentration.

To evaluate the concentration of H_2O vapour, an R-branch transition within the $\nu_1 + \nu_3$ combination band at 1368 nm was probed by a commercially available diode laser (NLK1E5EAA, NTT Electronics). This laser was employed in a similar way to that probing the CO_2 transition, controlled and housed within the MFS electronics module and utilising direct laser absorption spectroscopy to evaluate gas concentrations over an optical v-path with a path length close to 5 cm. The same InGaAs photodiode (Hamamatsu G12182-020K) is used for detecting the 1.37 μm radiation, providing a sufficient signal-to-noise ratio despite the spectral distance from the peak photosensitivity at 1.95 μm. The time-to-wavenumber calibration for the laser ramp was achieved using the same spectral analyser (Melles Griot, with a free spectral range of 0.067 cm^{-1}) as before. The analysis software described above was straightforwardly be adapted to determine gas concentrations from collected spectra. The spectroscopic parameters, pressure broadening and integrated cross section parameters, within the simulation of the Voigt lineshape were altered to the appropriate values for the targeted H_2O transition.

Figure 2.8 illustrates an example measured H_2O spectrum and the associated absorbance spectrum with the modelled best fit data in both cases. The minimum detectable concentration evaluated from this spectrum is 53 ppm of the gas composition at atmospheric pressure and a temperature of 298 K. This minimum detectable concentration value is approximately a ninth of that for the CO_2 channel. This is in large part a result of the larger integrated cross section for the H_2O transition given that the sources of noise are similar; the same detector is used and the two lasers have comparable power and signal stability. An exemplar H_2O profile for five volunteer breaths is shown in Figure 2.9. The inspired concentration is non-zero due to the humidity of the compressed air supply and rises during expiration to reach an end-expiratory gas fraction of 1.3%. The periodic variation of the q_1 parameter is more marked than was seen for the CO_2 spectrometer and the correction appears to become more significant as the H_2O concentration rises. Despite increasing the operating

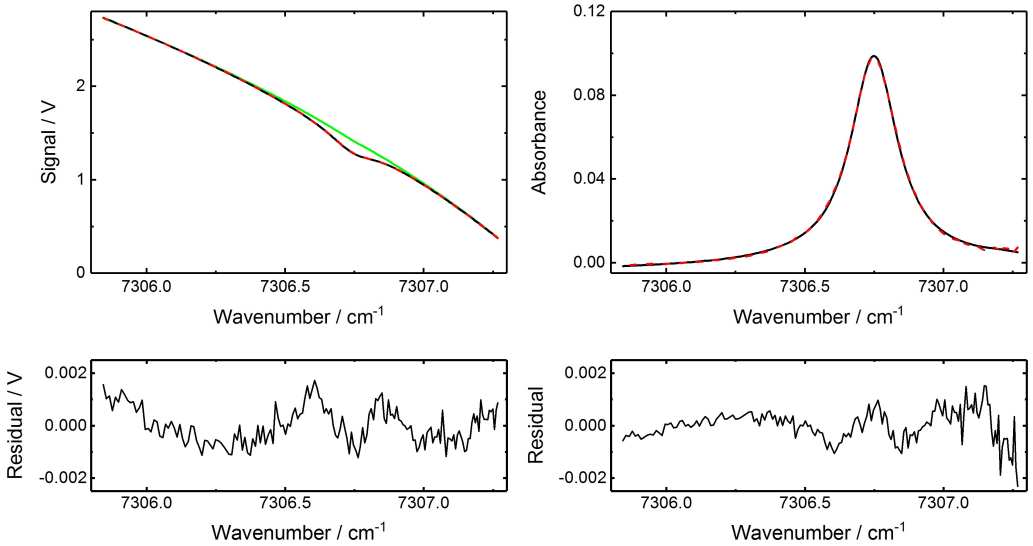


Figure 2.8: An example transmission (left) and absorbance (right) spectrum from H_2O. In the upper plots, detected signals are shown in black and best fit Voigt simulations are shown as dashed red lines. The optimised modelled transmission baseline (following application of q_1 adjustment) is shown in green. The lower plots show the residual spectra for the fits to the data.

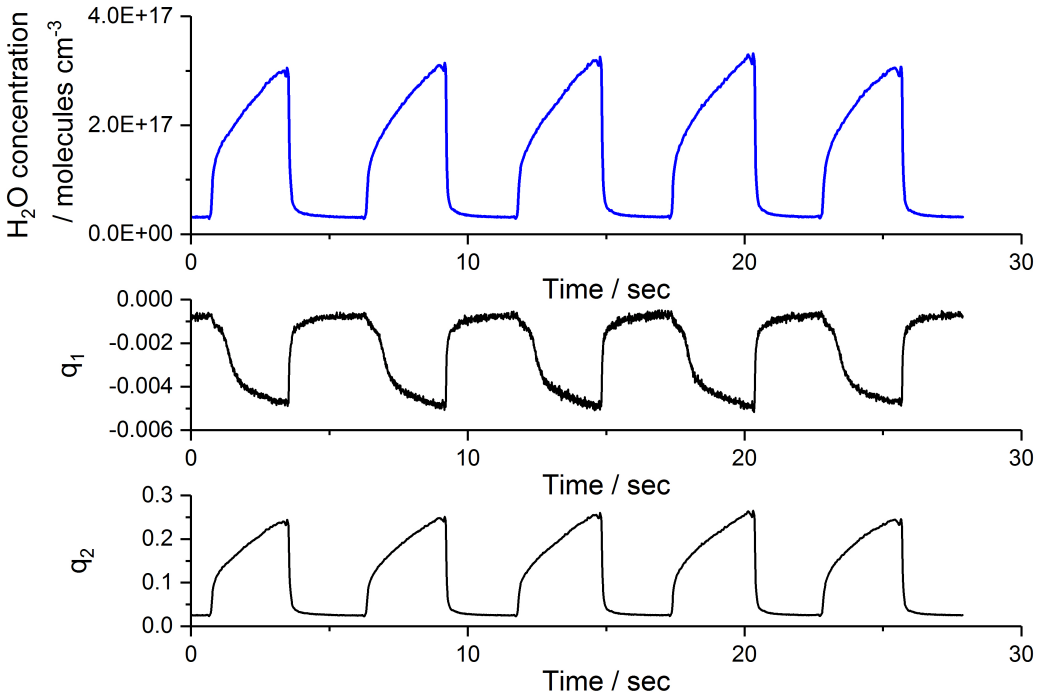


Figure 2.9: H_2O profile during volunteer breathing for 5 breaths. The upper plot shows the H_2O concentration profile determined in real time from recorded transmission spectra. The middle and lower plots show the variation in Voigt simulation model for parameters q_1 and q_2 respectively.

temperature of the measurement head to 31 °C, this is possibly a result of signal attenuation due to mirror reflectivity reduction as a result of slight fogging of the v-path mirror in humid conditions.

The capacity for sensitive evaluation of CO_2 and H_2O using direct laser absorption having been demonstrated, these spectroscopic systems were integrated into a device appropriate for use in breath analysis. With spectroscopic sensitivity optimised, emphasis was placed on producing a compact device. To reduce the volume requirements within the measurement cell, the spectroscopic systems followed a single, shared optical v-path. In this way, alterations to the cell used to initially evaluate systems were not required. A schematic of the fibre systems used within the multiplexed analysis is shown in Figure 2.10. The laser outputs are spatially multiplexed by a 2x2 fibre-optic coupler located in the control unit. Fibre couplers are, dependent on the core material used, optimised for transmission of radiation of a specific wavelength. The dual window coupler performance was optimised for radiation at wavelengths of 1310 and 1550 nm (Thorlabs 10202A-90-FC). The radiation was coupled in a 90:10 ratio: the CO_2 laser was coupled to the coupler input with higher transmission, a requirement due to the lower power of this laser and the reduced transmission suffered due to the greater spectral distance from coupler's optimal wavelength. The radiation is coupled from the laser to the coupler input via 1 m optical fibre which acts as a delay line, reducing the possibility of optical feedback into either laser. The H_2O laser was directly coupled to the lower transmission coupler input. The unused output from the coupler was connected to a fibre optic light trap (Thorlabs FTPC1), reducing back reflections from the fibre termination. The multiplexed radiation from the coupler output was transmitted to the measurement head through an optical fibre housed within a hybrid cable (LEMO). Within the measurement head a 2 m long optical fibre is used to reduce interference effects between the connection at the base of the head and the collimating lens. The signal attenuation within the fibre is low, so signal levels are not negatively affected despite the extended nature of this fibre. The attenuation of the detected radiation following transmission through the 5.4 cm v-path through the gas sample is recorded and analysed. The precise optical path length is evaluated spectroscopically, using a calibrated gas mixture containing 5 % CO_2 with a balance of N_2 (BOC Industrial Gases). Thirty seconds of CO_2 spectra are averaged, and path length determined by fitting Equation 2.17 with a known q_2 parameter. The precision of the gas mixture composition is ± 1 % of the quoted concentration, so this also becomes the precision of the optical path length calibration.

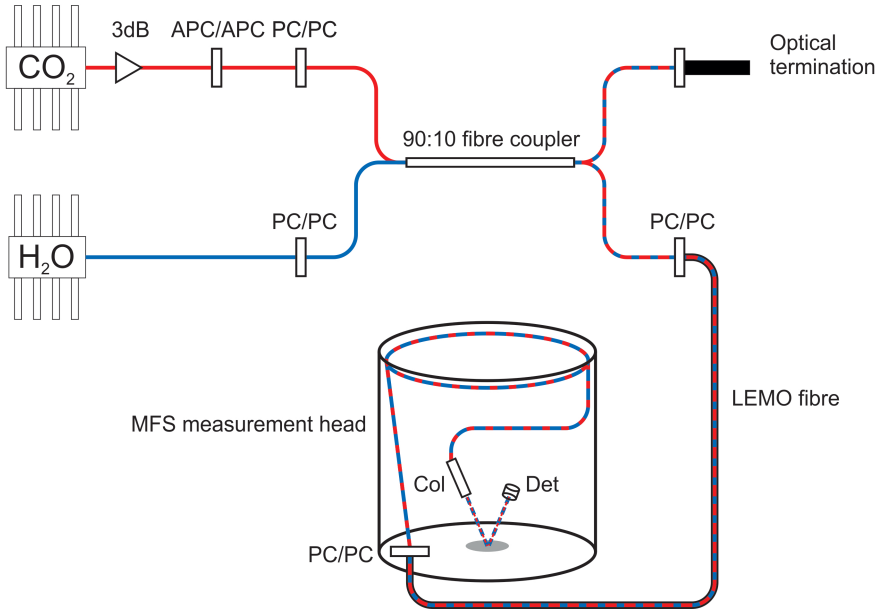


Figure 2.10: Schematic of coupling of spatially multiplexed CO_2 and H_2O lasers to optical v-path within measurement cell. The CO_2 laser is attenuated with a 3 dB attenuator, is coupled to a delay line optical fibre and then coupled to the fibre optic coupler as the input from which 90% of signal will be output. The H_2O laser is directly coupled to the coupler as the channel from which 10% of signal will be output. One output from the coupler is terminated and the other is coupled to the MFS measurement head via an optical fibre (LEMO). Within the measurement head, the multiplexed radiation is injected into the optical v-path by a collimating lens (Col), travels 5 cm through the gas sample, and is then detected by the housed photodiode (Det). The labels PC and APC refer to physical contact and angled physical contact optical connections respectively.

In order to utilise the multiplexed radiation to produce meaningful absorption spectra, the lasers were sequentially ramped. Whilst one laser was scanning over the appropriate spectral window, the other, stationary laser, was maintained at a constant 'offset current'. The stationary laser produces an approximately constant offset signal which must be recorded and then subtracted from the detected signals in order to calculate transmission spectra from which sample concentrations are determined. The offset signals are not precisely constant; following the reduction in the applied current from the top of the ramp to the stationary position, there is minor temperature oscillation within the laser chip, and variable signal levels as a result. The first 30 data points in each 200 data point spectrum are therefore excluded from the analysis to minimise the sensitivity loss as a result of multiplexing. The lasers are sequentially scanned for a period of 2.5 ms, with two spectra from each laser averaged and analysed to report a concentration measurement at a frequency of 100 Hz. The system is calibrated by flowing pure N_2 through the measurement cell at a rate of 5 l min^{-1}.

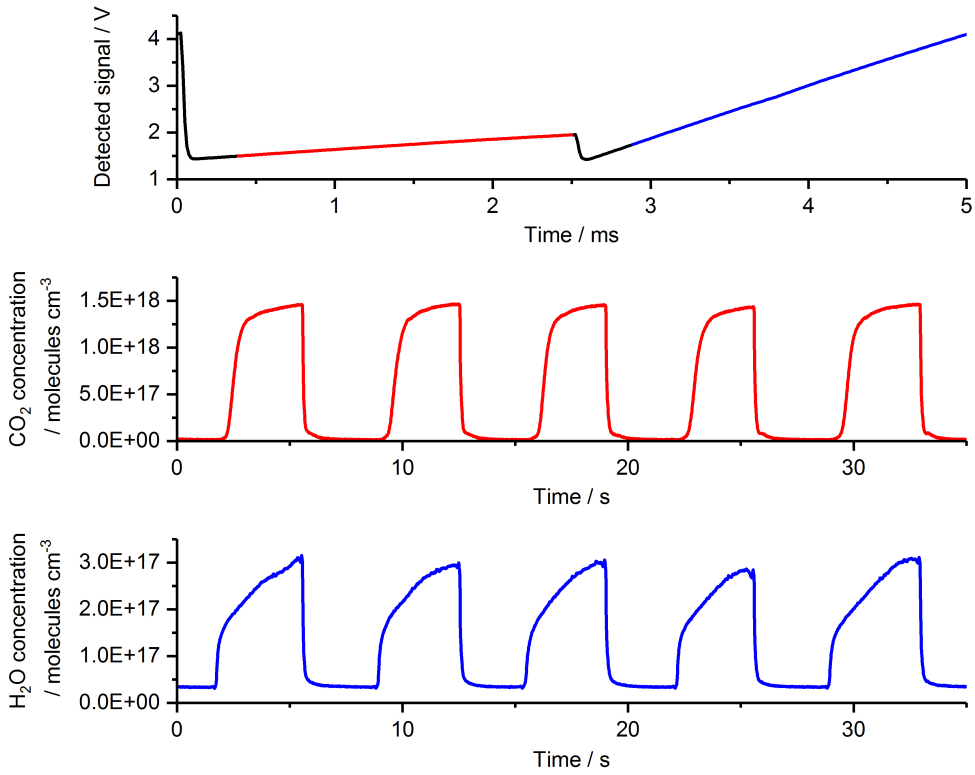


Figure 2.11: The upper plot shows the photodiode recorded signal for a 5 ms period during which the multiplexed CO_2 and H_2O lasers are ramped sequentially. Data shown in black at the start of each ramping period is excluded, with the data shown in red and blue analysed to evaluate CO_2 and H_2O concentrations respectively. The middle and lower plots show gas concentrations during volunteer air-breathing, determined contemporaneously in real time at a frequency of 100 Hz, for CO_2 and H_2O respectively.

In turn, photodiode offset signals, offset signals due to stationary lasers, and baseline signals in the absence of target species are recorded. Each calibration step lasts 30 seconds, spectra from the last 10 seconds of which are averaged to give reported spectra. Figure 2.11 shows a typical spectrum recorded over a 5 ms period in which both lasers are scanned. Examples of the contemporaneously evaluated concentration profiles during volunteer air-breathing are also shown. The rise in H_2O concentration at the start of expiration is shown to precede that of CO_2. The gas flowing through the measurement cell shortly after the start of expiration originates from the upper airway, the nose, mouth, and trachea. Gas within all areas of the human will be humid and hence the early rise in H_2O concentration is observed. The expirate with a significant amount of CO_2 originates in the lower airway, the alveoli within the lung, as a result of gas exchange with the blood. The CO_2 concentration evolves slowly after an initial sharp rise compared to the profile of H_2O. This is a

result of the heat and moisture (HME) filter that is used to separate the volunteer from the device; the filter saturates during the breath, allowing an increasing fraction of H_2O to be measured within the MFS as expiration continues. At the start of inspiration, both CO_2 and H_2O concentrations fall rapidly as gas from a compressed air supply is drawn through the MFS.

2.3.2 Oxygen Spectroscopy

Molecular oxygen is vital to metabolic function for all aerobic organisms, acting as the terminal electron acceptor for oxidative metabolism. Tissue function relies on efficient oxygen delivery and cellular utilisation according to metabolic activity.[128] When oxygen delivery or metabolic activity within tissues are disrupted, tissue hypoxia results, the presence of lower than normal oxygen content. The consequences of tissue hypoxia are dependent on the tissue type and metabolic demand, ranging from substantial adaptation to tissue death.[129] A number of inflammatory disease states, for example sepsis, are associated with disruptions in tissue extraction and mitochondrial utilization of oxygen.[130] Failure of oxygen delivery to meet metabolic needs is the feature common to all forms of circulatory failure or *shock*. Currently, diagnosis of conditions leading to tissue hypoxia is largely symptom based, a response to pyrexia, tachycardia or tachypnea. The ability to measure a fall in the body's oxygen uptake, which precedes symptom manifestation, would allow for earlier initiation of therapy. Previous work has reported improved patient outcomes, including mortality rates, with a reduction in patient time to treatment in shock and sepsis.[131,132] Clinical treatment of the symptoms of hypoxia generally involves efforts to improve oxygen delivery by providing supplemental oxygen to a patient via the inspiratory gas supply. The effect of this is beneficial in cases of acute tissue hypoxia, normalising blood oxygen levels and reducing the risk of generalised tissue hypoxia.[133] There are, however, risk factors associated with hyperoxia, the state in which oxygen supply to tissue is excessive. The risks of hyperoxia include coronary and cerebral vasoconstriction, decreased cardiac output and delays in treatment associated with high oxygen saturation masking major clinical deterioration.[134] Optimisation of oxygen therapy is currently difficult; there is no robust clinical measure for assessing the success of oxygen therapy beyond measurement of arterial oxygen saturation levels. The ability to titrate oxygen into a patient's inspiratory supply to the point at which oxygen consumption normalises before hyperoxia is reached would be powerful within acute care scenarios. Towards this objective, a technique for measuring patient oxygen consumption has

great clinical potential. This potential application, coupled with the number of conditions that lead to an oxygen uptake response, demonstrates the motivation for developing an accurate, non-invasive method of assessing oxygen consumption. The MFS seeks to provide this, coupling accurate measurement of oxygen concentration with time-aligned respiratory flow determination to provide breath-by-breath assessment of oxygen consumption.

The absorption cross-sections of the oxygen transitions within the spectral window of commercially available diode lasers are significantly lower than for CO_2 and H_2O. The molecule's dipole moment is unchanged as it vibrates, meaning that rovibrational transitions are electric dipole forbidden. Instead, a single rotationally resolved electronic transition within the atmospheric oxygen A band is targeted, details of which are shown in Table 2.2. This transition is formally spin-forbidden, but nevertheless has a large enough absorption cross-section to be probed in this work.[135] Direct laser absorption spectroscopy would not provide adequate sensitivity for the non-reentrant optical paths achievable in a compact MFS measurement cell. Hence, off-axis cavity enhanced absorption spectroscopy (CEAS) was used instead, with sensitivity increased by a pair of highly reflective mirrors employed to greatly enhance the effective path length, providing a larger absorption signal as a result.[136]

Table 2.2: Spectroscopic data of probed oxygen transition from HITRAN database.[118] The rotational assignment is reported as ${}^{\Delta N}\Delta J_{N"}(J")$ where N is the rotational angular momentum quantum number and J is the total angular momentum quantum number including spin.[137] The double prime (") symbol denotes the lower energy state of the molecule.

Molecule	ν_0 /cm^{-1}	σ_{INT} /cm^{2}cm^{-1}	γ_{air} /cm^{-1}atm^{-1}	γ_{self} /cm^{-1}atm^{-1}	Assignment
O_2	13084.20	7.44×10^{-24}	0.047	0.048	$(b^1\Sigma_g^+ \leftarrow X^3\Sigma_g^-)\ {}^{P}P_{11}(11)$

Typically, cavity based spectroscopic techniques, such as cavity ring-down spectroscopy (CRDS), rely on a mechanically stable, well-aligned optical cavity.[138] The cavity exhibits a comb-like intensity transmission function. The transmission maxima, equally spaced in frequency, are called cavity modes. These modes are, however, difficult to excite reproducibly on the timescale of a turbulent breath profile. The experimentally complex elements of CRDS, including fast optical components, can however be avoided by the use of CEAS.[110] These measurements require injected radiation to be aligned to excite as many high-order cavity modes as possible. A highly congested mode structure is

intentionally sought, such that the transmission function of the cavity is continuous and frequency-independent. The laser frequency is scanned over the spectral window of interest, with continuous and accidental excitation of many cavity modes leading to the detection of consistent baseline signal in the absence of absorbing species. High mode densities are achieved by off-axis cavity alignment or rapid modulation of the optical cavity length.[139] Mechanical instabilities within CEAS systems can be beneficial, and are often added to help randomise the resonance events and thus increase the mode density.

In the case of CEAS, a modified form of the Beer-Lambert law is used to retrieve the molecular concentration from the cavity transmission signal.[116]

$$\frac{I_0(\nu) - I(\nu)}{I(\nu)} = \frac{\alpha(\nu) l}{1 - R} \tag{2.18}$$

where $I(\nu)$ is the detected radiation that has been transmitted through the exit mirror, α is the frequency dependent absorption coefficient and l is the measured physical path length of the optical cavity. The $(1\text{-}R)^{-1}$ term represents the path enhancement offered by a linear cavity with the geometric mean mirror reflectivity R.

To evaluate CEAS spectra in real time to determine O_2 number densities, adjustments to the analysis software described in the previous section were made. To account for baseline variations whilst the system is running, it is assumed that the real time baseline is related to that measured in nitrogen by an adjustment factor, q_1.

$$I_{0,n} - I_{off} = q_1(I_{0,N_2} - I_{off}) \tag{2.19}$$

The gas concentration to be determined is related to a reference concentration in the same way as in the fitting model for the direct laser absorption spectroscopy, $c_n = q_2\, c_{ref}$. These assumptions, when combined with Equation 2.18 and photodiode offset signals are considered, lead to the expression

$$I_n - I_{off} = q_1(I_{0,N_2} - I_{off}) - q_2 \frac{\sigma c_{ref} l}{1 - R}(I_n - I_{off}) \quad . \tag{2.20}$$

This expression can be evaluated using the multiple linear regression module in LabVIEW with q_1 and q_2 as the regression parameters. The best fit spectrum can be reconstructed by:

$$I_{n,fit} = \frac{I_{off}\left(1 + q_2 \frac{\sigma c_{ref} l}{1-R}\right) + q_1(I_{0,N_2} - I_{off})}{1 + q_2 \frac{\sigma c_{ref} l}{1-R}} \quad . \tag{2.21}$$

Oxygen is probed at 764 nm by a 0.3 mW, single mode, vertical-cavity surface-emitting diode laser (VCSEL) (ULM763-01-TN-S46FTT, ULM Photonics). A VCSEL laser consists of an intrinsic 'active' region sandwiched between two Bragg reflectors.[140] The Bragg reflectors consist of alternating layers of p and n-doped semiconductor. These lasers differ from conventional diode lasers in that the optical beam travels at right angles to the active region instead of in the plane of the active region.[141] The laser was housed within the MFS measurement head, with temperature and current controlling electronics housed within the electronics module. A schematic showing the components within the O_2 spectrometer is shown in Figure 2.12. Radiation is collimated and then injected into the optical cavity via a 45° mounted steering mirror which can be manually translated or tilted to adjust the optical alignment of the cavity. The path length between collimating lens and the first mirror of the cavity was designed to be at least 10 cm on the grounds that this separation would minimise optical feedback into the laser.

The optical cavity consisted of a pair of spherical fused silica mirrors with 25 mm diameter and 6 mm thickness (Layertec). The mirrors were separated within the MFS measurement cell by 27 mm. Both surfaces of each mirror had a radius of curvature of 200 mm, with the high-reflectivity coating having a nominal reflectivity of 99.8%. This gives a theoretical best-case path length enhancement factor of 500. The 18x18 mm silicon photodiode detector (Hamamatsu S1337-21) was housed behind the second mirror of the optical cavity. A non-transmitting gasket is placed in front of the detector housing, reducing the capacity of stray light to affect the measurement. The gasket acts to define the aperture size through which radiation from the cavity travels to reach the detector. An amplified spontaneous emission (ASE) suppression filter is used between the second cavity mirror and detector housing to suppress broad spectral emission from the laser. In this way, the light reaching the detector is limited to single-mode radiation within the spectral range interest.

Transmission signals through optical cavities inherently contain additional noise features compared to those measured in direct laser absorption spectroscopy. Sinusoidal noise features, known as residual mode structure, resulting from etalons within a cavity are both very alignment dependent and difficult to prevent. The alignment of the optical cavity has a clear effect on measurement sensitivity; more spatially extended mode fields (the density of transmitted signal detected at the rear face of the exit mirror) avoid mode degeneracy and thus lead to improved baseline stability

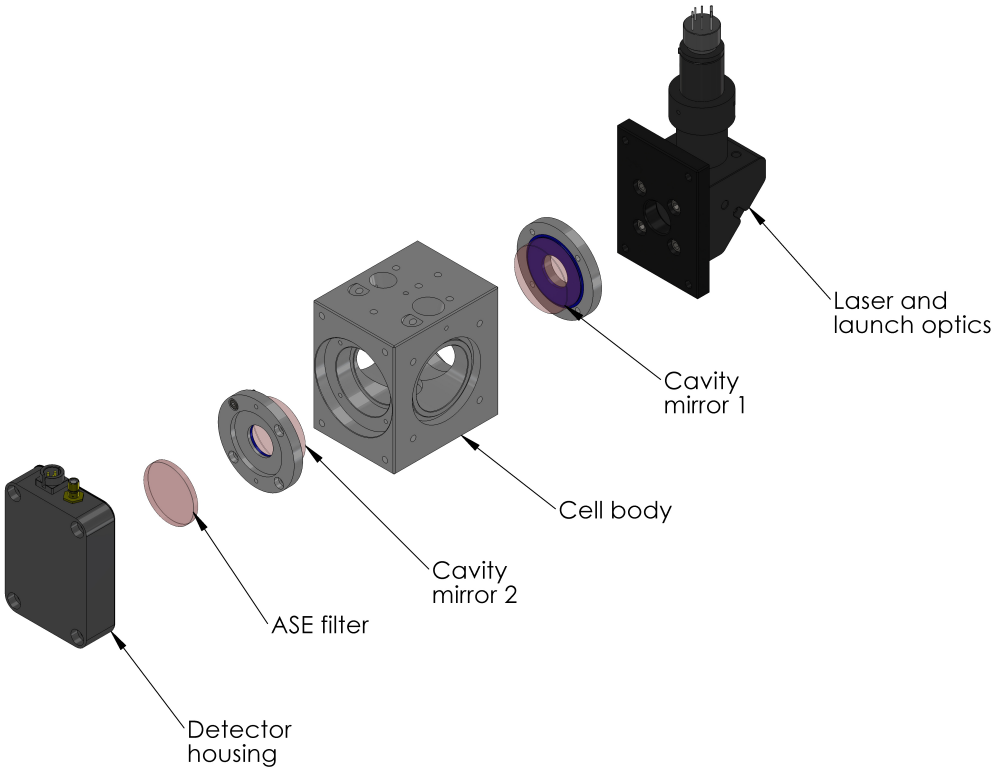


Figure 2.12: Schematic of O_2 off-axis CEAS spectrometer. The VCSEL laser, collimating lens and steering mirror are housed within the launch unit. The cavity mirrors are positioned either side of the gas flow axis, ensuring enhanced optical path length through the sample. The radiation exits the cavity, is transmitted through an ASE filter, and ultimately is detected by the silicon photodiode.

and reduced etalon amplitudes. There is, however, also a mechanical stability consideration. Alignments leading to signal density close to the mirror edges present two potential issues; the first being radiation not being collected onto the detector, and the second being the susceptibility to mechanical disturbance with the concern being radiation prematurely leaving the cavity by missing either mirror surface. A compromise is sought, providing both good measurement sensitivity and mechanical stability, requiring significant mode field dispersion whilst ensuring the radiation is maintained reasonably close to the mirror centres. The optimisation of the cavity alignment is achieved using a combination of imaging the mode field on the rear mirror and evaluation of the detected cavity transmission. The former is achieved using a CMOS sensor camera (Teledyne Dalsa Genie HM640) coupled to a telecentric lens (Edmund Optics 56-675), ensuring a spatially broad mode field, and the latter is performed to ensure that any etalons present in the spectra are minimised.

Despite optimised alignment, the evidence of residual mode structure remained present within the

cavity transmission spectra. The signal-to-noise ratio is improved by the injection of radio frequency (RF) white current noise into the diode laser source. The injected RF noise generates statistically uncorrelated, random fluctuations in the injection current, which are then translated into optical frequency noise.[142] The result is a minimisation of residual mode structure due to a reduction in the coherence time of the laser; the consequence is an improvement in spectral signal-to-noise ratio.

The time-to-wavenumber calibration for this channel was achieved with a spectral analyser (3SAE036, CVI) with a free spectral range of 0.251 cm^{-1}. The absolute wavenumber points versus the time stamps of the transmission maxima were fitted with a third order polynomial and the parameters used as inputs to the analysis software. The spectral window for probing O_2 was chosen to be 1.3 cm^{-1}. The calibration procedure for the O_2 spectrometer is as follows. Pure N_2 is flowed through the measurement cell at a rate of around 5 l min^{-1}. Initially, the photodiode offset is recorded, with the O_2 laser turned off, and then a baseline transmission signal is measured with the laser ramping periodically. A final calibration step is required to evaluate the reflectivity of the optical cavity. To do this, the gas supply is swapped from pure N_2 to pure O_2. With pure O_2 flowing through the measurement cell, Equation 2.20 can be used to evaluate the reflectivity, R, of the mirrors in the CEAS system. The calibration steps are 30 sec in duration, with spectra from the final 5 sec of each averaged to give the spectra used within the analysis software.

A measured transmission spectrum and the calculated absorbance profile recorded in the O_2 cavity are shown in Figure 2.13. These data were recorded while laboratory air flowed through the measurement cell. An O_2 profile determined during volunteer air-breathing is displayed in Figure 2.14. There is relatively low variation in the q_1 parameter during breathing, a standard deviation of 2×10^{-4} for the 40 sec shown in the figure. The stability of this parameter, quantifying the variation in cavity baseline transmission, contributes to a sensitive measurement of O_2 concentration with a high signal-to-noise ratio in the recorded profile. There are, transient features in the q_1 profile that can be observed at the points at which the direction of flow is reversed. This is attributable to a small degree of mechanical instability of the cavity at these points.

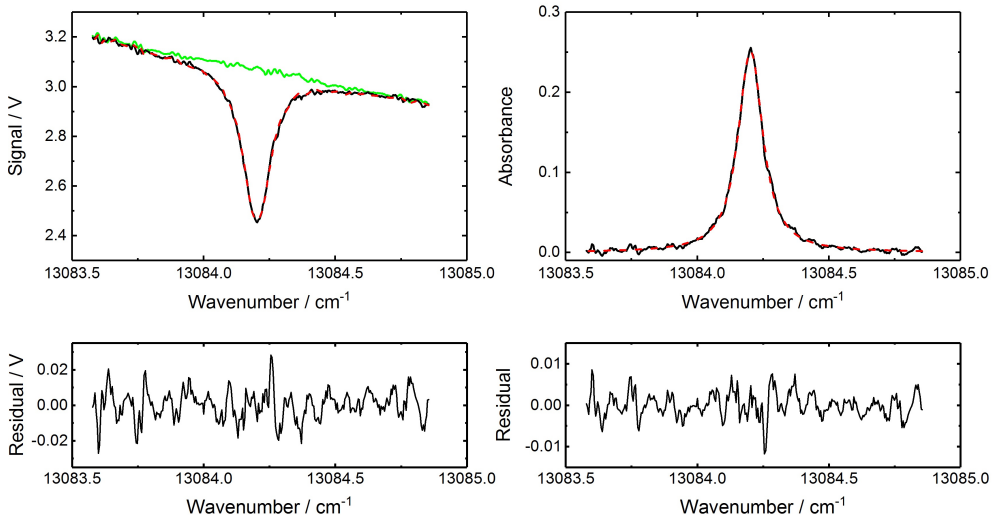


Figure 2.13: An example transmission (left) and absorbance (right) spectrum from O_2 CEAS spectrometer. In the upper plots, detected signals are shown in black and best fit Voigt simulations are shown as dashed red lines. The optimised modelled transmission baseline (following application of q_1 adjustment) is shown in green. The lower plots show the residual spectra for the fits to the data.

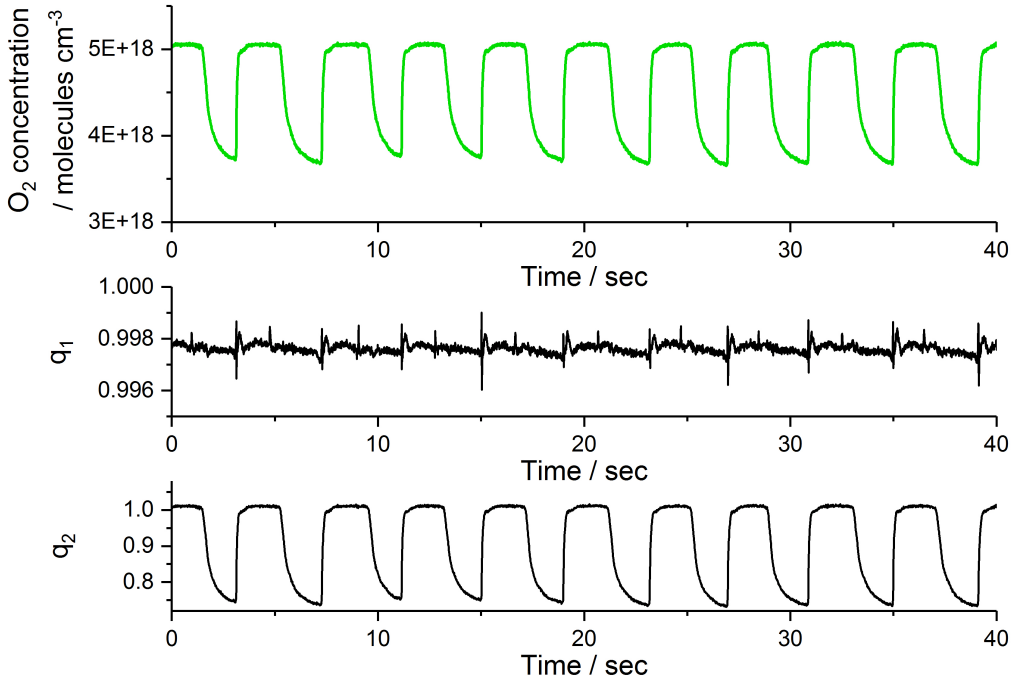


Figure 2.14: O_2 profile during volunteer breathing for 10 breaths. The upper plot shows the O_2 concentration profile determined in real time from recorded transmission spectra. The middle and lower plots show the variation in Voigt simulation model for parameters q_1 and q_2 respectively.

2.3.3 Temperature and Pressure Sensors

Temperature and pressure measurement within the MFS is required in order to calculate accurate pressure broadening parameters for gas concentration evaluation. The barometric pressure within the MFS measurement cell was measured using a miniature amplified barometric pressure sensor (HCA0811ARH8, First Sensor AG). This sensor measures absolute pressure in the range of 800 to 1100 mbar with 12-bit resolution and communicates with the system controller via an I^2C bus. The sensor has a single port, connected to the measurement cell by a flexible silicone tube.

Custom thermocouple assemblies for measuring gas temperature within the measurement cell have been designed and built. The system required a gas temperature response time within a few tens of ms. This necessitated the use of a low-mass sensor. The sensor selected was a welded-tip K-type thermocouple using 25 μm diameter wire. The sensing junction is exposed and protrudes unsupported a few mm into the gas flow, an arrangement which ensures good thermal contact between the gas and the thermocouple. The sensing thermocouple tip is fragile, although well-protected when installed within the measurement cell. The thermocouple assembly was constructed as a replaceable plug-in module. Four thermocouples were installed into the gas flow, two at either end of the cell. Of each pair, one thermocouple sampled the temperature at the periphery of the gas flow, protruding only 2 mm, and the second protruded further, sampling towards the centre of the gas flow. A temperature measurement that is representative of the average temperature within the bulk gas flow is found by averaging the measurements from the four thermocouples.

The measurement cell is heated to 31 °C during device measurement. By heating the cell, the temperature stability of the cell body during breathing is improved. It also increases the H_2O vapour pressure, reducing potential moisture droplet formation within the cell. The reflectivity of optical components, particularly cavity mirrors, is affected by both temperature and moisture and so optical baseline stability is improved by heating the cell. The temperature of the measurement cell is measured using another K-type thermocouple probe. The module is located in a blind hole in the upper surface of the cell body.

By combining sample temperature and pressure measurements, a total gas concentration can be evaluated from the ideal gas law. This allows the determined O_2, CO_2 and H_2O concentrations to be expressed as fractional compositions of sample. The concentration of non-physiologically significant

balance gas can be calculated from measured O_2, CO_2 and H_2O concentrations. Hereafter in this work, balance gas is referred to as nitrogen, but this term includes the other inert gases present, such as argon.

2.3.4 Respiratory Flow Measurement

An accurate determination of flow is crucial in the calculation of respiratory gas exchange. Assessment of respiratory flow is made harder by the changing physiochemical conditions between inspiratory and expiratory gas: changing humidity, gas composition, temperature and pressure result in variation in sample density and viscosity. The flow sensor employed within the MFS is based on a Lilly type pneumotachograph. This technique consists of measuring the pressure drop, Δp, across a known resistance in a breathing tube, and using that pressure drop to calculate flow rate. The overall aim of this apparatus is to provide a flow signal exhibiting very little integration error under conditions of constant gas composition, and that with dynamic adjustment of the density and viscosity values, is capable of very low integration errors under conditions that pertain to breathing. The pressure drop is measured across a pair of wire-mesh screens located at either end of the gas analysis space, enabling the gas composition, temperature and pressure to be determined centrally within the flow measurement system.

To minimise differences in temporal alignment of flow measurement and gas analysis between inspiratory and expiratory flow, the pneumotachograph is located symmetrically about the centre of the measurement cell. Eight ± 2.5 mbar piezoresistive membrane differential pressure sensors (HCLA02X5EB, First Sensor AG) are connected via eight-way manifolds which were connected to the differential pressure sampling ports. The sensors provide 12-bit resolution and communicate with the system controller via an I^2C bus. The sensors are connected as back-to-back pairs so that any device non-linearity partially cancels. The eight sensors are split into two functioning flow sensing units, each a bank of four HCLAs. Measurement noise in each bank is reduced by averaging the differential pressures of the four sensors. Miniature pneumatic solenoid valves (X-Valve, Parker Hannifin) are built into the sensor module to enable offset calibration. These switching valves are used to ensure that there is a zero pressure difference across the sensors during calibration.

A schematic of the components within the MFS that contribute to the measurement of respiratory flow is shown in Figure 2.15. The components are symmetric on either side of the device's

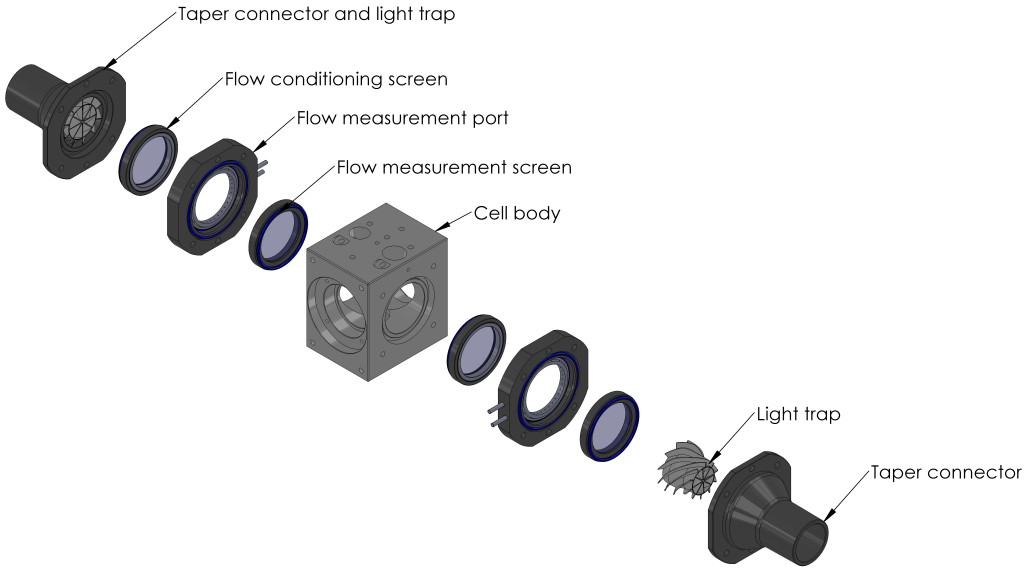


Figure 2.15: Schematic of MFS measurement head components in respiratory flow measurement system.

central measurement space. The taper connectors are designed to interface with standard 22 mm anaesthetic conical connectors (ISO 5356-1). This allows the device to be integrated into gas supply and ventilator circuits. The flow axis bore size increases from 18 mm at the taper connector's furthest point to 24 mm within the measurement cell. This bore size is essentially maintained within the cell, with optical components only slightly recessed. The light traps, housed within the taper connectors, consist of 3D printed metal structures with a pair of concentric counter rotating helices. The attenuation of light through these light traps has been measured as greater than 99.99%, ensuring spectroscopic measurements are not detrimentally affected by stray light following this path. A flow conditioning screen is housed between the taper connector and the flow measurement port. This woven stainless steel mesh screen, with a wire diameter of 100 μm and pitch size of 350 μm, is intended to reduce turbulence in the gas flow entering the measurement cell. The pressure of the gas at either end of the cell is sampled within the flow measurement port. The flow measurement ports are designed to provide the differential pressure sensors with gas at a pressure representative of that in the bulk sample. Within each flow measurement port is housed a flow sampling ring, a schematic of which is shown in Figure 2.16. Two series of 16 sampling holes are evenly spaced around the circumference of the sampling ring. Each series of angled holes leads to a separate annular space, enabling the two separate flow measurements to be made from the central sampling

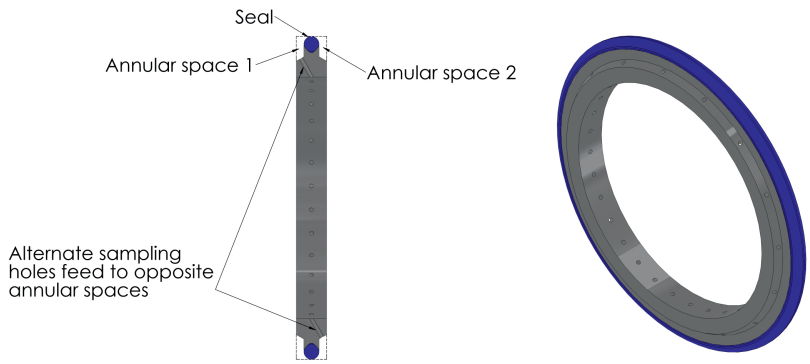


Figure 2.16: Schematic of the pressure sampling rings used for MFS flow measurement. The design allows two independent pressure measurements to be made from the same sampling plane.

plane independently. The flow measurement port outlets are connected to the differential pressure sensor manifold by flexible silicone tubing. The flow measurement screens provide the known resistance around which the pressure difference is measured in order to evaluate gas flow. These screens consist of a finer stainless steel mesh, wire diameter 36 μm and pitch size 111 μm, housed between the flow measurement port and body of the cell. A series of o-rings is used to ensure good seals are achieved at each component junction in the flow axis. Subtle variation in the flow axis components, particularly the nickel wire meshes, is to be expected. It is assumed that any potential effects on the flow measurement associated with this variation are nullified by the flow modelling and calibration procedure described below.

In order to use the pneumotachograph to determine respiratory flow rates, the relationship between pressure drop and flow was required.[143] The Reynolds number associated with peak respiratory flows is likely to exceed 2300 and thus laminar, translational and turbulent flow regimes are to be expected during a breathing cycle.[144] Standard pipe theory states that the pressure drop within a section such as this is due to a combination of major and minor losses, where major losses are due to friction and minor losses are attributed to sudden changes in geometry. Major losses are expected to be linearly proportional to both the dynamic viscosity, μ, and volumetric flow rate, $\dot{V}$, of the flowing gas, according to Poiseuille's law.[145] Minor losses are expected to be linearly proportional to the density, ρ, of the gas and proportional to the square of $\dot{V}$.[146] This leads to the following relationship:

$$\Delta p = \alpha \mu \dot{V} + \beta \rho \dot{V}^2 \quad , \tag{2.22}$$

where Δp is the measured pressure drop, and α and β are constants to be determined.

From the spectroscopic and sensor measurements within the MFS, gas density and viscosity can be calculated for every 10 ms period. Values for the densities and viscosities evaluated within the MFS were sought in the literature, including for the balance gas, which for this purpose was assumed to be composed of 99% N_2 and 1% Ar. The literature values used in this work are shown in Table 2.3.

Table 2.3: Density and viscosity data for respiratory gases. Density data are taken from [147], and viscosity data, including Sutherland constants, are from [148]. Densities and viscosities are measured at standard temperature (273.15 K) and pressure (1 atm).

Gas Species	Density / kg m^{-3}	Viscosity / μPa s	Sutherland Constant / K
O_2	1.429	18.90	127
CO_2	1.977	13.90	240
H_2O	0.804	8.82	NA
N_2	1.251	16.63	111
Ar	1.784	20.96	144

The literature values for density are measured for pure samples under conditions of standard temperature and pressure (STP), 273.15 K and 1 atm. The density contribution from each component is calculated as the literature value multiplied by the species' fractional contribution to composition. These component densities are then directly summed to give a calculated dynamic density at STP. The ideal gas law is used to account for the variation of the measured temperature and pressure within the measurement cell from STP. Combining these concepts, the dynamic density of the gas sample is calculated by

$$\rho(P,T) \;=\; \left(\frac{T_{ref}}{T}\frac{P}{P_{ref}}\right)\sum_i P_i\,\rho_{ref,i} \quad , \tag{2.23}$$

where T_{ref} and P_{ref} refer to standard temperature and pressure, T and P are the measured temperature and pressure respectively, and P_i and $\rho_{ref,i}$ are the measured pressure and literature value of gas species i.

The dynamic viscosities within the literature are also quoted for pure samples under STP conditions. The viscosities have temperature dependence, quantified using Sutherland's Law, which assumes a hard-sphere model perturbed by weak intermolecular attractions.[149] The dynamic viscosity at temperature T is calculated by:

$$\mu = \mu_{ref} \left(\frac{T}{T_{ref}} \right)^{3/2} \frac{T_{ref} + S}{T + S} \quad , \tag{2.24}$$

where μ_{ref} is the viscosity at temperature T_{ref}. S is the Sutherland constant, an experimentally determined parameter which is independent of temperature and characteristic of each gas species. Sutherland's Law has been shown to be accurate for a number of gases over a significant range of temperatures.[150] Due to the highly polar nature of H_2O, however, the assumption of weak intermolecular attractions in the Sutherland Law becomes less valid and a more complex model of the temperature dependence of viscosity published by Teske *et al.* is used instead.[151] Unlike for dynamic density, the viscosities of the gas components within the measurement cell cannot be summed to give an accurate estimation of sample viscosity. Instead, a method by Brokaw is used.[152] This approximate method was developed for predicting the viscosities of gas mixtures involving both non-polar and polar species and does so favourably when compared to the results of rigorous application of more complex empirical models. The largest mixture viscosity errors have been reported to be below 4%.[152]

In order to determine values for the constants α and β in Equation 2.22, a calibration scheme is required. A programmable mechanical pump was used for calibration, formed of a 3 L spirometer calibration syringe (Vitalograph, 36020) mounted in a custom designed actuator. A calibration scheme was written in Si Programmer (software from Applied Motion Products), to include a range of flow conditions, each with a well-defined stroke volume and peak flow rate. The optimal values for α and β were found through non-linear regression. The objective function minimised through the regression was the sum across all strokes of the differences between the estimated number of molecules moved and the number of molecules calculated from the known stroke volume. Previously, to calibrate this sensor, a sinusoidal pump with a poorly defined stroke frequency had been used.[119]

The pump was attached to one end of the MFS measurement cell, with the other end of the device open to laboratory air. A series of 22 pump strokes was used within each calibration run. The pump stroke flow rates were chosen to cover a wide range of possible respiratory flow rates:

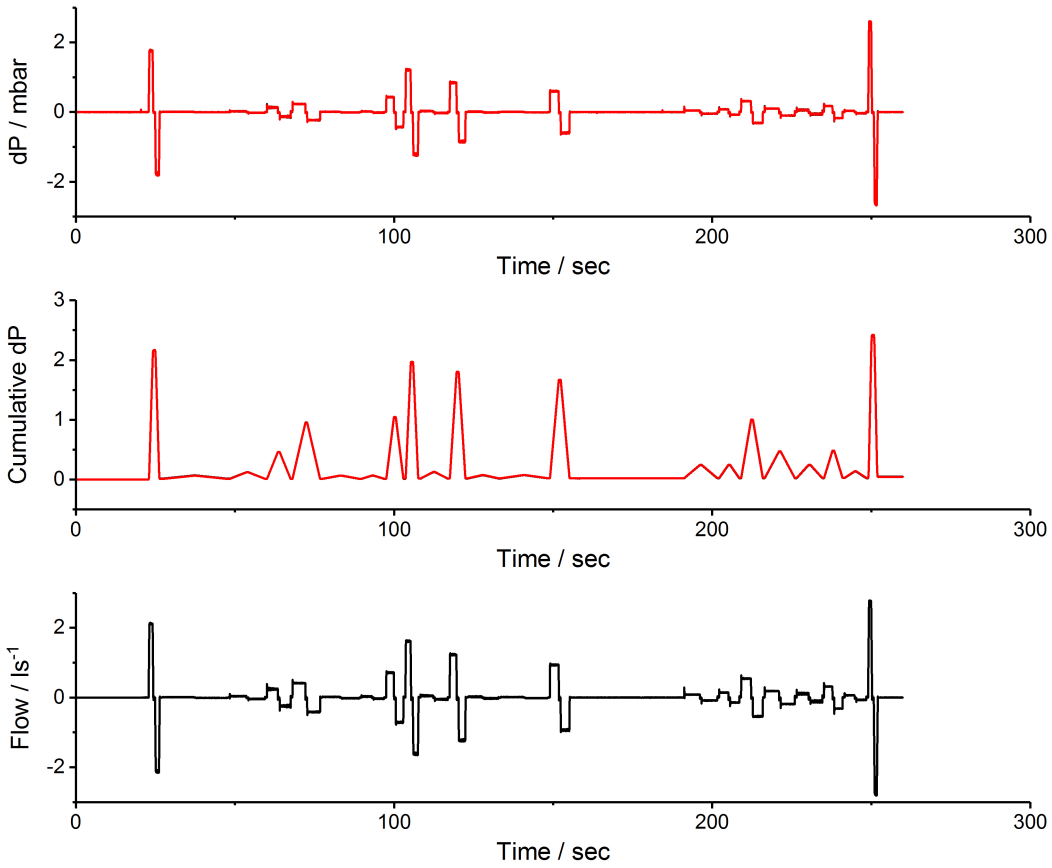


Figure 2.17: Data collected during calibration procedure of flow sensor. The measured differential pressures (upper) and cumulative differential pressure profiles (middle) are shown for both bank 1 (blue) and bank 2 (red). The lower plot shows the calculated flow profile for this dataset using the flow parameters determined by calibration. Data from both measurement banks contribute to the calculated flow profile.

at rest, respiratory flow rates greater than $1\,\mathrm{l\,s^{-1}}$ are rare, but including flow rates beyond twice this value in the calibration profile ensured the capacity of the device to perform with volunteers undertaking light exercise was not compromised. Data recorded during one calibration run is shown in Figure 2.17. The responses of the two banks of differential pressure sensors are similar enough that data from one bank obscures that of the other. A small amount of noise can be seen at the start of the pump strokes due to acoustic vibrations induced by the pump operation. During the calibration scheme, there are no pump strokes during the initial 20 sec during which the calibration of offset values for both sensor banks is performed. There is a further period without pump strokes between around 160 and 190 sec. This corresponds to the HCLA recalibration period of one of the flow sensor banks. By removing pump strokes from this period, calibration profiles for both measurement banks

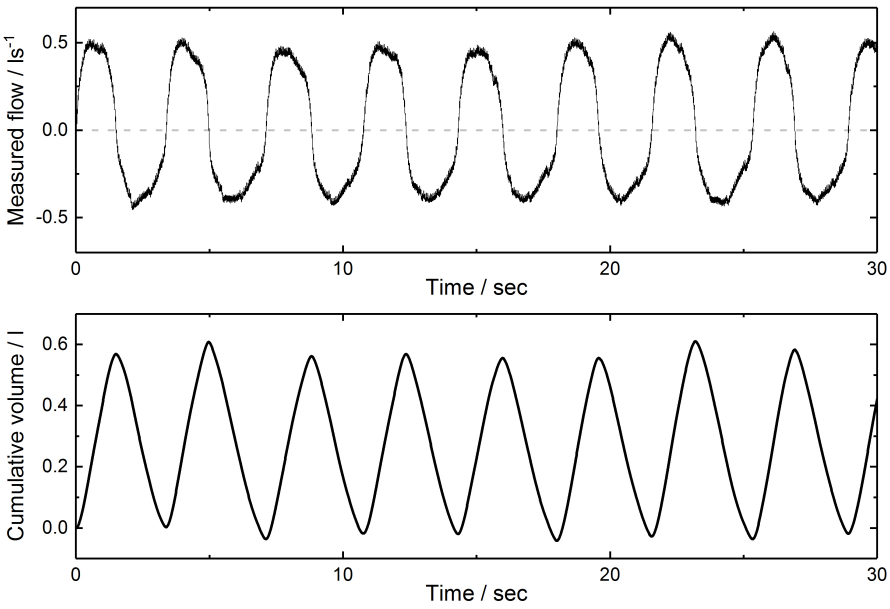


Figure 2.18: The upper plot shows a flow profile during 30 sec of volunteer breathing. Flows above zero indicate inspiration and those below zero indicate expiration. The lower plot shows the time-aligned volume (integrated flow) profile.

are equivalent. With values of α and β determined using this updated calibration program, the accuracy of the flow sensors was improved, thereby increasing the accuracy of the measured gas exchange values for any subject.

A flow profile determined in real time during volunteer breathing is shown in Figure 2.18. This flow profile is typical of breathing at rest, with peak inspiratory (flow above zero) and expiratory (flow below zero) flows close to $0.5\,\mathrm{l\,s^{-1}}$. Also shown is the cumulative volume profile, calculated as the integral of the flow profile. The tidal volume is shown to be approximately 0.6 l, again typical of breathing at rest. At the end of each expiration, the cumulative volume reaches approximately the same value, an indication of the fact that at the end of passive expiration approximately the same volume of gas will be left in the lung, the functional residual capacity (FRC).[153] There will always, however, be a degree of breath-to-breath variation in FRC.

2.3.5 Validation by Air and High Oxygen Breathing

A 30 minute validation of MFS performance was performed during which a volunteer breathed air for 10 min, medical O_2 for a further 10 min and then returned to air-breathing for the final 10 min. The inspiratory gas was supplied via a flow past system. The principal benefit associated with this set-up

is that volunteer participation is not required; breathing can remain spontaneous.[100] Volunteers are allowed to breathe as comfort dictates, without respiratory rate or tidal volume being restricted. The procedure was performed breathing via a mouthpiece and HME filter with the nose occluded.

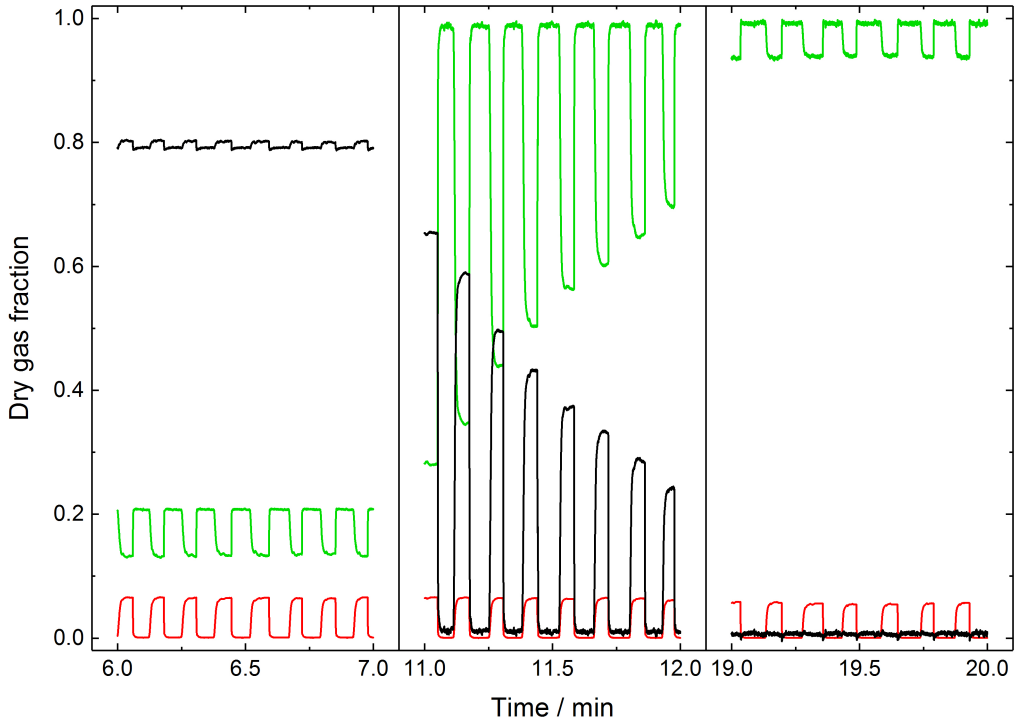


Figure 2.19: Contemporaneously evaluated gas composition data for three periods within a 30 min breathing procedure. The dry gas fractions are shown for O_2 (green), N_2 (black), and CO_2 (red). The first panel shows a minute of air-breathing data, the second shows data from early within the N_2 washout, and the third shows data recorded late in the washout period.

A series of gas concentration profiles for three representative periods during the validation procedure is shown in Figure 2.19. The profiles for O_2, N_2, and CO_2 are shown as dry gas fractions; the species concentration as a fraction of total gas concentration minus the measured H_2O vapour contribution. As a result of the progressive saturation of the HME filter during expiration, the H_2O vapour profile during breathing is largely dependent on breathing profiles: respiratory flow rates, tidal volumes, and respiratory rates. It is determined, therefore, that the physiologically significant information content is encoded in the morphology of the dry gas fraction profiles.

The cumulative volume profile for each gas species is calculated as the integral of the product of the respiratory flow and the measured gas fraction. The profiles measured during the validation procedure are shown in Figure 2.20. Gas exchange is calculated from the cumulative volume profiles;

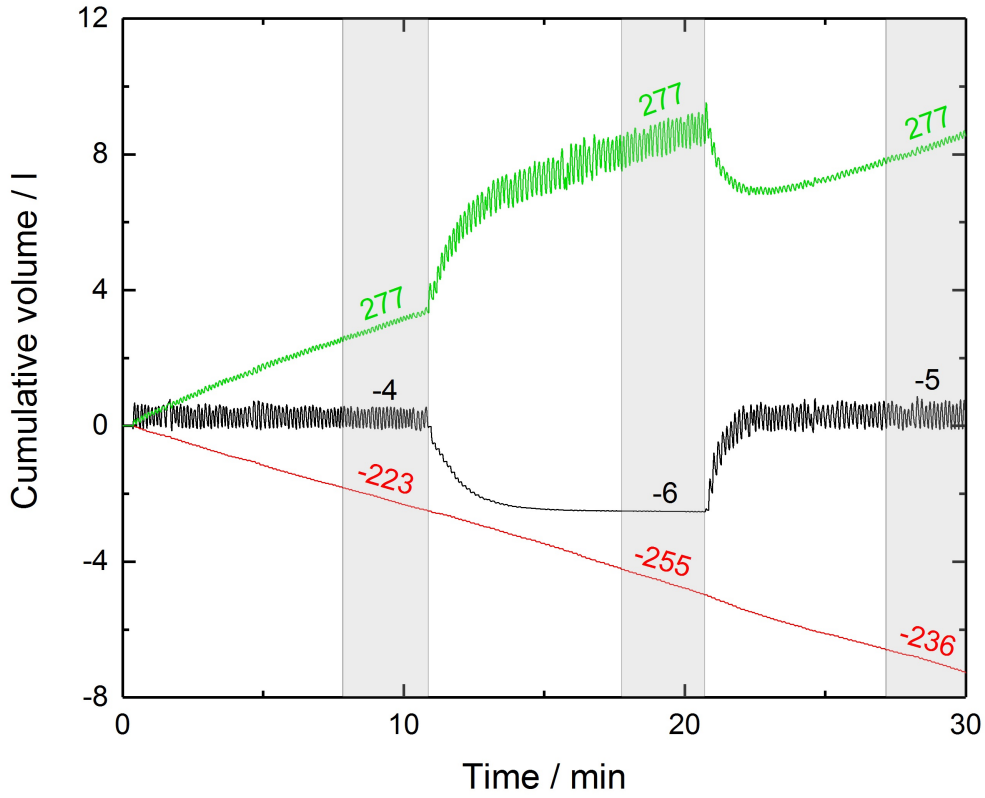


Figure 2.20: Cumulative gas volume profiles for 30 min breathing procedure for O_2 (green), N_2 (black), CO_2 (red). Data were recorded for 10 min air-breathing period, 10 min period breathing medical O_2, and finally a further 10 min of air-breathing. The numbers indicate the consumption rates for each gas in units of ml min^{-1} calculated for the final 3 min of each breathing phase (shown by shaded regions). The upward trend for O_2 indicates the body's consumption, the downward trend for CO_2 indicates production. The absence of trend for N_2 during air-breathing reflects the lack of net uptake or production by the body.

the gradient of these profiles from end-tidal points (minima of the total volume profile) is evaluated. This has been performed for the final 3 min of each breathing phase of the validation procedure. At the end of the initial air-breathing phase, the measured O_2 consumption and CO_2 production rates were 277 and 223 ml min^{-1} respectively. The N_2 production rate was measured to be 4 ml min^{-1}. As N_2 is neither consumed nor produced by the body, the expectation is that this value should be equal to zero. Variations in breath profiles and posture changes over time, however, contribute to a degree of breath-to-breath variation in N_2 consumption or production. The respiratory quotient, RQ, is defined as the rate of CO_2 production normalised to the rate of O_2 consumption.[154] RQ reflects the substrate being metabolised to give the body energy; RQ is 1.0 when carbohydrate is metabolised, 0.8 for protein, and around 0.7 when fat or alcohol is metabolised. RQ can be greater

than one in the case of hyperventilation[155], or during extreme anaerobic exercise.[156] Typically, during normal breathing an approximate RQ for a mixed diet is expected to be around 0.8.[157] In the initial air-breathing period of this procedure, the measured RQ was 0.81.

During the medical O_2 breathing phase, the rate of O_2 consumption rises sharply as the inspired gas mixes with the alveolar gas. There is an associated N_2 production early during this period. The gas exchange rates were calculated for the final 3 min of this breathing phase. By this time, the inspiratory gas is expected to be well equilibrated with the alveolar gas and so the rates of gas exchange should again reflect metabolic processes. The measured O_2 consumption and CO_2 production rates were 277 and 255 $ml\,min^{-1}$ respectively. The increased carbon dioxide production rate raises RQ to 0.92. Encouragingly, the N_2 production rate during this period is low, measured as 6 $ml\,min^{-1}$. Following the end of the N_2 washout phase, the second air-breathing phase begins. Again, the inspiratory mixture equilibrates with the gas in the lung, which is shown by the initial O_2 production and N_2 consumption. Towards the end of this period, the N_2 volume profile has recovered the form shown during the initial air-breathing period. The N_2 production rate during the final 3 min of this phase was 5 $ml\,min^{-1}$ and with O_2 consumption and CO_2 production rates of 277 and 236 $ml\,min^{-1}$ respectively. This gives an RQ value of 0.85.

Evaluation of the N_2 production rate during breathing provides a complete integrated test of the MFS; this value is dependent on the measured concentrations for O_2, CO_2, and H_2O, the measured temperature and pressure, and the determined flow profiles. Experience with the MFS showed that a fully calibrated device is capable of consistently recording N_2 production rates with a magnitude lower than 10 $ml\,min^{-1}$. This was consequently adopted as the device's performance specification. The production rates measured for each analysed period within the validation procedure illustrate the precision and accuracy of the MFS. That this can be achieved both during air-breathing and high O_2 breathing illustrates the success of the spectroscopy across the expected range of working conditions. Furthermore, the quality of the respiratory flow measurement is illustrated by the N_2 cumulative volume profile measured during the first 10 min being re-established towards the end of the second air-breathing period. This result is dependent on the successful calculation and application of dynamic gas density and viscosity over a full range of working conditions.

2.4 Lognormal Lung Model

The principal applications of the MFS are twofold. The device can be used within unconscious patients in environments such as intensive care wards to directly assess breath-by-breath gas exchange. The second application lies within respiratory physiology, relying on the concept that if measured with sufficient accuracy, there is enough information contained within the way that expiratory gases emerge from the lungs to evaluate the level of *inhomogeneity* within the lung. Data from the MFS can be used alongside a computational model of the lung, termed the Lognormal Lung, in order to provide a new method of assessing lung health non-invasively by quantifying lung inhomogeneity. [158] Given the limitations of currently used diagnostic techniques within respiratory medicine, described in Chapter 1, this method has the potential to provide opportunities for secondary prevention of respiratory disease via earlier disease diagnoses.

In a homogeneous lung, each unit volume receives the same amount of fresh gas, ventilation, and fraction of the lung's blood flow, perfusion. Inhomogeneity in the lungs generally refers to a mismatch between either ventilation and perfusion, or ventilation and alveolar volume. Healthy lungs have a degree of inhomogeneity, basal lung units have lower $\dot{V}/\dot{Q}$ ratios than those at the lung apex. [3] It has been recognised that the degree of inhomogeneity increases with disease. [43,44] The Lognormal Lung model aims to represent the underlying physiology of the lung. Within the model, the inhomogeneities of three physiological concepts are quantified, the inhomogeneity of compliance, which is the ability of the lungs to stretch or expand when ventilated, the inhomogeneity of conductance, the fractional share of perfusion across the lungs, and the inhomogeneity of deadspace pathlength to gas exchanging regions. In addition to these inhomogeneities, the alveolar and anatomical deadspace volumes of the lung are quantified. The model, described further in the next section, requires, as inputs, the various parameters that describe the lung, the total flow rate of gas at the mouth and the inspired gas fractions. The outputs are the simulated expired gas fractions at the mouth. By comparing the model outputs with experimental data, the physiological parameters which best describe an individual's lungs can be determined.

2.4.1 Parameterisation of Inhomogeneity

The computational model of lung inhomogeneity considers a total alveolar volume (VA_{tot}) composed of a set of N lung units. Each unit has equal volume at the lung's functional residual capacity (FRC),

the volume of air present in the lung at the end of passive expiration. However, the units vary in terms of their fractional share (F_{CL}) of total lung compliance (CL_{tot}), fractional share (F_{Cd}) of total pulmonary vascular conductance (Cd_{tot}) and fractional share (F_{VD}) of total deadspace (VD_{tot}). To minimise the parameter count, its is assumed, based on previous studies,[159,160] that both the fractional compliance to fractional alveolar volume ratio, F_{CL}: F_{VA}, and fractional vascular conductance to volume ratio, F_{Cd}: F_{VA}, are log-normally distributed at FRC. This results in a bivariate log-normal distribution for these parameters, with the correlation between the two distributions defined as ρ. The standard deviations of lung compliance and conductance are strictly $\sigma_{\ln F_{CL}:F_{VA}}$ and $\sigma_{\ln F_{Cd}:F_{VA}}$, but hereafter in this work are given as σCL and σCd respectively for simplicity of notation. The variation of deadspace between lung units is described by a normal distribution with standard deviation σVD. The schematic shown in Figure 2.21 illustrates three modelled lung units, each with an equal volume at FRC, but with variety in deadspace volume, compliance and conductance. One aspect of lung physiology that is unaccounted for within the model is airway obstruction. In reality, the ventilation to the lung's alveolar regions will be affected by both airway obstruction and alveolar compliance. In this model, the parameter describing the distribution of compliance is expected to capture the combined inhomogeneities of these factors.

Gas within the modelled lung's alveolar compartments is assumed to be perfectly mixed. It is also assumed that alveolar and arterial gas partial pressures are in equilibrium. Thus, by conservation of mass, the rate of change of the volume of a species in the alveolar unit is equal to the sum of the flux entering via ventilation from the associated deadspace compartment, and the flux due to exchange with the blood across the alveolar membrane. The low tissue solubilities of N_2 and O_2 lead to the assumption that the volume of these gases dissolved in the lung tissue is negligible. CO_2, however, is significantly more soluble that N_2 or O_2 and appreciable volumes are found in lung tissue as a result.[161] To account for this, tissue volume is assumed to be a constant fraction of the total alveolar volume at FRC that is equally distributed among the alveolar compartments. The CO_2 pressures in this tissue and the alveoli are assumed to be at equilibrium. Flux due to CO_2 dissolving or emerging from lung tissue is included in the calculation of the rate of volume change of each alveolar unit.

The gas flux between the alveolar compartments and the blood is dependent on the gas concentrations within the venous blood reaching the lung. These data cannot be measured by the MFS, and so they are estimated within the model. The venous concentrations of O_2 and CO_2 are

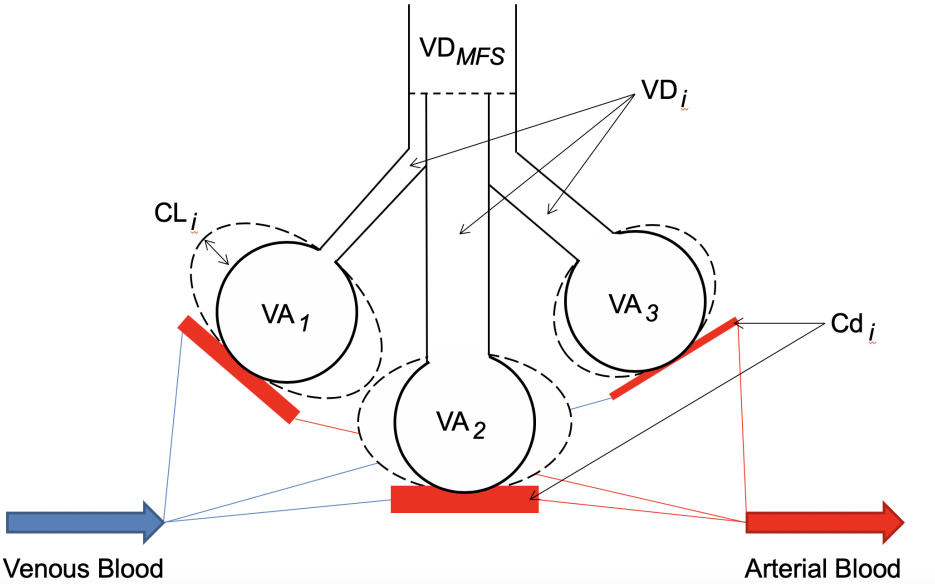


Figure 2.21: Schematic diagram of the Lognormal lung. N (here N=3) perfectly mixed aveolar compartments, N personal deadspace compartments (VD_i) and a common deadspace compartment (VD_{MFS}) that arises due to the introduction of the measurement device are shown. Fractional compliances (F_{CL}), fractional conductances (F_{Cd}) and fractional deadspace volumes are shown varying between lung units.

estimated, matching the modelled net volumes passing through the mouth during expiration to the experimental data. This model falls down during the N_2 washout period, however, as the arterial O_2 concentration rises during pure O_2 breathing. Recirculation is therefore modelled by assuming a single body O_2 store which continues to consume O_2 at the rate recorded during air-breathing. To model the body's N_2 stores, and their exchange with the blood, a model described by Baker and Farmery is implemented.[162] The solubility of N_2 in blood is very low, and hence the volume of N_2 exchanged with the gas during air-breathing is close to zero. The requirement to utilise a model the body's gas stores is most apparent during the N_2 washout period, when falling N_2 pressure within the lung leads to flux from the body stores via the blood.

Gas transport within the modelled lung's conducting airways is assumed to occur by convection. Experiments using simultaneous multi-breath washouts of helium and sulphur hexafluoride have previously shown that within the conducting airways gas transport via diffusion was negligible compared to that by convection.[163] The deadspace compartments through which gas is transported are assumed to be cylindrical with uniform cross section. Flow through the conducting airway is modelled as plug flow, representative of turbulent flow in a cylindrical pipe geometry.[164]

2.4.2 Experimental Protocol

This method of assessing lung function relies upon the highly accurate nature of the MFS measurements. The model of the lung makes the assumption that there is sufficient information content in MFS data collected during steady air-breathing and during a subsequent period of inert gas washout to infer much of the form and degree of inhomogeneity present within the lung. The multi-breath N_2 washout is the experimental protocol used to provide the model with suitable information. During this procedure, an individual breathes normal air through the MFS for 10 minutes, followed by a 5 minute period of breathing medical grade O_2 (>99.5% pure). The rate at which the air-filled lung volume equilibrates with the pure O_2 is used to lend insight into the distribution of the ventilation-volume ratio. The volunteer's nose is occluded and a good seal on the mouthpiece is required throughout. A pulse oximeter (Masimo, Radical-7) is worn on a finger, measuring the fraction of total haemoglobin that is oxygen-saturated in arterial blood (SpO_2) and the pulse rate. These values are reported to the MFS. The N_2 washout has the advantage of being a non-invasive procedure that is relatively easy for even individuals with diseased lungs to accomplish, with no sustained breath holding or even steady breathing required.

To run the model, it must be supplied with a total flow profile of gas at the mouth, and the inspiratory gas composition profile. The outputs of the model are the compositions of the expired gas during exhalation. The differential equations within the model are solved at 10 ms intervals. Within this work, the number of alveolar compartments used within the model is chosen to be 125. This number represents a compromise between the quality of the model's fit to the measured data and computational overheads required to run the model. The parameters produced by the model, VA_{tot}, VD_{tot}, and the inhomogeneity parameters σCL, σCd, and σVD are those that minimise the sum of squared differences (the cost function) between the airway fluxes output by the model for each gas species during expiration and the data recorded by the MFS. During air-breathing, the CO_2 and O_2 flux differences are used in the cost function, and during pure O_2 breathing, the N_2 flux differences are used.

The exclusion criterion for determined parameter sets is dependent on SpO_2 values. Specifically, the measured SpO_2 values during the final five minutes of air-breathing are compared with the modelled arterial SpO_2. In the case that the modelled SpO_2 is greater than the measured value, the

difference is attributed to pulmonary shunt, the fraction of perfusion to the lung that is not exposed to ventilated alveolar space. The contribution of this perfusion to gas exchange is zero owing to the $\dot{V}/\dot{Q}$ ratio of zero. In the case where the modelled SpO_2 is less than the measured value by 3.5% or more, the determined parameters are excluded. The choice for this value is somewhat arbitrary, but its basis is that at differences beyond this, the physiology being modelled is clearly significantly removed from the volunteer's true physiology. The error associated with the pulse oximeter SpO_2 measurement is significant, an independent study finding a bias of 0.31% and precision of $\pm$ 1.98%.[165] The root mean square measurement error is typically used to evaluate the error associated with pulse oximetry measurements.[166] This is calculated by taking the square root of the sum of the squares of the bias and the precision, which, in this case, gives an error $\pm$ 2.00%. The permitted SpO_2 difference for an accepted model solution must be at least equal to this measurement error.

2.4.3 Model Fit to MFS Data

This section describes the fit of the Lognormal Lung model to an exemplar MFS N_2 washout dataset. The dataset used is the first 15 min of the MFS validation procedure shown in Figure 2.20. This dataset consists of 10 min of air-breathing followed by 5 min of N_2 washout with medical O_2 as the inspiratory gas. For each experimental dataset, the fitting procedure was initially repeated four times from different, randomised starting points to check that the same minimum would be found. If this were not the case, additional randomised starting points were used as a practical check to ensure that the minimum associated with the best fit (lowest cost function) was identified. The model's best fit to this dataset is shown in Figure 2.22. The fit of the model to the measured data is extremely good, such that the model fit is obscured. Figure 2.23 illustrates expiratory profiles for representative breaths during air-breathing, early in the N_2 washout phase, and later in the N_2 washout. The model described the within-breath morphology of these expiratory profiles well.

The parameters determined to minimise the model's cost function, and thus represent the best fit to the experimental data, are shown in Table 2.4. To give context to these determined parameters, comparisons with the proof of principle study by Mountain *et al.*[158] are made. In that work, six young healthy volunteers, six older healthy volunteers, and six chronic obstructive pulmonary disease (COPD) patients each undertook a series of six N_2 washout procedures. The determined Lognormal Lung parameters for each of the volunteers were compared. For each inhomogeneity

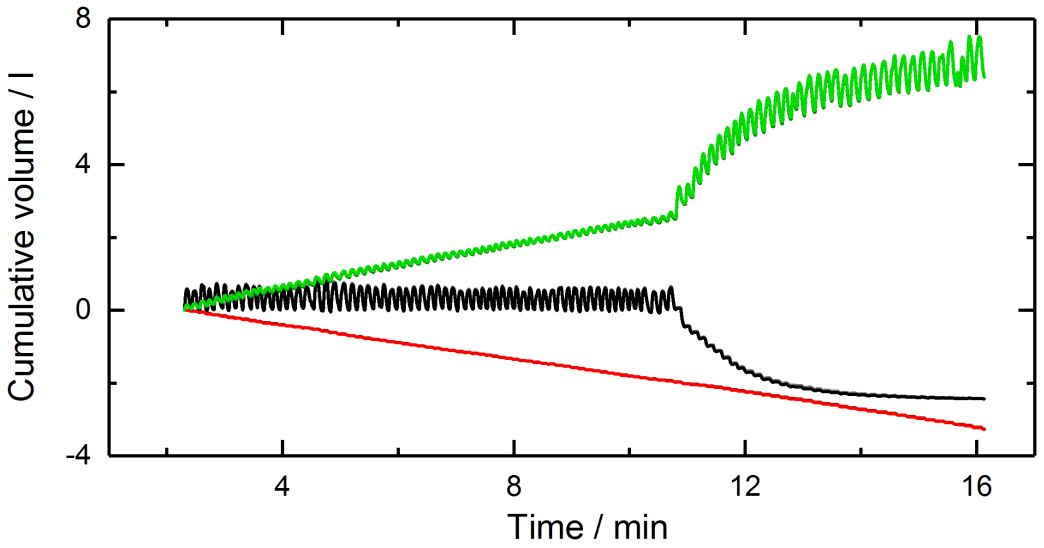


Figure 2.22: Cumulative volume record for the N_2 washout procedure for O_2 (green), N_2 (black), and CO_2 (red). Measured MFS data are shown by solid lines and best fit model simulations are shown by dashed lines in darker shades. The modelled data are almost entirely obscured because of their excellent agreement.

parameter, highly significant differences were found between the three volunteer groups, with the COPD group showing significantly elevated parameters. Each parameter showed very strong within-subject reproducibility for the repeat measurements.

Table 2.4: Lognormal Lung parameters determined from MFS validation dataset. Included for comparison are the average parameters determined for young healthy volunteers and COPD patients from work by Mountain *et al.*.[158] The alveolar and deadspace volumes are given in units of litres under conditions of body temperature and pressure saturated (BTPS).

Model parameter	Determined value	Young healthy average	COPD patient average
VD_{tot} /l	0.166	0.179	0.330
σVD	0.329	0.409	0.475
VA_{tot} /l	3.309	3.403	3.340
σCL	0.318	0.377	0.821
σCd	0.542	0.617	1.337

The volunteer for the example dataset considered here was a 26 year old healthy male. The determined parameters show good agreement with the published average values for the young healthy group. The three determined inhomogeneity parameters are all lower than the average values for the healthy group. The alveolar and deadspace volumes determined by the model are reasonably typical given the volunteer's characteristics, providing an FRC of 3.4751 (the sum of VD_{tot} and VA_{tot})

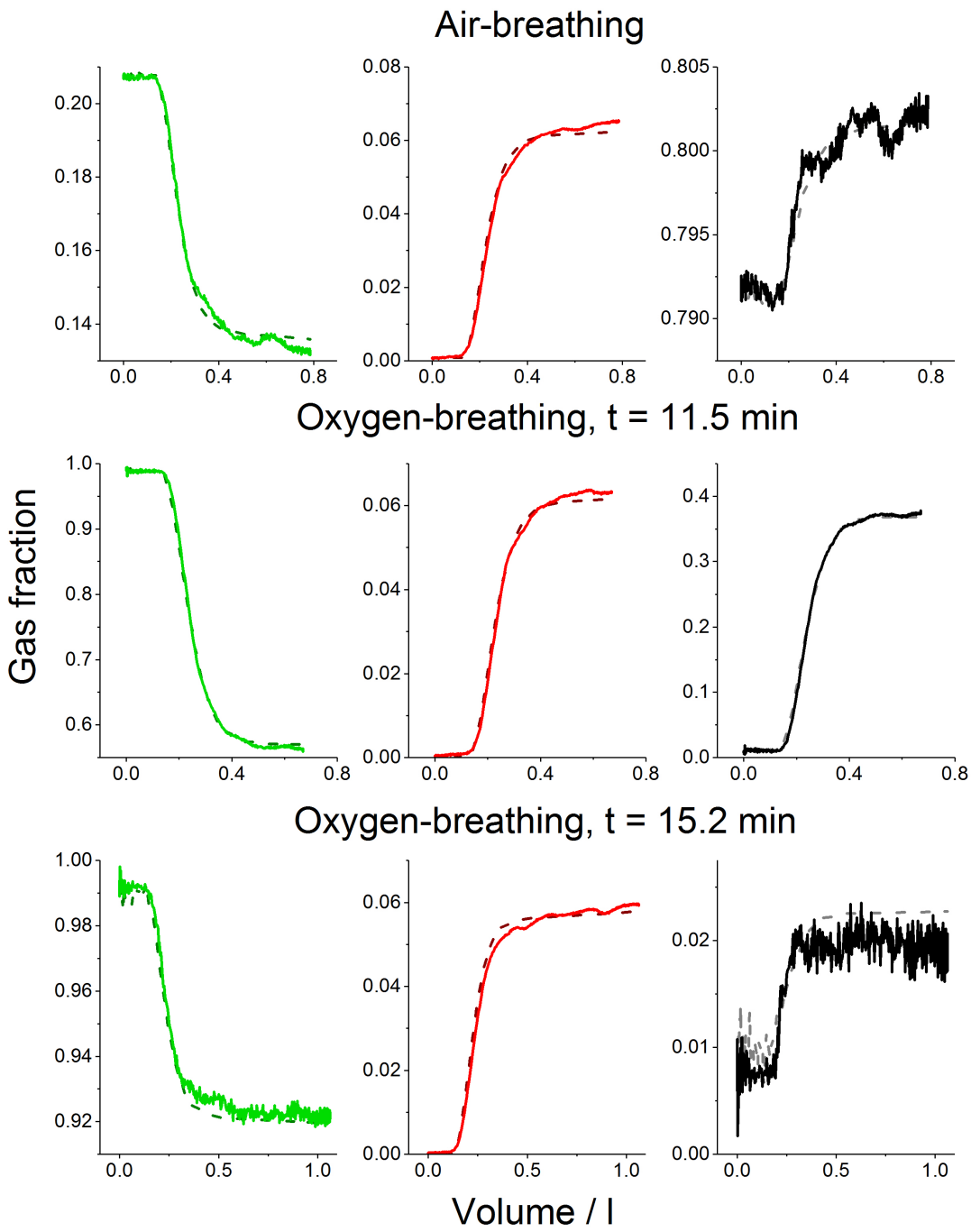


Figure 2.23: Expiraotry profiles showing dry gas fractions for measured MFS data (solid lines) and best fit modelled Lognormal Lung data (dashed). Data for O_2 are shown in green, for CO_2 in red, and for N_2 in black. The upper row shows expiratory profiles from a breath in the air-breathing period, the profiles shown in the middle row are taken from a breath early in the N_2 washout period, and the lower expiratory profiles are taken from a breath towards the end of the washout.

that is only 236 ml greater than that predicted by the European Respiratory Society's regression determined formula.[167] The calculated normalised deadspace (VD_{tot} /VA_{tot}) is 0.050, just 7% lower than the average value for the young healthy group. The averaged pulse-oximeter measured arterial SpO_2 during the air-breathing period was 96.0% and the modelled arterial SpO_2 during this period is 96.7%: this difference provides an estimated pulmonary shunt of 3.0%. The model parameters determined for this dataset are representative of a healthy lung. The mean squared error of the model's simulated concentrations from the measured data is 1.19×10^{-6}. This represents an excellent level of agreement. The mean squared error has previously been shown to be on average greater for the COPD patient group (8.05×10^{-6}) than the healthy group (2.88×10^{-6}), but a good fit to the data is observed in all cases.

2.5 Summary

The molecular flow sensor, MFS, a device capable of making highly accurate measurements of gas exchange at the mouth, has been described in this chapter. The MFS contemporaneously measures O_2, CO_2, and H_2O vapour concentrations in the airway. Measurements of gas temperature, pressure, and flow, via a sensor based on a pneumotachograph, are utilised in order to evaluate gas exchange. The accuracy of the MFS has been demonstrated, with the device capable of measuring N_2 production rates lower than $10\,ml\,min^{-1}$. In the latter part of this chapter, a model of lung physiology has been presented, the Lognormal Lung model. This model quantifies three aspects of inhomogeneity within the lung. It has been fit to exemplar MFS data from a young healthy volunteer, with the best-fit parameters showing good agreement with those for similar volunteers published by Mountain *et al.*.[158]

In the following two chapters, a series of studies utilising the MFS and Lognormal Lung model are presented. In Chapter 3, the inhomogeneity parameters of patients with COPD are investigated in a cross-sectional study seeking to evaluate the potential of this technique to aid in earlier diagnosis of this chronic condition. This chapter also describes a validation study in COPD patients comparing derived parameters from the Lognormal Lung model with parameters determined using the MIGET technique.

A pair of studies investigating the lung inhomogeneity of patients with asthma are presented in Chapter 4. Initially, a cross-sectional study of asthma patients was performed. The clinical

potential of the derived inhomogeneity parameters as a means of assessing disease activity is evaluated. In the last presented study, this technique was used in a longitudinal study to describe the lung inhomogeneity responses to a range of therapeutic interventions in severe eosinophilic asthma patients.

Chapter 3

Investigation of Chronic Obstructive Pulmonary Disease Patient Group

Chronic obstructive pulmonary disease (COPD) affects around 200 million people worldwide.[8] The disease is characterised by airflow limitation, and is associated with high morbidity and mortality. Smoking is the major risk factor associated with COPD.[168] As many as 50 % of smokers develop COPD, although the risk falls by about half following smoking cessation.[169] The use of solid fuels, either for cooking or heating, presents further significant risk.[170]

COPD presents two major clinical challenges. The first is the identification of early stage disease. The measurement of obstructive spirometry ($FEV_1/FVC<0.7$) is currently used for diagnosis.[171] FEV_1, however, is known to primarily reflect large airway dysfunction and is therefore insensitive to active disease in the smaller airways. Many current and former smokers suffer exacerbations, display activity limitation and evidence of airway disease, but have preserved spirometry and therefore COPD is undiagnosed.[29] Reliance on spirometric measurements therefore can result in missed diagnoses despite the presence of significant symptoms, or diagnoses delayed until structural lung damage becomes irreversible.[30] Opportunities for early therapy or secondary prevention are missed.[11,28] Furthermore, the fixed threshold of $FEV_1/FVC<0.7$ does not take into account the age-related decline of FEV_1/FVC in the normal non-smoking population.[172] Thus, while the younger population suffers from missed and/or late diagnosis, the older population suffers from overdiagnosis and unnecessary therapeutic intervention. These issues are illustrated in Figure 3.1, which shows the decline of the FEV_1/FVC lower limit of normal with age. The implementation of a non-invasive assessment of

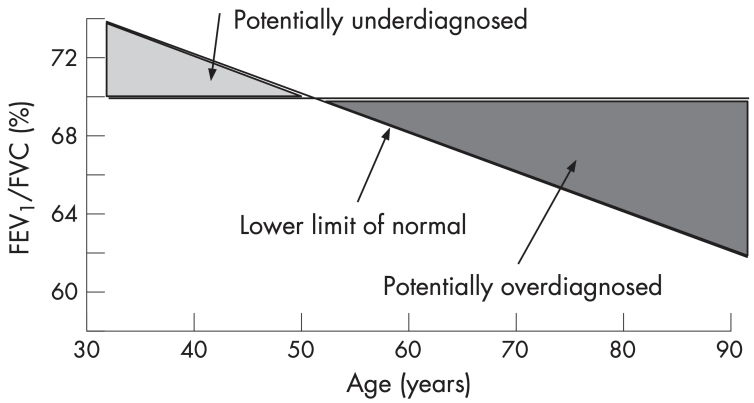


Figure 3.1: Age-related decline of FEV_1/FVC with age among white never-smoking women in the third National Health and Nutrition Examination Survey.[172] The light shaded region illustrates younger adults who are 'potentially underdiagnosed' with COPD and the darker region illustrates elderly individuals who are 'potentially overdiagnosed' with COPD. The trends for other race-gender groups are comparable, with the lower limit of normal crossing 70 % at a younger age in men compared to women. Figure reproduced from Mannino *et al.*.[173]

lung function that is simple to perform and can sensitively diagnose early stage COPD would present significant clinical opportunities for therapeutic intervention and smoking cessation.

The second major challenge associated with the management of COPD is the classification of disease severity. Currently, patients diagnosed with COPD are divided into four disease stages according to their FEV_1 % predicted. The characteristics of the four stages are shown in Table 3.1. Spirometry has been found to be predictive of mortality and patient outcomes at a population level.[174] In many individual cases, however, there is a significant discord between measured FEV_1 and symptoms, exacerbation frequency and disease progression. The aim of COPD clinical management is to match treatment type and dosage to treatable disease activity, something with which large airway dysfunction does not correlate well. To achieve this aim, a measurement representing underlying pathophysiology, and therefore disease activity, is required. A measurement of this type might offer opportunities for patient stratification, or the identification of treatable disease traits.

Spirometry is used to diagnose and measure the severity of COPD, but contains no information about disease phenotype. One method of assessing phenotype is computerised tomography (CT) scanning, in which a series of x-ray images is recorded and used to reconstruct digital cross-sectional images of the thorax.[175] This assessment can be used to demonstrate the presence, distribution, and extent of emphysema in COPD.[176] Emphysema is characterised in CT scans by areas of abnormally

Table 3.1: COPD disease staging definitions and characteristics.[171] FEV_1 is the forced expiratory volume in one second, and FVC is the forced vital capacity.

COPD disease stage	Characteristics
Stage 1	$FEV_1/FVC < 0.7$
Mild	$FEV_1 > 80\,\%$ predicted
Stage 2	$FEV_1/FVC < 0.7$
Moderate	$50\,\% < FEV_1 < 80\,\%$ predicted
Stage 3	$FEV_1/FVC < 0.7$
Severe	$30\,\% < FEV_1 < 50\,\%$ predicted
Stage 4	$FEV_1/FVC < 0.7$
Very severe	$FEV_1 < 30\,\%$ predicted

low attenuation which contrast the surrounding normal lung parenchyma.[177] Parameters that assess emphysema from CT images have been found to correlate with clinical outcomes including symptoms and disease progression.[178,179] The principal limitation of CT scanning is the potentially harmful dose of ionising radiation prescribed with each examination. The radiation dose of each chest examination is approximately twice the average annual effective dose from background radiation.[180]

This chapter describes three studies, each performed in a clinical setting, utilising molecular flow sensing and the Lognormal Lung model to evaluate patient lung inhomogeneity. The first study is a cross-sectional assessment of patients with COPD in which lung volumes and inhomogeneity parameters were evaluated for patients with a broad range of disease severities. The determined parameters were compared with those from an age-matched group of healthy volunteers. The second study presented assessed lung inhomogeneity in a different patient group, those following recovery from a primary spontaneous pneumothorax. The hypothesis of this study was that an accurate measurement of lung inhomogeneity could elucidate subtle underlying differences between the pulmonary physiology of pneumothorax patients and healthy volunteers. This is included within the chapter on COPD as a result of the relevance of smoking status on the results. The final study presented in this chapter was performed to validate the indices of inhomogeneity determined from the MFS in combination with the Lognormal Lung model. Derived parameters of ventilation and perfusion inhomogeneity were compared with those measured by the highly invasive MIGET technique.

3.1 Cross-sectional Investigation of Lung Inhomogeneity in COPD

Inhomogeneity in the lung, both of ventilation and perfusion, is abnormally elevated in patients with established COPD.[181] This results in the compromised gas exchange which characterises COPD. When measured by the MIGET technique, inhomogeneity abnormality has been shown to increase with disease severity.[45] Abnormal lung inhomogeneity in COPD patients has also been established using parameters derived from multiple breath washout data.[182] For patients with mild COPD, significant inhomogeneity abnormalities are measured despite only limited airflow limitation measured by spirometry. In early stage disease, COPD is likely most active in smaller airways, alveolar spaces and blood vessels. Spirometry, which predominately reflects large airway function, is insensitive to disease activity of this type.

The method of lung inhomogeneity assessment described in Chapter 2 utilises a mechanistic model of the lung that is fitted to highly accurate, highly precise data recorded by the molecular flow sensor, MFS. This technique provides estimates of the inhomogeneity of lung conductance, compliance, and deadspace volume distribution, and deadspace and alveolar volumes at FRC. The Lognormal Lung model parameters of a group of 32 patients with COPD were investigated in this cross-sectional study. This group consisted of patients with a broad range of disease severities, from mild to very severe. The initial objective of this study was to compare the parameters determined in COPD patients with those of an age-matched group of healthy controls. The study's second objective was to assess the potential of this non-invasive technique to meet the requirements of contemporary COPD management; providing sensitive markers of early stage disease and patient classification based on underlying pathophysiology. This study, undertaken at Oxford's Churchill Hospital, was the first example of N_2 washout data recorded in a clinical setting by the MFS being used to determine lung inhomogeneity parameters.

3.1.1 Methods

Thirty two patients with a diagnosis of COPD volunteered to take part in this study. The experimental work was conducted in accordance with the general ethical principles of the Declaration of Helsinki, with the study approved by the South Central Oxford A Research Ethics Committee

(17/SC/0172). Informed written consent was taken from each patient. Each patient underwent standard forced spirometry and a pair of N_2 washout lung inhomogeneity tests. The lung inhomogeneity tests were performed using the MFS and subjects were connected to the MFS via a mouthpiece and a heat and moisture (HME) filter, and breathed with nose occluded. Arterial O_2 saturation, SpO_2, was measured by a pulse-oximeter. Subjects breathed air for 10 minutes and then pure O_2 for the final 5 minutes. The two washout procedures were separated by a 15 min recovery period, necessary to allow re-equilibration of the lung with room air.

The Lognormal Lung model of an inhomogeneous lung was fitted to the measured gas-exchange data. The process of fitting the model to the measured data provided estimates of anatomical deadspace and alveolar volumes at functional residual capacity, and three measures of inhomogeneity, σVD, σCL and σCd, which are the standard deviations for distributions across the lung volume for deadspace volume, alveolar compliance and vascular conductance, respectively. For each dataset, the parameter optimisation procedure was performed four times, from different parameter starting points.

Lung inhomogeneity parameters were compared with those determined for an age-matched healthy group consisting of 10 participants. This participant group included lab volunteers and the members of the older healthy group reported by Mountain *et al.* with non-obstructive spirometry.[158] Anthropometric data for the two subject groups are shown in Table 3.2. Statistical analyses were performed using OriginPro software. Welch's t-tests were performed to evaluate the significance of parameter differences between groups. This method of hypothesis testing is an adaptation of the Student's t-test, and is more reliable when the two groups have unequal variances and/or unequal

Table 3.2: Anthropometric data for COPD patients and healthy controls. Data are shown as group mean ± standard deviation where applicable.

	COPD	Healthy
Group size	32	10
Female, # (%)	5 (16 %)	3 (30 %)
Age / years	66.7 ± 8.5	69.5 ± 4.1
Height / m	1.71 ± 0.11	1.73 ± 0.09
Weight / kg	83.5 ± 23.5	71.4 ± 16.3
BMI / kg m^{-2}	28.1 ± 6.2	23.1 ± 3.6

sample sizes.[183] Correlations were assessed using the Spearman rank order method. Unlike other statistical measures of correlation, for example Pearson's method, the Spearman method does not assume linear relationships between variables.[184]

3.1.2 Results

The N_2 washout experimental procedure was generally well tolerated by the patients with COPD, although two subjects chose to perform only a single inhomogeneity test. Thus, 62 experimental procedures were performed in total. Data recorded during a washout performed by one of the patients are shown in Figure 3.2. For these data, the O_2 consumption and CO_2 production rates were 311 and 271 $ml\,min^{-1}$ respectively during the final 5 mins of the air-breathing period. The measured respiratory quotient was therefore 0.87. The measured N_2 balance during this period was -9 $ml\,min^{-1}$. Low N_2 balances such as this illustrate both the accuracy of MFS measurement and a good seal at the nose and mouth of the subject.

The Lognormal Lung model was fitted to the recorded data from each N_2 washout procedure. In three cases, the model failed to successfully fit to the measured data, failing to converge on an optimised set of parameters. These failures occurred for datasets with recorded N_2 balances considerably beyond the MFS measurement specification and as a result of leaks from the participants' nose or mouth. In all other cases, the cost function minimisation was successful, returning a set of best fit estimated lung parameters. The parameters determined from a further seven datasets were excluded on the grounds that the modelled SpO_2 during air breathing being more than 3.5 % below the pulse-oximeter measured value during the same period. In these cases, the modelled lung was deemed to be physiologically unrepresentative of the participant lung. There were two patients for whom parameters from both experimental procedures were excluded, and hence no lung inhomogeneity data are presented. Two accepted sets of lung parameters were determined for 22 subjects, for whom averaged parameters are presented. A single parameter set was determined for the remaining 8 subjects. In all, 52 of the 62 recorded experimental procedures, 84 %, returned parameters of lung inhomogeneity.

Comparisons of the determined Lognormal Lung model parameters between the patients with COPD and the control group are shown in Figure 3.3. The three parameters of lung inhomogeneity, the standard deviations of lung compliance distribution, σCL, vascular conductance distribution,

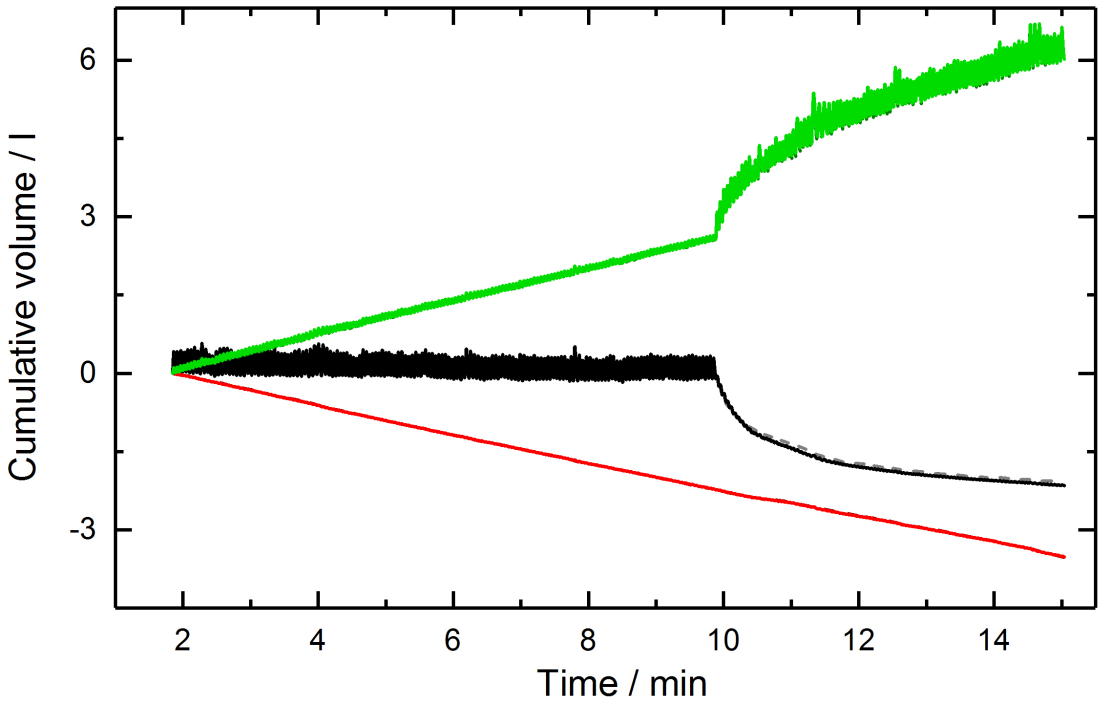


Figure 3.2: Cumulative volume profiles for a N_2 washout procedure undertaken by a patient with COPD. O_2 is shown in green, N_2 in black, and CO_2 in red. Measured MFS data are shown by solid lines and the best fit model simulations are shown by dashed lines in darker shades.

σCd, and anatomical deadspace volume distribution, σVD, were all significantly elevated in the COPD patient group. In each case, analysis by Welch's t-test returned p-values below 10^{-4}. The vast majority of the COPD patients (28 of 30) returned σCL parameters greater than the upper limit of normal, defined as the parameter $mean + 1.98\,\sigma$ for the control group. For σCd and σVD, the number of patients who returned parameters elevated beyond the upper limits of normal were 23 and 17 of 30, respectively. The average determined alveolar volume at FRC was greater for the COPD patients than the healthy controls, although this difference was not significant. Both anatomical deadspace volume and this quantity normalised by the determined alveolar volume were significantly larger in COPD patients, $p<0.005$ and $p<0.001$ (Welch's t-tests), respectively.

Parameter repeatability was assessed for the 22 subjects for whom two Lognormal Lung parameter sets were determined. For each parameter, the standard deviation, σ, of the two determined values was calculated by $\frac{1}{\sqrt{2}}|x_1 - x_2|$, where x_1 and x_2 are the two determined values. The average of these standard deviations were calculated across the 22 subjects for each parameter. This σ was

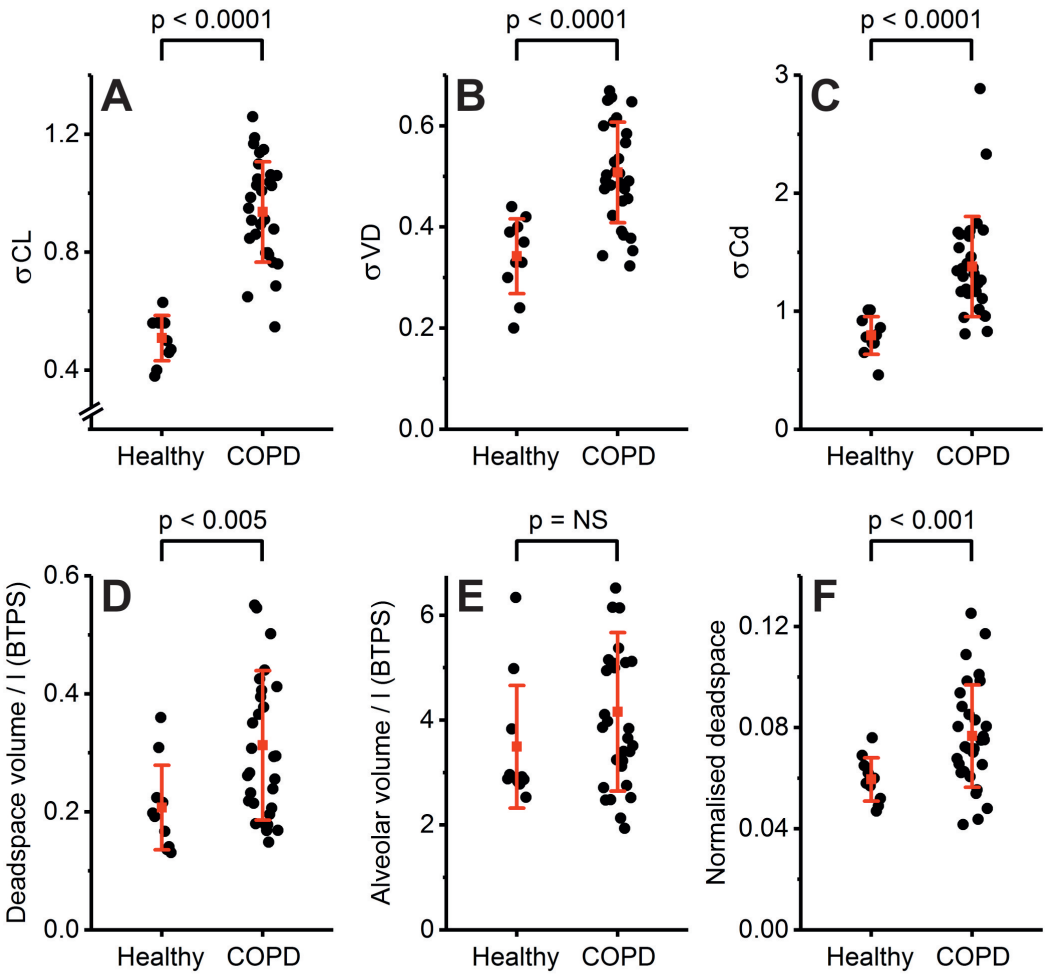


Figure 3.3: Comparisons of Lognormal Lung parameters for COPD patients and aged-matched healthy participants. (A) Standard deviation for the distribution of lung compliance, σCL. (B) Standard deviation for the distribution of anatomical deadspace, σVD. (C) Standard deviation for the distribution of vascular conductance, σCd. (D) Anatomical deadspace volume. (E) Alveolar volume at FRC. (F) Anatomical deadspace normalised to alveolar gas volume at FRC. Significant differences were identified between the COPD patients and healthy controls (Welch's t-tests) for σCL, σVD, σCd, deadspace volume, and normalised deadspace.

then normalised to the averaged determined parameter across the group in order to evaluate repeatability. The repeatability of the airway parameters was very good, illustrated within Table 3.3. The mean standard deviations of the determined volumes were 8.5 % and 3.3 % of mean parameter values for deadspace and alveolar volume, respectively. The resulting mean standard deviation of deadspace volume normalised to alveolar volume is 8.6 % of the mean value. The repeatability of the airway inhomogeneity parameters was comparable: for the standard deviation of the deadspace volume distribution, σVD, the mean standard deviation was 4.9 % of mean determined parameter, and for the standard deviation of the lung compliance distribution, σCL, this value was 5.2 %. The variability was, as expected, greater in the circulatory parameters. The standard deviation of the vascular conductance distribution, σCd, returned a mean standard deviation that was 22.5 % of the mean parameter value. The difference between the modelled and measured arterial O_2 saturations also showed substantial variability, the average standard deviation being 51.2 % of the mean parameter.

Table 3.3: Repeatability of Lognormal Lung parameters in COPD patients. For each patient in whom a pair of parameter sets were obtained, the standard deviations, σ, of the pairs of parameters were calculated. Here, the mean σ is compared to the mean determined parameter values for this patient group. The alveolar and deadspace volumes are given in units of litres under conditions of body temperature and pressure saturated (BTPS).

Lognormal Lung parameter	Mean determined value	Mean σ from consecutive washouts	Mean σ normalised to mean value / %
VD_{tot} / l	0.31 ± 0.13	0.03	8.5
σVD	0.51 ± 0.10	0.02	4.9
VA_{tot} / l	4.16 ± 1.51	0.14	3.3
σCL	0.94 ± 0.17	0.05	5.2
σCd	1.38 ± 0.42	0.31	22.5

The group of patients with COPD was divided by disease stage, evaluated based on measured FEV_1. The patient numbers, and demographic and spirometric data are shown in Table 3.4 for each COPD disease stage. The average ages are similar in all of the four COPD disease stages. By definition, the measured FEV_1 % predicted decreased as disease severity worsened. A similar trend was observed in the FEV_1/FVC ratio, with airflow obstruction increasing with COPD disease stage. The stage 1 COPD patients displayed minor abnormalities in FEV_1/FVC ratio, and normal FEV_1.

Table 3.4: Demographic and spirometric data of COPD patients grouped by disease severity. Data are shown as patient group mean ± standard deviation.

Characteristic	Stage 1	Stage 2	Stage 3	Stage 4
Group size	4	14	9	3
Female, # (%)	2 (50 %)	2 (14 %)	1 (11 %)	0 (0 %)
Age / years	66.8 ± 12.3	66.4 ± 7.8	69.7 ± 6.3	59.7 ± 6.8
Height / m	1.65 ± 0.10	1.74 ± 0.11	1.69 ± 0.11	1.74 ± 0.06
Weight / kg	87.3 ± 28.5	84.0 ± 21.6	76.8 ± 23.5	95.8 ± 17.5
FEV_1/ % predicted	92.5 ± 6.7	62.0 ± 8.1	39.5 ± 4.7	23.0 ± 0.8
FVC / % predicted	113.6 ± 9.9	85.1 ± 18.5	82.8 ± 15.7	59.2 ± 11.6
FEV_1/FVC	0.68 ± 0.08	0.56 ± 0.06	0.38 ± 0.08	0.31 ± 0.06

Figure 3.4 compares the determined σCL and σCd parameters between the control group and each spirometrically assessed stage of COPD disease. The mean standard deviation of the compliance distribution, σCL, was significantly elevated ($p<0.005$, Welch's t-test) in patients with stage 1 COPD compared to healthy controls. The mean σCL parameter was essentially unchanged from stage 1 to stage 2 patients, but is then significantly elevated from stage 2 to stage 3 ($p<0.005$, Welch's t-test). In all COPD disease stages, the vast majority of patients presented abnormal σCL parameters. The standard deviation of the vascular conductance distribution, σCd, was also significantly elevated ($p<0.0005$, Welch's t-test) in the stage 1 COPD patients compared to healthy controls. The average determined σCd decreased modestly from stage 1 to stage 2, and then again for stage 3. Neither of these decreases, however, were statistically significant (Welch's t-test).

The variations of standard deviation of anatomical deadspace, σVD, and deadspace volume normalised to alveolar volume at FRC with COPD disease stage are shown in Figure 3.5. In stage 1 patients, both parameters were elevated compared to the healthy controls. In both cases, however, these increases were not significant (Welch's t-tests). From stage 1 to stage 2, mean σVD abnormality was unchanged, before a significant increase from stage 2 to stage 3 ($p>0.05$, Welch's t-test). This elevated abnormality was maintained in the stage 4 patients. Across the range of COPD disease severities, the average normalised deadspace was virtually unchanged.

Correlations between spirometric measurements and the Lognormal Lung parameters within the COPD patient group were assessed by the Spearman rank-order method.[184] The strongest corre-

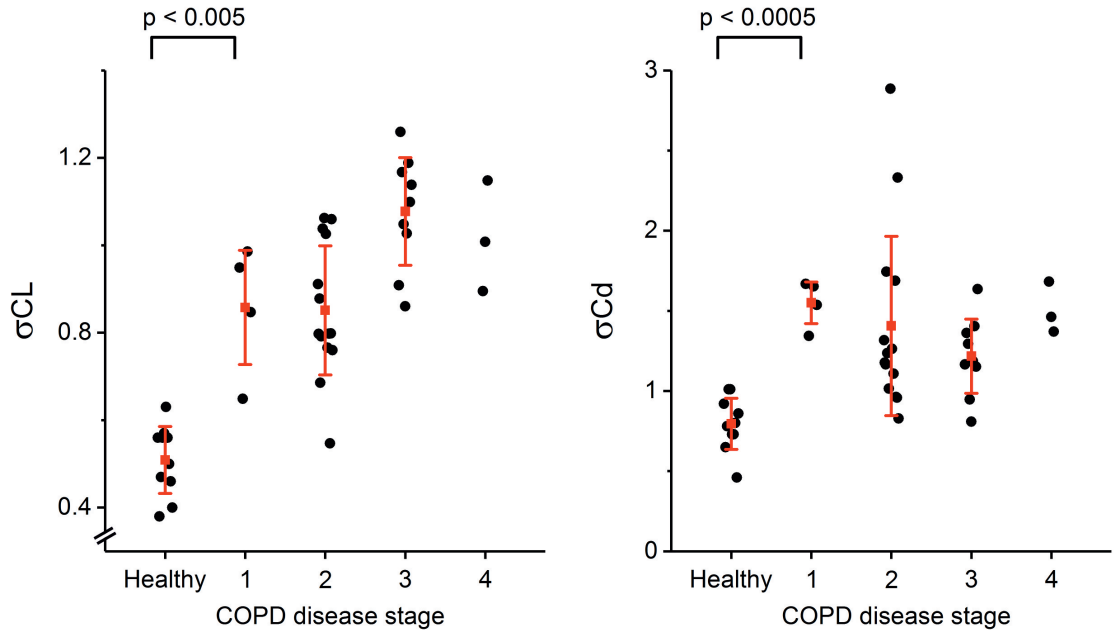


Figure 3.4: Progression of σCL (left) and σCd (right) with COPD disease severity. Data are shown for individuals in black, and stage-by-stage averages and standard deviations are shown in red. Group averages are not shown for stage 4 due to low group population. Significant differences were identified (Welch's t-tests) between the stage 1 COPD patients and healthy controls for both of these parameters of inhomogeneity.

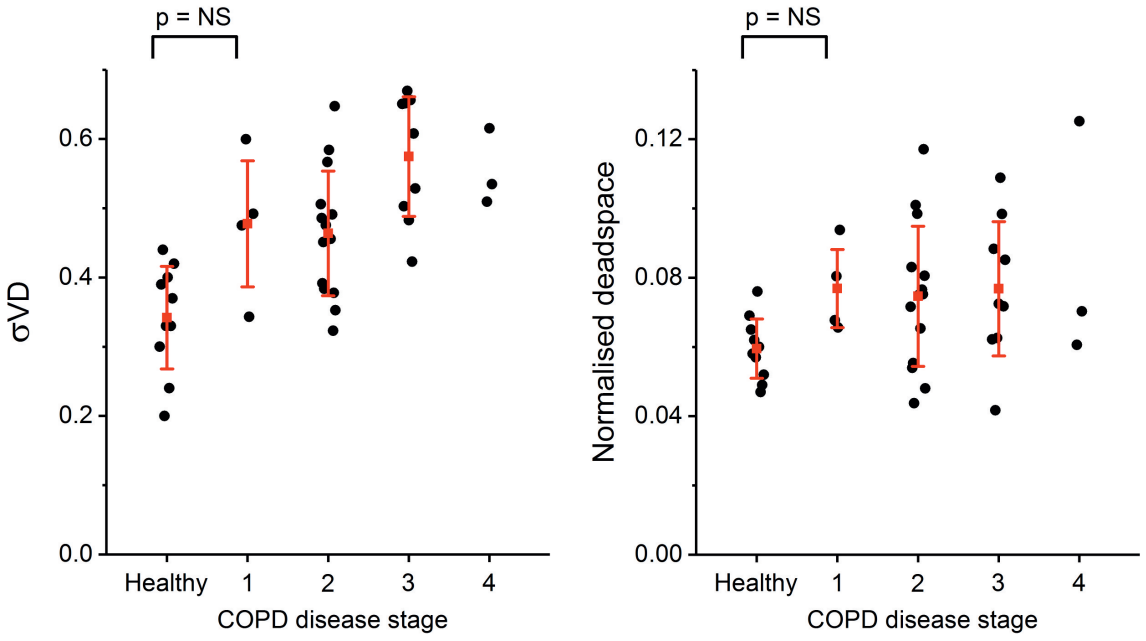


Figure 3.5: Progression of σVD (left) and normalised deadspace volume (right) with COPD disease severity. Data are shown for individuals in black, and stage-by-stage averages and standard deviations are shown in red. Group averages are not shown for stage 4 due to low group population. The differences between the stage 1 COPD patients and the healthy controls were found not to be statistically significant (Welch's t-tests).

lations with the spirometric measurements were identified for σCL. There was strong, significant negative correlation with FEV_1/FVC (Spearman correlation coefficient -0.66, $p<0.0001$), and a weaker, but nonetheless significant, negative correlation with FEV_1 % predicted (Spearman correlation coefficient -0.53, $p<0.005$). These relationships are shown in Figure 3.6. A significant negative correlation existed between σVD and measured FEV_1/FVC (Spearman correlation coefficient -0.58, $p<0.001$), and a weaker correlation with FEV_1 % predicted (Spearman correlation coefficient -0.46, $p<0.01$) was also identified. Neither the normalised deadspace, nor σCd correlated significantly with spirometric measures (Spearman correlation $p>0.05$ in all cases).

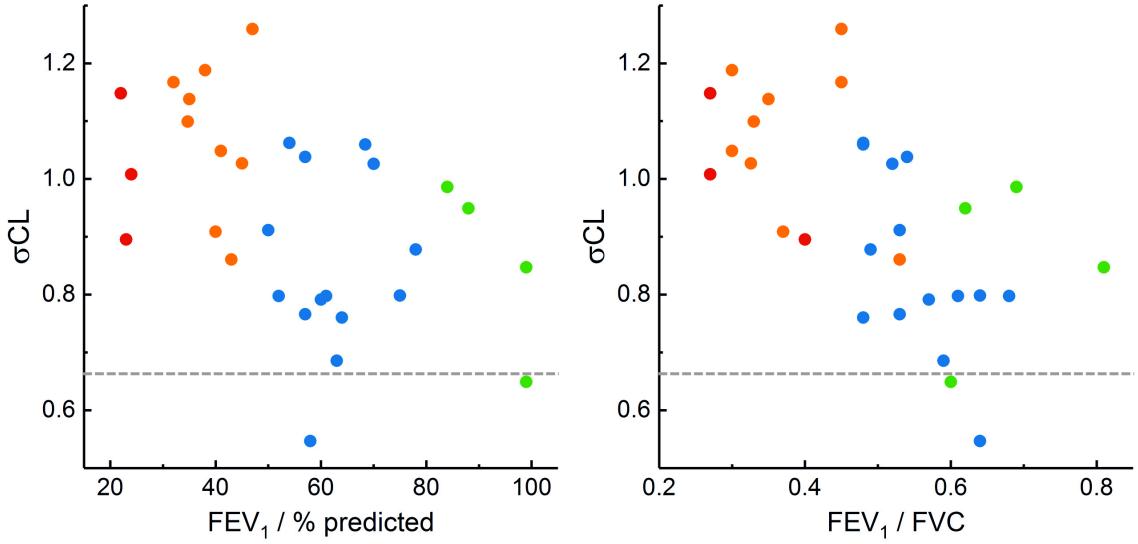


Figure 3.6: Correlation of σCL with FEV_1 % predicted (left) and FEV_1/FVC ratio (right) for COPD patient group. Data are shown in green for stage 1 patients, blue for stage 2, orange for stage 3, and red for stage 4. The upper limit of normal ($mean + 1.98\,\sigma$) for σCL for the aged-matched control group is shown by grey dashed lines.

3.1.3 Discussion

In this study, a new non-invasive technique was used to assess lung inhomogeneity within a group of COPD patients with disease severities ranging from mild to very severe. Good patient tolerance of the N_2 washout procedure demonstrated the clinical feasibility of this technique. The repeatability of the determined parameters for pairs of measurements performed by one subject was generally very good. The exception was the repeatability of the recovered values of σCd, which were found to be less precisely determined. Unlike the airway parameters, σCd relates to perfusion, and so its

estimation is dependent upon more subtle features within the recorded gas phase data.

Each of the three lung inhomogeneity parameters was found to be significantly elevated in COPD patients compared to the healthy control group. This result is in agreement with the literature, previously having been established for lung inhomogeneity assessed by MIGET [181] and the multiple breath washout technique. [182] Lognormal Lung parameters cannot be directly compared with those determined by MIGET or the multiple breath washout; these techniques assess inhomogeneities of ventilation and perfusion, whereas the inhomogeneities of compliance and conductance are intrinsic features of the lung. Intrinsic lung characteristics are independent of subject breathing patterns, allowing subjects to breathe as comfort dictates without the need for breath holding or defined tidal volumes. Distributions of ventilation and perfusion can, however, be derived from the Lognormal Lung parameter sets. Later in this chapter, these derived indices are described and directly compared with those measured using the MIGET technique.

There was a modest correlation between σCL and FEV_1 % predicted in the COPD patient group. Spirometric measurements, FEV_1 and FEV_1/FVC, primarily reflect airflow limitation in the large airways, and thus are relatively insensitive to disease within the small airways. The clinical manifestations of COPD are highly variable and as mentioned previously spirometry is a poor predictor of many clinical features such as breathlessness, health status, and exercise capacity. [185] Furthermore, spirometric measurements contain very limited information on extent of disease control; whether or not patient symptoms could be improved by altering therapeutic doses or approaches. Clinical management of COPD would benefit from an assessment of underlying respiratory physiology that provides a better measurement of patient disease burden. That σCL and FEV_1 are not simple proxies for one another, they are not strongly correlated, might reflect measurement of different facets of the underlying pathophysiology. Where FEV_1 primarily measures airflow obstruction in the larger airways, σCL could reflect smaller airway obstruction. This hypothesis is supported by the significantly elevated σCL parameters determined within the stage 1 patient group. Mild COPD is associated with increased small airway flow resistance, the loss and narrowing of smaller conducting airways preceding emphysematous disease activity within the larger airways. [13] Extensive small airway damage and obliteration can occur before it is detectable with conventional spirometric tests. [186]

The range of the determined σCL parameters within each stage of COPD disease was broad and significant overlap between the groups was displayed. These features are consistent with σCL as a marker of disease activity within the smaller airways. The extent of disease activity in the smaller airways is chiefly dependent on disease phenotype rather than spirometrically assessed disease severity.[187] A novel index of small airway disease therefore has the potential to positively alter clinical management of COPD, enabling therapeutic strategies to be guided by the nature of disease activity. Such an index might also play a role assessing the efficacy of therapeutic interventions.

The degree of inhomogeneity parameter abnormality estimated for stage 1 patients must be highlighted given the minimal degree of spirometrically detected airflow limitation of these patients. The mean airflow limitation, as assessed by FEV_1/FVC ratio, is only 3 % below the value of the normal threshold, 0.7. In contrast, the mean σCL and σCd parameters determined for these patients were 30 and 40 % greater than the upper limit of normal, defined as the control group $mean + 1.98\,\sigma$, respectively. All of the stage 1 patient σCd parameters were above the upper limit of normal, and this was true for 75 % of the group's σCL parameters. Thus, the significantly elevated group averages cannot be ascribed to outliers within the group. As noted earlier, a major concern regarding the use of the fixed FEV_1/FVC ratio of 0.7 to diagnose COPD is the risk of both false-positive and false-negative cases, leading to inappropriate classification and prescribed treatment.[173] The finding of relatively greater lung inhomogeneity than spirometric abnormalities in the stage 1 patients would seem to substantially mitigate that risk. The number of stage 1 patients in this study is very modest however, and whether or not these findings can be extended to larger COPD populations remains to be seen.

The increased anatomic deadspace determined for COPD patients was a more surprising result than the elevated compliance and conductance inhomogeneities. Alveolar deadspace is known to increase with disease, arising through increased $\dot{V}/\dot{Q}$ mismatch, particularly due to emphysema.[188] Both the absolute anatomical deadspace volume and the anatomical deadspace volume to alveolar volume ratio were found to be significantly larger in COPD patients than healthy controls. This must result by an alternative mechanism. One form of emphysema, centriacinar emphysema, acts to dilate and/or destroy the respiratory bronchioles, the larger airways within the lung.[14] Emphysema of this type is strongly associated with smoking. By this mechanism, enlargement of the conducting

airways could lead to increases in COPD patient deadspace that are anatomical rather than simply alveolar in nature.

3.1.4 Conclusions and Future Work

The novel physiological indices investigated in this study, the parameters of the Lognormal Lung model, showed elevated lung inhomogeneity in a group of COPD patients. This result was true even in patients with mild respiratory disease. These results confirm that it is possible to extract sensitive measures of lung inhomogeneity in COPD patients from highly precise measurements of respiratory gas exchange. It was hypothesised that the elevated inhomogeneity parameters, particularly σCL, could reflect COPD disease activity in the small airways, something to which spirometry is insensitive. In this way, this new approach to quantifying lung function has the potential to fulfil the role of a long sought-after marker of early lung damage that occurs before COPD diagnosis.[29] This technique has significant practical advantages over existing methodologies of assessing early-stage COPD, the limitations of which are summarised in Section 1.4. Briefly, this new technique is safe and non-invasive, whereas other methods can be either highly invasive, for example MIGET, or require ionising radiation, as is the case for CT scanning. The parameters of this technique are based on underlying lung physiology, providing a sensitive, repeatable, multi-dimensional series of novel indices.

To strengthen the conclusions of this study in the future, a more extensive clinical study is required. The size of the COPD patient group must be significantly increased, with particular focus on recruitment of stage 1 patients. Recruitment of stage 1 patients in a hospital setting proved difficult; spirometry is rarely preserved in patients being treated in this environment. Assessment of the capacity of this technique to stratify COPD patients in a way that is clinically useful will require determined parameters to be evaluated in the context of patient phenotypes. COPD is a very heterogeneous disease with a range of established phenotypes, most obviously emphysema and bronchitis, but patients are also clinically stratified based on frequency of acute exacerbations, and the rate of lung function decline over time. Initial phenotyping typically requires CT images to assess the extent of emphysema, a method which exposes patients to ionising radiation. Further clinical phenotyping is typically performed longitudinally owing to the absence of a method capable

of predicting exacerbation frequency or future trajectory of airflow limitation. A non-invasive assessment with the ability to usefully phenotype COPD patient disease activity would allow stratified therapeutic intervention to be implemented.

The following section describes another clinical cross-sectional study evaluating patients with a different respiratory disease, primary spontaneous pneumothorax. This study failed to identify inhomogeneity abnormality in these patients, but the results were valuable nonetheless, illustrating the potential of the Lognormal Lung indices to detect early lung damage caused by smoking.

3.2 Cross-sectional Study Evaluating Patients Following Primary Spontaneous Pneumothorax

Patients who suffer a Primary Spontaneous Pneumothorax (PSP) have conventionally been considered to have no underlying lung disease. More recently, however, this view has been challenged, with increasing evidence of patients displaying emphysema-like blebs and bullae in the lung parenchyma, bronchial inflammation, and abnormalities in the parietal pleural layer, the lung's outer membrane.[189–192] Clinically useful assessment of lung function in PSP patients is currently limited. Spirometry is well-established and routinely used in pulmonary disease diagnosis and monitoring. It is, however, relatively insensitive to subtle changes in region pathology or heterogenenity in the lung.[193] Region pathology such as that associated with PSP patients may be visible on computed tomography (CT) imaging, but this technique is associated with ionising radiation.[194] This study sought to investigate the Lognormal Lung inhomogeneity parameters in patients who have recovered from a PSP.[195]

3.2.1 Methods

Twelve pneumothorax patients were studied, recruited as part of the OX-RAMPP (Oxford Sub-study of Randomised Ambulatory Management of Primary Pneumothorax) trial. All patients were initially enrolled into the parent study (RAMPP), then offered inclusion in OX-RAMPP at completion of their treatment. The trial was approved by the NHS Research Ethics Committee (Ref 16/SC/0412).

Participants were provided with information leaflets along with verbal explanation of the technique. Written consent was taken in every case. Each participant performed forced spirometry and two N_2 washout experimental procedures, breathing air for 10 min followed by medical O_2 for the final 5 min. The two procedures were separated by a 15 min recovery period. Participants breathed through the MFS via a mouthpiece with nose occluded. Arterial O_2 saturation, SpO_2, was measured by a pulse-oximeter. The data were analysed using the Lognormal Lung model, with parameters quantifying lung inhomogeneity and lung volumes used to assess lung physiology.

Lung inhomogeneity parameters were compared with those determined an age-matched healthy group consisting of 24 participants. This participant group included lab volunteers and the young healthy group published by Mountain *et al.*.[158] Statistical analyses were performed using OriginPro software. Welch's t-tests were performed to evaluate parameter differences between groups.

3.2.2 Results

Each of the twelve participants performed two experimental procedures. For the first dataset of one participant, the lung model's regression failed to converge. The parameters determined from the first dataset of another participant were deemed physiologically unreasonable due to the modelled SpO_2 being more than 3.5 % below the pulse-oximeter measured value. These parameters were therefore excluded. Thus, 22 of 24 (92 %) experimental procedures returned lung parameters. For the ten participants in whom both datasets returned lung parameters, averaged parameters are presented. The average age was 29.8 ± 8.9 years for the pneumothorax group and 27.4 ± 8.3 years for the healthy group. Four of the twelve participants were current smokers, with a single ex-smoker. The healthy group consisted entirely of non-smokers.

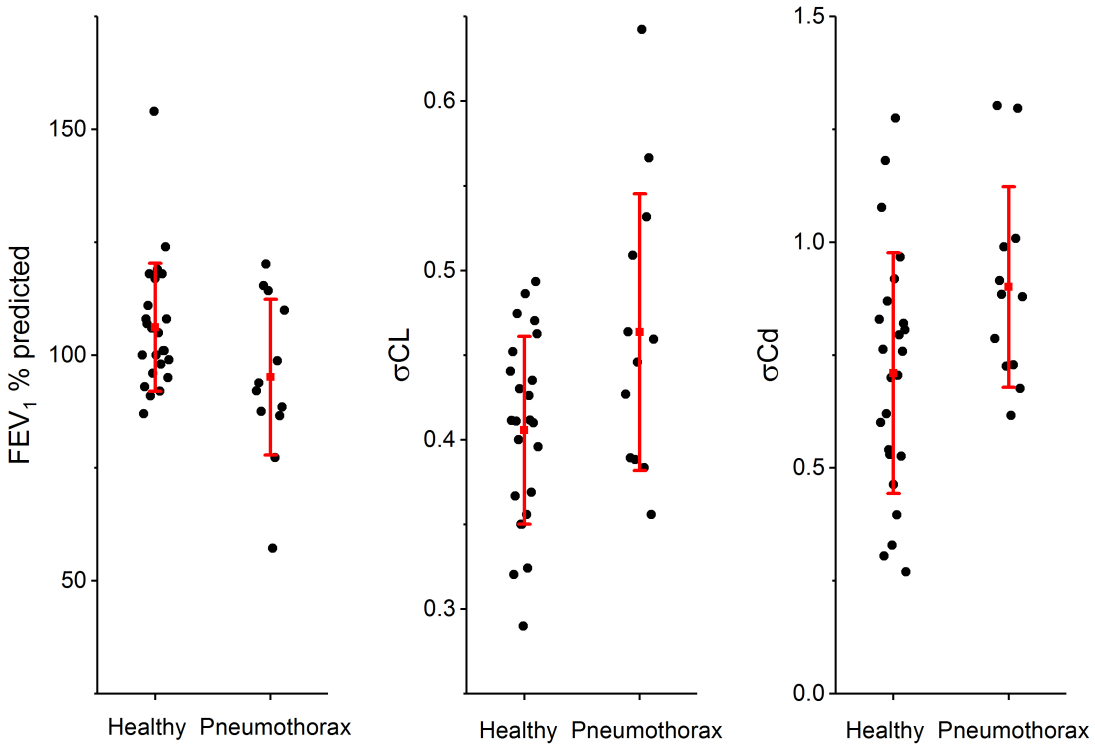


Figure 3.7: Comparison of FEV_1 (left), σCL (centre), and σCd (right) for pneumothorax patient group and age-matched healthy group. Individuals are shown by filled black circles, and the group averages and standard deviations are shown in red.

In the recovered pneumothorax patients, σCL and σCd were significantly elevated ($p<0.05$, Welch's t-test), but there was no significant difference in FEV_1 % predicted ($p>0.08$, Welch's t-test).

Comparisons of these three parameters in the two groups are shown in Figure 3.7. Notably, σCL was significantly higher in the 5 pneumothorax patients with a smoking history when compared to the non-smokers in both pneumothorax patient and healthy groups (p=0.02, Welch's t-test). FEV_1 was significantly lower in the smoking group (p=0.02, Welch's t-test), shown in Figure 3.8. If the data from the single ex-smoker (marked with + in Figure 3.8) are excluded, leaving the smoking group to be comprised only of current smokers, the significance of the σCL elevation increases (p<0.01, Welch's t-test). With this data excluded, the FEV_1 difference between the two groups become insignificant (p>0.05, Welch's t-test). There is no significant difference between the recovered pneumothorax patients without a smoking history and the healthy groups in terms of σCL, σCd nor FEV_1.

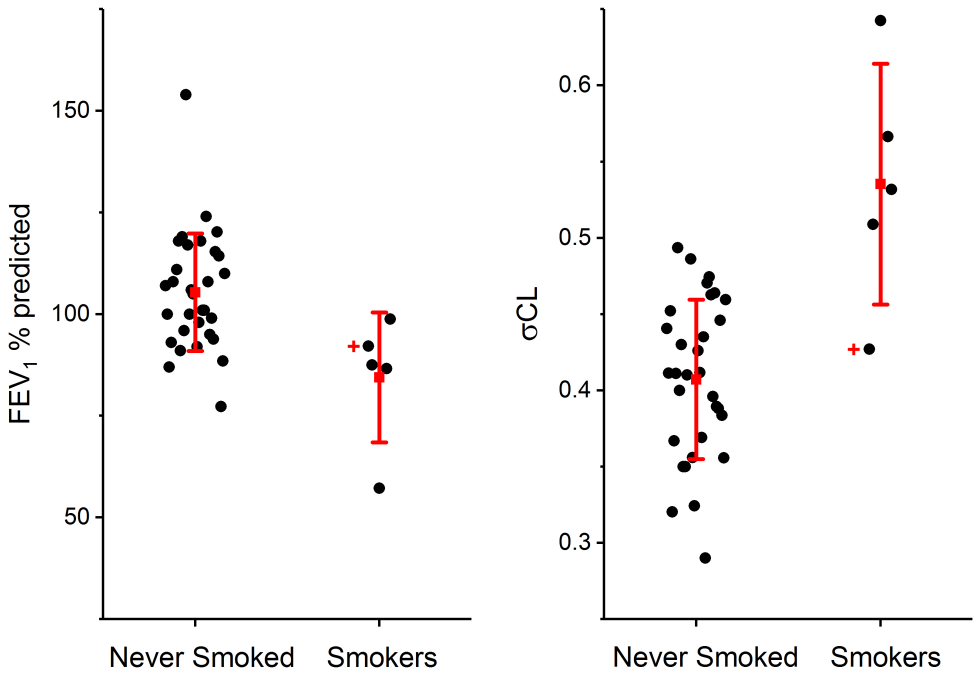


Figure 3.8: Comparison of FEV_1 (left), and σCL (right) for smokers within the pneumothorax patient group and a non-smoking group comprised of pneumothorax patients and healthy volunteers. Individuals are shown by filled black circles, and the group averages and standard deviations are shown in red. The patient marked with a red + is an ex-smoker, whereas the other individuals in the smokers group are currently smokers.

3.2.3 Discussion

This study represents the first use of this non-invasive technique for assessing lung inhomogeneity in patients who have had primary spontaneous pneumothorax. These data demonstrate statistically significant differences between the determined compliance and conductance distributions of the recovered pneumothorax patients and an age-matched healthy group. Whilst this might be illustrative of a sensitive method capable of identifying subtle difference in the lung physiology of pneumothorax patients, further analysis suggested that the most significant indicator of abnormal lung inhomogeneity was smoking status.

Smoking is well established as the primary cause of COPD, causing pathological changes in terms of lung inflammation, fibrosis, and the destruction of alveolar compartments.[196] The effect of smoking, however, varies in different individuals. Many smokers develop chronic bronchitis, characterised by chronic cough and sputum production, but without chronic airway obstruction.[197] A significant proportion of smokers never report chronic symptoms or display abnormal lung function. Even these 'healthy smokers' show subtle changes in lung morphology and lung inflammation.[198] Smoking, it appears, inevitably has an effect on the lungs, although the presentation varies significantly. The patient group is clearly small, but the four current smokers in this study returned the highest four σCL parameters across both the pneumothorax and healthy groups. Lung inhomogeneity, quantified by this non-invasive method, again appears to offer a more sensitive measurement of the subtle changes in the lung due to smoking than spirometry; three of the four current smokers show normal FEV_1 % predicted, greater than 80 %. The nature of spirometry means that it largely reflects obstruction in the large airways; the small airways make only a minor contribution to the total airway resistance.[199] The σCL parameter might reflect to a greater extent the state of the smaller airways, likely to be susceptible to inflammation and structural damage as a result of smoking. Obtaining a reliable marker of early smoking-related lung disease has recently been identified as a priority by the COPD community, both to facilitate early therapeutic intervention, and to enhance our understanding of the pathological progression of COPD.[200]

The single ex-smoker in the patient group returned a normal σCL value, well within the determined range of the non-smoking group. One explanation for this is that the elevated σCL parameters of the current smokers reflect smoking-related lung disease that is reversible with smoking cessation.

Short term lung inflammation in response to smoke exposure appears to be a possible candidate.[201] Smoking cessation is beneficial at any time, and the sooner an individual quits, the more this benefit is amplified.[202] This patient's FEV_1 was within a normal range, suggesting smoking cessation preceded significant irreversible destruction of lung structure.

To strengthen the conclusions of this study in terms of the lung inhomogeneity of smokers with normal spirometry, further investigation is required. A study designed to assess the effect of smoking on lung inhomogeneity would have the obvious advantage of expanding the size of the smokers' group. If volunteers were studied longitudinally, the progression of σCL abnormality with smoking could be evaluated. A study of current smokers hoping to quit would enable the reversibility of elevated σCL to be fully established. Over a longer time period, the predictive power of σCL in young smokers to differentiate between those who develop COPD and those who will never develop chronic symptoms would be assessed.

The conclusion of this study is that the elevated lung inhomogeneity in some recovered pneumothorax patients is largely a result of smoking-related lung disease, rather than representing an indicator of either susceptibility to pneumothorax or lung physiology changes resulting from suffering a pneumothorax. The remaining clinical question in terms of pneumothorax is whether elevated lung inhomogeneity might be an indicator of susceptibility to recurrence of pneumothorax. The rate of pneumothorax recurrence has variably been reported as 20-60 %. Sadikot *et al.* reported a 54 % recurrence rate over a four year period.[203] Risk factors have been identified, including smoking, height, and age, but there is currently no robust method of identifying patients at high risk of recurrence.[204] The twelve patients in this study will be prospectively followed up in the future to capture recurrence data, and thus assess the strength of elevated lung inhomogeneity to describe risk of recurrence.

3.3 Validation of Inhomogeneity Assessment by Comparison with MIGET

This study sought to compare the parameters of lung inhomogeneity determined by the Lognormal Lung model and the Multiple Inert Gas Elimination Technique (MIGET). MIGET was first introduced within the Introduction, described in Section 1.4.3.1. Briefly, six inert gases with differing solubilities are intravenously infused into an individual, before the retention of these gases is calculated based on measured arterial and expired gas partial pressures. The distribution of ventilation and perfusion that best fits, according to least-squares principles, the measured gas retentions is established using a 50 compartment model, each with a defined ventilation-perfusion ratio.[47] The most commonly reported parameters from the MIGET technique are LogSD$\dot{V}$ and LogSD$\dot{Q}$, measures representing the standard deviations of the ventilation and perfusion distributions of the modelled units' $\dot{V}/\dot{Q}$ ratios, respectively.[205] These parameters quantify the degree of $\dot{V}/\dot{Q}$ inhomogeneity in the lung.

MIGET has contributed significantly to understanding the mechanisms by which COPD affects patient gas exchange. COPD patients have been shown to have severe degrees of $\dot{V}/\dot{Q}$ mismatching, leading to abnormally large lung inhomogeneity.[206] Furthermore, the nature and severity of $\dot{V}/\dot{Q}$ mismatch has been found to vary markedly among COPD patients. One pattern of $\dot{V}/\dot{Q}$ mismatch, in which some regions of the lung display a very high $\dot{V}/\dot{Q}$ ratio, is prevalent in patients displaying emphysematous COPD.[207] $\dot{V}/\dot{Q}$ mismatch characterised by regions with very low $\dot{V}/\dot{Q}$ is also frequently seen in COPD patients, although no link has been established between this and patient clinical features.[181] MIGET parameters have also been found to display abnormality even in COPD patients with relatively well preserved spirometry.[208] Beyond this, MIGET has been used to illustrate that $\dot{V}/\dot{Q}$ mismatch, and inhomogeneity in the lung as a result, evolves as airflow obstruction, the traditional marker of COPD disease severity, deteriorates. MIGET has also been utilised to show that COPD patients undergoing acute exacerbations of their disease display severe $\dot{V}/\dot{Q}$ mismatching.[209] The same study found that following exacerbations, the degree of $\dot{V}/\dot{Q}$ inequality improved as clinical symptoms were alleviated and spirometry recovered.

Despite the potential clinical value of MIGET measurements, the experimental complexity of this technique has limited it to use within a small number of research centres. The work presented

here was carried out at the Univeristy of California San Diego Radiology Imaging Laboratory in collaboration with a team led by Professor Peter Wagner, Professor Kim Prisk and Professor Susan Hopkins.

3.3.1 Methods

3.3.1.1 Subjects

Ethical approval for this study was obtained from the Human Subjects Research Protection Program of the University of California San Diego (UCSD). Nine patients (7 men, 2 women aged 49-70 years) were recruited to be studied and participated in this study after giving written informed consent. All subjects had a diagnosis of COPD and their physical characteristics are shown in Table 3.5. Participants attended the UCSD Radiology Imaging Laboratory where they performed standard forced spirometry and underwent both the MIGET and Lognormal Lung experimental procedures (both described below).

3.3.1.2 Experimental Setup

A radial artery cannula and a peripheral venous cannula are inserted, the former for collection of arterial blood samples for measurement of respiratory and inert gases, and the latter allowing infusion of the inert gas mixture. The six inert gases (sulphur hexafluoride, ethane, cyclopropane, enflurane, ether, and acetone) were placed into solution in sterile 0.9% sodium chloride solution and infused intravenously at a rate of 2-3 ml min^{-1} for 40 min before collection of the first samples. Mixed expired gas samples and a 6 ml arterial blood sample obtained in gas-tight glass syringes comprised a measurement set.

Prior to measurement commencing, the subjects spent a 20 min period in an upright seated position, allowing the lung to equilibrate following a supine period whilst the cannulas were inserted. Three measurement sets were obtained in an upright seated position from each subject; results from these measurements were appropriate for comparison with the Lognormal Lung determined parameters. The concentrations of the inert gases in the gas and blood samples were measured using gas chromatography (Hewlett-Packard, 5890).[210] Using cardiac output measurements from impedance cardiography and the arterial and mixed expired gas concentrations, mixed venous concentrations were calculated by the Fick principle.

Table 3.5: Physical characteristics of MIGET study subjects.

Subject ID	Sex	Age / years	Height / m	Weight / kg
MIGET_01	Male	64	1.78	102
MIGET_02	Male	57	1.87	72
MIGET_03	Male	67	1.78	104
MIGET_04	Male	70	1.72	85
MIGET_05	Male	55	1.58	45
MIGET_06	Female	49	1.78	106
MIGET_07	Male	53	1.59	88
MIGET_08	Female	66	1.54	82
MIGET_09	Male	69	1.78	77

3.3.1.3 Lognormal Lung Experimental Setup

Nitrogen washouts were performed after the final MIGET measurement sets had been made. Each subject was asked to perform two washouts, separated by a 15 min recovery period. The participants breathed through a mouthpiece, connected in series with a HME filter (Hans-Rudolph) and the MFS. Participants breathed air for 10 min, followed by a 5 min N_2 washout period breathing medical O_2. Arterial oxygen saturation measurements were obtained from a pulse oximeter. The nose was occluded using a nose clip throughout. Three arterial blood samples, each of 3 ml, were taken during the air breathing period of each washout at minutes 5, 7 and 9. These samples were studied with blood gas analysis and co-oximetry. Data recorded by the MFS were analysed using the Lognormal Lung model. Initially four repeats of the estimation algorithm from different starting points were used for each dataset, with further repeats used if more than one solution point (cost function minimum) was found. Parameter sets associated with the closest agreement of measured and modlled data were determined for each dataset. Where two parameter sets were determined for a participant, averaged parameters were calculated for comparison with the MIGET data.

3.3.2 Results

Seven of the subjects tolerated the study well, each providing 3 MIGET measurement samples and performing two N_2 washout procedures. One participant (MIGET_04) completed the MIGET measurements, but only performed a single washout. The remaining participant (MIGET_07) did

not tolerate the MIGET procedure and thus did not reach the N_2 washout section of the study visit. Subject spirometry data for the eight participants who performed at least one N_2 washout procedure are shown in Table 3.6. Two participants, MIGET_06 and MIGET_08, show normal spirometry, with FEV_1 greater than 90 % predicted and FEV_1/FVC greater than 0.7, indicating non-obstructive spirometry. The remaining six participants do show obstructive spirometry, with five Stage 2 patients and a single Stage 4 patient, MIGET_01.[171]

Table 3.6: Spirometry data for MIGET study subjects. FVC is the forced vital capacity and FEV_1 is the forced expiratory volume in one second.

Subject ID	FVC /l	FVC /% pred	FEV1 /l	FEV1 /% pred	FEV1/FVC
MIGET_01	2.00	43	0.80	23	0.40
MIGET_02	3.99	73	2.11	50	0.53
MIGET_03	2.29	59	1.55	52	0.68
MIGET_04	3.00	74	1.82	61	0.61
MIGET_05	3.37	91	2.14	75	0.64
MIGET_06	4.31	99	3.47	101	0.81
MIGET_08	2.52	92	1.90	92	0.75
MIGET_09	3.51	78	1.99	60	0.57

3.3.2.1 MIGET Results

Three of the $\dot{V}/\dot{Q}$ distributions measured during the MIGET experiments in this work are shown in Figure 3.9. These examples are chosen to illustrate the variation in measured $\dot{V}/\dot{Q}$ distribution profiles within the COPD group. Across the group, only one of the determined $\dot{V}/\dot{Q}$ distributions was unimodal, with data for two participants describing a bimodal distribution with a second peak at low $\dot{V}/\dot{Q}$. Data for the remaining five subjects showed a bimodal distribution with a second peak at high $\dot{V}/\dot{Q}$. The MIGET parameters calculated from the measured $\dot{V}/\dot{Q}$ distributions are shown for each subject in Table 3.7. The residual sum of squares averaged 3.87 ± 2.58 indicating adequate agreement between the data and the 50-compartment model. Of the eight participants who completed upright MIGET measurements, five Log$SD\dot{V}$ and six Log$SD\dot{Q}$ measurements were above the normal limits for the subject's ages, as shown in Figure 3.10.[211,212]

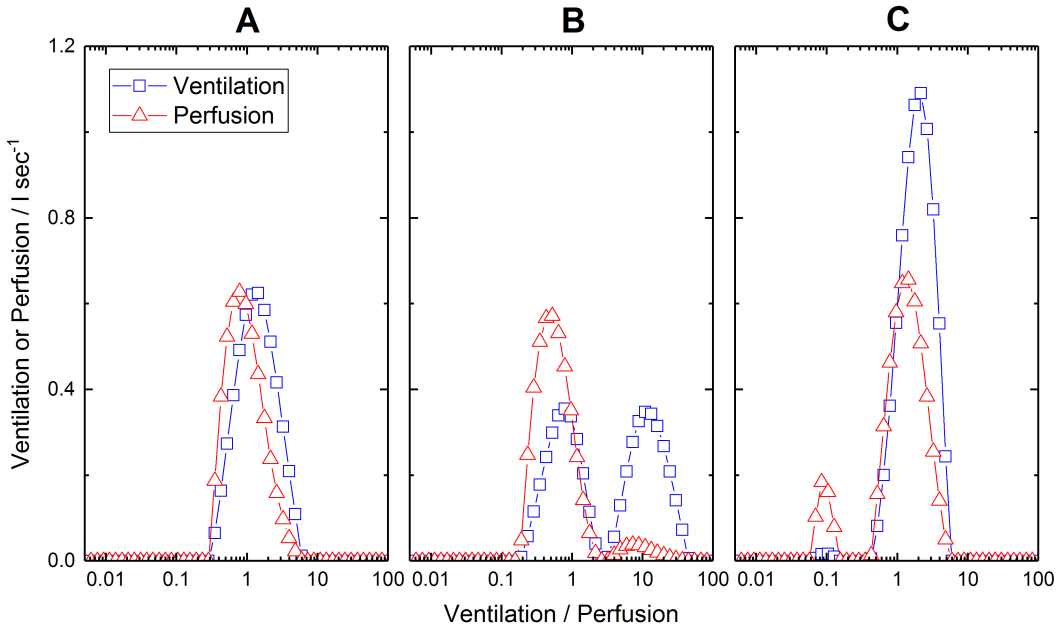


Figure 3.9: Example $\dot{V}/\dot{Q}$ distributions measured by MIGET for three participants. $\dot{V}/\dot{Q}$ distributions are determined for a 50 compartment model. **A** shows data for a unimodel $\dot{V}/\dot{Q}$ distribution (MIGET_03), **B** for a bimodal distribution with a second peak showing ventilation to poorly perfused regions (MIGET_05), and **C** for a bimodal distribution with a second peak indicating perfusion to poorly ventilated regions of the lung (MIGET_06).

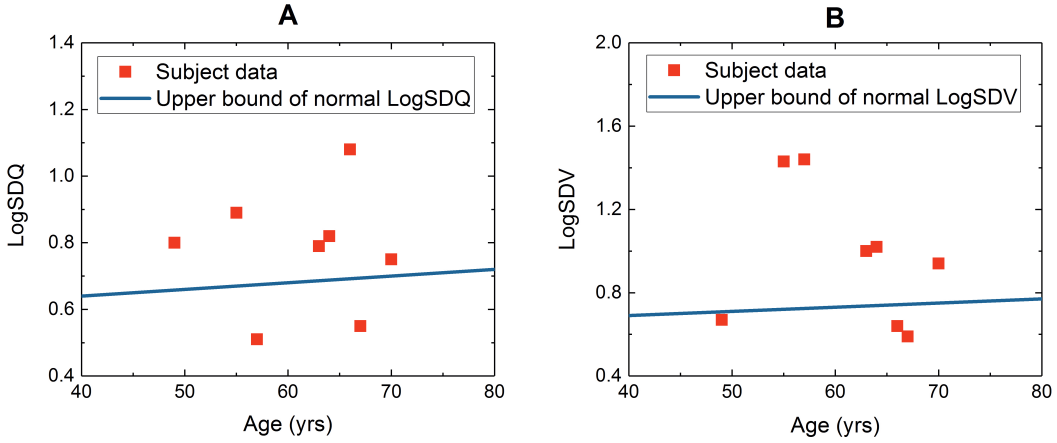


Figure 3.10: Comparison of MIGET measured LogSD$\dot{Q}$ values (**A**) and LogSD$\dot{V}$ values (**B**) with age corrected normal upper bounds (given as 95 % confidence intervals). Normal upper bounds determined using measurements made in Cardús *et al.*.[212] LogSD$\dot{Q}$ is the standard deviation log scale of the perfusion vs $\dot{V}/\dot{Q}$ distribution and LogSD$\dot{V}$ is the standard deviation log scale of the ventilation vs $\dot{V}/\dot{Q}$ distribution.

Table 3.7: Measured MIGET data. RSS, residual sum of squares; $\dot{Q}$ shunt, percentage of perfusion to regions of shunt ($\dot{V}/\dot{Q} < 0.005$); $\dot{V}$ dead, fraction of ventilation to deadspace ($\dot{V}/\dot{Q} > 100$); Mean $\dot{Q}$, the mean of the perfusion distribution; LogSD$\dot{Q}$, the standard deviation log scale of the perfusion vs $\dot{V}/\dot{Q}$ distribution, an index of $\dot{V}/\dot{Q}$ heterogeneity; Mean $\dot{V}$, the mean of the ventilation distribution; LogSD$\dot{V}$, the standard deviation log scale of the ventilation vs $\dot{V}/\dot{Q}$ distribution, an index of $\dot{V}/\dot{Q}$ heterogeneity.

Subject ID	RSS	$\dot{Q}$ shunt /%	$\dot{V}$ dead	Mean $\dot{Q}$	LogSD$\dot{Q}$	Mean $\dot{V}$	LogSD$\dot{V}$
MIGET_01	3.35	0.3	0.41	1.06	0.82	2.65	1.02
MIGET_02	8.94	0.5	0.49	0.68	0.51	2.43	1.44
MIGET_03	2.37	0.1	0.32	0.97	0.55	1.35	0.59
MIGET_04	3.72	3.1	0.46	0.80	0.75	1.68	0.94
MIGET_05	2.22	1.6	0.47	0.61	0.89	2.61	1.43
MIGET_06	6.57	0.1	0.37	1.12	0.80	1.85	0.67
MIGET_08	1.43	1.1	0.29	1.50	1.08	2.70	0.64
MIGET_09	2.38	0.7	0.43	0.56	0.79	1.29	1.00
Mean	3.87	0.9	0.40	0.91	0.77	2.07	0.97
±SD	2.58	1.0	0.07	0.32	0.18	0.59	0.33

3.3.2.2 Lognormal Lung Results

Fifteen N_2 washout experimental datasets were recorded and analysed with the Lognormal Lung model. For two datasets, the model failed to converge on a determined set of lung parameters. In both cases, this failure was associated with issues within the recorded data; data from the first washout of participant MIGET_06 showed physiologically unreasonable levels N_2 production, a result of a poor seal at the mouthpiece. A similar issue occurred for the first washout of participant MIGET_03 owing to this participant's difficulty wearing a noseclip. Thus, of the eight participants who performed washouts, a single set of lung parameters were determined for three, and two sets of parameters were determined from the remaining five. Where two parameter sets were obtained for a participant, they have been averaged.

For one participant, MIGET_02, the 5 minute washout period was insufficient to satisfactorily washout the N_2 from the lungs. This is illustrated in Figure 3.11, which shows the measured end-tidal N_2 fraction for the final breath of the washout period for each participant. Reliable lung parameter estimation using the Lognormal Lung model is dependent on near-complete washout of

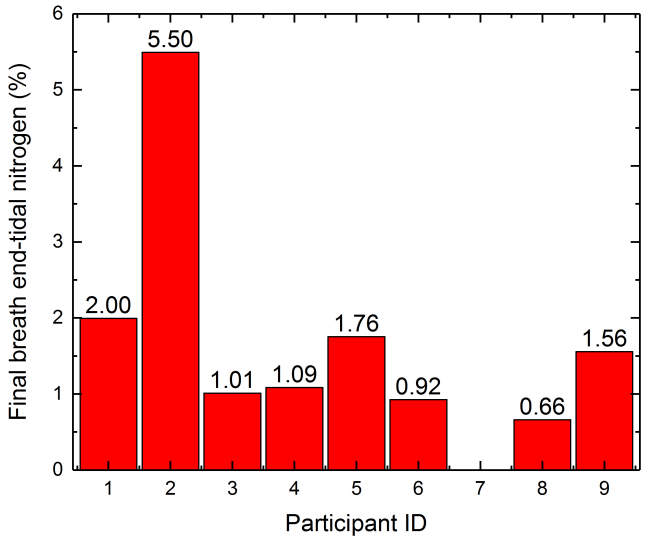


Figure 3.11: Comparison of the end-tidal nitrogen fractions between participants for the final breath of the nitrogen washout period (5 minutes). Where two washouts were performed by a participant, an average value is shown. One participant's (MIGET_02) washouts were clearly incomplete.

N_2 from the lung, something that isn't achieved in either of the experimental procedures performed by MIGET_02. Thus, although two parameter sets were determined for this participant, the data for this participant is excluded from further analysis within this work. The Lognormal Lung parameters obtained for the seven remaining patients are shown in Table 3.8. The lung inhomogeneity parameters are abnormally elevated in this group of subjects. The σCL and σCd parameters are within a normal range for the two subjects in whom normal, non-obstructive spirometry was measured, MIGET_06 and MIGET_08. Indeed, in each of the five subjects displaying obstructive spirometry, both σCL and σCd parameters were abnormally elevated. The Lognormal Lung parameters describe the inhomogeneities of intrinsic lung characteristics, compliance and conductance, and should not be directly compared with MIGET measured indices of ventilation and perfusion distributions. The next section describes parameters derived from the Lognormal Lung model which enable the two techniques to be compared directly.

Table 3.8: Lognormal Lung parameters determined for MIGET study subjects. VD_{tot} is the anatomical deadspace volume, σVD is the standard deviation of the deadspace volume distribution, VA_{tot} is the alveolar volume, and σCL and σCd are the standard deviations of the alveolar compliance and vascular conductance distributions, respectively. VD_{tot} and VA_{tot} are given in units of litres under conditions of body temperature and pressure saturated (BTPS).

Subject ID	VD_{tot} / l (BTPS)	σVD	VA_{tot} / l (BTPS)	σCL	σCd	$\dot{Q}$ shunt / %
MIGET_01	0.40	0.51	6.52	0.90	1.68	4.0
MIGET_03	0.18	0.49	2.13	0.80	1.18	-1.8
MIGET_04	0.17	0.39	3.12	0.80	1.17	12.6
MIGET_05	0.18	0.45	3.22	0.80	1.75	3.5
MIGET_06	0.13	0.48	1.71	0.56	0.90	8.0
MIGET_08	0.14	0.47	1.77	0.56	0.51	2.4
MIGET_09	0.15	0.38	3.40	0.79	1.24	9.0
Mean	0.19	0.45	3.13	0.74	1.20	5.4
±SD	0.09	0.04	1.53	0.12	0.40	4.4

3.3.3 Discussion

The governing bivariate lognormal distribution within the Lognormal Lung model was first introduced by Wilson and Beck[159] to try and reconcile experimentally measured ventilation-volume ($\frac{\dot{V}}{V}$) and perfusion-volume ($\frac{\dot{Q}}{V}$) distributions with the ventilation-perfusion ($\frac{\dot{V}}{\dot{Q}}$) distributions estimated using MIGET. If the ventilation-volume and perfusion-volume distributions are lognormal, with standard deviations $\sigma_{\frac{\dot{V}}{V}}$ and $\sigma_{\frac{\dot{Q}}{V}}$ respectively, then since

$$\log\left(\frac{\dot{V}}{\dot{Q}}\right) = \log\left(\frac{\dot{V}}{V}\right) - \log\left(\frac{\dot{Q}}{V}\right) \quad , \tag{3.1}$$

the ventilation-perfusion distribution is necessarily also lognormal with standard deviation $\sigma_{\frac{\dot{V}}{\dot{Q}}}$, given by

$$\sigma^2_{\frac{\dot{V}}{\dot{Q}}} = \sigma^2_{\frac{\dot{V}}{V}} + \sigma^2_{\frac{\dot{Q}}{V}} - 2\rho\sigma_{\frac{\dot{V}}{V}}\sigma_{\frac{\dot{Q}}{V}} \quad , \tag{3.2}$$

where ρ is the correlation between the ventilation and perfusion. This formula lends insight into the behaviour of the width of the ventilation-perfusion distribution: as either the ventilation-volume or perfusion-volume distributions get broader, or their correlation decreases, the width of the ventilation-perfusion distribution will increase.

Equation 3.2 cannot be used to estimate the width of the ventilation-perfusion distribution from the Lognormal lung parameter estimates, however. Within the Lognormal lung model, ventilation is not lognormally distributed. It is assumed, instead, that the compliance rather than ventilation is lognormally distributed. The Lognormal Lung model quantifies the inhomogeneity of characteristics that are intrinsic to the lung, compliance and conductance, rather than those which reflect extrinsic factors, such as total ventilation and total pulmonary blood flow.

To estimate a ventilation-perfusion distribution comparable with MIGET from the Lognormal Lung model, the alveolar ventilation to each modelled compartment ($\dot{V}_{Ai}$) is estimated over the final 5 minutes of the air-breathing period. The model is run with the parameter values set to those estimated from the washout dataset under consideration. The alveolar ventilation is the volume of fresh gas (i.e. gas that is beyond the deadspace at the start of inspiration) that enters each alveolar compartment during the period, divided by the duration of the period. For any breath, the alveolar ventilation to compartment i is given by:

$$\dot{V}_{Ai} = \sum_m \left(\frac{\dot{V}_i^m (V_T^m - V_{DC}) - v_i V_{DP}}{T_b^m} \right) \quad , \tag{3.3}$$

where V_T^m and T_b^m are the tidal volume and duration of breath m, and $\dot{V}_i^m$ is the fractional ventilation entering compartment i during breath m. The perfusion to each compartment is given by $Q_i Q_T$, where Q_T is total blood flow and Q_i is the fractional perfusion to compartment i. Thus, the ventilation-perfusion ratio of the compartments can be defined, $\frac{\dot{V}_{Ai}}{Q_i Q_T}$. To produce parameters that are directly comparable with the MIGET outputs LogSD$\dot{V}$ and LogSD$\dot{Q}$, the standard deviations of the ventilation and perfusion distributions of $\log(\frac{\dot{V}_{Ai}}{Q_i Q_T})$ respectively are calculated. The determined values of LogSD$\dot{V}$ and LogSD$\dot{Q}$ in each individual are generally similar, lying close to the line of identity, illustrated by Figure 3.12. This has previously been reported in MIGET.[213] Indeed, if both ventilation and perfusion were exactly lognormally distributed, these parameters would be equal.[160]

Figure 3.13 compares estimates of LogSD$\dot{Q}$ from the Lognormal Lung model with the values from MIGET. There is reasonable agreement, with the exception of the datapoint from one of the participants who had a second peak at low $\dot{V}/\dot{Q}$ detected by MIGET. To assess the level of correlation between the two measures, a linear fit is made to the data. The coefficient of determination, R^2, was 0.08 with a Pearson's R of -0.29, suggesting very little concordance between the two measures. There is not, however, a very wide range of values for LogSD$\dot{Q}$ between the participants. Figure 3.13B

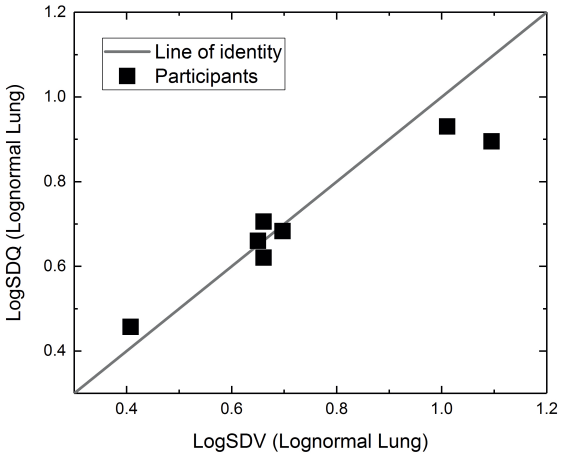


Figure 3.12: Comparison of LogSD$\dot{V}$ and LogSD$\dot{Q}$ parameters determined from the Lognormal Lung model.

shows the Bland-Altman plot comparing the two measures. This analysis was introduced in 1983 as a graphical method of assessing the level of agreement between two measurement methods.[214] For each participant, the parameter difference between the two methods is plotted against the parameter average from the two methods.[215] Plotting difference against mean allows investigation of any possible relationship between measurement error and the true value. Since the true value is not known, the mean of the two measurements is the best available estimate.[216] The intra-participant standard deviation for the MIGET data, calculated from the three MIGET measurements, is also shown in the Bland-Altman plot for comparison. The LogSD$\dot{Q}$ parameters determined by the Lognormal Lung model lie within or close to the uncertainty associated with the MIGET measurement for the only participant with a unimodal $\dot{V}/\dot{Q}$ distribution and the four participants displaying a second peak at high $\dot{V}/\dot{Q}$. For the two participants displaying bimodal $\dot{V}/\dot{Q}$ distributions with a second peak at low $\dot{V}/\dot{Q}$, the Lognormal lung determined LogSD$\dot{Q}$ parameters are significantly lower than the MIGET measured values.

In Figure 3.14, in contrast, the values for LogSD$\dot{V}$ appear to agree well between the two methods, apart from the presence of some degree of bias. In particular, all but one of the participants are ordered by value of logSD$\dot{V}$ in exactly the same way by both methods. A linear fit to this data returned an R^2 of 0.72 and a Pearson's R of 0.85, a significant level of correlation. The bias was estimated to be 0.18, with the Lognormal Lung underestimating the value of LogSD$\dot{V}$ compared

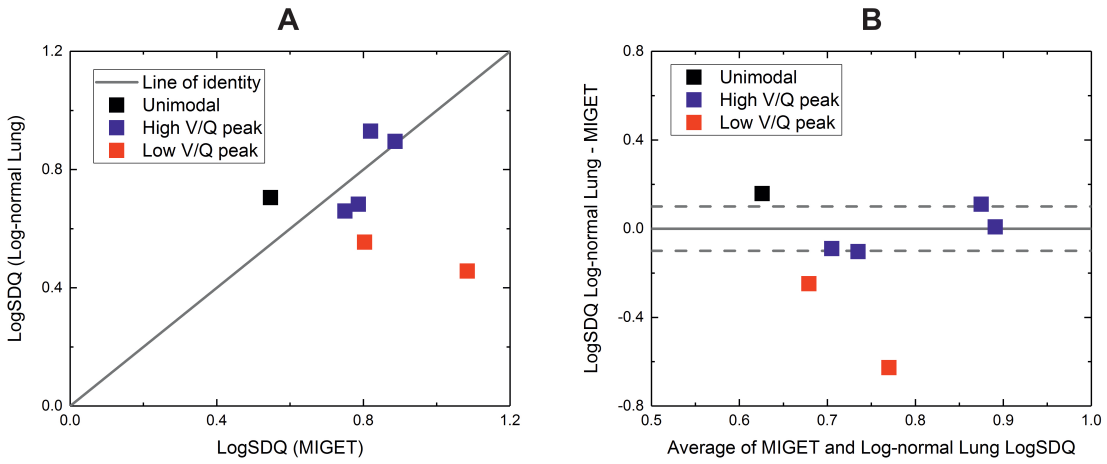


Figure 3.13: A. Comparison of LogSD$\dot{Q}$ for MIGET and Lognormal Lung techniques. Data from participants where MIGET describes a unimodal perfusion distribution are shown in black, data from participants with a second peak at high $\dot{V}/\dot{Q}$ are shown in blue, and data from participants with a second peak at low $\dot{V}/\dot{Q}$ are shown in red. Data from the participant excluded due to insufficient washout is shown by an open square. **B.** Corresponding Bland-Altman plot comparing techniques for evaluating perfusion distributions. Broken horizontal lines show $\pm 1\,\sigma$ for intra-participant comparisons of the MIGET technique with itself.

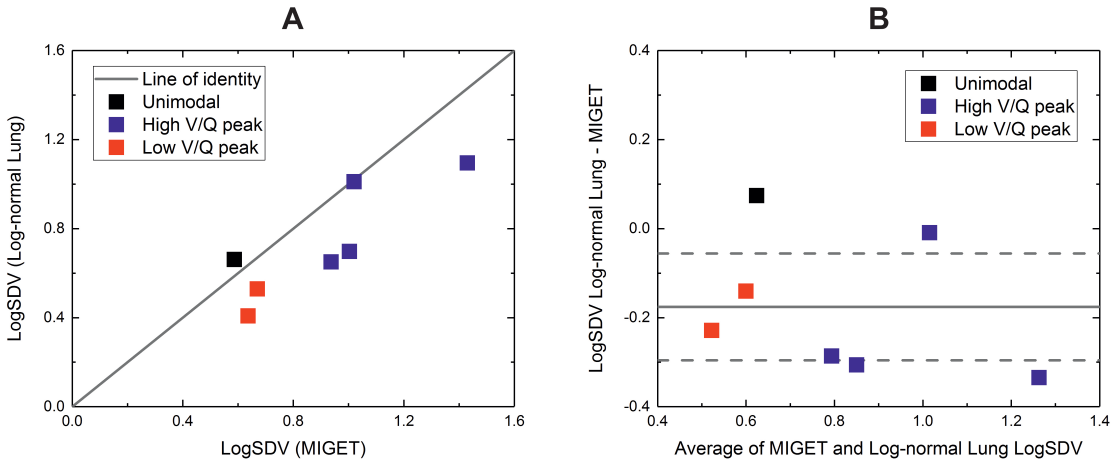


Figure 3.14: A. Comparison of LogSD$\dot{V}$ for MIGET and Lognormal Lung techniques. Data from participants where MIGET describes a unimodal perfusion distribution are shown in black, data from participants with a second peak at high $\dot{V}/\dot{Q}$ are shown in blue, and data from participants with a second peak at low $\dot{V}/\dot{Q}$ are shown in red. Data from the participant excluded due to insufficient washout is shown by an open square. **B.** Corresponding Bland-Altman plot comparing techniques for evaluating ventilation distributions. Full horizontal line illustrates the bias between the two techniques. Broken horizontal lines illustrate $\pm 1\,\sigma$ for intra-participant comparisons of the MIGET technique with itself. These are illustrated around the bias line.

with MIGET. This bias is at a level that could be physiologically important; 0.18 is approaching the LogSD$\dot{V}$ physiological range from the low end to the high end of this parameter for young subjects.[212] The bias is illustrated in the Bland-Altman plot of Figure 3.14B where the data points are generally close to the mean bias. Also shown for comparison is the intra-participant standard deviation for the MIGET data.

There appeared to be a significant bias between the CO-oximetry measurements of arterial oxygen saturation, SpO_2, and estimates from the blood gas analyser and the pulse oximeter. Three arterial blood samples were taken during the air-breathing phase of each experimental procedure. For each of these samples, SpO_2 is determined by blood gas analysis and CO-oximetry. These values are compared with the recorded pulse-oximeter and CO-oximetry for the preceding 20 seconds, representing roughly the length of time required to collect each arterial blood sample. The blood gas analyser estimated SpO_2 was, averaged over every sampling period, 0.3 % greater than that recorded by the pulse oximeter. Given that both estimation methods have uncertainties of at least ± 1 %, this is an acceptable level of bias. The CO-oximetry measurements of SpO_2, however, were larger than the other techniques, on average 1.8 and 2.1 % larger than blood gas analysis and pulse oximetry respectively. This significant bias could potentially be explained by a left shift in the oxygen dissociation curve caused by the presence of carboxyhaemoglobin. Carbon monoxide selectively binds to haemoglobin in the blood, thereby increasing the affinity of O_2 to the remaining haemoglobin. This has the effect of raising SpO_2 as O_2 release to the tissue is limited.[217] However, a number of the participants had quit smoking and the bias was present for all participants.

The shunt fraction and lowest $\dot{V}/\dot{Q}$ ratios (less than 0.1) from MIGET were combined to form a single"effective shunt", as these will not be separable when using oxygen saturation to assess shunt. This effective shunt is used in the comparison shown in Figure 3.15. The estimates of shunt using the Lognormal Lung technique are generally larger than those from MIGET, such that the points do not scatter around the line of identity. This is evident in the averages shown in Figure 3.15B. If the pulse-oximeter measured saturations are replaced with saturations estimated from the blood gas data, there is little bias in the Lognormal Lung measurement of shunt compared with MIGET, but the individual points remain scattered. This is evident from the large standard deviation displayed. Measurements of shunt using the CO-oximetry data are clearly highly biased.

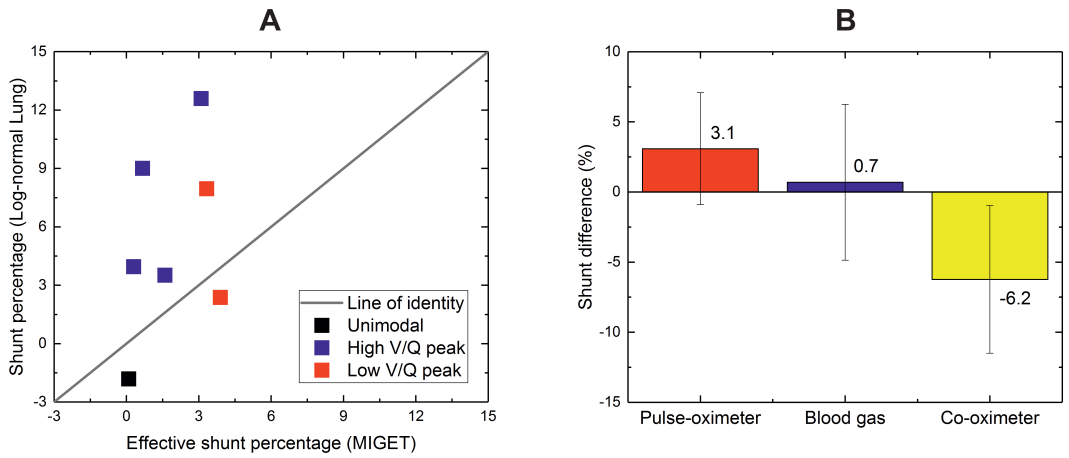


Figure 3.15: A. Participant-by-participant comparison of shunt fraction estimates from the Log-normal Lung technique with the effective shunt fractions measured by MIGET. Effective shunt is defined as the measured fraction of perfusion with $\dot{V}/\dot{Q}$ less than 0.1. Data from participants where MIGET describes a unimodal perfusion distribution are shown in black, data from participants with a second peak at high $\dot{V}/\dot{Q}$ are shown in blue, and data from participants with a second peak at low $\dot{V}/\dot{Q}$ are shown in red. **B.** Average differences between MIGET effective shunt and Lognormal Lung determined shunt using arterial oxygen saturations determined in three different ways. Bias between the two methods is least when using saturations determined from blood-gas analysis. Error bars show $\pm 1\,\sigma$.

The determined fractional deadspace ventilations from the Lognormal Lung model and MIGET are compared in Figure 3.16. Fractional deadspace ventilations appear either close to the line of identity between the two techniques, or else below it. MIGET includes deadspace that arises from ventilation of unperfused lung volume, whereas the deadspace estimate from the Lognormal Lung only includes the anatomic deadspace. Thus it is likely that those individuals who have a larger deadspace fraction with MIGET compared with the Lognormal Lung will have volumes in the lung that are ventilated but unperfused. This is supported by the fact that the two participants who lie furthest below the line of identity show bimodal $\dot{V}/\dot{Q}$ distributions from MIGET measurements, with a second peak at a high $\dot{V}/\dot{Q}$ ratio.

The Lognormal Lung assumes that compliance and conductance within the lung can be described by a bivariate lognormal distribution. The compliance and conductance distributions are, therefore, defined as unimodal. As a result, the underlying ventilation and perfusion distributions will also be unimodal in nature. Whilst this assumption can be confidently made in healthy individuals [160], all but one of the COPD patients studied in this work showed bimodal $\dot{V}/\dot{Q}$ distributions by MIGET measurement. Some differences between the Lognormal Lung parameters and MIGET measurements

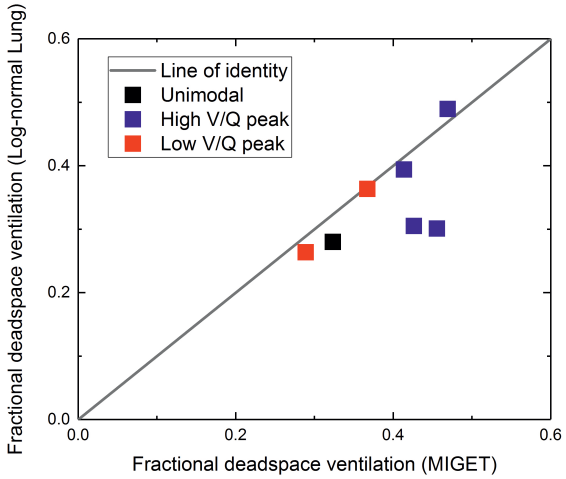


Figure 3.16: Comparison of fractional deadspace ventilation measured by MIGET and by the Lognormal Lung technique. Data from participant where MIGET describes a unimodal perfusion distribution are shown in black, data from participants with a second peak at high $\dot{V}/\dot{Q}$ are shown in blue, and data from participants with a second peak at low $\dot{V}/\dot{Q}$ are shown in red.

may well be a result of the bimodal nature of the measured $\dot{V}/\dot{Q}$ distributions, which the Lognormal Lung simply cannot model. This is most readily apparent in the comparison of LogSD$\dot{Q}$, where the two participants lying furtherest from the line of identity are participants with bimodal $\dot{V}/\dot{Q}$ distributions with a second peak at low $\dot{V}/\dot{Q}$. This feature will result in a large MIGET measured LogSD$\dot{Q}$, and it is perhaps no surprise that the best-fit unimodal $\dot{V}/\dot{Q}$ distribution from the Lognormal Lung model returns a lower LogSD$\dot{Q}$ in both cases. The majority of the subjects studied in this work were Stage 2 COPD patients illustrating well established disease. If the relationships between Lognormal Lung parameters and MIGET measurements were to be explored further, it would be valuable to compare healthy individuals and patients with early stage respiratory disease. Unimodal $\dot{V}/\dot{Q}$ distributions would be expected in the majority of these participants, allowing a comparison of the two techniques in a group where this underlying assumption within the Lognormal Lung model has more validity.

It is perhaps to be expected that the Lognormal Lung method compares more favourably with MIGET measurements of ventilation inhomogeneity and deadspace ventilation than for perfusion inhomogeneity and shunt percentage. Fundamentally, one of the most significant differences between the Lognormal Lung method and MIGET is the fact that MIGET relies on information encoded within the tracer gas concentrations of both exhaled gas and arterial blood. In terms of clinical

feasibility, the fact that the Lognormal Lung technique relies only on respiratory gas exchange data is a real asset as it is non-invasive, safer and more simple to perform, both from the clinician and patient perspective. However, without information directly from the blood, the uncertainties of Lognormal Lung parameters that are circulatory in nature are inherently greater than for the airway parameters.

3.4 Conclusions

This chapter has described a series of 3 studies performed in clinical settings evaluating the lung inhomogeneity parameters determined by the Lognormal Lung model from gas exchange data recorded by the MFS. The first study was a cross-sectional investigation of COPD patients. The N_2 washout procedures performed by each subject were well tolerated. The determined parameters were found to be highly repeatable in all cases but one, σCd. All three of the parameters of lung inhomogeneity, σCL, σVD, and σCd, were significantly elevated in COPD patients compared to an age-matched healthy control group. Significant differences between the two groups were also found for deadspace volume and the deadspace volume to alveolar volume ratio. In patients with mild COPD, inhomogeneity parameters σCL and σCd were found to be significantly abnormal, despite preserved FEV_1. The relatively greater abnormality displayed by σCL and σCd compared to airflow limitation assessed by FEV_1/FVC illustrated the potential of the Lognormal Lung method to provide a sensitive, non-invasive assessment of early stage disease.

The second clinical study investigated the lung inhomogeneity of patients who have recovered from a primary spontaneous pneumothorax. The inhomogeneity parameters of the pneumothorax patients without a smoking history were not statistically different to that of an age-matched healthy group. The pneumothorax patients who were either current or ex-smokers, however, displayed a significantly elevated σCL when compared with the healthy group. This result, paired with the well preserved spirometry, is suggestive of the potential of this technique to assess subtle smoking-related lung damage.

Parameters of lung inhomogeneity determined using the Lognormal Lung model were validated by comparison with those from the well-established but highly invasive multiple inert gas elimination technique (MIGET). Derived parameters were compared for a group of COPD patients across a range of disease severities. The Lognormal Lung model was found to show reasonably good agreement with MIGET on airway parameters; ventilation inhomogeneity and deadspace ventilation. The concordance was weaker for the circulatory parameters; perfusion inhomogenity and shunt percentage. The differences between the two techniques were most apparent in the participants with bimodal $\dot{V}/\dot{Q}$ distributions, primarily a consequence of the underlying assumption within the Lognormal Lung model that the alveolar compliance and vascular conductance distributions are unimodal.

Ultimately, the clinical application of the Lognormal Lung method of assessing respiratory function will be dependent on the result of clinical trials based on Lognormal Lung parameter driven therapeutic interventions. Patient outcome improvement as a result of Lognormal Lung assessment of treatable disease traits and monitoring of therapeutic effects would be the endpoint of these clinical trials.

Chapter 4

Investigating Lung Inhomogeneity in Asthma

In asthma, lung function measures are often discordant with clinical features such as symptoms, exacerbation rates or disease control.[218] There is no single diagnostic test for asthma, and both clinical assessment of symptoms and objective tests have false positive and false negative rates.[219] The limitations of current techniques of assessing lung function present issues for asthma diagnosis, severity staging, and intervention. Clinical management of asthma is therefore often significantly influenced by patient self-assessment of asthma-related symptoms. One commonly used asthma control questionnaire, the ACQ-5, asks patients to evaluate five key symptoms on a scale of zero (well controlled) to six (extremely poorly controlled).[220] Asthma symptoms during the night and upon waking, activity limitation, shortness of breath, and wheezing are assessed. The ACQ-5 score is taken as the mean of the five items.[220] The ACQ-5 score offers clinicians an assessment that describes disease control based on symptoms and may relate to exacerbation risk.[221] It does not, however, provide indication of patient endotype or prediction of patient response to therapeutic interventions. A series of common asthma therapies are presented in this section and two studies assessing the within-patient Lognormal Lung parameter responses to these therapies are presented later in this chapter. These responses are evaluated to illustrate the potential of this non-invasive assessment of lung inhomogeneity within current clinical practice in asthma.

Salbutamol is a short-acting beta agonist, often prescribed as a first-line symptomatic relief in asthma therapy.[222] Salbutamol is a bronchodilator, increasing airflow to provide relief of acute asthma symptoms. Treatment effects begin in about 10-15 minutes and peak effect is usually within 30 minutes.[223] Patients experience prompt benefits, with reductions in coughing, wheezing, chest

tightness and shortness of breath. The measured spirometry response to Salbutamol is assessed as 'bronchodilator reversibility'. Responders are defined as the patients in whom the post-Salbutamol FEV_1 is at least 12 % and 200 ml larger than the pre-Salbutamol measurement. [1]

Salbutamol provides sufficient symptom relief for patients with mild asthma, but those with greater disease severity require longer-acting therapeutic interventions to provide symptom control. [224] One asthma endotype, eosinophilic asthma, is characterised by inflammation that can be assessed using a number of biomarkers, principally the fractional exhaled nitric oxide (FeNO) and the eosinophil count in the blood. Eosinophils are a type of white blood cell that is thought to have a pro-inflammatory role in eosinophilic asthma. [225] Nitric oxide is synthesised within the body by enzymes called nitric oxide synthases. These enzymes are generated in response to stimuli, including inflammation pathways within airway epithelial cells. [226] In these cells, the nitric oxide levels will reflect the degree of inflammation. Nitric oxide passes into the airways, such that elevated levels in exhaled breath are observed in eosinophilic asthma patients. [227] In clinical environments FeNO is typically measured using electrochemical sensing, with abnormal FeNO defined as > 25 ppb, and eosinophilic asthma likely where FeNO > 50 ppb. [219] Studies of blood eosinophil count [228] and FeNO [229] have identified correlations with airway inflammation. These biomarkers have aided the stratification of asthma patients by endotype, allowing greater understanding of different treatment responses and targeted therapies. [230,231] The baseline biomarkers are not, however, predictive of patient responses to therapy.

Corticosteroids are therapies that can provide patients with effective control of eosinophilic asthma. Airway inflammation is suppressed by switching off multiple activated inflammatory pathways. [232] This reduces airway hyperresponsiveness, the exaggerated airway response to stimuli that leads to airway obstruction, and provides control of asthma symptoms. [233] Corticosteroids can be administered locally, in the form of inhaled therapy (ICS), or systemically, either orally or by intramuscular injection. One example of a frequently prescribed ICS is Fluticasone. This is most commonly taken in parallel with the long-acting bronchodilator Salmeterol [234] in a combination inhaler called Seretide. [235] Seretide is typically taken twice daily, with the dosage progressively reduced to the lowest dosage that provides good symptom control. In 20-40 % of eosinophilic asthma patients, however, ICS treatment does not improve symptoms or adequately control disease, indicating the need for systemic therapy. In these patients, one possible explanation for the inefficacy of ICS

is that disease could be primarily active within the small airways, and thus inaccessible to inhaled therapy.[236,237]

In patients for whom ICS treatment provides insufficient control of asthmatic symptoms, systemic therapy, such as monthly high-dosage injections of corticosteroids, have been used to improve symptom control.[238] Injected, systemic, steroid treatment can provide significant improvements to lung function and quality of life, and a reduction in hospital admissions. One example of an injected corticosteroid therapy is Triamcinolone, which provides an improved anti-inflammatory profile for many patients, and removes the variable of patient compliance.[239] The drawbacks associated with this treatment are the side-effects that result from long term steroid use, notably steroid myopathy.[240]

Mepolizumab (Mepo) is an alternative steroid-sparing asthma therapy for patients with severe eosinophilic asthma that has recently been approved by NICE.[230] Mepo is a systemic biologic therapy, providing humanised anti-interleukin-5 monoclonal antibody, which selectively inhibits eosinophil production, and thus airway inflammation.[241,242] Patients prescribed with Mepo will typically have monthly injections. Clinical trials have shown Mepo to reduce rates of asthma exacerbation by almost a half, despite only modest improvements in symptom questionnaire scores and spirometry.[243,244] More recent studies have attributed symptom improvements to improvements in small airway function, measured using the multiple breath N_2 washout method.[245] A significant issue associated with Mepo is the high cost of treatment, with each injection priced at £840.[246] To give an idea of the potential financial burden of this treatment, there are ca. 100,000 patients with severe eosinophilic asthma in the UK who could potentially benefit from Mepo.[247] Current lung function measures cannot predict the success of Mepo treatment, nor provide an early response signal after the introduction of the therapy.[248] The identification of an index capable of predicting patient response to Mepo remains important from a medical economic perspective as it may provide 'stopping rules' for patients who are unlikely to benefit.[249]

This chapter describes two clinical studies evaluating the lung inhomogeneity of patients with asthma. In the first study, a cross-sectional study of patients, the capacity of the novel indices to assess disease control is evaluated. To investigate whether these indices could provide good measures of patient response to treatment, the within-subject responses of the parameters to a range of asthma therapies, including inhaled and systemic steroid, and biologic treatment, were

measured in the second study. These inhomogeneity parameter responses were compared to the responses of existing biomarkers of lung inflammation.

4.1 Cross-sectional Study of Lung Inhomogeneity in Asthma

The second chapter of this thesis described a new approach to lung function testing that involves assessing the inhomogeneity of gas exchange in the lung.[158] A study was performed to provide a first look at whether this technique can provide indices quantifying disease activity in the lungs of asthmatic patients. The potential clinical usefulness of these indices was assessed by comparison with standard forced spirometry.

4.1.1 Methods

Seventeen patients with asthma, recruited from the Oxford University Hospital-based asthma clinic, and seventeen healthy volunteers were studied. The average ages of the asthma patients and healthy group were 57.8 ± 13.9 years (mean $\pm\, \sigma$) and 50.6 ± 17.3 years, respectively. The other anthropometric characteristics for the asthma patient and healthy groups were heights of 1.68 ± 0.08 m and 1.73 ± 0.10 m, respectively, and weights of 82 ± 19 kg and 70 ± 16 kg, respectively. Eight out of 17 of the asthma patients were female (47 %) while 6 out of the 17 participants were female (35 %) in the healthy group. Fourteen out of 17 patients had severe asthma; on Step 4 or 5 asthma treatments.[17]

Each patient underwent standard forced spirometry and a lung inhomogeneity test before and 30 min after bronchodilation with inhaled salbutamol (0.4 mg via a spacer). For the salbutamol reversibility test, patients were asked to refrain from inhaled maintenance therapies for at least 12 hours (24 hours for once-daily preparations) and short-acting bronchodilators at least 4 hours before attending the hospital. The study was approved by the South Central Oxford A Research Ethics Committee (17/SC/0172). The lung inhomogeneity tests were performed using the MFS, with participants breathing air for 10 min and then pure O_2 for 5 min. The Lognormal Lung model was fit to the gas-exchange data. Measured and simulated integrated volume profiles and expirograms are shown for an example dataset in Figure 4.1. The process of fitting the model to the measured data provided estimates of anatomical deadspace, alveolar volume at functional residual capacity, and three measures of inhomogeneity, σVD, σCL and σCd, which are standard deviations for distributions across the lung volume for deadspace, alveolar compliance and vascular conductance, respectively. This study focuses particularly on σCL as a measure of unevenness of lung inflation/deflation during breathing.

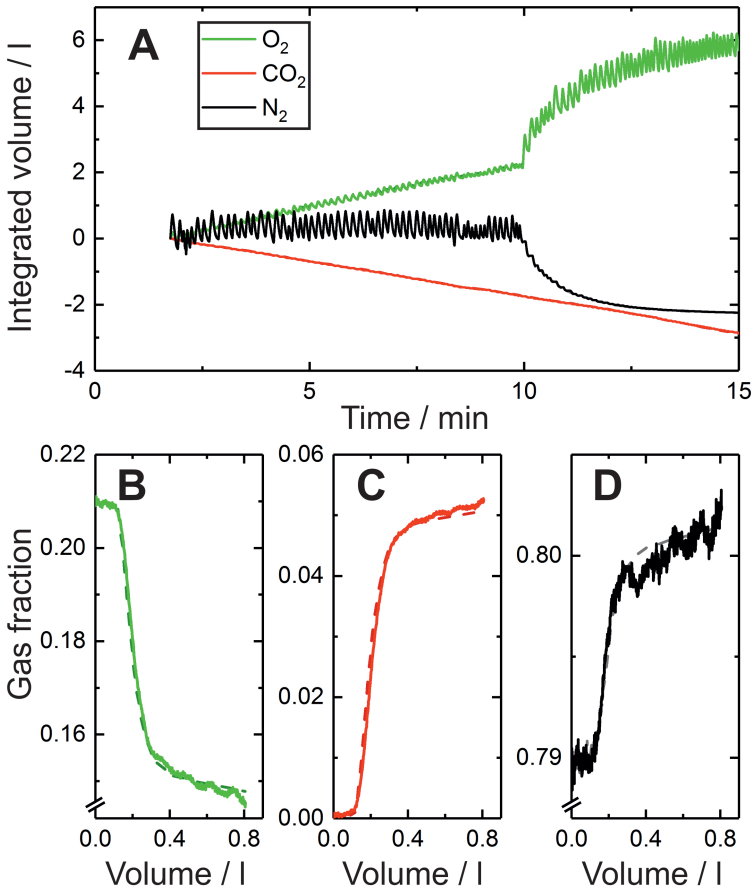


Figure 4.1: Example recording of lung inhomogeneity measurement and model fit. (A) Tidal gas flows at the mouth for N_2 (black), O_2 (green) and CO_2 (red) over a 10 min period of breathing air, followed by a 5 min period of breathing pure oxygen, as recorded using the MFS every 10 ms. Also plotted (broken lines) for each gas are the fits of the model to the data, but these are obscured because the quality of fit is so high. (B), (C), (D) Measured expirogram records for a single representative breath during the air-breathing phase for (B) O_2, (C) CO_2 and (D) N_2 gas fractions. The broken lines indicate the gas fractions simulated by the model.

Statistical analyses were performed using OriginPro software. Shapiro-Wilk tests were first performed on the data to check that there were no significant deviations from normality.[250] Student's t-tests were then performed to evaluate the significance of parameter differences between groups. Correlations were assessed using the Pearson's r parameter, a measure of linear correlation between two variables, where a value of 1 indicates total positive correlation, 0 indicates no correlation, and -1 indicates total negative correlation.[251] Logistic regression is used within this work, evaluating logistic functions of measured predictors to model binary patient descriptors.[252] Logistic regression was performed in MATLAB using the function `fitglm` to return logistic binomial models. For

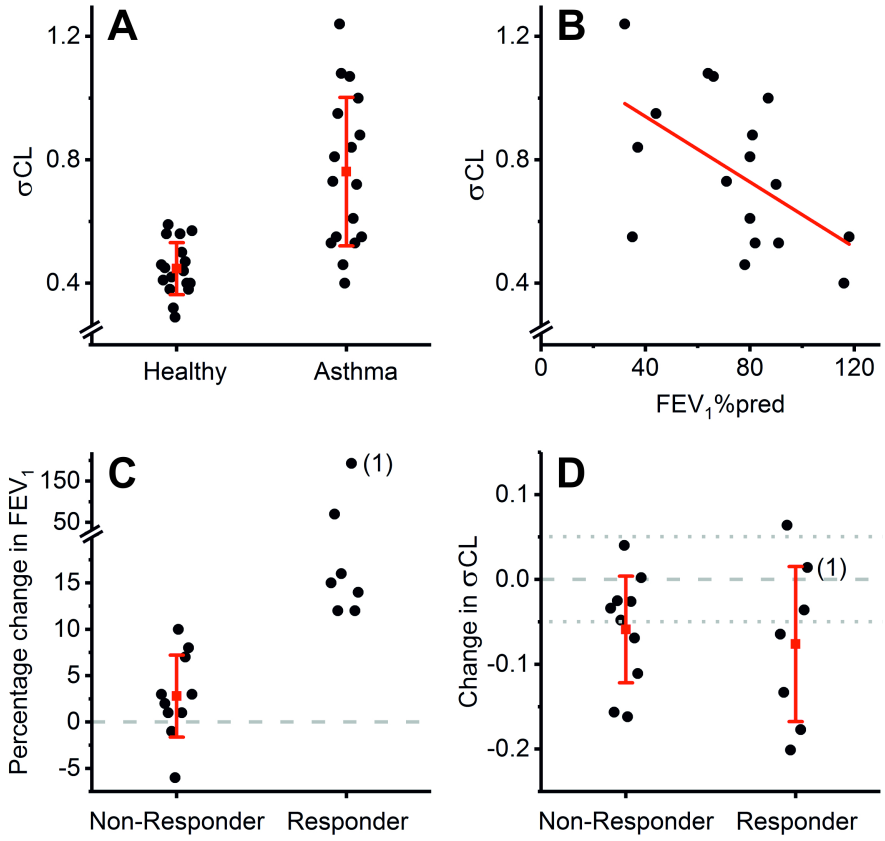


Figure 4.2: σCL is not a proxy measurement for FEV_1 % predicted (FEV_1%pred). (A) σCL values for healthy controls and patients with asthma. The average value for σCL is higher in the asthma group than in the control group (0.762±0.241, versus 0.447±0.084, respectively, mean±SD, $p<0.001$ Student's t-test). (B) Relationship between σCL and FEV_1%pred for the asthma group. The correlation is significant (Pearson's r=-0.54, $p<0.05$), but leaves 71 % of the variance in σCL unexplained. (C) Effect of bronchodilation with salbutamol on FEV_1 in asthma. The asthma patients have been divided into "responders" and "non-responders" based on their degree of bronchodilator reversibility. (Responders exhibit an effect size greater than 12 % with a minimum increase in FEV_1 of 200 ml). The patient labelled (1) is discussed in the Results. (D) Effect of bronchodilation with salbutamol on σCL in asthma. The asthma patients have again been divided on the basis of their FEV_1 response, as described in (C). Note that salbutamol reduces σCL in both groups, but the effects do not differ between the "responders" and "non-responders". In keeping with this finding, there was an absence of significant correlation (r=0.10, p=0.70) between the effect size of salbutamol on FEV_1 and the effect size on σCL. For (A), (C), (D), red symbols and lines represent means and SD, respectively. For (A) and (B), data shown are pre-salbutamol. In (D), the limits of normal reproducibility are shown by grey dotted lines, calculated from within-participant repeats measurements presented for COPD patients in Chapter 3.

each of the measured predictors, a probability of the binary patient descriptor taking one value is calculated. The predictive power of fitted logistic models were illustrated using receiver-operator curves, which plot the rate of true positive patient classification against the rate of false positive patient classification at a series of thresholds.[253] These were computed using the MATLAB function `perfcurve` with the logistic models and binary patient descriptors as inputs. The area under these curves quantifies a model's capacity to correctly classify patients into the binary descriptor groups.

4.1.2 Results

Initially, Shapiro-Wilk tests confirmed that FEV_1%pred and σCL data could be assumed to be normal, with p-values shown in Table 4.1. Values for σCL were significantly larger in asthma patients compared with healthy volunteers, shown for pre-salbutamol measurements in Figure 4.2A. Comparisons for other model parameters and FEV_1 % predicted (FEV_1%pred), also assessed pre-salbutamol, are shown in Figure 4.3. The σCL parameter remained significantly elevated in the asthma patients post-salbutamol, illustrated in Figure 4.4A.

Table 4.1: Shapiro-Wilk tests confirmed the normality of FEV_1%pred and σCL distributions. Reported p-values are shown for patients with asthma and controls, both pre- and post-salbutamol. Where $p>0.05$, the hypothesis that the data came from a normally distributed population can't be rejected.

	Shapiro-Wilk test p-value			
	Pre-salbutamol		Post-salbutamol	
	Healthy	Asthma	Healthy	Asthma
FEV_1%pred	0.96	0.24	0.53	0.42
σCL	0.49	0.56	0.47	0.50

There was a significant correlation between σCL and FEV_1%pred, both before and following salbutamol, shown in pane B of Figures 4.2 and 4.4, respectively. In both cases, however, the majority of the variance in σCL was unexplained by FEV_1%pred, 71 % pre-salbutamol and 52 % post-salbutamol. Following salbutamol, σCL fell in the asthma patients, but the effects of salbutamol on σCL were independent of whether the patients showed FEV_1 bronchodilator reversibility. Indeed, for patient 1 in Figure 4.2, FEV_1 rose following salbutamol by 193 % while σCL hardly changed (0.55 to 0.57), demonstrating that σCL is not a surrogate for FEV_1.

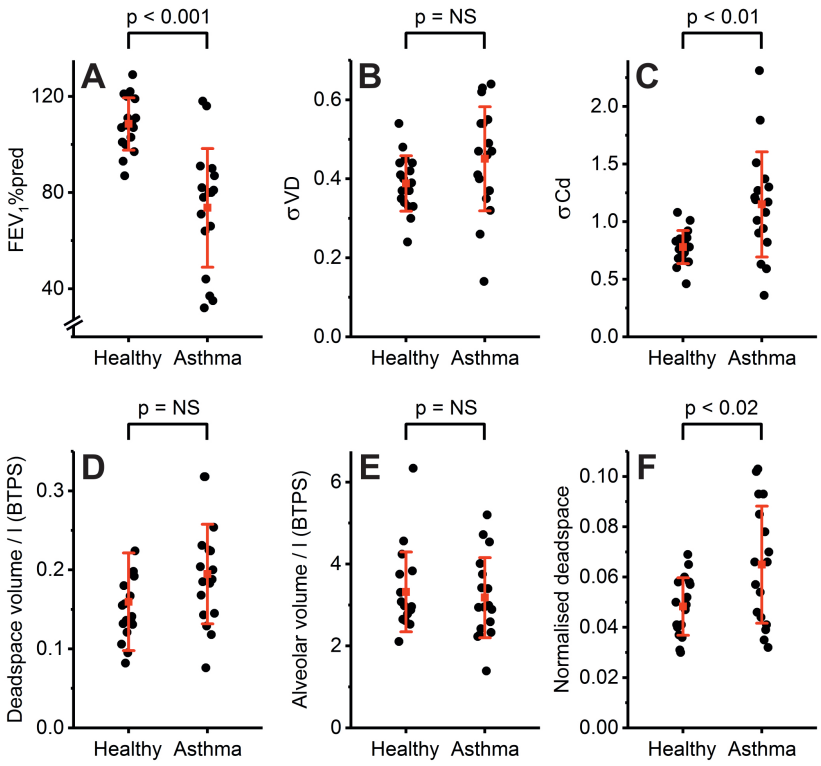


Figure 4.3: Comparisons of FEV_1 % predicted (FEV_1%pred) and model parameters, other than σCL, for healthy participants and for patients with asthma. Red symbols and lines represent means and SD, respectively. (A) FEV_1%pred. (B) Standard deviation for the distribution of standardised anatomical deadspace across the lung volume, σVD. (C) Standard deviation for the distribution of standardised vascular conductance across the lung volume, σCd. (D) Anatomical deadspace volume for healthy controls and patients with asthma. (E) Alveolar volume at FRC. (F) Anatomical deadspace normalised to alveolar gas volume at FRC. Significant differences were detected (Student's t-tests) between the asthma patients and healthy controls for FEV_1%pred, σCd and normalised anatomical deadspace.

Figures 4.5A and B illustrate that prior to bronchodilator administration neither FEV_1 nor σCL correlated significantly with symptom severity in the patients, quantified by ACQ-5 score. For an index of "disease control", we defined control as "bad" if the physician at the clinic visit before measurement deemed that an increase/escalation in therapy was necessary (either increased therapy on the day or referred further for biologic treatment). Control was defined as "good" in all other patients, where the physician felt no therapy escalation was needed and either decreased or left unchanged a patient's therapy. There was no significant difference in FEV_1%pred between patients with "good control" versus those with "bad control" (Figure 4.5C). In contrast, σCL was

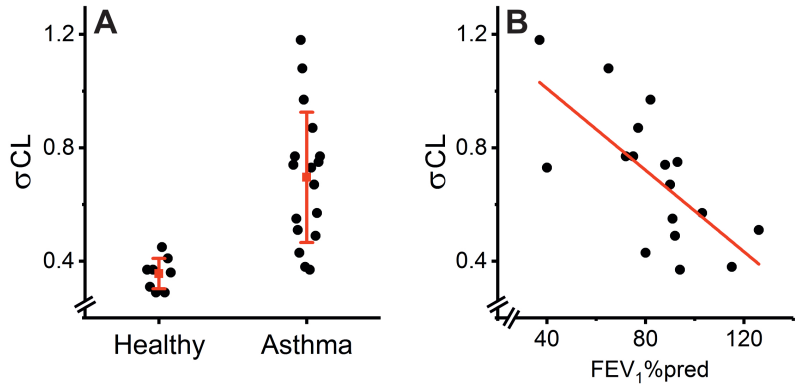


Figure 4.4: σCL is not a proxy measurement for FEV_1 % predicted following bronchodilation. (A) σCL values for healthy controls and patients with asthma. Red symbols and lines represent means and SD, respectively. The average value for σCL is higher in the asthma group than in the control group (0.696±0.230, versus 0.356±0.054, mean±SD, respectively, $p<0.001$ Student's t-test). Note, 8 of the 17 healthy participants also undertook the post-salbutamol study. (B) Relationship between σCL and FEV_1%pred for the asthma group. The correlation is significant (Pearson's r=-0.69, $p<0.005$), but leaves 52 % of the variance in σCL unexplained.

significantly higher in patients with "bad control" than those with "good control" (Figure 4.5D). Figures 4.5E and F illustrate an analysis using logistic regression that demonstrates that σCL is a better predictor of disease control than FEV_1%pred. Very similar results were obtained for the post-salbutamol parameters, shown in Figure 4.6.

4.1.3 Discussion

The results indicate that σCL is not simply a proxy for FEV_1%pred, but rather that it captures different aspects of the disease's pathophysiology, beyond airflow obstruction. FEV_1 changes are generally thought to arise from hyper-reactivity of smooth muscle in the large airways resulting in increased airways resistance. In contrast, σCL may preferentially reflect the effects of hyper-reactivity of smooth muscle in the small airways through an effect on ventilation distribution. An alternative hypothesis is that σCL reflects small airways inflammation. Small airways inflammation is associated with localised oedema which increases the stiffness of that part of the lung. As the distribution of disease across the lung tends to be uneven, then so too is the distribution of stiffness. This mechanism can explain an increase in σCL without invoking any change in airways resistance. Indeed, distinct mechanisms of action of salbutamol on σCL (enhanced lung-water clearance) and FEV_1 (smooth muscle relaxation in large airways) may explain why the effects of salbutamol on

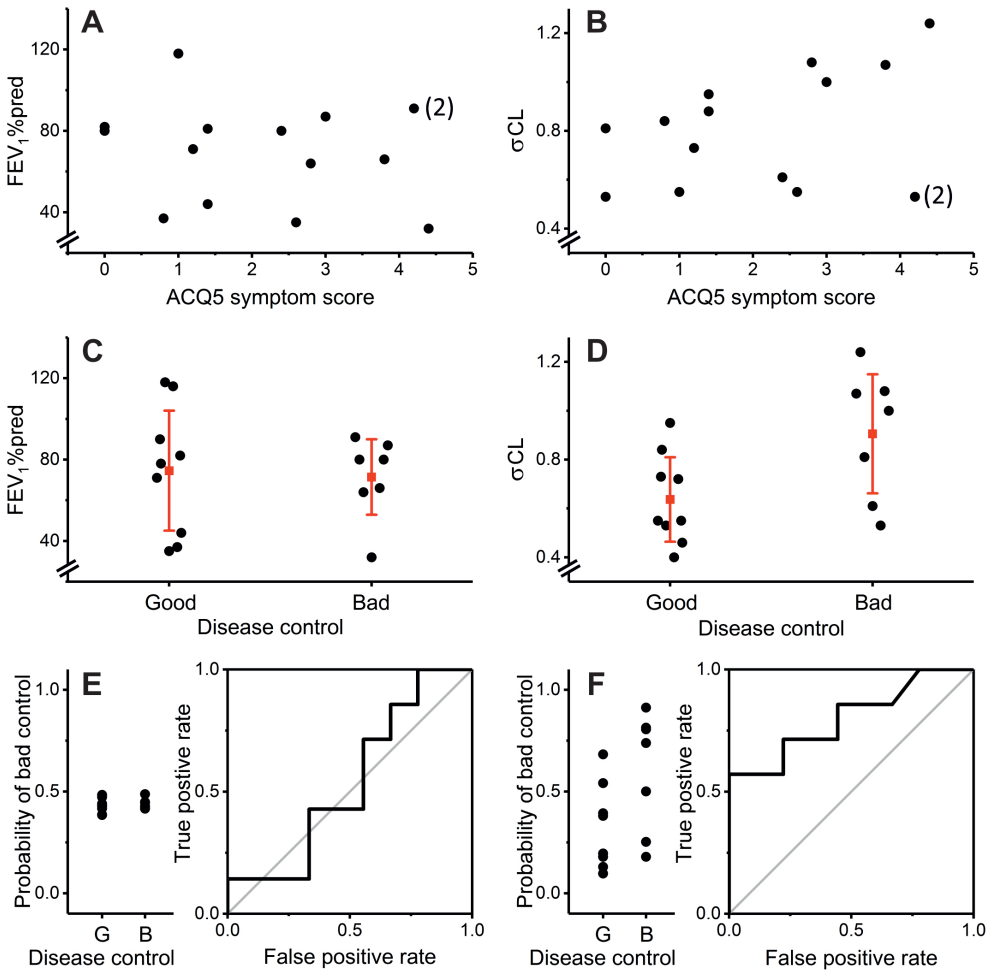


Figure 4.5: σCL reflects disease activity more tightly than FEV_1%pred. (A), (B) FEV_1%pred and σCL as a function of asthma symptom questionnaire (ACQ5) score, respectively. Neither variable correlated significantly with symptoms (Pearson's r=-0.27, p=0.40 and r=0.43, p=0.15, for FEV_1%pred and σCL, respectively). The patient labelled (2) is considered further in the Discussion. (C), (D) FEV_1%pred and σCL by physician assessment of "disease control", respectively. "Good control" was defined as therapy either unchanged or reduced at clinic visit, "bad control" was defined as therapy increased at clinic visit. There was no significant difference in FEV_1%pred between the two groups (p=0.81 Student's t-test). σCL was significantly higher in the "bad control" group compared with the "good control" group ($p<0.05$). Red symbols and lines represent means and SD, respectively. (E), (F) Logistic regressions to predict "disease control" using FEV_1%pred or σCL as predictors, respectively. σCL was the better predictor, as judged by the probabilities for individual patients (left panels) and area under the curve of the receiver-operator plots, which were 0.540 for FEV_1%pred and 0.802 for σCL. Data illustrated are pre-salbutamol.

σCL were similar for both FEV_1 responders and non-responders to salbutamol.

Neither FEV_1%pred nor σCL correlated significantly with symptoms. Patient 2, shown in Figures 4.5 and 4.6, had a very high symptom score, but had normal values for σCL and FEV_1%pred regardless of bronchodilator status. Before salbutamol, σCL was 0.53 and FEV_1%pred was 91 %, and post-salbutamol those values changed to 0.37 and 94 %, respectively. On review of this patient's clinical records, their symptoms appeared to have a multifactorial origin including significant nasal/upper airway symptoms, breathlessness from hyperventilation/dysfunctional breathing, depression and fibromyalgia. This patient demonstrates the value that an objective measure of disease activity within the lung could have in managing asthma. Apart from this patient, the four patients with the highest symptom scores also had the highest σCL values. Indeed, without this outlier, the correlation between σCL and symptoms would have been significant ($p<0.02$ and $p<0.01$, pre- and post-salbutamol, respectively). Unlike FEV_1, σCL predicted whether the physician deemed an escalation of therapy necessary. This is consistent with the hypothesis that σCL reflects small airways disease, which is increasingly recognised as associated with severe refractory asthma.[254,255]

While the current study involved only a small number of participants and is preliminary, the results are promising and suggest that the method may provide a powerful new objective measure of disease activity in the lung. To determine whether this early promise is fulfilled, and if so, whether the measurement is useful in the management of asthma, will require larger studies across different patient populations using longitudinal and interventional designs.

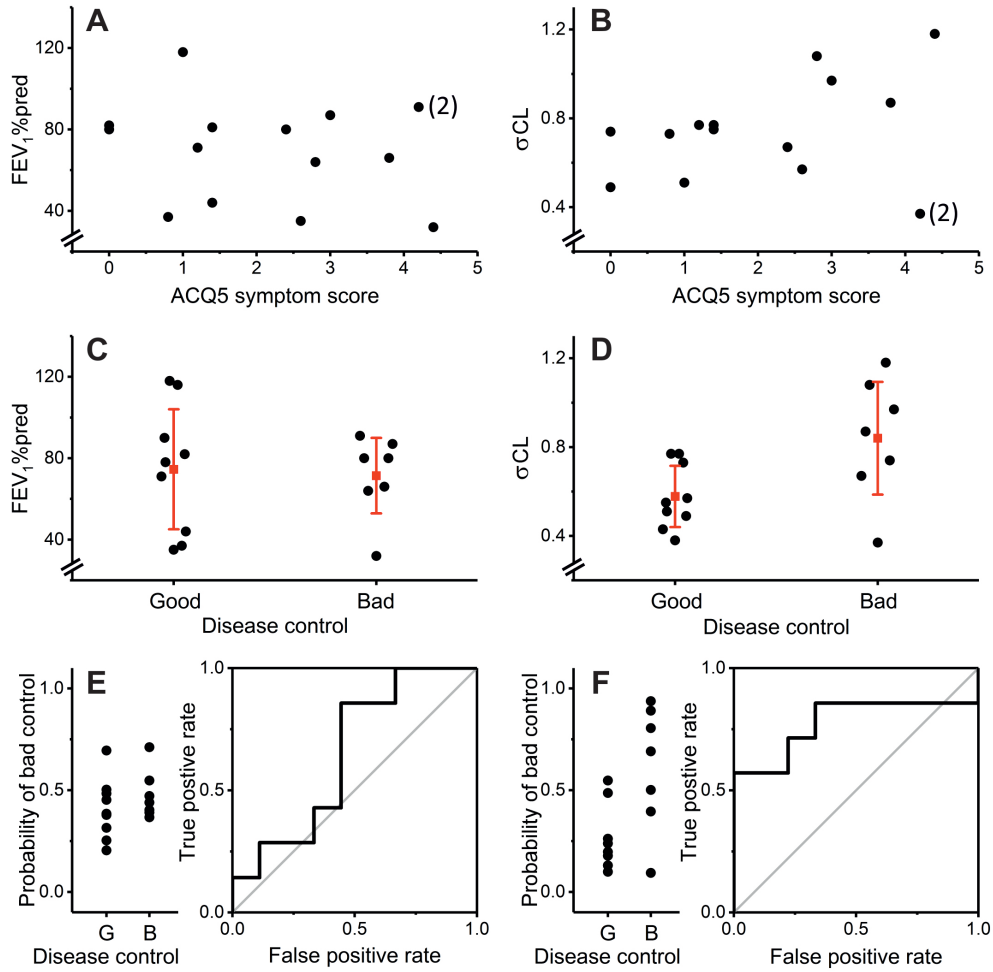


Figure 4.6: σCL reflects disease activity more tightly than FEV_1%pred following bronchodilation. (A), (B) FEV_1%pred and σCL as a function of asthma symptom questionnaire (ACQ5) score, respectively. Neither variable correlated significantly with symptoms (Pearson's r=-0.24, p=0.40 and r=0.36, p=0.21, for FEV_1%pred and σCL, respectively). The patient labelled (2) is considered further in the Discussion. (C), (D) FEV_1%pred and σCL by "disease control", respectively. "Good control" was defined as therapy either unchanged or reduced at clinic visit, "bad control" was defined as therapy increased at clinic visit. There was no significant difference in FEV_1%pred between the two groups (p=0.30 Student's t-test). σCL was significantly higher in the "bad control" group compared with the "good control" group ($p<0.05$). Red symbols and lines represent means and SD, respectively. (E), (F) Logistic regressions to predict asthma control using FEV_1%pred or σCL as predictors, respectively. σCL was the better predictor, as judged by the probabilities for individual patients (left panels) and area under the curve of the receiver-operator plots, which were 0.65 for FEV_1%pred and 0.78 for σCL.

4.2 Longitudinal Study of Patients with Asthma

The Lognormal Lung model presents novel indices of lung inhomogeneity with the potential to provide clinicians with useful measures of disease activity and/or control in asthma patients. This longitudinal study of asthma patients was performed to investigate for the first time whether these indices can track treatment response and to compare the treatment driven responses of these indices with the responses of established biomarkers of lung inflammation in severe eosinophilic asthma patients.

To establish the optimal therapeutic intervention for patients with eosinophilic asthma, clinicians utilise treatment pathways. In a treatment pathway, different treatment types are prescribed for short periods, and the response to each is evaluated. In the complex airways disease clinic at the Oxford University Hospitals, severe eosinophilic asthma patients (FeNO > 50 ppb, blood eosinophil count >0.35 cells nl^{-1}, on Step 4 or 5 asthma treatments[17]) are eligible for the pathway. In the first week of the pathway a FeNO suppression test is performed.[256] This test provides an objective test to distinguish adherent and non-adherent patients.[231] High dose inhaled corticosteroid (ICS) therapy, in the form of inhaled Seretide (1 mg Fluticasone daily), is prescribed for the week. Adherence to inhaled treatment is ensured by the inhaler's incorporated adherence chip. Responses to this therapy are assessed using a range of biomarkers, including spirometry, ACQ-5 symptom score, blood eosinophil content, and fraction of exhaled nitric oxide (FeNO) measurement. The FeNO suppression test classifies eosinophilic asthma patients as 'responders' or 'non-responders' to ICS treatment. Following the week of Seretide, responders display a reduction of FeNO by $\geq 40\,\%$ and a clinically significant ACQ-5 improvement (≥ 0.5). At this point, the pathway splits, with responders prescribed with a further month of chipped inhaled Seretide (1 mg Fluticasone daily). The response to extended ICS therapy is assessed at the third clinical visit, with the long-term outlook being ICS prescription in the majority of cases. Non-responders, who are adherent to ICS but don't exhibit FeNO and ACQ-5 improvements, are given an injected dose of systemic steroid Triamcinolone and re-assessed a month later. Non-responders may ultimately be prescribed biologic therapy such as Mepolizumab (Mepo).

In this study, research visits, which included evaluation of lung inhomogeneity by the Lognormal Lung method, were aligned with clinical appointments. Data collected during these visits allowed a

series of hypotheses to be investigated. The first was that a patient's Lognormal Lung parameters would change significantly in response to established asthma therapies that are known to reduce the biomarkers of airway inflammation, e.g. ICS, systemic steroids, and biologic therapy. The second was that underlying pathophysiology differences between ICS 'responders' and 'non-responders', for example that disease activity in responders might be characterised by more small airways disease, would be identifiable by Lognormal Lung inhomogeneity parameters. Extending this study longitudinally, to assess long-term symptom improvement with Mepo therapy, would provide an indication of whether indices of inhomogeneity can provide the early-response signal that is required for this therapy.

4.2.1 Methods

Eleven patients with a diagnosis of eosinophilic asthma (baseline FeNO > 50 ppb and blood eosinophil count > 0.35 cells nL^{-1}) were recruited from the Oxford University Hospitals' complex airways disease clinic to participate in this study. The experimental work was conducted in accordance with the general ethical principles of the Declaration of Helsinki, with the study approved by the South Central Oxford A Research Ethics Committee (17/SC/0172). Informed written consent was taken from each patient. Of the eleven patients, seven were studied longitudinally during the asthma treatment pathway described above, with lung inhomogeneity assessed during three clinical appointments.

The remaining four patients were recruited prior to commencing Mepo treatment. A further two participants were prescribed Mepo following the conclusion of the treatment pathway. Mepo was given as monthly high-dose injections, with these six patients studied during two clinical visits, initially preceding their first injection (pre-Mepo), and later following 3 months of treatment. Two of these subjects were also studied following 11 months of Mepo treatment. Anthropometric data for the asthma patient group is shown in Table 4.2.

At each research visit, the patient underwent standard forced spirometry and lung inhomogeneity tests before and 30 min following bronchodilation with inhaled Salbutamol (0.4 mg via a spacer). Patients were asked to refrain from inhaled maintenance therapies for at least 12 hours (24 hours from once-daily treatment) and short-acting bronchodilators for at least 4 hours prior to attending the clinic. The lung inhomogeneity tests were performed using the MFS. Subjects were connected to the MFS via a mouthpiece and a heat and moisture (HME) filter, and breathed with the nose

Table 4.2: Anthropometric data for asthma patients undergoing therapeutic intervention. Data are shown as group mean ± standard deviation where applicable.

	All	Treatment Pathway	Mepolizumab Treatment
Group size	11	7	6
Female, # (%)	2 (18 %)	0 (0 %)	2 (33 %)
Age / years	55.5 ± 13.3	55.1 ± 16.7	55.8 ± 9.4
Height / m	1.73 ± 0.08	1.73 ± 0.09	1.73 ± 0.08
Weight / kg	77.3 ± 11.4	74.7 ± 7.5	80.3 ± 14.9

occluded. Arterial O_2 saturation, SpO_2, was measured by a pulse-oximeter. Subjects breathed air for 10 minutes and then pure O_2 for the final 5 minutes. The recorded MFS data were analysed using the Lognormal Lung model. Parameter sets associated with the best fit of the model to the measured data were taken as the determined parameter values.

All MFS recorded washout data were processed using the Lognormal Lung model, but it was primarily the post-bronchodilator measurements, both for the lung inhomogeneity parameters and spirometry, that were used to assess therapy driven responses. The previous study demonstrated that inhomogeneity parameters obtained both before and after bronchodilator provide good indices of disease control within patients with asthma. The rationale for focussing on the post-bronchodilator measurements in this work is that they would better reflect typical patient lung physiology; frequent bronchodilator administration is ubiquitous in severe asthma patients. Thus, reported symptom scores, as well as measured biomarkers of airway inflammation, are likely to chiefly reflect post-bronchodilator disease and physiology.

4.2.2 Results

4.2.2.1 Asthma Treatment Pathway

Each of the seven pathway patients attended three clinical visits: baseline, post-Seretide, and post-Triamcinolone. For two of these patients, N_2 washout data were not obtained during the post-Seretide visit due to technical reasons. For a separate subject, the pre-bronchodilator test during the baseline visit was unsatisfactory due to an alternate bacterial filter type being used in the experimental set-up. In all, 37 experimental datasets were satisfactorily recorded during treatment pathway research visits and these were then used as inputs to the Lognormal Lung model. The model

successfully fit to each of these datasets, producing best-fit estimates of lung parameters. None of these determined parameter sets met the exclusion criteria of modelled SpO_2 during air-breathing being more than 3.5 % below the pulse-oximeter measured value during the same period, so all were used in further analysis.

The profiles of assessed clinical details, FEV_1, ACQ-5, FeNO, and blood eosinophil count, during the treatment pathway are shown for each participant in Figure 4.7. The colours and symbols used to identify participants within this figure remain consistent throughout this chapter, and so are also used as identifiers within the text. Of particular interest were the responses of FeNO and ACQ-5 to ICS; these markers are used to stratify 'responders' and 'non-responders'. FeNO decreased in response to ICS therapy in six of the seven patients, but in only three of these were the decreases ≥ 40 % (brown triangle, open blue hexagon, and grey triangle). Of these patients, only one (open blue hexagon) reported an ACQ-5 decrease of ≥ 0.5, improving from 2.6 to 1.0. Thus, this single patient was classified as an ICS responder. As a responder to ICS, this therapy was continued for a further month, such that data recorded during the third visit reflects response to extended ICS treatment rather than injected steroid therapy. In the non-responders, the ACQ-5 response to ICS was mixed, two patients reported symptom decline, one unchanged symptoms, and three improved symptoms. Another mixed response was recorded in the blood eosinophil content marker, where increases were measured in three patients, and decreases in the remaining four, including the responder. Post-bronchodilator spirometry improved in response to ICS in five patients, again including the responder, but decreased in the other two, in one case by 18 % (brown triangle).

In each patient classified as a non-responder to ICS, post-bronchodilator FEV_1 increased following systemic steroid therapy. The ACQ-5 symptom score showed a similar trend; five of the six patients reported symptom improvements after Triamcinolone compared to baseline. The remaining patient reported no symptom changes throughout the duration of the treatment pathway. The measured FeNO values following systemic steroid were lower than baseline measurements in five of the six participants; in four of these cases, the decrease was clinically significant, ≥ 40 %. The only FeNO increase was measured for the patient with the lowest baseline value (purple diamond). Although systemic therapy substantially reduced FeNO in this patient group compared to baseline, only four of the patients had lower FeNO at the final visit than following ICS. Measured blood eosinophil levels were lower following systemic treatment than at baseline in each of the six patients.

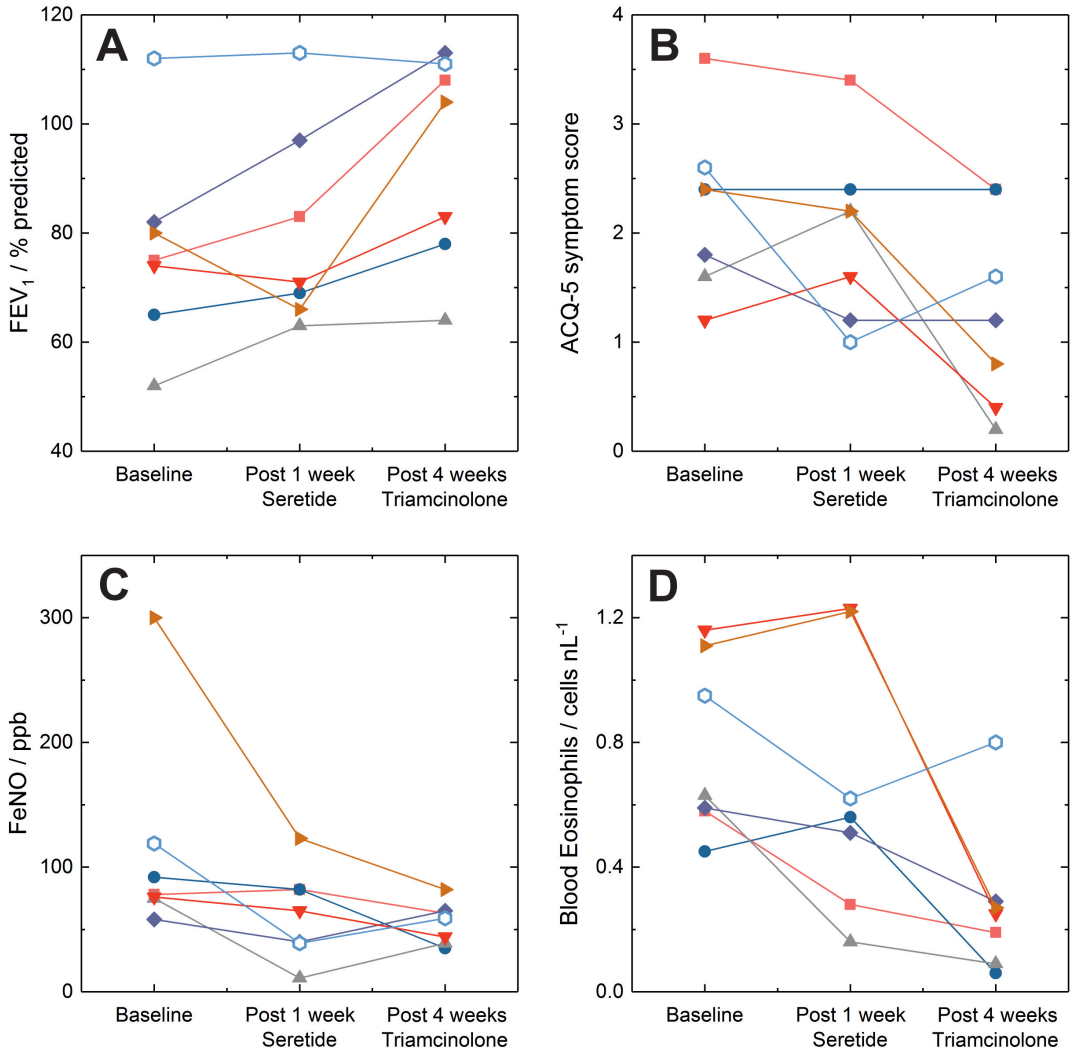


Figure 4.7: Measured clinical details for asthma patients during treatment pathway. **A** shows post-bronchodilator FEV_1 % predicted, **B** shows reported ACQ-5 symptom score, **C** shows end-tidal nitric oxide concentration, and **D** shows measured blood eosinophil concentration. Data are shown for three clinical visits: baseline, following a week of inhaled steroid Seretide, and following a month of treatment by systematic steroid Triamcinolone. Each patient is shown with a unique symbol and colour combination. One patient (open blue hexagon) was an ICS responder, so the third visit follows a month of ICS therapy rather than injected steroid treatment.

As noted above, for the single responder (open blue hexagon), data shown for the third clinical visit represent the response to a further month of ICS treatment. The post-bronchodilator FEV_1 showed little variation in response to ICS, after both a week and the additional month, remaining normal ($\geq 80\,\%$ predicted) throughout. The remaining three clinical measures were higher following extended ICS therapy than at the second visit. All three, however, were lower than the baseline measurement following the month of ICS.

The post-bronchodilator standard deviation of lung compliance distribution, σCL, and standard deviation of anatomical deadspace volume distribution, σVD, parameters determined during the asthma treatment pathway are shown in Figures 4.8 and 4.9, respectively. The repeatability of these parameters was found to be $\pm 5\,\%$ by the cross-sectional study of patients with COPD in Chapter 3, and that level of uncertainty was assumed to also be present in these measurements. At baseline, six of the seven σCL parameters were elevated beyond the upper limit of normal for the control group of the cross-sectional study - 0.62. In contrast, only one estimated σVD parameter was abnormally elevated (> 0.52), partially reflecting the heterogeneity of this parameter within the control group. It should be noted that Lognormal Lung parameter responses to ICS are limited to five patients; no data were recorded during the second visits of two individuals (brown triangle, grey triangle). Of the five patients assessed following ICS, σCL increased in two participants, and decreased in the remaining three, most significantly by $28\,\%$ for the single responder to this therapy (open blue hexagon). In general, the σVD responses to ICS therapy were modest in magnitude, the exception being one patient (purple diamond) for whom a $38\,\%$ decrease was observed. In terms of parameter response to Triamcinolone, a lower σCL was determined after systemic therapy compared to baseline for each of the six patients. For each of the four non-responders to ICS who were studied at all three clinical visits, the σCL parameter determined for the final visit was also lower than that determined during the second visit. In response to a month of ICS therapy, a modest σCL increase was observed for the single responder (open blue hexagon). In this patient, σCL remained $23\,\%$ lower than the baseline parameter. The response of σVD to systemic treatment was again mixed, decreasing from baseline in four cases.

The post-bronchodilator standard deviation of vascular conductance distribution, σCd, changes during the treatment pathway are shown in Figure 4.10. Again, the estimated parameters at baseline displayed abnormality (greater than the upper limit of normal - 1.07) in six of seven cases. In

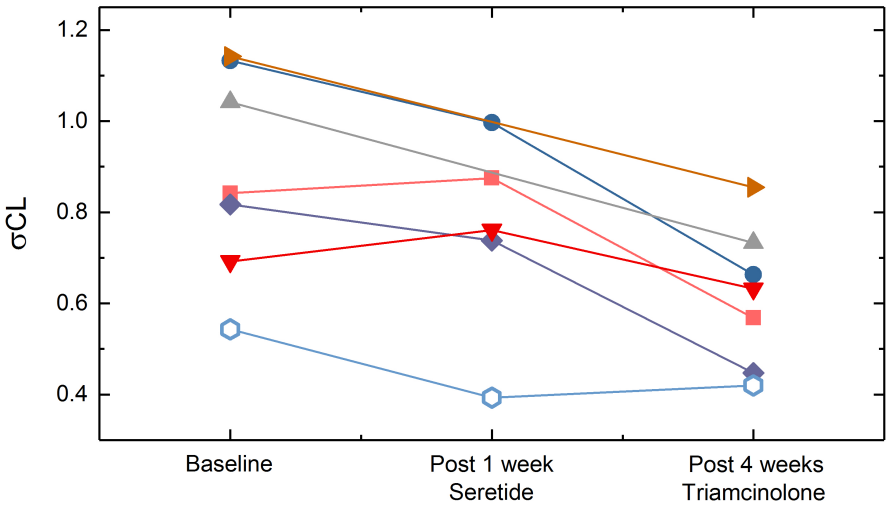


Figure 4.8: Determined σCL parameters for asthma patients undergoing treatment pathway. Each patient is shown with a unique symbol and colour combination. Data are shown for three clinical visits: baseline, following a week of inhaled steroid Seretide, and following a month of treatment by systematic steroid Triamcinolone. One patient (open blue hexagon) was an ICS responder, so the third visit follows a month of ICS therapy rather than injected steroid treatment. For two participants (brown and grey triangles), data are missing for the second visit. Washout procedures performed post-bronchodilator.

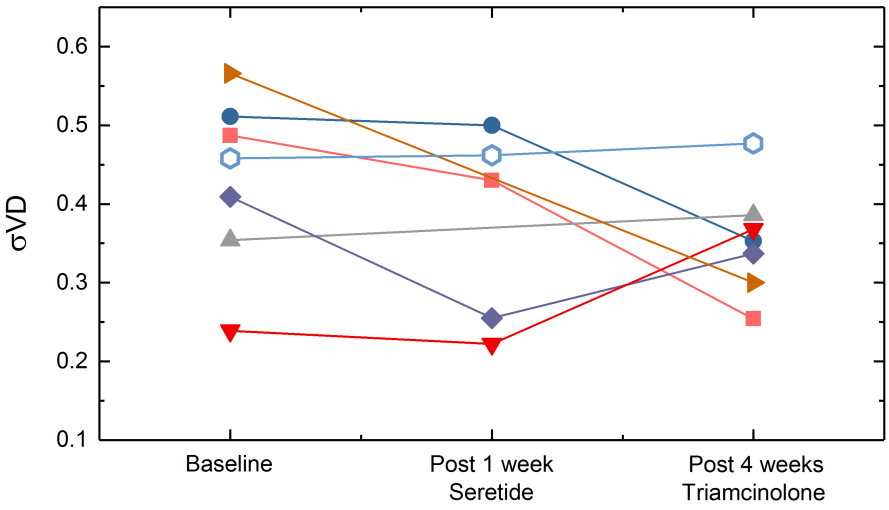


Figure 4.9: Determined σVD parameters for asthma patients undergoing treatment pathway. Each patient is shown with a unique symbol and colour combination. Data are shown for three clinical visits: baseline, following a week of inhaled steroid Seretide, and following a month of treatment by systematic steroid Triamcinolone. One patient (open blue hexagon) was an ICS responder, so the third visit follows a month of ICS therapy rather than injected steroid treatment. For two participants (brown and grey triangles), data are missing for the second visit. Washout procedures performed post-bronchodilator.

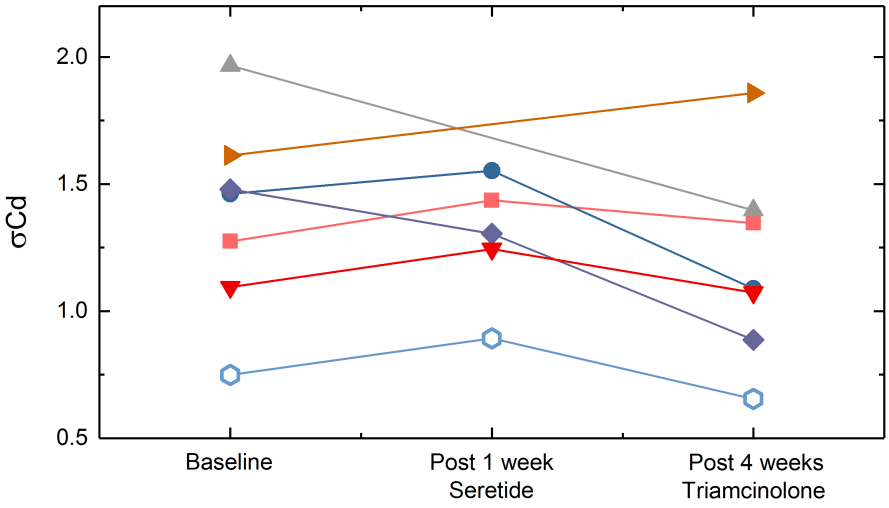


Figure 4.10: Determined σCd parameters for asthma patients undergoing treatment pathway. Each patient is shown with a unique symbol and colour combination. Data are shown for three clinical visits: baseline, following a week of inhaled steroid Seretide, and following a month of treatment by systematic steroid Triamcinolone. One patient (open blue hexagon) was an ICS responder, so the third visit follows a month of ICS therapy rather than injected steroid treatment. For two participants (brown and grey triangles), data are missing for the second visit. Washout procedures performed post-bronchodilator.

response to ICS therapy, σCd increased in four patients, including the single responder (open blue hexagon), but decreased for the remaining subject by 12 %. A range of responses to systemic therapy were recorded; one participant showed minimal change from baseline (red triangle), three reported decreases from baseline, and the parameter increased in two individuals. Following the month of ICS therapy, the σCd parameter of the responder essentially returned to its baseline value, well below the upper limit of normal (open blue hexagon). The relatively large uncertainty in σCd, calculated to be $\pm$ 23 % in the cross-sectional study of COPD patients, must be considered when evaluating the responses of this parameter to therapy.

4.2.2.2 Mepolizumab Treatment

The six patients undertaking Mepo treatment (two of whom had previously been studied during the asthma treatment pathway) were studied during two clinical visits: prior to the first Mepo injection, and following three months of Mepo treatment. Two of the subjects were also studied following 11 months of therapy. At each visit patients performed two N_2 washout procedures, before and following bronchodilator. In total, 28 experimental procedures were performed. In one case,

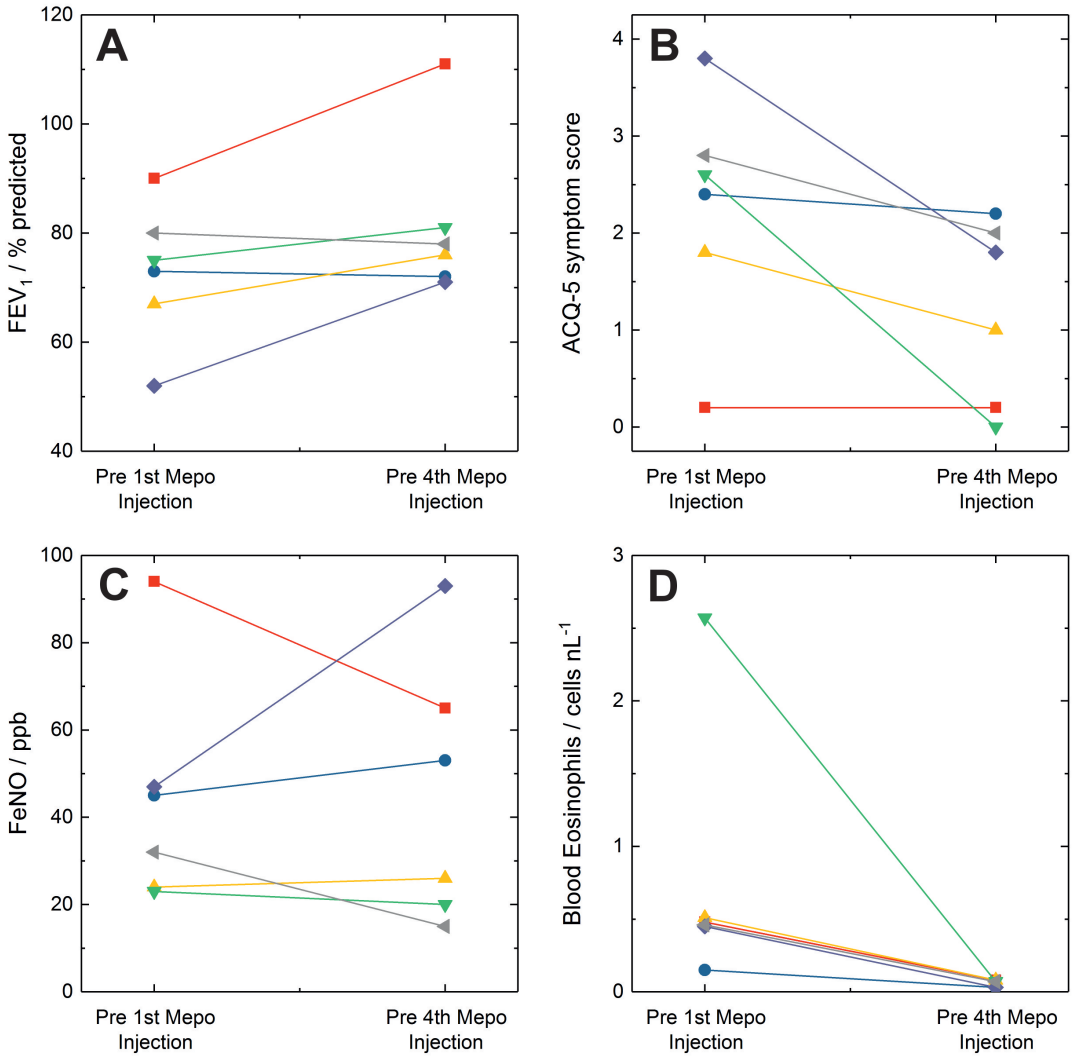


Figure 4.11: Measured clinical details for asthma patients during injected biologic therapy. **A** shows post-bronchodilator FEV_1 % predicted, **B** shows reported ACQ-5 symptom score, **C** shows end-tidal nitric oxide concentration, and **D** shows measured blood eosinophil concentration. Data are shown for two clinical visits: prior to the first Mepo injection, and following three months of therapy. Each patient is shown with a unique symbol and colour combination.

a pre-bronchodilator washout during the second visit, the model failed to fit to the recorded data; the washout was abnormally slow, so a leak was suspected. In another participant, determined parameter sets for pre-bronchodilator procedures during both visits were excluded due to differences between measured and modelled SpO_2 during the air-breathing period that were $> 3.5\,\%$. Thus, 25 sets of accepted lung parameters were generated from the 28 (89 %) performed N_2 washout tests.

The clinical details measured during the pair of visits are shown in Figure 4.11 for the six Mepo patients. Prior to treatment, normal post-bronchodilator spirometry was measured in two of the six patients, with $FEV_1 > 80\,\%$ predicted. In four of six patients, FEV_1 increased in response to Mepo, by greater than 10 % in three cases. The two remaining patients reported essentially unchanged FEV_1. Mepo therapy improved symptoms within this patient group. The ACQ-5 symptom score is lower following three months of Mepo in five patients, in four cases by a clinically significant amount (≥ 0.5). The one patient who reported no symptom improvement displayed low symptoms at both visits (red square). Prior to commencing Mepo treatment, the FeNO measurements displayed limited abnormality, two patients were below the upper limit of normal (25 ppb), and only a single patient was above the 50 ppb eosinophilic asthma criterion. In response to therapy, FeNO showed mixed responses; there were three increases and three decreases. In contrast, another biomarker of airway inflammation, the blood eosinophil count, showed a consistent response to biologic therapy, reduced in all six patients.

The post-bronchodilator σCL, σVD, and σCd parameters are shown in Figures 4.12, 4.13, and 4.14, respectively. Prior to commencing Mepo treatment, the σCL parameters for all of the patients were abnormally elevated (greater than upper limit of normal - 0.62). Following three months of therapy, this parameter was reduced in every patient, on average by $21 \pm 8\,\%$. At this point, two patients' σCL parameters were below the upper limit of normal. Only a single patient's σVD parameter was abnormally elevated at the first clinical visit, although a further three patients were less than 10 % beneath the upper limit of normal (0.53). In response to Mepo therapy, the σVD parameters generally reduced, observed in five patients. The magnitude of reduction was variable, ranging from 3 to 29 %. Three of the σCd parameters for the patients prior to Mepo were above the upper limit of normal (1.07). The measured responses of σCd to Mepo were highly variable, with three increases and three decreases. In each case, the magnitude of the change was significant.

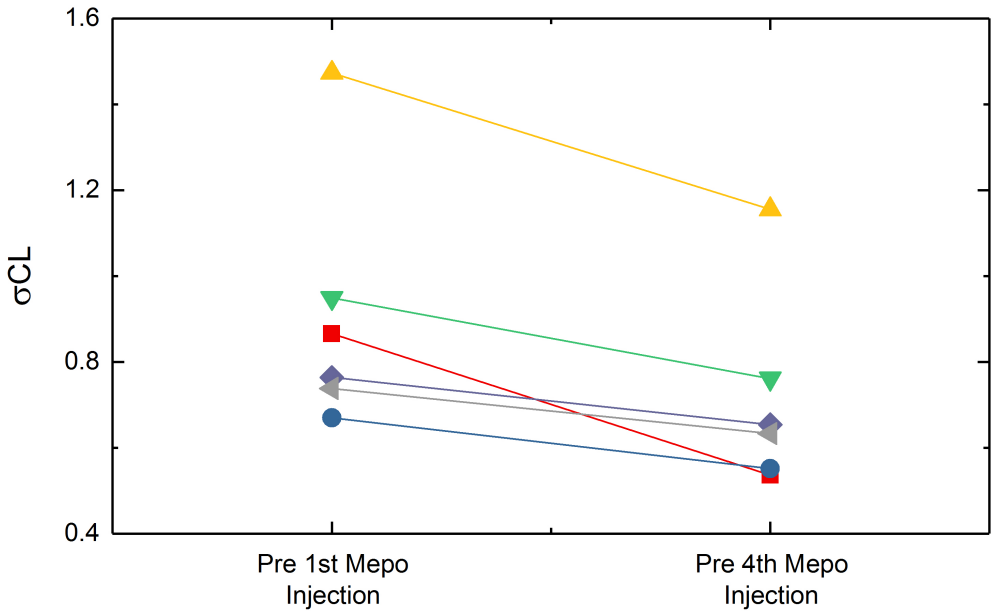


Figure 4.12: Determined σCL parameters for asthma patients receiving Mepo treatment. Each of the six patients is shown with a unique symbol and colour combination. Data are shown for two clinical visits: prior to first Mepo injection, and following three months of Mepo treatment. Washout procedures performed post-bronchodilator.

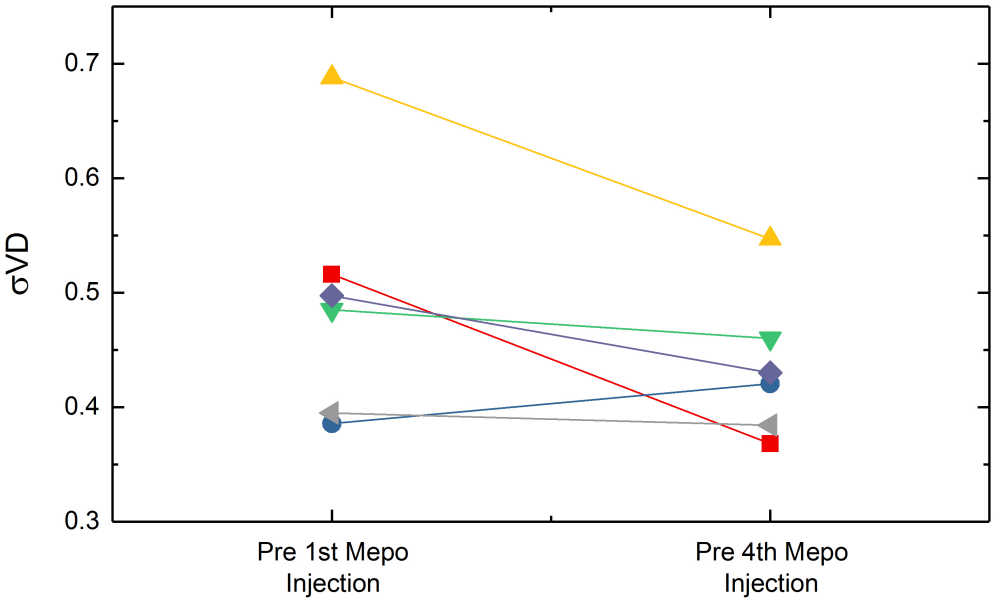


Figure 4.13: Determined σVD parameters for asthma patients receiving Mepo treatment. Each of the six patients is shown with a unique symbol and colour combination. Data are shown for two clinical visits: prior to first Mepo injection, and following three months of Mepo treatment. Washout procedures performed post-bronchodilator.

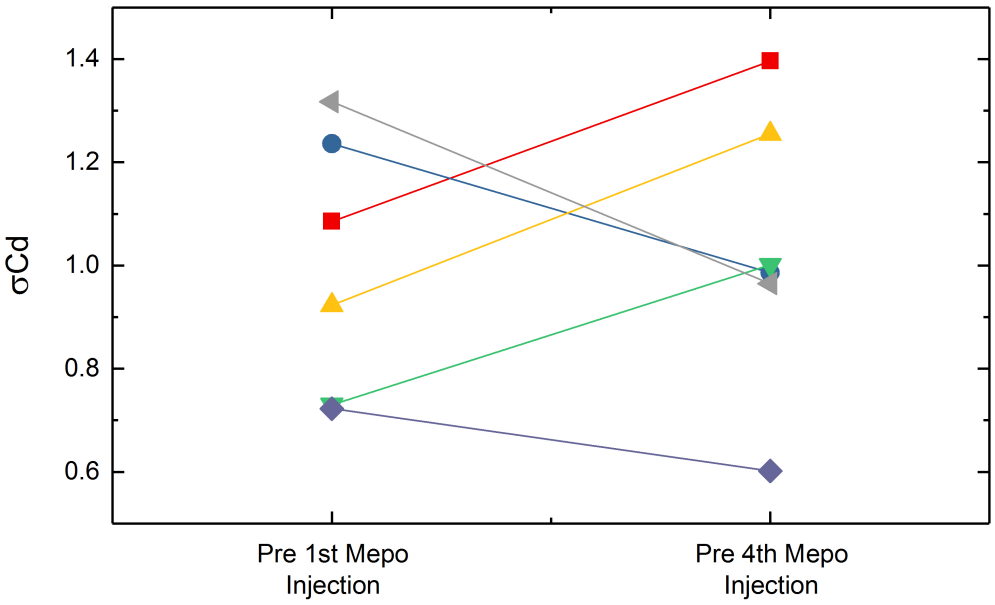


Figure 4.14: Determined σCd parameters for asthma patients receiving Mepo treatment. Each of the six patients is shown with a unique symbol and colour combination. Data are shown for two clinical visits: prior to first Mepo injection, and following three months of Mepo treatment. Washout procedures performed post-bronchodilator.

Two patients were further studied following 11 months of Mepo treatment. Figure 4.15 shows the profiles of post-bronchodilator σCL, σVD, σCd, FEV_1 over the these patients' three research visits. The behaviour of the Lognormal Lung model inhomogeneity parameters was similar in these two individuals. In both patients, σCL and σVD displayed a significant reduction from baseline value following three months of biologic treatment. After 11 months of therapy, however, these parameters had returned to baseline values; within 10 % of initial value for both parameters of both patients. The σCd responses to Mepo were also somewhat similar, increasing with duration of Mepo treatment. The spirometric response, however, was distinctly different for the two patients. FEV_1 had improved in both cases at the second research visit. At the third visit, one patient (green triangle) displayed further improvement, to the point FEV_1 was normal (>80 % predicted), but the other patient's FEV_1 declined to 57 % predicted, significantly below the value prior to commencing biologic treatment. In both patients, the measured FeNO was consistent (± 5 ppb) at all three visits, while the blood eosinophil level remained suppressed at the third visit. In terms of symptoms, one patient (yellow triangle) reported the same ACQ-5 score at the second and third visits; a clinically significant improvement from baseline. In the other patient (green triangle), the ACQ-5 increased

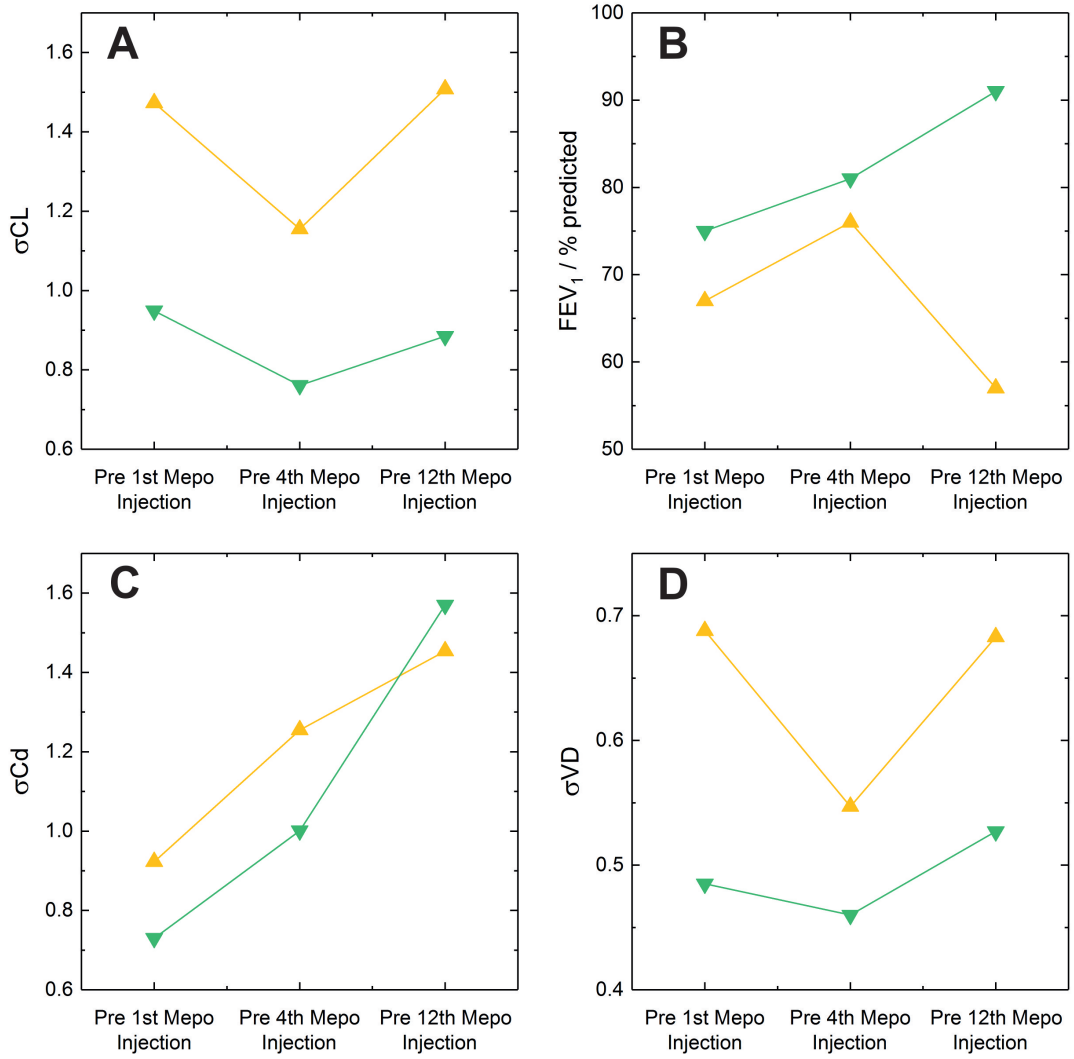


Figure 4.15: Post-bronchodilator Lognormal Lung inhomogeneity parameters and FEV_1 for two asthma patients undergoing 12 months of Mepo treatment. **A** shows determined σCL, **B** measured FEV_1 % predicted, **C** determined σCd, and **D** shows determined σVD. Data are shown for three clinical visits: prior to first Mepo injection, following 3 months of Mepo treatment, and finally following 11 months of Mepo treatment.

from the second visit, where it was zero, to 0.8 at the third visit, although this remained significantly below the baseline value of 2.6.

4.2.3 Discussion

This study was performed to assess the response of Lognormal Lung parameters to therapeutic intervention in patients with severe eosinophilic asthma. Currently, the classification of asthma treatment pathway patients as ICS responders or non-responders relies on changes in measured

FeNO and ACQ-5 symptom score in response to therapy. In the case of the single responder within this patient group blood eosinophil count was also reduced after a week of ICS, whilst spirometry remained normal. In the non-responders, however, the clinical measures were often discordant, and did not provide a clear description of therapy efficacy. The σCL parameter, describing the inhomogeneity in lung compliance, showed a clear response following a week of ICS therapy in the single responder; it was reduced by 28 %. For two non-responders, this parameter also decreased following ICS, but by a lesser fraction of baseline value. In one of these patients (purple diamond), improvements were also measured in all four of the clinical measures, although changes in FeNO and ACQ-5 symptom score were not significant enough to classify this patient as a responder. The strength of any conclusion is clearly tempered by the fact that only a single responder was studied, but the results presented in this work suggest that changes in σCL might well reflect efficacy of inhaled corticosteroid therapy.

Later in the treatment pathway, six patients were studied following a month of injected steroid treatment. Triamcinolone provides an anti-inflammatory profile that has been shown to improve symptoms and lower biomarkers of inflammation in severe eosinophilic asthma patients.[257] Indeed, in this work each of the patients responded well to this therapy; improvement from baseline was measured in at least three of the four clinical measures. Symptom improvements were reported in five of the six patients, the exception being an individual who reported no symptom variation during the pathway. The efficacy of this systematic treatment was reflected in the responses of each patient's σCL parameter, reduction during the 3 months of therapy was measured in every case. In five of six patients, the magnitude of this reduction was greater than 25 %, significantly larger than the previously measured reproducibility of this parameter.[158] Following both therapies within the asthma treatment pathway, σCL provided a response that correlated well with changes in symptoms and existing biomarkers of lung inflammation.

The capacity of the baseline Lognormal Lung parameters to predict patient responses during the treatment pathway must be considered with caution; only a single ICS responder was studied. Encouragingly, however, the baseline parameters for this individual were distinctly different from the rest of the group; both σCL and σCd parameters were abnormally elevated in each of the non-responding patients, but within the normal range for the ICS responder. Should this distinction continue to be recorded in further patients, the Lognormal Lung technique could provide a method

of stratifying severe eosinophilic asthma patients based on likely treatment response. In this way, the asthma treatment pathway could be avoided, reducing the required number of clinical visits, thus lowering the burden placed on both clinical services and patients by frequent appointments. The principal benefit to the patient of predictive indices of treatment efficacy would be faster prescription of optimal therapy.

Mepolizumab therapy selectively inhibits eosinophil production, reducing symptoms, particularly acute exacerbations, as a result.[241] This therapeutic mechanism was clearly visible within the data from patients treated with Mepo in this study; blood eosinophil count fell after three months of treatment in every case. The improvements in ACQ-5 symptom score recorded in this work in response to Mepo therapy conform with those previously reported by Ortega *et al.*.[244] These symptom improvements, however, were not necessarily reflected in the responses of FEV_1 and FeNO. The Lognormal Lung parameters changed significantly following three months of Mepo therapy, most notably σCL which was reduced in each of the six patients. In a recent study, Farah *et al.* concluded that improved symptom control following Mepo therapy was linked to improvements in small airway function, measured by parameters derived from multiple breath nitrogen washout data.[245] The changes in patient symptoms correlate better with the responses of the σCL parameter, previously suggested to reflect peripheral airway function, than FEV_1, which is known to primarily reflect large airway dysfunction. Thus, the conclusion of this study matches that of Farah *et al.*, suggesting a significant contribution to disease control from the smaller airways. That σCL has sufficient sensitivity to quantify these changes within the lung is clearly very encouraging. The recorded changes in σVD and σCd were variable from patient to patient, much like FEV_1 and FeNO, perhaps describing physiological changes that affect symptom control to a lesser extent.

It was an interesting result that in the two Mepo patients studied following 11 months of therapy, the improvements in σCL and σVD were not maintained. In both patients, pre-Mepo parameters were recovered at the final study visit. Albers *et al.* previously reported that ACQ-5 improvements and reductions in exacerbation rate were maintained over a period of up to 4.5 years of Mepo therapy.[258] In contrast, Cormier *et al.* presented two cases of severe eosinophilic asthma patients in whom a loss of response to Mepo developed following two years of treatment.[259] Despite blood eosinophil counts remaining low, recurrence of airway inflammation and symptoms were reported. Whilst the lung inhomogeneity parameter profiles were similar for the pair of patients in the study presented

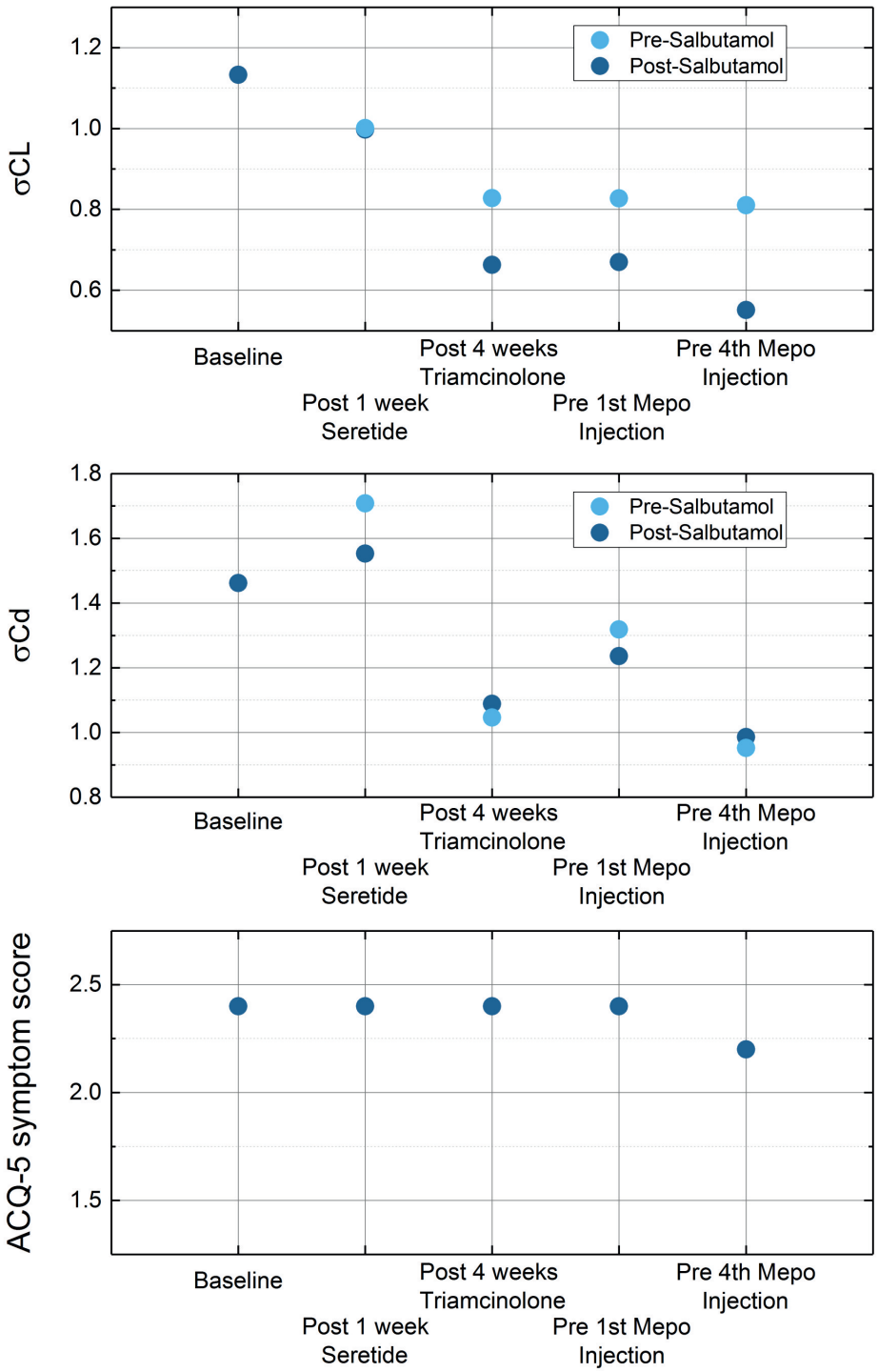


Figure 4.16: Determined σCL (upper) and σCd (middle) parameters and reported ACQ-5 symptom scores (lower) for asthma patient at five clinical visits. Data are shown for asthma treatment pathway, prior to Mepo treatment, and following three months of Mepo treatment. Pre-bronchodilator measurements are shown in lighter shade than post-bronchodilator parameters. Pre-bronchodilator measurements at baseline are not available; washout procedure was performed without correct filter type.

in this thesis, the symptom and FEV_1 profiles were not. Both patients showed improved ACQ-5 scores and spirometry following three months of therapy, but following 11 months, one displayed further improvement in FEV_1 but a clinically significant increase in the symptoms, whereas the other reported no symptom changes and FEV_1 decline to below pre-treatment levels. FeNO and blood eosinophils remained low at the final visit of both patients, suggesting that secondary inefficacy was not significant at this point. These patients will be followed longitudinally, with particular interest paid to symptom changes to evaluate whether the increased lung inhomogeneity after 11 months is indicative of poor sustained control in the future.

Two patients were studied on five different occasions as Mepo was prescribed following the treatment pathway. The determined σCL and σCd parameters, both before and after bronchodilator, are shown separately for these patients in Figures 4.16 and 4.17. In the parameters of these patients, it was common to see the lung inhomogeneity reduced following short-acting bronchodilator therapy, something described in the cross-section study earlier in this chapter. In the first patient (blue circle), both σCL and σCd reached minimum values following three months of Mepo treatment. At this clinical visit the lowest ACQ-5 score was also reported, although even at this point the difference from baseline was clinically insignificant (< 0.5). For the second patient (purple diamond), however, σCL was substantially lower following systemic steroid injection than at any other point. This finding again correlated well with ACQ-5 symptom score, which reached its minimum value following ICS and was sustained following systemic steroid therapy. The ACQ-5 symptom scores illustrate the relative efficacies of systemic steroid and Mepo treatment by directly quantifying patient symptoms. That σCL correlates well with ACQ-5 score following these therapies serves to validate both this as an index of symptom control, and σCL responses as measures of treatment efficacy.

A large difference between the two patient profiles was identified in the σCL change between the final visit of the treatment pathway and the visit prior to commencing Mepo treatment. In the first patient (blue circle) the σCL parameters are very similar at these points, whereas in the second patient (purple diamond), σCL increased to a value that is close to the baseline measurement. One explanation for this is the time between these two clinical visits. In the first case, two months passed between the conclusion of systemic steroid treatment and the commencement of biologic therapy, whereas in the second individual, this period was six months. A second proposed explanation is that at commencement of Mepo treatment the second patient may have been exacerbating. This is

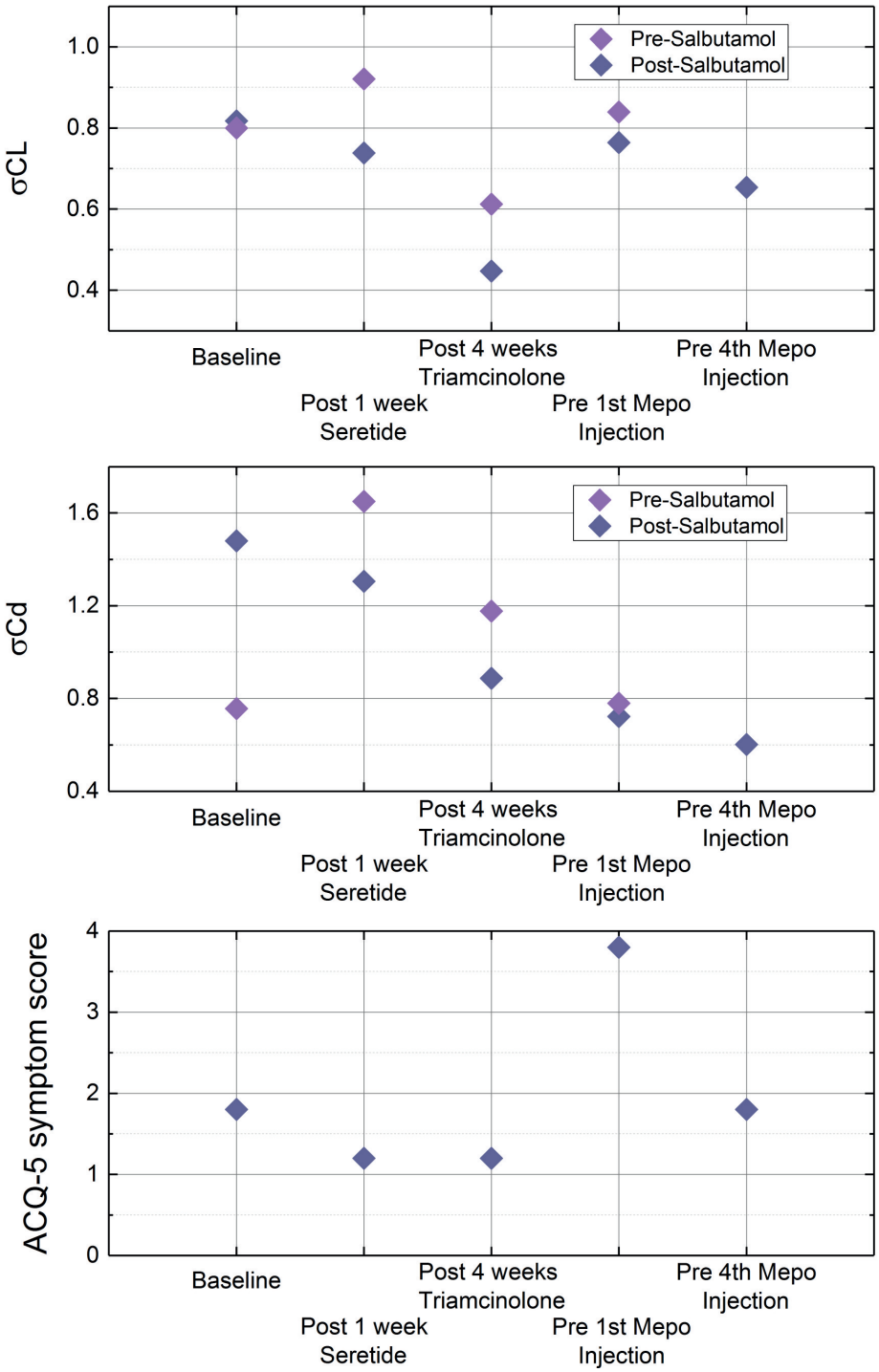


Figure 4.17: Determined σCL (upper) and σCd (middle) parameters and reported ACQ-5 symptom scores (lower) for asthma patient at five clinical visits. Data are shown for asthma treatment pathway, prior to Mepo treatment, and following three months of Mepo treatment. Pre-bronchodilator measurements are shown in lighter shade than post-bronchodilator parameters. Pre-bronchodilator measurements for the final visit are not available; significant leak present during experimental procedure.

suggested by the reported ACQ-5 score being significantly greater at this time than at baseline, and FEV_1 also having declined in this interval, from 82 to 52 % predicted.

This study explored the effects of therapy on lung inhomogeneity parameters in a reasonably niche population of asthma patients; those with severe eosinophilic disease. An alternative approach, which would be more representative of the spectrum of patients with asthma, would have been to devise a study within the setting of primary care. To recruit sufficient numbers of patients from primary care who are starting a steroid inhaler for the first time, however, would require a large multicentre study with substantial associated cost and complexity. At this stage, MFS availability also limits the feasibility of multicentre studies. Another approach could have been to investigate patients in primary care whose ICS dose is changed due to inadequate symptom control. The first stage of the treatment pathway studied here is not unlike that, however, with a high dose ICS that is chipped to confirm adherence.

One limitation of this study is the difficulty recruiting patients that are truly treatment naive. Asthma symptoms are initially treated within the setting of primary care, usually with a combination of bronchodilators and inhaled steroids. As a result of these therapies failing to control symptoms, patients are then referred to the complex airways disease clinic where this study, tied to the treatment pathway, took place. Although the first pathway visit is termed the baseline visit in this work, the underlying physiology will, to some extent, reflect the effects of hitherto prescribed therapy, rather than simply the underlying pathophysiology of disease. Thus, care must be taken when ascribing changes in clinical briomarkers and lung inhomogeneity parameters simply to the therapeutic interventions within the treatment pathway. This issue resurfaces at the start of Mepo treatment; clinical presentation and measures, and lung inhomogeniety parameters, will reflect previous therapy and the duration without systemic therapy prior to this clinical visit. Parameter responses to Mepo therapy are likely to be masked if pre-treatment measurements reflect the effects of previous systemic therapies.

This study was necessarily conducted in parallel with existing clinical care pathways. Had the study been designed as a standard clinical trial, the severe eosinophilic asthma patient group would be randomised to either follow the treatment pathway or remain on existing therapy. Without this second patient group, there were no control data with which the lung inhomogeneity parameter responses to therapy could be compared. More generally, the conclusions of this study are

limited by the absence of longitudinal within-individual Lognormal Lung parameter reproducibility data. Short-term reproducibility of these parameters has been shown to be good, both by Mountain *et al.*,[158] and in the cross-sectional study of COPD patients presented in Chapter 3 of this thesis. The long term reproducibility, however, has yet to be established.

Despite the afore mentioned limitations around the group studied, the potential of the Lognormal Lung parameters of inhomogeneity to provide indices which quantify the response of eosinophilic asthma patients to therapy has been demonstrated in this study. The responses of Lognormal Lung parameters to therapeutic intervention were compared with responses in FEV_1, FeNO, blood eosinophil count, and ACQ-5 symptom score in patients with severe eosinophilic asthma. The σCL parameter responses correlated well with patient symptoms and clinical evaluation of treatment efficacy. The Lognormal Lung method was shown to have the sensitivity to provide early-response signals in ICS, systematic steroid, and biologic treatment. There is also the potential that lung inhomogeneity parameters could provide useful predictive indices of therapy response; within this study the only patient with normal σCL and σCd parameters at baseline was found to respond to ICS therapy.

Eosinophilic asthma is characterised by elevated biomarkers of eosinophilic inflammation, notably FeNO and blood eosinophil count.[260] In another asthma endotype, non-eosinophilic (neutrophilic) asthma, however, these biomarkers are not elevated and inflammation cannot be assessed.[19] Lognormal Lung parameters, which directly reflect the physiology of the lung, could therefore provide effective indices of disease activity within non-eosinophilic asthma. Current therapeutic approaches in non-eosinophilic asthma have limited efficacy, providing poor disease control and impairing quality of life.[21] No single medication will be effective for all patients with non-eosinophilic asthma, but Lognormal Lung parameters could provide a valuable method of stratifying patients. If patients could be usefully stratified, further studies could elucidate non-eosinophilic inflammation pathways and provide routes towards targeted therapies.

4.3 Summary

This chapter has described the first two clinical studies assessing lung inhomogeneity in asthma patients using MFS technology. In the first study, a cross-sectional study of patients recruited from an complex airways disease clinic, σCL was compared with FEV_1 % predicted (FEV_1%pred) as measures of disease activity in the asthmatic lung. σCL correlated modestly with FEV_1%pred, but was found not to simply be a proxy for FEV_1%pred as the effects of the bronchodilator salbutamol on the two parameters were unrelated. Importantly, σCL was found to reflect disease control better than FEV_1. It is concluded that σCL shows promise as an objective measure of disease activity in asthma.

In the second study, a longitudinal study of asthma treatment pathway and Mepolizumab patients, significant changes in lung inhomogeneity were reported in response to therapeutic interventions. In the single patient classified as a responder to inhaled corticosteroid therapy, σCL was significantly reduced following treatment of this type, whilst the response was mixed in non-responding patients. Following injected steroid treatment, which improved clinical measures such as FeNO and ACQ-5 symptom score in this patient group, σCL was reduced to well below baseline levels in all patients. Interestingly, at baseline, normal values of σCL and σCd were determined for the single responder, whereas these parameters were abnormally elevated in all non-responding patients. Following three months of Mepo treatment, the σCL parameters were reduced in all six patients despite mixed spirometric and FeNO responses, suggesting that this index might also provide a useful measure of a patient's response to therapy. Two patients studied following 11 months of Mepo treatment displayed inhomogeneity parameters that returned to baseline levels, despite clinical biomarkers and reported symptoms showing little indication of secondary inefficacy. The patients studied in this work will be followed longitudinally to assess long-term symptom profile during Mepo treatment, elucidating whether the Lognormal Lung method can provide the early-response signal that this treatment requires. Recruitment to this study must continue to investigate whether these results hold in a greater number of patients. If so, the Lognormal Lung method would provide indices of lung physiology with the capacity to predict response to asthma therapies, allowing the implementation of targeted treatment.

Chapter 5

Development of a Non-invasive Technique for Determination of Cardiac Output

The open circuit method of determining cardiac output, $\dot{Q}$, has shown potential as a safe, non-invasive technique. Two foreign gases, present in trace concentrations ($<1\,\%$), one of which is soluble in blood, are breathed in by a patient. The exhaled concentration profiles of these gases are recorded and analysed, allowing $\dot{Q}$ to be estimated. The limitations of existing respiratory tracer gas analysers have prevented the open circuit method from being widely adopted, with issues associated with accuracy, precision, and time response. This chapter presents the development of a molecular flow sensor capable of contemporaneously measuring the fluxes of five molecular species, adding the evaluation of two tracer gases to the existing MFS device. The required sensitivity of the tracer gas measurements was deemed to be $0.5\,\%$ of maximum inhaled tracer gas concentration, providing a minimum detectable concentration target of 50 ppm. Direct laser absorption spectroscopy was utilised to evaluate concentrations of the tracer gases methane, CH_4, and acetylene, C_2H_2. The lasers were initially characterised, before the potential of each for use in a molecular flow sensor was established using short path direct absorption spectroscopy. This having been achieved, the lasers were spatially multiplexed and used within a miniature Herriott cell to allow this system to be integrated with those used in the existing 3-gas sensing device. The increased functionality of this molecular flow sensor enabled data to be collected from which $\dot{Q}$ could be estimated.

In the second half of this chapter, a computational model of methane and acetylene uptake by the body is described. The model is fit to experimental data collected during tracer gas washin

procedures, allowing evaluation of the physiological parameters cardiac output and lung volume. A proof of principle study of this method has been performed, assessing the cardiac output of eight volunteers on five consecutive days at rest and during mild exercise. Finally, the potential clinical applications of the 5-gas molecular flow sensor are discussed. A method of non-invasive cardiac output assessment that is accurate and reproducible has great clinical potential, providing diagnostic information on a range of cardiovascular diseases.

5.1 Development of 5-gas Molecular Flow Sensor

Distributed feedback (DFB) diode lasers operating within the near-IR region were used as the radiation sources to evaluate the concentrations of methane and acetylene. The spectral window used to probe each species was chosen to provide sufficient sensitivity and to avoid interference from transitions arising from other major components of breath, principally carbon dioxide and water. The targeted transitions are shown in Table 5.1.

Table 5.1: Spectroscopic data of acetylene and methane transitions from HITRAN database.[118] The rotational assignment is reported as $\Delta J(J")$ for C_2H_2 and as $(J,\kappa)' \leftarrow (J,\kappa)"$ for CH_4, where κ is the quantum nuclear spin function. The double prime (") and single prime (') symbols denote the lower and upper rotational energy states of the molecules, respectively.

Molecule	ν_0 /cm^{-1}	σ_{INT} /cm^{2}cm^{-1}	γ_{air} /cm^{-1}atm^{-1}	γ_{self} /cm^{-1}atm^{-1}	Assignment
C_2H_2	6534.36	1.211×10^{-20}	0.082	0.158	$\nu_1 + \nu_3$ P(8)
CH_4	6046.94	8.325×10^{-22}	0.064	0.078	$2\nu_3(4,F_1) \leftarrow (3,F_2)$
CH_4	6046.95	8.325×10^{-22}	0.064	0.078	$2\nu_3(4,F_2) \leftarrow (3,F_1)$
CH_4	6046.96	1.486×10^{-21}	0.064	0.078	$2\nu_3(4,A_1) \leftarrow (3,A_2)$

Direct absorption spectroscopy was initially tested using an existing MFS measurement head. To evaluate C_2H_2 detection, a 10 mW DFB diode laser (NTT Electronics, NLK1C5EAAA) operating at 1.53 μm was used to probe the P(8) transition within the $\nu_1 + \nu_3$ combination band. Another 10 mW DFB diode laser (NTT Electronics, NLK1U5EAAA), this one operating at 1.65 μm was used to probe the CH_4 absorption feature at 6047 cm^{-1} resulting from three overlapping R(3) transitions within the first overtone band of the ν_3 vibration. This feature has previously been used to quantify atmospheric methane concentrations in field conditions.[261] The pair of lasers was housed within the MFS electronics module, along with the laser chip temperature and applied current control circuits.

In order to establish the potential of this technique, these lasers were tested using an existing MFS v-path with an optical path length of 5.4 cm.

The two lasers were spatially multiplexed, allowing radiation from both to share a single optical path. A fibre coupler is required, the choice of which is made in the knowledge that multiplexing is most effective in situations where the power of each of the lasers at the detector is roughly equal without substantial power reduction. Fortunately, the 1.53 and 1.65 μm lasers have roughly equal output powers (10 mW). Fibre couplers are optimised for transmission of radiation at a given wavelength, dependent upon the core material used; radiation away from this stated wavelength will necessarily suffer reduced transmission. A 2x2 fibre coupler with a 50:50 coupling ratio, optimised for radiation at 1.55 μm (Thorlabs PN1550R5A2) was chosen to best facilitate the multiplexing of this system. A fibre optic light trap (Thorlabs FTAPC1) was coupled to the unused coupler output, reducing back reflections from the fibre termination. An InGaAs photodiode (Hamamatsu G12181-020K) was used in this work with a circular photosensitive area with a 2 mm diameter that was housed in a sealed package. The upper wavelength limit of this detector's photosensitivity was quoted as 1.9 μm, a narrower sensitivity range than that used in the v-path, a reflection of the fact that both CH_4 and C_2H_2 could be probed in the near-infrared spectral region. The detector's maximum permitted power was 10 mW. Thus, attenuation of the remaining fibre coupler output is required before the radiation is transmitted to the measurement head, ensuring that the photodiode remains comfortably within a regime with a linear response to laser intensity. The detector was initially installed in the existing MFS 5.4 cm v-path along with the collimator in the appropriate injection housing. Signal attenuation, both as a result of coupling to the measurement head and the process of multiplexing, reduces the sensitivity of the concentration determination of the gases due to a decreasing signal-to-noise ratio, but these losses are unavoidable. Once multiplexed, the lasers could be ramped sequentially, as previously described for the CO_2 and H_2O system within the 3-gas MFS. As one laser is scanned over an appropriate frequency range, the other 'stationary' laser is held at a constant current above threshold. During calibration, an 'offset amplitude spectrum' must be determined for each laser, and subtracted before any data analysis is performed.

Baseline data for the multiplexed system were recorded with pure N_2 flowing through the MFS measurement cell at 5 l min^{-1}. The procedure followed was to record photodiode offset spectra with both lasers switched off, measure the offset spectra for each laser while it is 'stationary' and finally

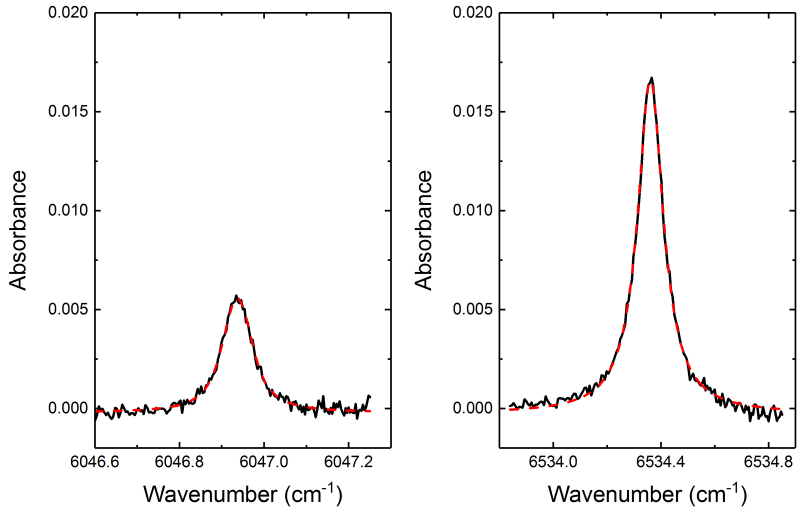


Figure 5.1: Absorption spectra for 0.3% CH_4 (left) and 0.3% C_2H_2 (right) in synthetic air. Existing v-path is used, providing an optical path length of 5.4 cm. Measured absorption spectra are shown with solid black lines and the fitted Voigt profiles with a dashed red line.

the baselines are recorded with both lasers running. Each calibration step lasts 30 sec with the final 5 sec of recorded spectra averaged to give baseline signals. Absorption spectra were then evaluated using a calibrated gas mixture (BOC Industrial Gases) of 3030 ppm CH_4 and 2760 ppm C_2H_2 in synthetic air. For these tracer gas concentrations, spectral windows of 0.65 and 1.02 cm^{-1} were deemed appropriate to probe CH_4 and C_2H_2 respectively. A time-to-wavelength calibration was achieved for each optical system using a spectral analyser (Melles Griot) with a free spectral range of 2.015 GHz. Spectra for each species were recorded at a frequency of 200 Hz, with 200 data points recorded per spectrum. Two spectra were averaged, providing a spectrum every 10 ms. The first 30 data points of each spectrum were excluded to allow the 'stationary' laser sufficient time to establish a constant 'offset amplitude' signal level. Instantaneous establishment of 'offset amplitude' signal level following ramping is prevented by the finite response time of the laser driving electronics and the transient laser chip temperature oscillation as the current across the chip is rapidly reduced.

Example spectra, each representing the average of two spectra recorded at a frequency of 200 Hz, are shown in Figure 5.1 along with best-fit Voigt profiles. The combination of the transition absorption cross sections, a short optical path length, and the relatively low concentrations of these species required for potential applications, presents absorption spectra with maximum absorption values of ca. 1 %. The absorption signal-to-noise ratio here is lower than is required in order to facilitate

measurement with adequate sensitivity. The minimum detectable concentrations calculated from these spectra using the method described in Section 2.2 are 505 and 159 ppm for CH_4 and C_2H_2 respectively. This represents a spectrometer incapable of providing the sensitivity required for the target applications.

5.1.1 Design and Implementation of Herriott Cell

Multipass optical cells provide a method of increasing the sensitivity of laser based absorption systems by increasing the optical path length through the sampled gas. In these cells, radiation is reflected a number of times, in a well defined spatial pattern, by high reflectivity mirrors. In this way, the optical path length is extended with the radiation travelling back and forth through the sample gas. Significant path lengths can be achieved in a low volume without loss of optical power, whilst systems remain both rugged and reliable, leading to the implementation of multipass optical cells in a range of portable field systems and airborne applications.[262]

A spherical Herriott multipass cell consists of two spherical concave mirrors. The light enters and exits the optical cell via strategically placed holes on the mirrors.[263] The nature of the spot pattern within a Herriott cell is dependent on a number of factors: the radius of curvature of the mirrors, the separation of the mirrors, and the angle and position of the radiation injection. When correctly aligned, the spot pattern, describing the positions of the reflections on the pair of mirrors, can be circular or elliptical. Clearly, the reflection points must not overlap with the entrance or exit holes, and interference is minimised when spot separation is kept above beam width size. The optical and mechanical stability of Herriott cell-based systems has been found to be superior to other similar multipass optical systems, such as White cells.[264]

To increase the sensitivity of the tracer gas concentration evaluation, a new measurement cell based on a Herriott cell was designed. The chosen design was based on modelled reflection spot patterns using a ray propagation model described by Tarsitano and Webster.[264] Within the model, the coordinate system of the Herriott cell is as follows: the near and far mirrors are located at z=0 and z=d, respectively. Both mirrors of the cell are centred at x=y=0 and the radius of curvature of both mirrors is R. An optical beam is injected in an off-axis direction through an injection aperture located in the near mirror. The beam's propagation within the Herriott cell can be modelled as

a paraxial ray, a small reflection angle ray tracing approximation.[265] A propagating ray can be represented as a column vector:

$$\mathbf{r} = \begin{bmatrix} x \\ Sx \\ y \\ Sy \end{bmatrix} \quad , \tag{5.1}$$

where x and y are the projected distances of the ray on the x and y axes with their corresponding slopes Sx and Sy, respectively. The transformation of $\mathbf{r}$, as a result of the ray propagating through free space or the intervention of mirror, occurs via a transfer matrix $\mathbf{T}$:

$$\mathbf{r}' = \mathbf{T}\mathbf{r} \quad . \tag{5.2}$$

Within the Herriott cell, the only transfer matrices that require consideration are the ray propagating through free space and the ray reflecting off a concave spherical mirror. The transfer matrix for a ray propagating through free space is

$$\mathbf{T}(d) = \begin{bmatrix} 1 & d & 0 & 0 \\ 0 & 1 & 0 & 0 \\ 0 & 0 & 1 & d \\ 0 & 0 & 0 & 1 \end{bmatrix} \quad . \tag{5.3}$$

The transfer matrix for a ray reflecting off a concave spherical mirror with radius of curvature R is

$$\mathbf{T}(R) = \begin{bmatrix} 1 & 0 & 0 & 0 \\ -2/R & 1 & 0 & 0 \\ 0 & 0 & 1 & 0 \\ 0 & 0 & -2/R & 1 \end{bmatrix} \quad . \tag{5.4}$$

For a single trip across a Herriott cell, the transfer matrix is obtained from the free-space propagation $\mathbf{T}(d)$ and the mirror reflection $\mathbf{T}(R)$ matrices:

$$\mathbf{T} = \mathbf{T}(R)\mathbf{T}(d) \quad . \tag{5.5}$$

By this method, the reflection position of the beam on each mirror may be modelled for a given mirror separation, radius of curvature, and beam injection position and angle. In order to produce a mirror system capable of being introduced into an existing MFS measurement head without demanding a very significant structural redesign, a series of design criteria was introduced. First, apertures to

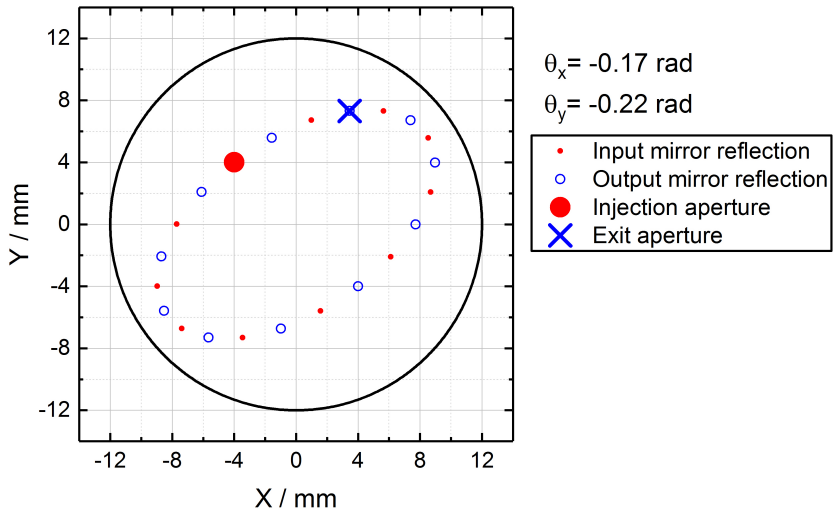


Figure 5.2: Calculated reflection spot pattern for Herriott cell designed for tracer gas concentration determination. Reflections on the input mirror are shown by red circles, with a large circle indicating the injection point. Reflections on the output mirror are shown by blue circles, with a blue cross overlaying the reflection at which the exit aperture will be positioned. Required radiation input angles are stated.

hold the spherical mirrors within the measurement head were limited to a 24 mm diameter and the mirror separation limited to values between 26 and 28 mm, to prevent a significant change in the flow-axis bore size at the Herriott cell. Secondly, the target optical path length was determined to be 60 cm; the minimum detectable concentration measured for CH_4 in the v-path was roughly ten times the target value, and thus a tenfold path length was required.

Ultimately, the Herriott cell design selected used a spherical mirror separation set to 27.61 mm, each with radius of curvature of 80 mm. Radiation was to enter the cell through an injection aperture in the first mirror, positioned at the (-4,4) mm position with an angle of θ_x of -0.17 rad and θ_y of -0.22 rad from the normal of the mirror's back surface. Radiation is then reflected between the mirror surfaces, before exiting the optical cell via an off-centre exit aperture on the second mirror. The designed optical path utilised 20 reflections, resulting in an overall path length of 56.7 cm. Radiation is ultimately detected with a photodiode placed behind the exit aperture in the second mirror. The calculated spot pattern for a Herriott cell with this design is shown in Figure 5.2. The spot pattern is contained well within the maximum mirror surface diameter of 24 mm and both injection and exit apertures are positioned away from the edges of the mirror surfaces, allowing sufficient space to incorporate the collimator and photodiode housing packages.

In order to assess the potential of the Herriott cell described above, modelling the width of a theoretical radiation beam propagating over the entire optical path was required. The series of reflections leads to successive focusing and defocusing of an optical beam, the precise profile of which might have implications for the performance of a spectroscopic system. The major assessment criterion was the requirement that radiation intensity should remain a significant distance from both the injection and exit apertures when following the elliptical optical path. Large beam widths at reflection points neighbouring the apertures have the potential to lead to signal loss and detection of radiation that has not traversed the entirety of the designed optical path.

The modelling of the beam width evolution started with the assumption that the optical beam could be modelled as a Gaussian beam. This assumption states that a beam's transverse magnetic and electric field amplitude profiles are given by the Gaussian function; also implying a Gaussian intensity profile. The properties of a Gaussian beam at a given point are characterised by a *complex beam parameter*, q, calculated by:[266]

$$\frac{1}{q} = \frac{1}{P} - \frac{i\lambda}{\pi n \omega^2} \quad , \tag{5.6}$$

where P is the radius of curvature of the beam's phase front, n is the index of refraction, λ is the wavelength of the radiation, and ω is the beam radius, defined as the radius at which the radiation intensity falls to $1/e^2$ of the axial value. To quantify the beam width evolution within the Herriott cell, the evolution of q must be considered. In order to achieve this, the paraxial ray tracing model described above is used. The evolution of q following a beam's interaction with an optical element can be quantified by:

$$q = \frac{A\,q_0 + B}{C\,q_0 + D} \quad , \tag{5.7}$$

where q_0 is the incident complex beam parameter, and A, B, C, and D are coefficients taken from the (2×2) upper left square sub-matrix of the optical element's transfer matrix, a pair of examples of which are given in Equations 5.3 and 5.4. In this way, the evolution of q within the Herriott cell can be quantified from the evolving transfer matrix as successive free-space propagation and mirror reflections are considered. The beam widths at the optical path's reflection positions are then calculated from Equation 5.6 which, if P is assumed to be infinite, can be rearranged to give:

$$\omega = \sqrt{\frac{\lambda}{-\pi \mathrm{Im}(q^{-1})}} \quad . \tag{5.8}$$

The beam width profile was modelled by this method for the Herriott cell described above, using inputs of 1.55 μm for wavelength, 27.6 mm for mirror separation, and 80 mm for mirror radii of curvature. An injected beam width of 1 mm was assumed, typical for the radiation leaving the collimators used in this work. The radius of curvature of the injected beam's phase front was assumed to be zero. The modelled beam waist profile as a function of reflection number, shown in Figure 5.3, is encouraging for two reasons: firstly, the beam is well focused at the exit aperture, increasing the tolerance of the modelled aperture position, and secondly, the maximum beam waist is only a little greater than 1 mm so reflections shouldn't overlap either with one another or, crucially, the mirror apertures.

The ray-tracing and beam width modelling used in the design of this Herriott cell relies on the paraxial approximation.[265] This assumption holds for mirrors with large radii of curvature, but becomes less appropriate when the radius of curvature is comparable to the mirror separation (as is used in this design). The consequences of this were hard to predict, but slight deviation from the modelled optimal mirror separation was expected, along with small deviations from the modelled beam widths at points in the elliptical optical path.

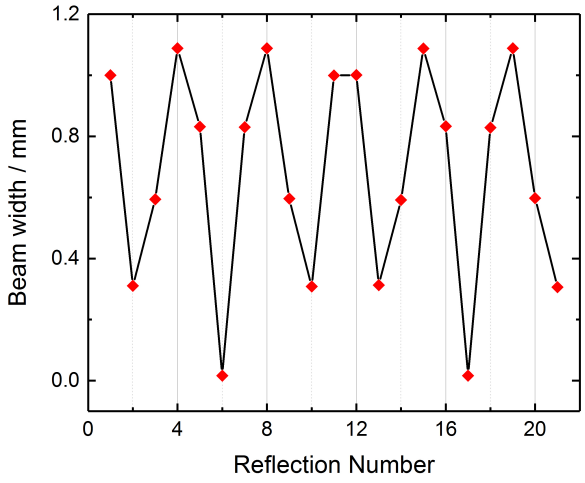


Figure 5.3: Modelled optical beam width profile within Herriott cell. The beam is sequentially focussed and defocussed before it is ultimately focussed onto the photodiode at the exit aperture (21st reflection).

The advantage of the Herriott cell designed above, beyond the extended optical path length, is the potential to facilitate additional gas sensing channels within this pair of spherical mirrors. Crucially for the target application in this work, there is sufficient space at the centre of the injection mirror to allow the inclusion of an optical v-path similar to that in the existing MFS, with both injection and exit apertures on the extended path's input mirror. This has the potential to facilitate sensitive measurement of CH_4, C_2H_2, CO_2, and H_2O concentrations within an MFS without negatively affecting the sensitivity of the device or increasing the deadspace of the device. In addition to the v-path, there is also sufficient space to introduce a second extended optical path length. A counter propagating elliptical optical path could be added, with injection and exit apertures on the same mirror faces as the first extended path. This could be achieved without bringing any of the reflections on either mirror into close proximity with injection or exit apertures. In the future, the second extended path length could be utilised to provide additional functionality, for example by including a carbon monoxide, CO, sensing channel. CO displays overtone transitions within the near-IR region with absorption cross sections that are comparable to those probed for CH_4 in this work and has previously been utilised in trace concentrations (up to 0.3%) in order to evaluate the *lung diffusing capacity*, a physiological parameter assessing an individual's capacity for gas exchange between the alveoli and pulmonary blood.[267,268]

Mirrors with the specified diameter, radius of curvature, and aperture positions and angles were manufactured (LBP Optics). Each of these specifications was required with relatively close tolerances, ± 0.1 mm for distances and $\pm 0.2^\circ$ for angles, preventing issues resulting from poor alignment such as radiation prematurely clipping the exit aperture or missing the exit aperture after the 21 passes. The mirrors comprised of nickel plated aluminium blanks. The nickel offers an easily polished, chemically inert substrate to protect the aluminium, which reacts with the atmosphere and thus degrades over time. The mirror surfaces were gold coated in a thin layer, approximately 1 micron thick, applied by electroplating. Gold provides a further chemically inert substrate, with high reflectivity across the range of near-infrared wavelengths.[269] It was preferred to silver, which has comparable reflectivity, because gold will not tarnish and so will maintain a high reflectivity for longer. The gold surface was untreated, meaning that polishing and cleaning is difficult owing to the material's mechanically delicate nature; care to limit any surface deposition during handling was essential.

The mirrors were housed in an adapted MFS measurement head, with mirror separation adjustment achieved using a series of plastic shims with widths between 50 and 150 μm. The optical paths followed by the pair of extended paths were strongly dependent on the mirror separation and the relative angular mirror orientation of the two mirrors. In order to ensure optimal mirror separation, a visible laser operating at 637 nm (Thorlabs, S1FC637) was utilised for alignment. The radiation entered the cell via a collimator at either of the injection apertures in the top mirror and could be clearly observed leaving the Herriott cell after the correct number of reflections via the correct exit aperture. To test the cell's performance, the position and angular orientation of the lower spherical mirror was fixed by clamping the mirror's rear surface. For non-optimal mirror separations, different angular orientations of the top mirror were required in order for radiation from the two extended optical paths to reach their respective exit apertures. The extent of rotation of the top mirror that was required to move from one path exiting efficiently to the other reduced as the mirror separation trended towards an optimal value. Ultimately, at the optimal mirror separation, radiation from both extended paths reached the exit apertures without any rotation of the top mirror. At this point, the angular orientation of the top mirror was also fixed by clamping the rear surface. The optical path followed by the v-path was independent of the relative orientations of the mirrors, as both injection and exit apertures were in the top mirror, but was dependent on mirror separation. The success of the Herriott cell's design was illustrated by the fact that the optimal separation for the extended optical paths also served as an optimal value for the v-path; the radiation exited the cell via the centre of the exit aperture.

Utilisation of the Herriott cell system is demonstrated by example spectra shown in Figure 5.4. These spectra were recorded whilst the 3030 ppm CH_4, 2760 ppm C_2H_2 in synthetic air calibrated mixture flowed through the measurement head housing the Herriott cell. As with previous system testing, spectra for each species were recorded at a frequency of 200 Hz, with 170 data points reported per spectrum. Two spectra were averaged, providing a spectrum every 10 ms. The improved absorption signal-to-noise ratio reflects the significant absorption increase that results from the extended optical path length, but also the fact that the principal sources of noise within this system are the photodetector and electronics utilised in signal acquisition. The noise within the system is thus virtually unchanged by the path length increase. The spectra represent an improvement in the minimum detectable concentrations, to 48 ppm for CH_4 and 15 ppm for C_2H_2. A spectrometer

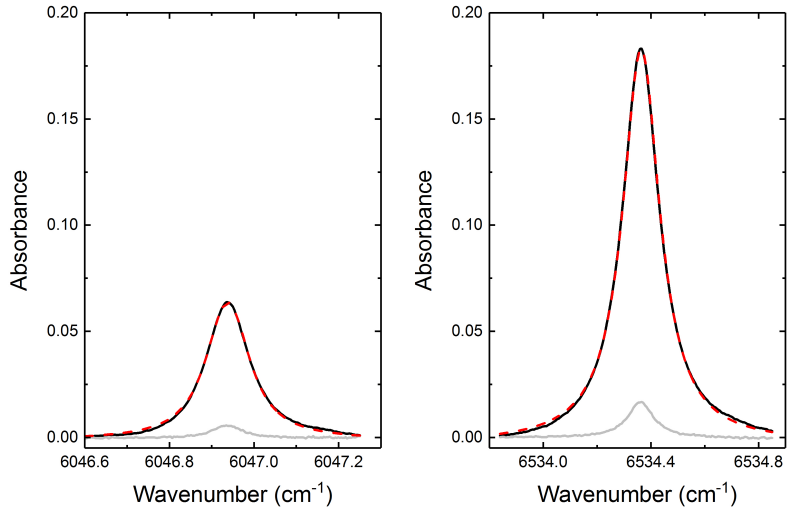


Figure 5.4: Absorption spectra for 3030 ppm CH_4 (left) and 2760 ppm C_2H_2 (right) in synthetic air. Spectra are obtained using the Herriott cell, providing an optical path length of 56.7 cm. Measured absorption spectra are shown with solid black lines and the fitted Voigt profiles with dashed red lines. For comparison, absorption spectra taken under the same conditions using a 5.4 cm optical path length are shown in grey.

capable of evaluating CH_4 and C_2H_2 concentrations at this level of sensitivity at a measurement frequency equal to that of the 3-gas MFS represented a milestone in terms of the completion of benchtop testing and development of this device.

5.1.2 Integration into 5-gas Analyser

The development of a miniaturised Herriott cell presented an opportunity to integrate spectroscopic evaluation of trace amounts of CH_4 and C_2H_2 into an MFS without disrupting the function of the existing sensors and spectroscopic systems. An optical v-path was integrated into the spherical mirrors, with both collimator and photodiode packages on the upper mirror, allowing CO_2 and H_2O concentrations to be evaluated with a similar path length, and thus sensitivity, as in the previous version of the MFS. A schematic of the mirror system within the measurement cell is shown in Figure 5.5. This system allowed significant extension of the optical path of radiation probing the tracer gas concentrations whilst maintaining the MFS's capacity to evaluate CO_2 and H_2O concentrations; the v-path is essentially unaltered. Measurement of gas sample and measurement cell temperatures, barometric pressure and gas flow, along with the determination of O_2 concentration could be facilitated in an unaltered fashion.

In the integrated 5-gas sensing device, the 1.53 and 1.65 μm lasers, accompanying fibre optic

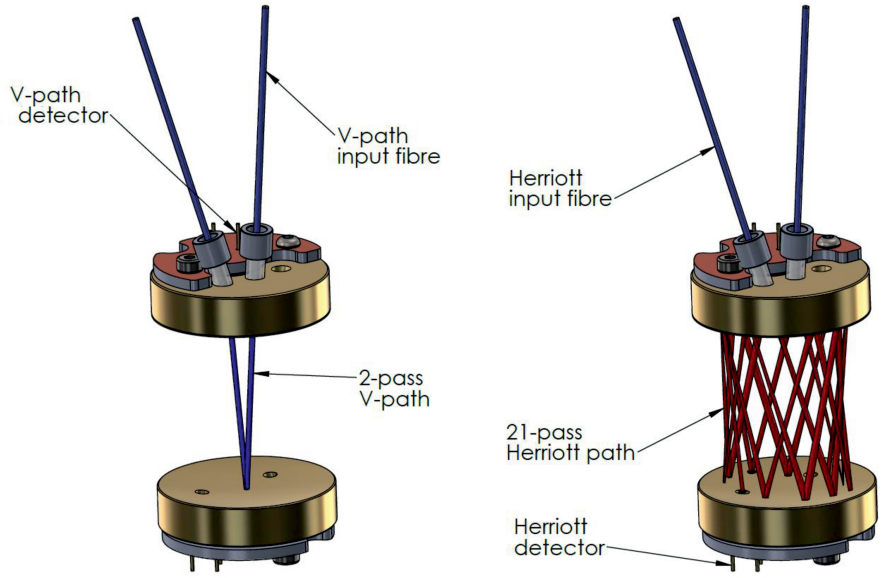


Figure 5.5: Schematic of Herriott cell system within the 5-gas analyser. The optical system of the multiplexed radiation for probing CO_2 and H_2O is shown on the left. Light is injected by a collimator, follows a simple v-path, and is detected by the photodiode labelled 'v-path detector.' The spatially multiplexed radiation for probing CH_4 and C_2H_2 is injected into the cell via a collimator, follows the 21-pass optical path shown in the right-hand figure, and is then detected by the photodiode labelled 'Herriott detector.'

components, and controlling electronics were housed within the electronics module, along with the similar set-up used for the 2.00 and 1.37 μm lasers. The laser used to probe O_2 is controlled from the electronics module but housed within the measurement head. The alignment protocol of the off-axis CEAS system was unchanged; evaluated and optimised by considering the imaged output of the mode field and nature of the cavity's detected signal. A pair of optical fibres sharing a hybrid cable (SMPTE connector, LEMO) were used to couple the multiplexed radiation for the v-path and extended Herriott cell optical path from the electronics module to the measurement head. The electrical signals from each of the three photodiodes, along with thermocouple, pressure, and flow sensor signals were returned to the electronics module via a lead carrying 24 paired coaxial electrical signals.

The analysis software to determine gas concentrations in real time from experimentally recorded transmission spectra was updated to include evaluation of CH_4 and C_2H_2. The nature of the analysis follows that previously described for CO_2 and H_2O, these species also probed via direct

laser absorption spectroscopy by two spatially multiplexed lasers. The calibration procedure was virtually unchanged with the incorporation of the additional optical path; photodiode offset spectra, offset spectra due to multiplexing, and baselines in the absence of target gas were recorded with pure N_2 gas flow through the measurement head before pure O_2 is flowed to allow the mirror reflectivity of the O_2 cavity to be evaluated. As previously, the duration of each calibration step was 30 sec, with spectra from the final 5 sec averaged to evaluate baseline signals.

An issue of optical crosstalk between the optical paths sharing the spherical mirrors was identified. Despite the modelled spot pattern for the Herriott cell showing a good separation between the reflection points and the v-path exit aperture, a significant level of signal from the 1.53 and 1.65 μm lasers was detected on the v-path photodetector. A photodiode with a broad spectral sensitivity is required for the v-path owing to the large wavelength variation in the radiation used to determine CO_2 and H_2O concentrations, probed at 2.00 and 1.37 μm respectively. The sensitivity to radiation from lasers used to evaluate CH_4 and C_2H_2 is thus essentially unavoidable. A similar, and perhaps more surprising issue, given that only a single reflection is used, arose as optical crosstalk from the 1.37 μm radiation was detected on the photodetector of the extended path. The 2.00 μm radiation which follows the same optical path did not contribute to optical crosstalk; the extended path photodiode is insensitive to radiation at this longer wavelength. In order to overcome this issue, the following solution was used. An additional optical attenuator was used to reduce the output radiation power in the v-path. This represented a compromise: reducing the power decreases the signal-to-noise ratio of the v-path measurement, but also reduces the optical crosstalk detected on the photodiode of the extended optical path to a point at which it could be considered negligible. In this way, the issue of optical crosstalk was limited to the signal detected by the v-path photodiode due to the CH_4 and C_2H_2 spectroscopic systems. This phenomenon was corrected for within the data processing by assuming that the 1.53 and 1.65 μm radiation intensity detected by the v-path photodiode was proportional to that detected by the extended path photodiode. Thus, a correction could be applied in the following way:

$$I_{vpath} = I_{measured} - (B_{Herriott \rightarrow vpath} \times I_{Herriott}) \quad , \tag{5.9}$$

where $I_{measured}$ is the signal detected by the v-path photodiode, $I_{Herriott}$ is the signal detected by the extended path photodiode, B is the optical crosstalk coefficient, and I_{vpath} is the corrected

v-path signal to be used in gas concentration evaluation analysis. The optical crosstalk coefficient is evaluated from contemporaneously recorded spectra from both photodiodes with only the extended path length lasers running. The v-path signal is normalised by the extended path signal and the datapoint-by-datapoint values are averaged in order to quantify the necessary crosstalk correction. In practice, two different optical crosstalk coefficients are used, describing the crosstalk due to the 1.53 and 1.65 μm radiation respectively. These parameters are similar, with small variation due to the low relative detector sensitivities differences over this reasonably narrow spectral window.

The capability of the integrated device to contemporaneously evaluate the concentrations of 5 gases in real-time at a frequency of 100 Hz is shown in Figure 5.6. The gas mixture flowing through the measurement head is swapped between pure N_2 and a mixture containing 3030 ppm CH_4 and 2760 ppm C_2H_2 in a balance of synthetic air approximately every 10 sec. Concentration data are measured contemporaneously at a frequency of 100 Hz.

In order to continue to make accurate measurements of flow using the pneumotachograph system, parameterisation of gas density and viscosity for the additional tracer gases was required. These data are shown in Table 5.2. The calibration of the gas flow measurement system remained unchanged from that described in Section 2.3.4. The calibration, performed in air, would hold for all gas mixtures if component density and viscosity were correctly parameterised.

Table 5.2: Density and viscosity data for CH_4 and C_2H_2. Density data are taken from [147], and viscosity data, including Sutherland constants, are from [148].

Gas Species	Density / kg m^{-3}	Viscosity / μPa s	Sutherland Constant / K
CH_4	0.717	10.25	175.84
C_2H_2	1.170	9.36	285.89

To evaluate the capacity of the integrated 5-gas analyser to record human respiratory profiles, a 12 min test was performed, with a volunteer breathing through the measurement head with nose occluded. Following 4 min of air-breathing, the inspiratory gas was changed to a mixture nominally containing 9000 ppm CH_4 and 3000 ppm C_2H_2 in a balance of synthetic air. This mixture was chosen to ensure similar maximum absorptions for the tracer gases, with the integrated absorption cross section roughly three times greater for C_2H_2. This mixture was breathed as the inspiratory gas for a

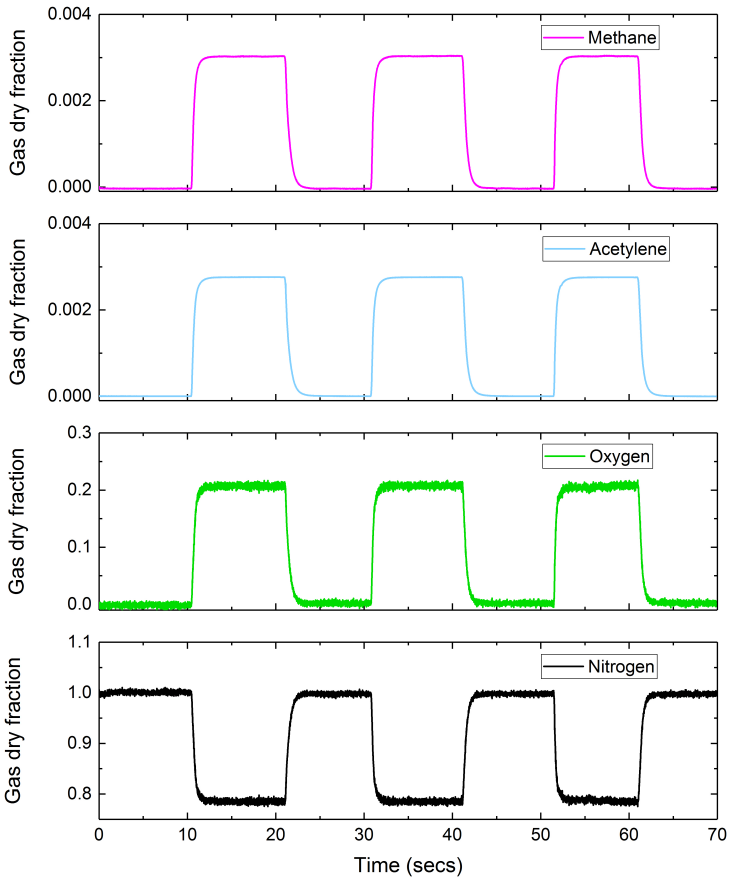


Figure 5.6: Gas fraction profiles for CH_4 (upper), C_2H_2 (second), O_2 (third), and N_2 (lower). Gas flow input to 5-gas molecular flow sensor was swapped between pure N_2 and a mixture containing 3030 ppm CH_4 and 2760 ppm C_2H_2 in a balance of synthetic air. Contemporaneously determined concentrations for CO_2 and H_2O are not shown; the nominal concentrations of these species is zero in both gas mixture.

further 4 min, before air-breathing returned for the final 4 min. Data collected during this procedure is shown in Figure 5.7. During the washin phase, the expiratory gas fraction trends towards that of the inspired gas mixture more rapidly for CH_4 than C_2H_2; C_2H_2 is ca. 20 times more soluble, ensuring that a large fraction is taken up by the blood. During the washout phase, a similar result is observed with the expiratory gas fraction of CH_4 dropping quickly, whilst C_2H_2 continues to be removed from the body with a far greater time constant. The tracer gas cumulative volume profiles demonstrate the volumes of CH_4 and C_2H_2 remaining in the body following the 4 min washout period, 2.6 and 12.6 ml respectively. Throughout the 12 min procedure the trends in the cumulative volumes of O_2, CO_2, and N_2 remain consistent. The absence of trend in the N_2 profile is particularly significant, returning a N_2 balance of -7.6 ml min^{-1} from the first to last breath of this procedure,

well within the specification of the molecular flow sensors. This illustrated the success of the flow measurement system, both in terms of calibration in air and the capacity to maintain accurate flow measurement when tracer gases are present. The test described above illustrates the quality of the data obtainable using the integrated 5-gas analyser and the data demonstrate the readiness of this device for experiments involving human volunteers.

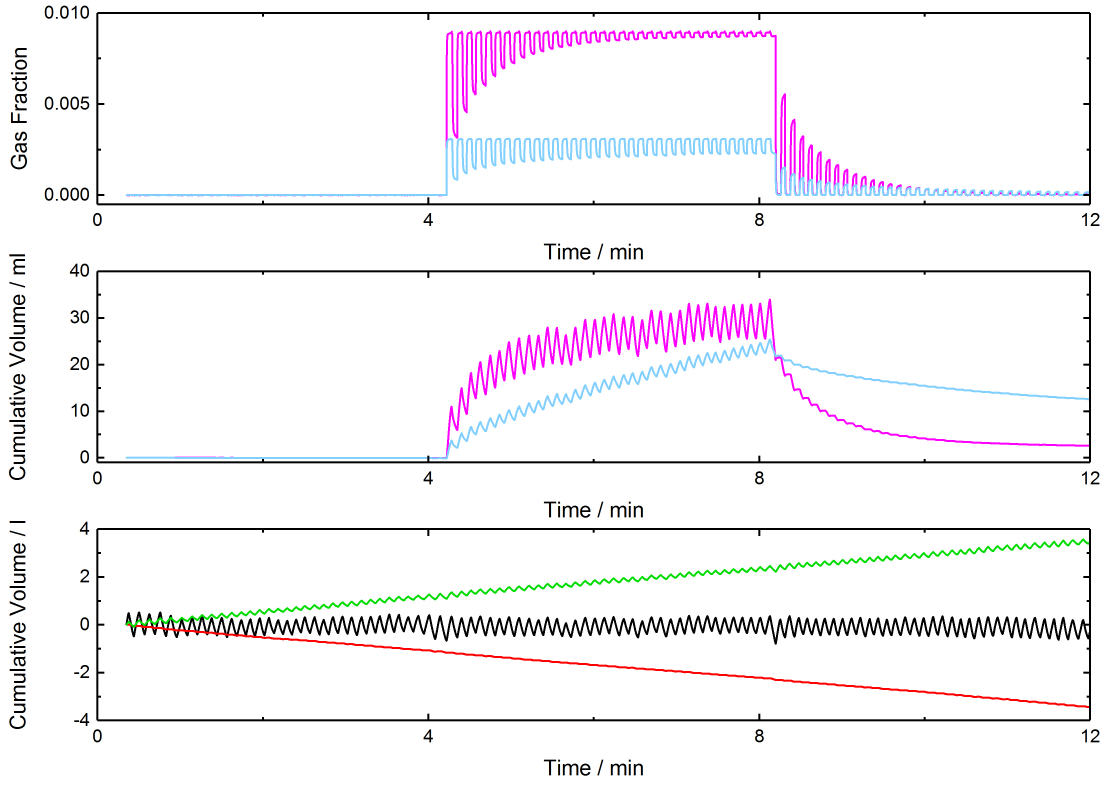


Figure 5.7: Data collected during 4 min tracer gas washin and subsequent 4 min washout. The gas fraction data for CH_4 (magenta) and C_2H_2 (blue) are shown in the upper plot, with the middle plot showing the cumulative volume profiles for these two species. The cumulative volume profiles for O_2 (green), N_2 (black), and CO_2 (red) are shown on the lower plot.

5.2 Determination of Cardiac Output

There is a long history of attempts to measure cardiac output using non-invasive techniques. A summary of these methods is presented earlier in this thesis in Section 1.5. The accuracy, precision and time response of existing respiratory tracer gas analysers have to this point limited the clinical applicability of the rebreathing and open circuit methods of assessing cardiac output, $\dot{Q}$. The clinical potential of the highly accurate contemporaneously measured gas compositions and respiratory

flows relies on the computational model used to interpret the recorded data. Ultimately, a holistic mechanistic model of the cardiopulmonary and respiratory systems, written to evaluate both cardiac output and parameters of lung function, would be required. Development of this model, integrating a sophisticated blood circulatory model into the existing Lognormal Lung model, represents a significant undertaking. In this first instance, a simpler model was written, allowing evaluation of cardiac output without consideration of lung inhomogeneity or recirculation of blood.

5.2.1 Cardiac Output Modelling

A model of methane and acetylene uptake in the body was written in order to determine cardiac output, $\dot{Q}$, from data collected by the 5-gas analyser. Tracer gas uptake is assumed to occur by three mechanisms: equilibration with the gas in the lung (tracer gas volume remaining in the lung at the end of each breath is equal to the product of the lung volume and end-tidal tracer gas fraction), uptake into the lung tissue (volume equal to the product of the lung tissue volume, end-tidal tracer gas fraction, and solubility of the tracer gas), and uptake by the blood (volume of which in each breath is given by the product of gas solubility, $\dot{Q}$, alveolar pressure of the tracer gas, and the duration of the breath). Thus, the basis of the uptake modelling is the following equation:

$$\dot{V}_E^g(i) = Vol\, F_E^g(i) + V_{tiss}\, \beta^g\, F_E^g(i) + \dot{Q}\, \beta^g \sum_i P_A^g(i)\, \{t_E(i) - t_E(i-1)\} \quad , \tag{5.10}$$

where $\dot{V}_E^g(i)$ is the cumulative uptake volume of gas g at the end of expiration of breath i, Vol is the lung's gas volume at functional residual capacity (FRC), $F_E^g(i)$ is the end-tidal gas fraction of gas g for breath i, V_{tiss} is the lung's tissue volume, β^g is the solubility of gas g, $P_A^g(i)$ is the alveolar pressure of gas g of breath i, and $t_E(i)$ time of the end-tidal point of breath i.

In order to try and maintain consistent lung volumes, for both gas and tissue, Equation 5.10 is evaluated when the lungs are at FRC. A participant breathing spontaneously will, by definition, reach an end expiratory lung volume of FRC. There is, however, significant breath-to-breath variation in this quantity, making it hard to identify a consistent volume at which the lungs are at FRC. To estimate where FRC is on the tidal volume record, a cubic smoothing spline is fitted to the local minima of the tidal volume record using the MATLAB function `csaps`. This function has a single adjustable parameter that sets the degree of smoothing. The value of this parameter used in all cases was 10^{-5}, with zero representing a straight line and unity a spline going through every point.

In order to identify the data indices when the lung is at FRC, the fitted spline is shifted upwards by a value that is equal to one standard deviation of the differences between the minima of the tidal volume record and the fitted spline at these points. The FRC indices are then identified as the times at which the shifted spline crosses the tidal volume record during expiration (descending volume). Associated end-inspiratory points are identified as the maxima of the tidal volume record. Figure 5.8 shows an example of the spline fitting to the end-tidal points of the tidal volume record, identification of the points at which the shifted spline crosses the tidal volume record, and the identified FRC and end-inspiratory indices.

The gas fractions are directly measured by the 5-gas analyser, and the uptake volumes calculated as the cumulative integral of the product of the measured flow and gas fractions. The alveolar pressure of gas g for breath i, $P_A^g(i)$, cannot be measured directly and so an average pressure during the breath is estimated using:

$$P_A^g(i) = k\left[\left\{t_{ins}(i)\left(\frac{F_E^g(i-1)+F_E^g(i)}{2}\right)+t_{ex}(i)F_E^g(i)\right\}\frac{1}{t_{breath}(i)}\right] \quad , \tag{5.11}$$

where $t_{ins}(i)$ is the inspiratory time period of breath i, defined as $t_I(i) - t_E(i-1)$, $t_{ex}(i)$ is the expiratory time period of breath i, defined as $t_E(i) - t_I(i)$, and $t_{breath}(i)$ is the time period of breath i, defined as $t_E(i) - t_E(i-1)$. k is a constant conversion factor from a dry gas fraction to a pressure in units of atm under body temperature and pressure saturated (BTPS) conditions.

The solubility constant, β^g, presented in Equation 5.10 is a *Bunsen coefficient*, with units of 'volume of gas at STPD per volume of fluid measured at atmospheric pressure and body temperature'.[270] Literature values for methane and acetylene Bunsen coefficients in blood display significant variation, with a range of determined values presented in Table 5.3. The greater number of studies seeking to determine the acetylene solubility in human blood reflects the long standing use of this gas within physiological experiments. The Bunsen coefficients for methane, β^{CH_4}, and acetylene, $\beta^{C_2H_2}$, in blood used in this work are taken from Wagner.[271] This publication quotes determined solubility constants for these gases in whole human blood and in a 5% dextrose solution. The measurements in dextrose solution are found to show little difference from the well-established values of gas solubility in pure water, presented in Wilhelm *et al.*.[272]

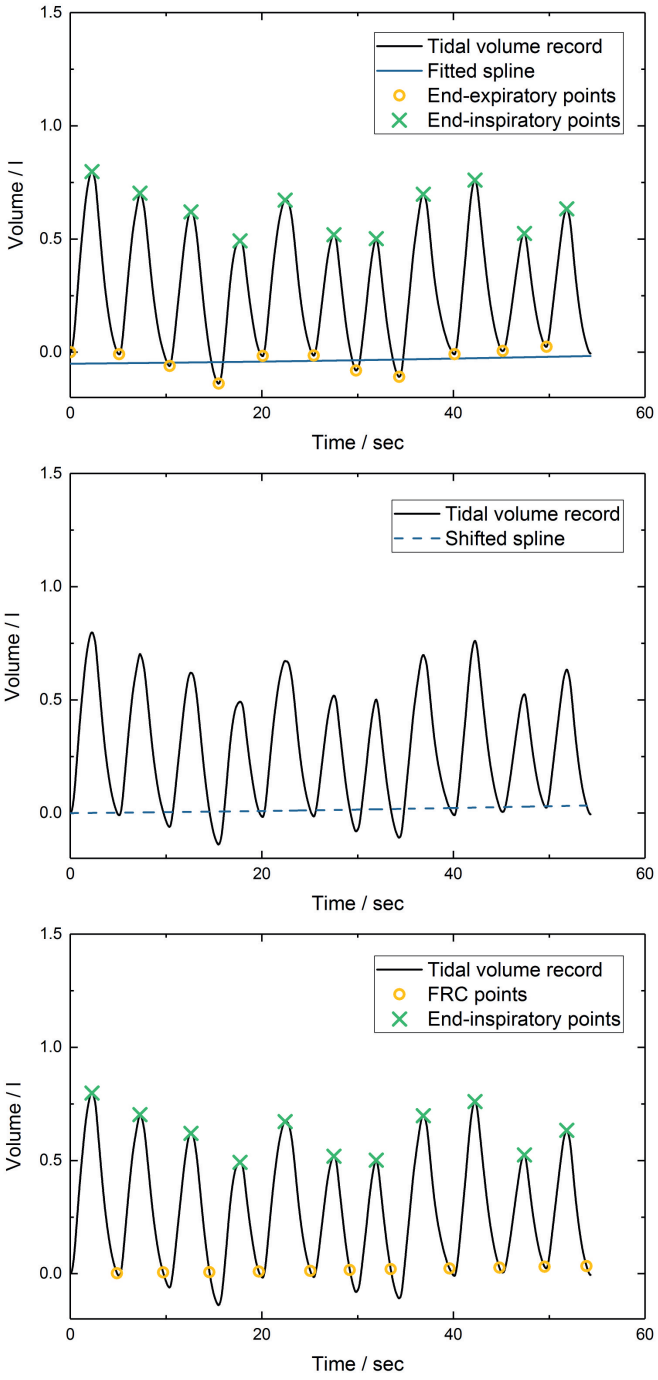


Figure 5.8: Identification of FRC points within tracer gas washin procedure. Upper plot shows tidal volume record for first 10 breaths of the washin period. Maxima and minima in this record are shown as end-inspiratory and end-expiratory points respectively. The cubic spline fitted to the end-expiratory points is shown. Middle plot shows tidal volume plot with spline shifted up by one standard deviation of the end-expiratory residuals. Points where these profiles intersect during expiration are identified as FRC points. Lower plot shows the tidal volume record with identified FRC and end-inspiratory points to be used in modelling of tracer gas uptake.

Table 5.3: Variation in methane and acetylene Bunsen Coefficients in blood from literature.

Gas	Bunsen Coefficient /ml gas (ml blood)$^{-1}$ atm^{-1}	Blood Type	Reference
CH_4	0.036	human	Wagner *et al.*[271]
	0.033	rabbit	Ohta *et al.*[273]
	0.026	dog	Meyer *et al.*[274]
	0.039	dog	Wagner *et al.*[271]
	0.032	rat	Levitt *et al.*[275]
C_2H_2	0.783	human	Wagner *et al.*[271]
	0.749	human	Priestley *et al.*[276]
	0.740	human	Grollman[277]
	0.766	human	Meyer *et al.*[278]
	0.872	dog	Wagner *et al.*[271]
	0.705	dog	Chapman *et al.*[279]
	0.739	ox	Priestley *et al.*[276]

A number of assumptions are present within this model of tracer gas uptake. The first to note is that $\dot{Q}$ and Vol are assumed to be constants over the range of breaths used for analysis. Second, the lung gas volume Vol is assumed to be equivalent for CH_4 and C_2H_2 where in reality there may be deviations owing to the different solubilities in lung parenchyma and variations in the distributions of the two tracer gases within the lung. Third, the tracer gas solubilities in lung tissue volume are assumed to be the same as those used for blood.

Associated with the assumption that Vol is constant from breath to breath is the fact that the model assumes a homogeneous lung. The Vol parameter determined from this modelling is, in reality, an estimation of the lung volume into which the inspired tracer gas mixture is well mixed. In a lung with inhomogeneous ventilation, peripheral lung units may require multiple breaths before good mixing with the inspired tracer gas mixture is achieved. Inhomogeneity inherent within the lungs provides deviation from two further modelling assumptions. The first is that the calculated parameter $P_A^g(i)$ represents an effective mean alveolar pressure for the period of the ith breath, and the second is that measured end-tidal fraction $F_E^g(i)$ represents an effective end expiratory fraction within the lung.

The model makes no consideration of the recirculation of tracer gases from the blood. Both tracer gases are non-physiological gases and as such the blood concentrations are assumed to be

zero before inspiration of a tracer gas mixture. During the tracer gas breathing period C_2H_2, and to a lesser extent CH_4, will be taken up by the blood. Following a circulation period, about 30 seconds, during which the blood passes from lungs to heart to body, back to the heart and out to the lungs, mixed venous blood containing tracer gas will return to the lungs. The recirculation of tracer gas-laden blood reduces the uptake of further gas from the lungs into the blood, and thus from the perspective of this model which does not take this into account, an associated reduction in estimated $\dot{Q}$ would be predicted.

5.2.2 Experimental Procedure

The experimental procedure adopted was a tracer gas washin. Data were collected by the 5-gas analyser for 4 min of air breathing, followed by 4 min of tracer gas washin. An open circuit method was used, with a flow pass system providing inspiratory gas supply, which is changed from compressed air to a 0.9% CH_4, 0.3% C_2H_2, and 21% O_2 with a balance of N_2 mixture for the tracer gas washin period. The benefits of open circuit experimental techniques centre around the fact that breathing can remain spontaneous, ensuring the participants can breathe with tidal volumes and respiratory rates dictated by comfort. Figure 5.9 shows a example dataset collected during this experimental procedure.

5.2.3 Model Fitting Methods

To determine cardiac output values from the collected datasets, the tracer gas uptake model can be solved in a series of ways. The first method uses multiple linear regression. For a series of n breaths, a series of $2n$ gas uptake expressions will be formed. The three variables, $\dot{Q}$, Vol and V_{tiss} can then be evaluated using the MATLAB function `regress`. The parameters determined by this method were neither as reliable nor as reproducible as hoped.

If the Equation 5.10 is limited to only two variables, either by further simplifying the model by setting the lung tissue volume equal to zero or by assuming that $V_{tiss} = X \times Vol$, where X is a constant tissue volume multiplier, then the model can be solved as a series of simultaneous equations. For each breath, a pair of tracer gas uptake expressions are generated, one for CH_4, the other for C_2H_2, allowing breath-by-breath values of $\dot{Q}$ and Vol to be calculated. These breath-by-breath values can be averaged over the range of analysed breaths to give final parameter values.

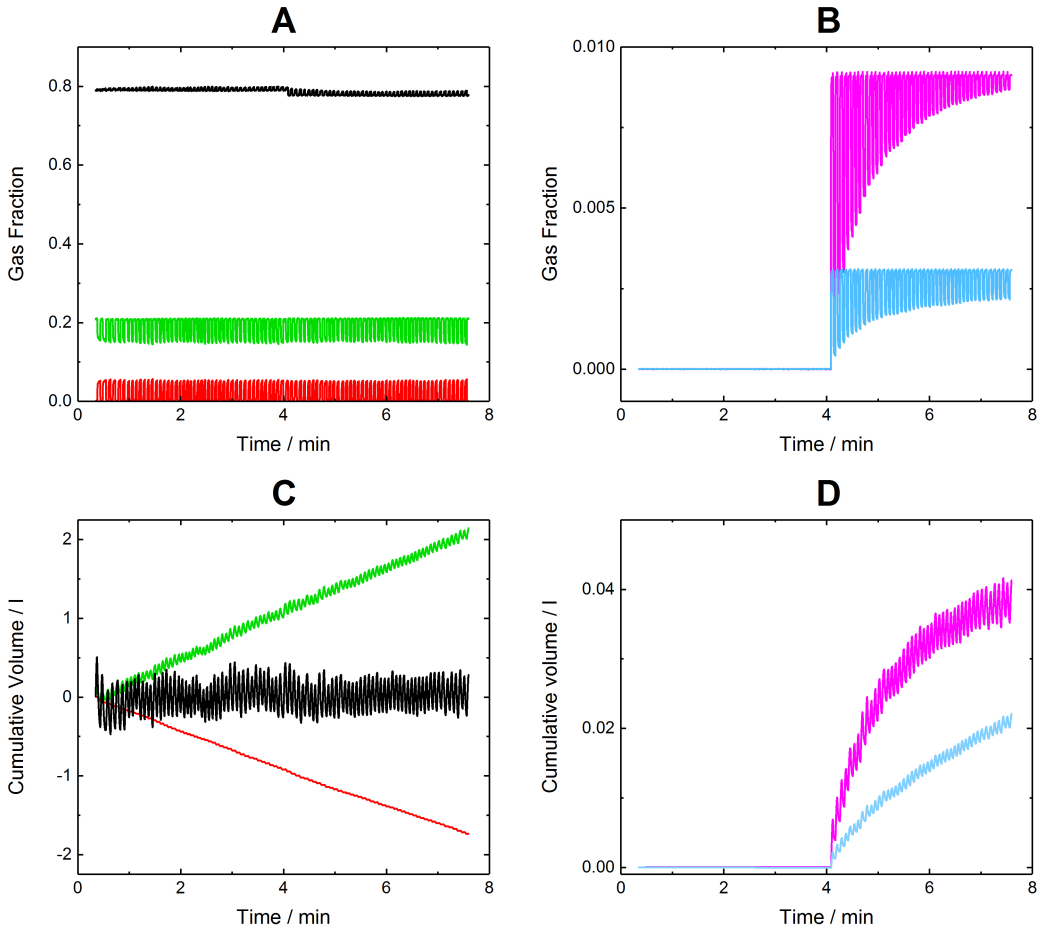


Figure 5.9: Gas fraction and cumulative uptake volume profiles for an example tracer gas washin procedure. Procedure consists of 4 minutes of air-breathing followed by 4 minutes of breathing with tracer gas mixture as inspiratory gas. **A** and **B** show dry gas fractions during procedure and **C** and **D** show cumulative uptake volume profiles. O_2 is shown in green, N_2 in black, CO_2 in red, CH_4 in magneta, and C_2H_2 in blue.

The model solution method ultimately adopted was to reduce the number of variables within the multiple linear regression to two. This was achieved by reintroducing the constant tissue volume multiplier, X. Determined $\dot{Q}$ and Vol parameters were found to be relatively independent of the breath ranges used for analysis. Tracer gas uptake expressions for the 3rd to 10th breaths of the tracer gas washin were used within this analysis. The first two breaths are excluded due to the significant effects of ventilation inhomogeneity within the lung in these early breaths; lung inhomogeneity isn't considered within the model. Data from breaths beyond the 10th were excluded to avoid the estimation utilising data in which the recirculation of the tracer gases into the lungs would contribute

significantly.

Figure 5.10 shows a typical dataset utilised as an input to the cardiac output evaluation model, consisting of data from the first 10 breaths of the tracer gas washin. The breath-by-breath gas fraction, cumulative uptake volume and alveolar pressure values at times at which FRC is reached, are illustrated. These values are directly used within the cardiac output model, Equation 5.10, providing the information content from which the lung volume and cardiac output are determined.

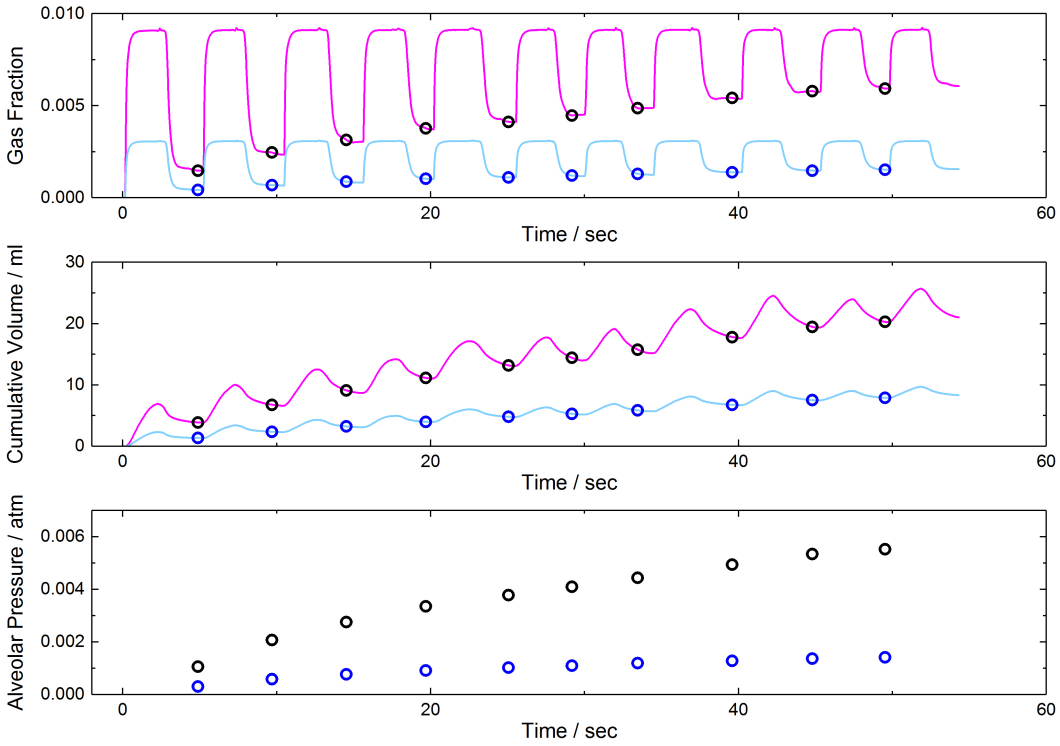


Figure 5.10: Input dataset for the cardiac output evaluation model. The upper plot shows the gas fraction profiles for the first 10 breaths of the tracer gas washin, the middle plot shows the cumulative volume profiles for the same period. The lower plot shows the estimated breath-by-breath alveolar pressures. In each plot, CH_4 is shown in magneta and C_2H_2 in blue, with values at estimated FRC points shown with open circles in black and blue respectively.

5.3 Cardiac Output Reproducibility at Rest and Exercise

A proof of principle study was performed in order to assess the success of the non-invasive cardiac output determination technique described above, combining the highly-precise 5-gas analyser with the physiological model of methane and acetylene uptake. A group of 8 volunteers were studied on 5 consecutive days, with cardiac output evaluated at rest and during exercise on each day. The

reproducibility of cardiac output measurements and the relationship between $\dot{Q}$ and measured O_2 consumption rate were analysed, showing good agreement with previous literature.

5.3.1 Methods

Seven men and a woman, aged 21-49 years, who had no history of cardiac or respiratory illnesses, volunteered for the study. The experimental work was carried out in accordance with the general principles of the declaration of Helsinki, ethics approval was obtained from the South Central Oxford A Research Ethics Committee (reference number 17/SC/0172) and all participants provided written informed consent prior to the study. The volunteers' anthropometric data and ages are presented in Table 5.4.

Each volunteer visited the laboratory on 5 consecutive days. On each visit, tracer gas washins were performed at rest and then during submaximal exercise. All experimental procedures were carried out with the volunteers seated on a bicycle erogometer, and consisted of a period of air-breathing, followed by a tracer gas washin. At rest, these two periods each lasted 4 min, whilst at exercise each period was shortened to 3 min, reflecting the potential for increased discomfort breathing through the MFS at greater flow rates and tidal volumes. Submaximal exercise was performed with the bicycle set to 50 W, with the volunteers asked to maintain a revolution rate of 60 rpm. Volunteers pedalled for 7 min prior to the start of data collection to ensure an elevated and approximately constant cardiac output throughout the procedure. The calibrated gas mixture (BOC Industrial Gases) used as the inspiratory supply during the washin periods contained 0.9% CH_4, 0.3% C_2H_2, and 21% O_2 with a balance of N_2. Inspiratory gas was supplied to the volunteers using a flow past system at flow rates of 30 and 60 l min^{-1} for the rest and exercise procedures respectively. The volunteers breathed via a mouthpiece with nose occluded. Experimental data were collected using the 5-gas analyser and the arterial O_2 saturation and pulse rate were recorded using a pulse oximeter. For each participant, a 4 ml venous blood sample was taken during one of the visits. The blood sample was analysed using a laboratory blood gas analyser (ABL700, Radiometer).

5.3.2 Results

The experimental protocol was well tolerated, with each of the participants completing their 10 washin procedures. Two representative datasets from one of the participants are shown in Figure 5.11, one from a procedure at rest and the other during exercise. The data are presented as measured

Table 5.4: Anthropometric data for cardiac output volunteers.

Volunteer ID	Sex	Age / years	Height / m	Weight / kg	BMI / kg m^{-2}
LP	M	29	1.77	74	23.6
SME	M	26	1.85	81	23.7
DB	F	23	1.70	63	21.8
CF	M	34	1.85	67	19.6
GR	M	40	1.78	95	30.0
RP	M	49	1.65	62	22.8
JC	M	21	1.84	68	20.1
AM	M	22	1.80	75	23.1

cumulative volume profiles. The larger gradients of the O_2 and CO_2 profiles during exercise indicate the higher rates of O_2 consumption and CO_2 production. There is no significant or sustained trend in either N_2 volume profile, indicating that this is neither consumed nor produced by the body. The amplitude of the oscillation of the N_2 profile reflects each breath's tidal volume, here shown to be around three times larger during exercise. Towards the end of the washin periods at rest and exercise, the end-tidal CH_4 volumes are comparable, roughly 25 ml. Given the relative insolubility of CH_4, this is expected, with the CH_4 within the lung having equilibrated reasonably well with the inspiratory mixture by the end of the washin period. The uptake of soluble C_2H_2 is more rapid at exercise, reflecting the increased pulmonary blood flow. C_2H_2 dissolved within blood will be transported around the body, a significant amount of which will then be stored in body tissue. It is this that prevents the levelling off of the cumulative volume profile during the washin periods; the washin would have to continue for a much longer time period before gas within the lung was well equilibrated with the inspiratory C_2H_2 content.

Of the 80 experimental procedures performed, only three failed to return data that could be used to determine a value of $\dot{Q}$. In two of these cases, the issue was a result of irregular breathing patterns during the first ten breaths of the tracer gas washin period, which meant that the algorithm failed to identify points at which the lung is at a reasonable FRC volume. A third dataset was excluded on the grounds of significant rebreathing during the early breaths of the washin period of an exercise procedure. Thus, 77 datasets remained for further analysis.

The pulse-oximeter measured SpO_2 and pulse rate data for each participant are shown in Ta-

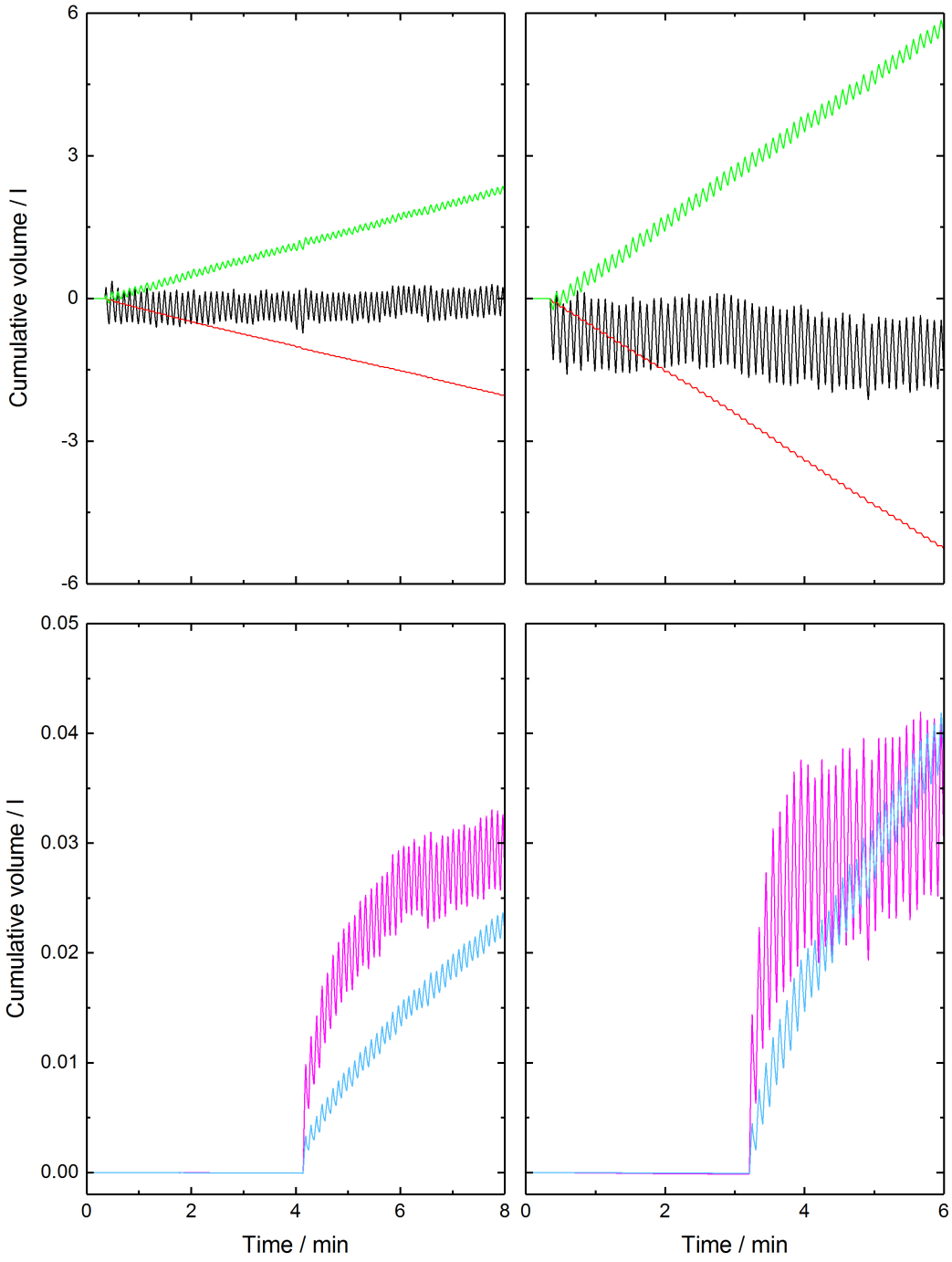


Figure 5.11: Comparison of tracer gas washin cumulative volume profiles for a participant at rest (left) and exercise (right). The upper plots show the cumulative volumes of O_2 (green), CO_2 (red), and N_2 (black). The lower plots show the data for CH_4 (magenta) and C_2H_2 (blue). The data illustrates the greater O_2 consumption, CO_2 production and tidal volumes during exercise. The end-tidal CH_4 volumes are comparable at rest and exercise, whilst C_2H_2 uptake is significantly greater during exercise.

ble 5.5. Unsurprisingly, the pulse rate of each participant was substantially higher when exercising. On average, the pulse rate was 41 % higher during the exercise procedure. Also shown in this table are the measured haemoglobin concentrations for each participant.

Table 5.5: Arterial oxygen saturation, pulse rate and haemoglobin (Hb) concentration for volunteers at rest (R) and during submaximal exercise (E). SpO_2 and pulse rate values are averages, averaged within procedures and then across the 5 visits. Quoted uncertainties are standard deviations of procedure averages. Haemoglobin concentration quoted with carboxhaemoglobin and fetal haemoglobin removed.

Volunteer ID	Rest (R) or Exercise (E)	SpO_2 / %	Pulse rate / min^{-1}	Hb conc. / g dl^{-1}
LP	R	99 ± 0	56 ± 2	15.6
	E	98 ± 0	78 ± 4	
SME	R	96 ± 1	72 ± 11	16.3
	E	96 ± 1	96 ± 5	
DB	R	99 ± 0	72 ± 3	13.8
	E	98 ± 0	113 ± 5	
CF	R	99 ± 1	52 ± 3	14.7
	E	99 ± 0	79 ± 6	
GR	R	97 ± 0	65 ± 5	15.0
	E	96 ± 0	86 ± 5	
RP	R	99 ± 0	68 ± 5	14.8
	E	98 ± 0	98 ± 2	
JC	R	98 ± 1	89 ± 4	15.7
	E	98 ± 1	116 ± 4	
AM	R	98 ± 1	69 ± 6	15.3
	E	98 ± 1	99 ± 4	

Before further analysis, data from two of the participants, DB and RP, were excluded. In the case of DB, significant hyperventilation was observed during each of the rest procedures. The extent of hyperventilation is assessed via the measured respiratory quotient, RQ, for each procedure. The body's production of CO_2 increases during hyperventilation, leading to an increased RQ. At values above one, RQ no longer reflects substrate usage but rather the extent to which a volunteer is hyperventilating.[155] For this volunteer's five experimental procedures at rest, the average measured RQ was 1.31 ± 0.15, with the lowest recorded RQ being 1.09. Significant voluntary hyperventilation of this type, also referred to as hypocapnic hyperventilation, will cause an increase in the cardiac output.[280] Previous studies have shown that the cardiac output increase associated

with hyperventilation can be as high as 40 %.[281]

In the case of RP, the data were excluded not for hyperventilation, but due to an unusually low respiratory rate. The measured respiratory rate for this volunteer was 3.6 ± 0.2 breaths min^{-1} at rest, and only rose to 5.7 ± 1.0 breaths min^{-1} during exercise. The issue associated with these respiratory rates is the substantial recirculation of the tracer gases that will occur during ten breaths, the model's analysis period. If blood within the pulmonary arteries is laden with dissolved tracer gas as a result of recirculation, further uptake from the lung into the blood will be reduced. The model of tracer gas uptake used in this work makes the assumption that recirculation during the analysis period will be negligible. Analysis of this volunteer's data would therefore return lower than predicted cardiac output values.

5.3.2.1 Evaluation of Tissue Volume Multiplier

For each dataset, the determined cardiac output and lung volume will vary with the chosen tissue volume multiplier, X. In order to optimise the value of X used in this work, the quality of the model fits to the measured data were evaluated for a range of X values. X was varied between 0 and 0.5 in steps of 0.1 and the model was fit to the data by multiple linear regression for each of the 57 remaining datasets. To evaluate the optimal X value, the sum of squared residuals between simulated and measured tracer gas uptakes for all of the datasets is analysed. The variation of this quantity with X is shown in Figure 5.12. The trend was fitted with a quadratic function, with the X value at the minimum of this fitted function taken as the optimal tissue volume multiplier, found to be 0.2.

A representative model fit to the measured cumulative volume data for a dataset recorded at rest is shown in Figure 5.13. There is no modelled data for the first two breaths; these are excluded from the analysis. The determined cardiac output values when $\dot{Q}$ and Vol are determined by multiple linear regression with a constant tissue multiplier, X, of 0.2 are shown in Figure 5.14. There is clear separation between rest and exercise procedures both in terms of measured O_2 consumption rate and determined cardiac output. During the exercise procedures, the average O_2 consumption rate was 1011 ml min^{-1}, a little more than three times the average value at rest, 314 ml min^{-1}. The fractional increase of average determined cardiac output from rest to exercise was slightly lower, rising from 4.4 to 9.7 l min^{-1}. The standard deviations of the determined $\dot{Q}$ parameters were comparable at rest

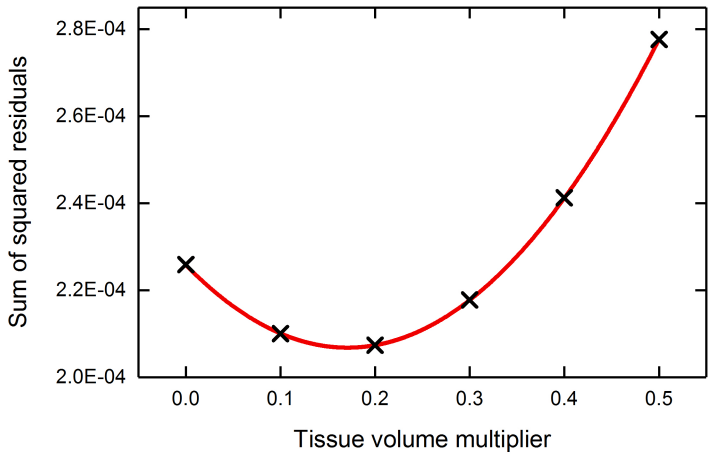


Figure 5.12: Variation of residual sum of squared error with tissue volume multiplier, X. Each of the 57 datasets were analysed with six tissue volume multiplier values, with the sum of squared residuals shown by the black crosses. A quadratic function is fitted to the data, shown with a red line.

and exercise, both equal to 0.7. The result is clear separation between cardiac outputs determined at rest and exercise, with 5.5 and 8.6 l min^{-1} being the highest $\dot{Q}$ at rest and the lowest $\dot{Q}$ at exercise respectively. Analysis by a Welch's t-test illustrated the significance of difference between the parameters determined at rest and exercise ($p<10^{-33}$).

The lung volumes determined by the tracer gas uptake model are shown in Figure 5.15. The model parameter Vol represents the volume of gas remaining within the respiratory system at the algorithmically estimated points at which the lungs are at function residual capacity, FRC. For all participants, the mean determined lung volumes are greater during exercise, with the average increase calculated as 9.9±9.6 %. The large uncertainty in this value illustrates the variation in response between participants. Previous work by Kiers *et al.* found FRC to decrease by 8.8 % when subjects were exercised at a comparable level with that used in this work.[282] One possible explanation for the difference in lung volumes measured at rest and exercise in this work is the unparameterised lung inhomogeneity. Lung inhomogeneity can lead to underestimation of FRC by tracer gas dilution techniques, as lung volume that is less well ventilated does not mix efficiently with the inspiratory tracer gas mixture. This is illustrated by the underestimation of FRC in COPD patients with regions of the lung that communicate poorly with the central airways when lung volumes are measured using a washout technique.[283] At exercise, where tidal volume and breath-by-breath ventilation are much

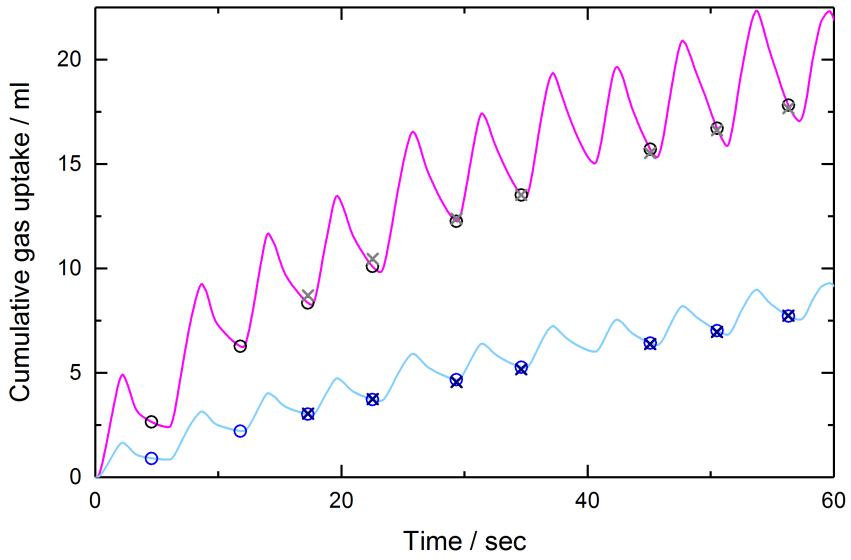


Figure 5.13: A representative fit of the tracer gas uptake model to cumulative uptake data measured by the MFS. The measured profile is shown in magenta for CH_4 and blue for C_2H_2. The measured cumulative gas uptake volumes at FRC are shown with circles, black for CH_4 and blue for C_2H_2. The modelled uptake volumes at FRC are shown by crosses, grey for CH_4 and navy for C_2H_2. Note that there was no FRC point identified for the breath close to 40 sec; this was deemed an incomplete shallow breath.

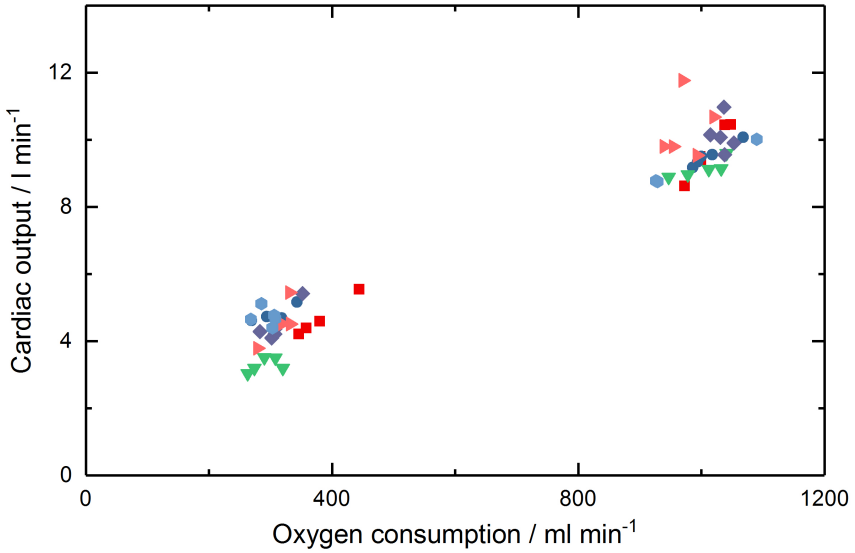


Figure 5.14: Cardiac outputs determined from tracer gas washin data at rest and exercise. Data for each participant are shown with a different symbol and colour. The tracer gas uptake model is fitted by multiple linear regression with a constant tissue multiplier of 0.2.

larger, the more poorly ventilated regions of the lung have a greater chance of equilibration with the inspiratory mixture. Thus, the extent to which the determined volume increases between rest and exercise may illustrate the poorly ventilated volume within each participant's lung.

The standard deviations of the determined lung volume vary substantially from participant to participant. In some cases, large standard deviations arise from a broad spread of lung volumes, whereas in other cases, one significant outlier is shown to lead to large standard deviations. The uncertainty as a fraction of mean volume is lower at rest than exercise, on average ± 5.9 and $\pm 8.7\,\%$ respectively. The reproducibility of the lung volumes determined by this method is not as good as for the lung volumes determined from fitting the Lognormal Lung model to N_2 washout experimental procedures. The Lognormal Lung model is fit to 10 minutes of recorded data, the final 5 minutes of which are the washout period. A great deal of the information that enables the determination of lung volume is encoded within the data from this period. Conversely, the tracer gas uptake model is fit to data from only 8 breaths, data which constitute only a partial washin. CH_4 is approximately four times more soluble in blood and pulmonary tissue than N_2,[270] introducing further uncertainty to the determination of the lung volume. Beyond the information content limitation associated with using only 8 breaths within the tracer gas uptake model fitting, the limited number of breaths provides additional uncertainty in FRC. Breath-to-breath variations in FRC are essentially accounted for by the algorithm identifying points at which the lung reaches effective FRC volumes. However, the gas volume remaining in the lung at these effective FRC points might well display significant variation from one dataset to another. Thus, significant day-to-day variation in determined FRC might be expected, particularly in individuals with less stable breathing patterns when using the MFS.

5.3.2.2 Maximal Bias of $\dot{Q}$ Measurement

The minimum detectable concentrations of the CH_4 and C_2H_2 spectrometers were used to estimate the potential bias of the cardiac output measurements. For twelve example experimental procedures, one at rest and one at exercise from each of the participants, the potential effects of tracer gas concentration measurement uncertainty were evaluated. The MFS measured datasets were altered such that the measured tracer gas concentrations were equal to the measured concentration profiles with the minimum detectable concentrations either added or subtracted. The resulting cumulative tracer gas uptake profiles were calculated as the cumulative integral of the fractional gas compositions

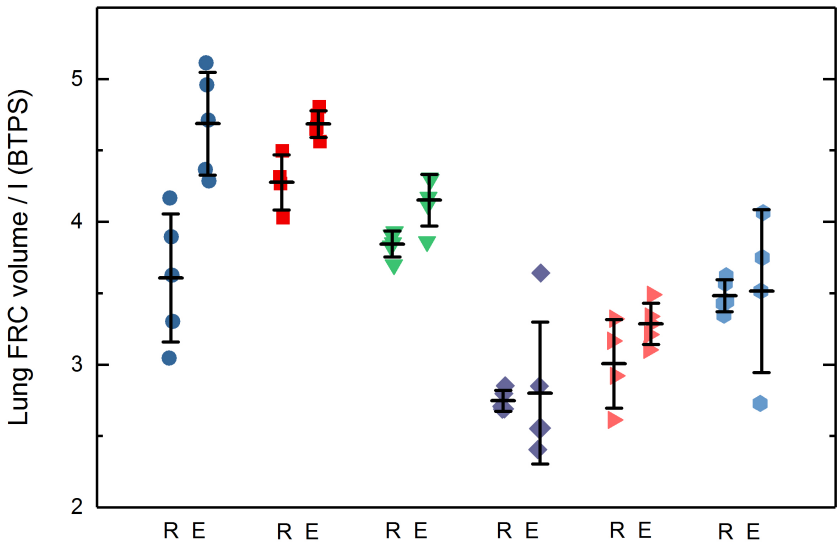


Figure 5.15: Lung volumes at estimated FRC determined by tracer gas uptake model. The volumes are shown at rest (R) and exercise (E) for each experimental procedure of each participant. Each participant's average and standard deviation at rest and exercise is shown in black.

and the measured flow. Thus four altered datasets were calculated from each experimental procedure; one in which both CH_4 and C_2H_2 are assumed to have been overmeasured by the minimum detectable concentrations, one in which both species are assumed to have been undermeasured by the minimum detectable concentrations, and two which assume that one species was undermeasured and the other overmeasured. The tracer gas uptake model was fit to each of these four altered datasets in order to evaluate $\dot{Q}$. The model was solved by two variable multiple linear regression with a constant tissue volume multiplier, X, of 0.2. The determined $\dot{Q}$ showing the largest deviation from that determined using the true measured data was identified in each case, with the difference established as the uncertainty due to bias. In all cases, the largest deviation was identified from the datasets in which one tracer gas was assumed to have been undermeasured and the other overmeasured. The estimated bias for each of the twelve studied datasets is shown in Figure 5.16.

In 75 % of cases, the uncertainty associated with measurement bias is less than 5 % of the determined $\dot{Q}$ value, and in all cases, is below 8 %. The average uncertainty was calculated to be ± 4.0 %. This uncertainty is described as the maximal bias because it assumes uniform mismeasurement of tracer gas concentrations throughout the duration of the experimental procedure. The measurement bias of the bioimpedance technique for evaluating $\dot{Q}$, when it is evaluated against the

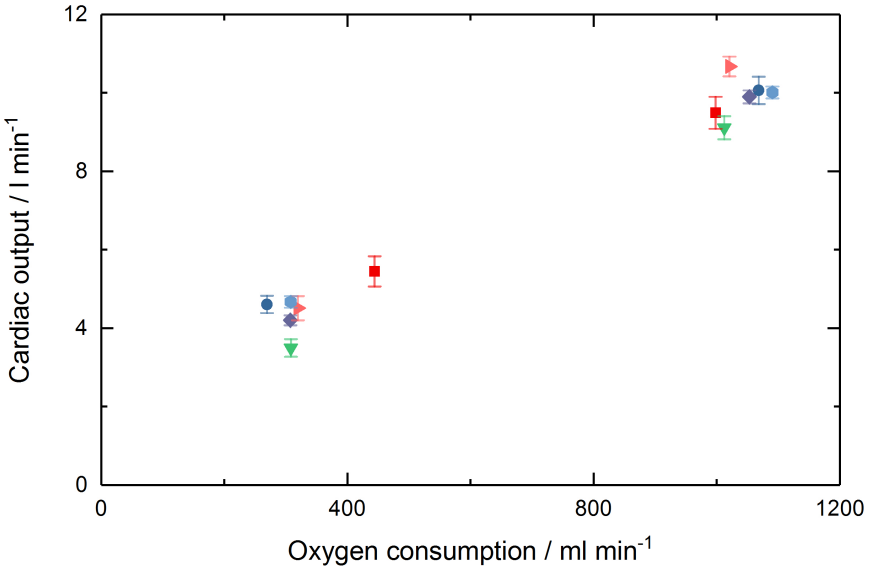


Figure 5.16: Maximal bias of determined $\dot{Q}$ due to tracer gas concentration measurement. The error bias illustrate the maximal bias about $\dot{Q}$ determined from measured data. Each participant is shown with a different colour and symbol.

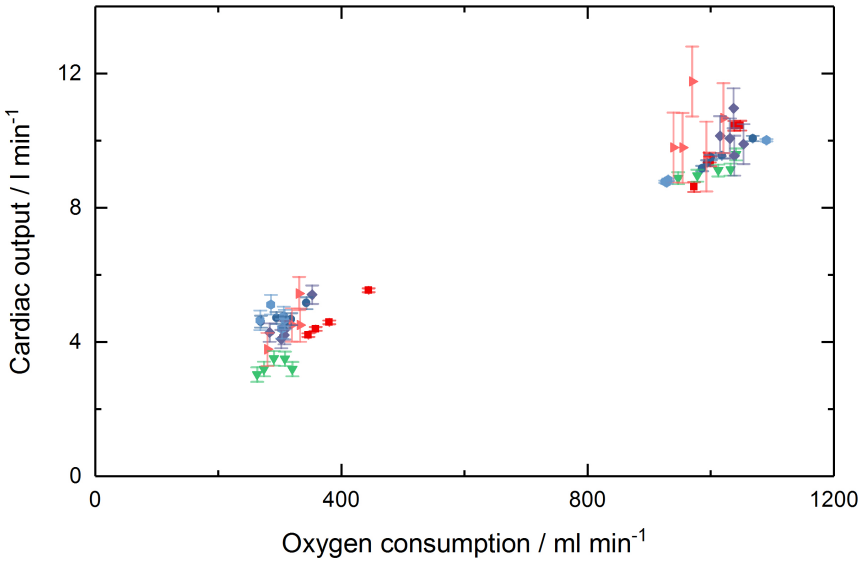


Figure 5.17: Determined $\dot{Q}$ parameters with associated measurement errors. Errors are evaluated for each participant separately for rest and exercise procedures. Each participant is shown with a different colour and symbol.

invasive thermodilution method, has been found to be as high as 13 % of the measured value.[284] Although evaluated by different methods, this comparison is clearly an encouraging one, speaking to the potential accuracy of the $\dot{Q}$ determination by this technique.

5.3.2.3 Estimation of Error

To estimate the degree of error associated with the measured $\dot{Q}$ parameters, the relationships between these parameters and O_2 consumption were evaluated by linear regression for each participant, separately for the rest and exercise experimental procedures. The residual squared errors from the linear fit were calculated, and the measurement mean squared error was calculated allowing for the degrees of freedom within the linear regression. The root mean square errors for each participant at rest and exercise are presented in Table 5.6, and illustrated in Figure 5.17. The average error is greater during exercise than rest, ± 0.35 and $\pm 0.25\,\mathrm{l\,min^{-1}}$ respectively. However, the increase in error is more than matched by the measured $\dot{Q}$ increase, such that the average error normalised by the mean $\dot{Q}$ is greater at rest than exercise, ± 5.8 and ± 3.4 % respectively. In five of six participants, the error associated with the cardiac output measurement at both rest and exercise is less than 10 % of the average determined value. The participant exhibiting the largest errors, both absolute and relative, at rest and exercise, is discussed in detail in the next section.

Table 5.6: Determined $\dot{Q}$ averages and root mean square errors at rest and exercise.

Volunteer ID	Rest (R) or Exercise (E)	Average $\dot{Q}$ / $\mathrm{l\,min^{-1}}$	$\dot{Q}$ error / $\mathrm{l\,min^{-1}}$	$\dot{Q}$ error / Average $\dot{Q}$ / %
LP	R	4.75	0.18	3.7
	E	9.53	0.08	0.8
SME	R	4.68	0.06	1.2
	E	9.68	0.15	1.5
CF	R	3.29	0.22	6.6
	E	9.14	0.18	1.9
GR	R	4.47	0.27	6.1
	E	10.13	0.60	5.9
JC	R	4.56	0.50	10.9
	E	10.31	1.04	10.1
AM	R	4.72	0.29	6.2
	E	9.10	0.03	0.4

5.3.3 Discussion

Evaluation of the optimal constant tissue multiplier, X, was performed seeking to maximise the level of agreement between the measured experimental data and the simulated tracer gas uptake volumes. The chosen value of 0.2 is in reasonably good agreement with previous experiments to measure pulmonary tissue volumes. A study by Mizuno *et al.*, which utilised an C_2H_2 rebreathing technique under artificial ventilation to assess lung tissue volume, found the average *pulmonary tissue volume per functional residual capacity*, equivalent to X used in this work, of healthy subjects to be 0.24 ± 0.04.[285] In 1980, Sackner *et al.* reviewed a series of approaches for measuring pulmonary tissue volume using C_2H_2 as a tracer gas.[286] Data from nine studies were compared, utilising either the single breath hold[287] or rebreathing[96] techniques. The studies measuring the highest and lowest pulmonary tissue volumes in healthy seated individuals used the rebreathing technique, with Farney *et al.*[288] and Sackner *et al.*[96] presenting volumes of 692 and 412 ml respectively. The weighted average across all nine studies for the pulmonary tissue volume in healthy subjects was found to be 557 ml. In this work, the within-subject averaged determined tissue volumes at rest ranged from 462 to 719 ml, with an average across the participants of 587 ml. The close agreement of the average tissue volume with existing literature is encouraging, serving to further justify the value of X used in this work.

The relationship between measured O_2 consumption and determined $\dot{Q}$ was established by a linear fit to the data from all 57 experimental procedures. This fit is illustrated in Figure 5.18. The correlation was very strong, returning Pearson's r of 0.98 with 95 % of the $\dot{Q}$ variance explained by the measured oxygen consumptions. The determined relationship was highly significant, $p<0.001$. The relationship between $\dot{Q}$ and O_2 consumption was previously measured by Åstrand *et al.*.[69] In 12 healthy male volunteers, 21-30 years of age, $\dot{Q}$ was measured by the invasive dye-dilution technique at rest, and when performing submaximal and maximal exercise. Oxygen uptake was determined by the Douglas bag method. During maximal exercise, oxygen consumption was typically as high as $4\,l\,min^{-1}$. The correlation between $\dot{Q}$ and oxygen consumption determined from data at rest and during submaximal exercise was therefore deemed the most appropriate for comparison with this work. This relationship from Åstrand is shown in blue in Figure 5.18. The intercept of the literature fit is a little over 50 % greater than that established in this work, whilst the gradient is ca. 20 %

lower. The $\dot{Q}$ values determined using the non-invasive technique developed in this work are lower than the literature values at rest, with estimated bias of $0.56\,\mathrm{l\,min^{-1}}$ at the mean oxygen consumption at rest. At the mean oxygen consumption for exercise, the bias is $0.58\,\mathrm{l\,min^{-1}}$ but this time with the parameters determined in this work being greater than those reported in the literature.

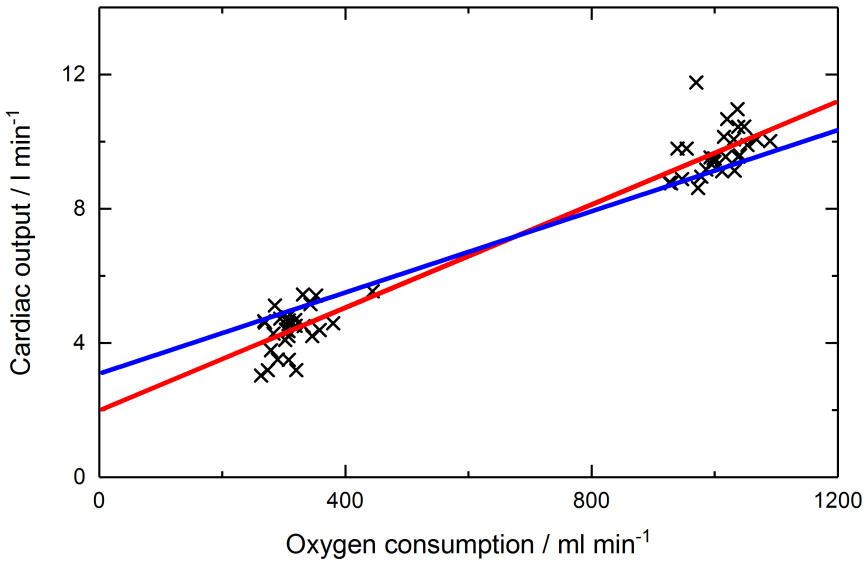


Figure 5.18: Evaluation of the correlation between O_2 consumption and $\dot{Q}$. The linear fit to the measured data is shown with a red line ($\dot{Q} = 1.99 + (7.67 \times 10^{-3})\dot{V}O_2$), and is compared with the trend reported by Åstrand *et al.*[69] which is shown with a blue line ($\dot{Q} = 3.07 + (6.01 \times 10^{-3})\dot{V}O_2$).

Another method to evaluate the determined $\dot{Q}$ values is by considering the global oxygen extraction ratio, O_2ER. This parameter is defined as the ratio of the rates of body oxygen consumption to oxygen delivery, $\dot{V}O_2/DO_2$.[289] Typically at rest only 20-30 % of the O_2 delivered to the tissues is utilised. Under these conditions, oxygen consumption is supply independent with an average O_2ER of 0.26.[290] At maximal exercise O_2ER can be as high as 0.8; the increase in $\dot{V}O_2$ during exercise is not matched by the increase in DO_2. The oxygen consumption is directly measured for each experimental procedure, and the oxygen delivery can be calculated from the measured venous haemoglobin concentration and determined cardiac output, $\dot{Q}$ by:

$$DO_2 = [\,Hb\,] \times 10 \times 1.34 \times \dot{Q} \quad , \tag{5.12}$$

where $[\,Hb\,]$ is the concentration of haemoglobin, in units of $\mathrm{g\,dL^{-1}}$. The factor of 1.34 represents the oxygen-binding capacity of haemoglobin in units of $\mathrm{ml\,O_2\,g^{-1}}$. The factor of 10 ensures that DO_2

has units of $\mathrm{ml\,min^{-1}}$. Consideration of DO_2 provides a possible explanation for the $\dot{Q}$ measured at rest in this work being lower than that measured by Åstrand *et al.*.[69] The mean haemoglobin concentration for the six participants in this work ($15.4\,\mathrm{g\,dl^{-1}}$) was greater than that for the male volunteers in the Åstrand study ($14.4\,\mathrm{g\,dl^{-1}}$). Thus, calculated DO_2 parameters in the two studies were comparable despite the difference in measured $\dot{Q}$.

The values for determined oxygen extraction for each experimental procedure are shown in Figure 5.19. For each of the participants, O_2ER was significantly higher for the procedures at exercise. In all subjects, the average O_2ER at rest was greater than 0.3. It was assumed that the day-to-day variation in haemoglobin concentration is negligible, therefore the single measurement could be used to assess the oxygen delivery of each experimental procedure. Previous work found the average haemoglobin concentration variation over five consecutive days to be 6.5 % of the mean measured value.[291] Uncertainty resulting from the day-to-day variations in blood haemoglobin is not substantially higher than that associated with the blood gas analyser measurement, so should not be a source of concern.

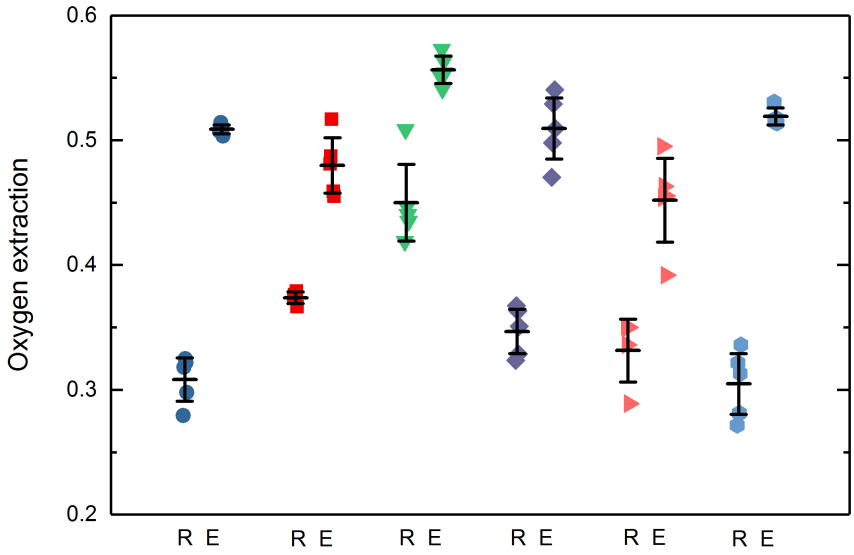


Figure 5.19: Determined O_2 extraction values for each experimental procedure of participant at rest (R) and exercise (E). Participant averages and standard deviations are shown in black.

The largest $\dot{Q}$ errors at both rest and exercise were found for the same subject. In both cases, the error associated with the measurement was greater than 10 % of the average value. Analysis of this participant's determined $\dot{Q}$ parameters, plotted in Figure 5.20, suggested a potential explanation

for this. Both for rest and exercise, the determined $\dot{Q}$ was found to be largest on the final day of the experimental protocol (shown in grey in Figure 5.20). On the final day, the participant reported significant alcohol consumption (estimated 112-144 g ethanol, or 14-18 UK alcohol units) during the previous evening. Alcohol consumption is known to cause an increase in $\dot{Q}$.[292] Two previous studies have evaluated the $\dot{Q}$ of healthy individuals following alcohol consumption. The findings were similar; Kupari reported a $\dot{Q}$ increase of 22 % 12 hours after alcohol consumption (1.75 g ethanol per kg body mass),[293] whilst Kelbaek *et al.* found a 23 % $\dot{Q}$ increase 9 hours after slightly lower consumption (1.4 g ethanol per kg body mass).[294] The determined $\dot{Q}$ parameters for the participant in question on the final day were 19.0 and 18.9 % larger than linear fits through the remaining data estimated for rest and exercise respectively. This finding of $\dot{Q}$ increase with alcohol consumption was incidental in this work and thus the significance must not be exaggerated, but the level of agreement with literature suggests that these particular increased $\dot{Q}$ parameters might well be explained by alcohol consumption approximately 12 hours before the experimental procedures. If this final day data for this participant were excluded from error analysis, the calculated $\dot{Q}$ error normalised by the averaged values drop to 3.3 and 4.9 % for rest and exercise respectively. This is in line with errors determined for the other five (abstemious) participants studied in this work.

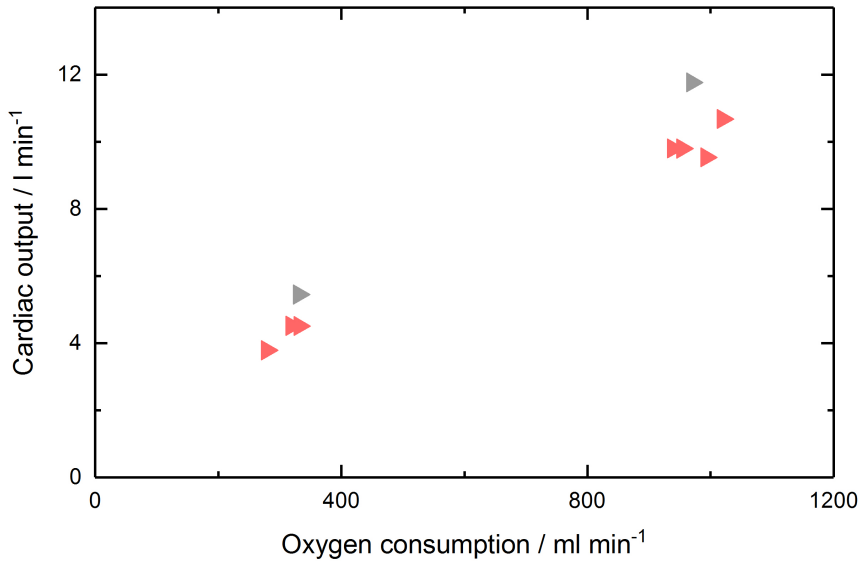


Figure 5.20: Determined $\dot{Q}$ values illustrating the effect of alcohol. Data from the final day of the experimental protocol is shown in grey. Experimental procedures were performed approximately 10 hours following alcohol consumption. Elevated $\dot{Q}$ was determined on this day, both at rest and exercise.

The level of error associated with the determined $\dot{Q}$ parameters in this work is encouraging, comparing favourably with the error levels in existing techniques of $\dot{Q}$ measurement. The lack of accuracy in measured $\dot{Q}$, particularly in non-invasive techniques, has limited the widespread $\dot{Q}$ monitoring within clinical settings. The technique developed in this work offers a non-invasive $\dot{Q}$ assessment with low measurement error and bias.

5.4 Future Developments and Applications

The $\dot{Q}$ values determined in this work show good agreement with literature trends established using invasive methods. In terms of future work, the priority is undertaking a method validation study, in which the $\dot{Q}$ values measured by this technique will be compared with those measured using a well-established invasive technique. As explained within the Introduction, clinical use of invasive methods of evaluating $\dot{Q}$ is limited in patient monitoring; patient outcome improvements associated with having the measurement are masked by the potential for clinical complications associated with making the measurement. There are, however, invasive cardiac output measurements made during diagnostic investigations. Pulmonary arterial catheters can be used to measure blood pressures and O_2 saturations as well as pulmonary flows. This information can be used to aid the diagnosis of pulmonary hypertension, valvular problems or intracardiac shunting of blood. During these diagnostic procedures, simultaneous measurement of $\dot{Q}$ by this non-invasive technique and an invasive technique would allow measurement accuracy, precision and bias to be easily assessed. This study will also provide an opportunity to optimise the clinical applicability of the technique developed in this work.

The tracer gas uptake model described in this work represents the first iteration of cardiopulmonary modelling that will exploit the information encoded within data recorded by the 5-gas analyser. This model simulates tracer gas uptake volumes at the FRC points of the first ten breaths of the washin period. In the future, a more complex model will be required which will simulate exhaled gas fractions every 10 ms, and thus can be fit to entire measured expiratory profiles rather than just single points within each breath. A mechanistic model of the cardiopulmonary and respiratory systems would potentially allow tracer gas washin data to be used to evaluate both cardiac output and lung inhomogeneity. The development of a model of this type from the current Log-normal Lung model is non-trivial, requiring a mechanistic description of the circulatory system to

be integrated with the existing model of the pulmonary system. The uptake and production of five gas species, CH_4, C_2H_2, O_2, N_2, CO_2, by a range of body tissue types requires quantification. The data recorded at rest and exercise in this work will be used as the input for the developed model. With an integrated circulation model, the assumption of negligible tracer gas recirculation would be removed, providing the ability to significantly improve the quality of model fitting with data from later in the washin period. The accuracy of model parameters obtained from a model's fitting procedure is reliant on the information content embedded within the measured data. By extending the size of the dataset used within the fitting process to include all of the recorded washin data, an improvement in the accuracy of determined parameters would be expected. This effect is likely to be most significant for the determined lung volumes, where partial washin data appears to lack sufficient information. With a recirculation model allowing more data to be utilised, the lung tissue volume parameter is also likely to become identifiable within the fitting procedure.

Currently, the Lognormal Lung uses an assumed cardiac output when estimating lung volume and inhomogeneity. The ability to elucidate an accurate cardiac output measurement within the fitting procedure would therefore remove a significant source of error within the Lognormal Lung model. Although it has been shown that the airway parameters (standard deviations of deadspace and compliance, and lung volumes) are largely independent of the assumed cardiac output, an accurate $\dot{Q}$ measurement should have a positive effect on the accuracy and reproducibility of the circulatory parameters, most notably the standard deviation of lung conductance. The ultimate objective is to be able to determine both $\dot{Q}$ and lung inhomogeneity parameters from a single experimental procedure, a washin of both CH_4 and C_2H_2. A shorter term objective, however, might be to use a less significantly edited version of the Lognormal Lung model to assess lung inhomogeneity parameters using a CH_4 washin in place of the currently used N_2 washout. There are potential benefits associated with this experimental procedure. The first is that the length of time of the procedure could be shortened. Currently, the level of disagreement between the measured and modelled expiratory O_2 and CO_2 fractions during 5 minutes of air-breathing, and the expiratory N_2 fractions during the washout period are used within the cost function of the fitting procedure. However, as inspiratory CH_4 content would be low, there is no reason that a cost function shouldn't include O_2, CO_2, and CH_4 expiratory fractions during the tracer gas washin period. Simultaneous evaluation of these three gases during the washin would remove the necessity for the preceding 5 minute air-breathing

period. Although patient tolerance of the 15 minute breathing procedure is very good, lowering the breathing period to 10 minutes would increase patient comfort. The second benefit associated with utilising a tracer gas washin is that the hyperoxia associated with the N_2 washout period would be avoided. Hyperoxia occurs as a result of inspiration of the medical O_2 supply.[295] Hyperoxia has the effect of decreasing $\dot{Q}$ by decreasing the heart rate and systemic vasoconstriction.[296] Studies into the effects of hyperoxia the lungs of dogs and sheep have found that ventilation distributions are unaffected, but perfusion distributions are broadened.[297,298] It is not unreasonable to suggest that the same will be true in human lungs. These physiological changes introduce an inherent uncertainty into lung inhomogeneity parameters determined from N_2 washout experimental data; the Lognormal Lung model assumes a constant $\dot{Q}$ and makes no consideration for changes in the conductance distribution associated with hyperoxia.

The clinical usefulness and applicability of monitoring $\dot{Q}$ by this method will need to be established in an intensive care unit. Critically ill patients are often haemodynamically unstable, leading to a mismatch between oxygen demand and delivery.[299] This can occur as a result of cardiac dysfunction, blood loss, or significant blood vessel constriction or dilation.[300] These conditions can lead to organ dysfunction, deterioration into multi-organ failure, and eventually death. Monitoring of $\dot{Q}$ in critically ill patients could guide medical management so as to prevent or treat organ failure and improve outcomes. Initial studies would utilise the tracer gas washin technique to monitor $\dot{Q}$ in patients following standard treatment, data from which would be used to assess the potential for outcome improvement. Ultimately, a study in which clinical management was to some extent driven by monitored $\dot{Q}$ evolution would serve to demonstrate the true value of this non-invasive technique for determining $\dot{Q}$.

5.5 Summary

This chapter has demonstrated the development and application of a molecular flow sensor capable of contemporaneous evaluation of 5 gas species. In order to facilitate highly sensitive measurements of CH_4 and C_2H_2 concentrations in a compact spectrometer, a multipass cell was developed. The Herriott cell was designed to enable tracer gas sensing to be performed in a way that could be integrated with existing O_2, CO_2, and H_2O spectroscopic systems. This integrated 5-gas MFS provided highly precise measurements of gas composition, temperature, pressure and respiratory

flow every 10 ms. The capability of this device was demonstrated by the quality of data recorded during a tracer gas washin and subsequent washout.

In order to exploit the physiologically significant information encoded within the data recorded by the 5-gas MFS, a model of CH_4 and C_2H_2 uptake in the body was written. The model simulates the uptake volumes of the tracer gases, dividing volumes between uptake into the blood, and into gaseous and tissue volumes within the lung. This model was used to quantify cardiac output, $\dot{Q}$, and lung functional residual capacity, FRC. The pulmonary tissue volume was assumed to be 20 % of FRC; the quality of the model fit to the measured data was maximised at this constant tissue multiplier. The model parameters are determined as those which minimise the differences between measured and simulated tracer gas uptake volumes. The reproducibility and response to exercise of the measured $\dot{Q}$ parameters were evaluated during a study in which 8 volunteers performed tracer gas washins at rest and exercise on 5 consecutive days. The non-invasive technique developed in this work showed good agreement with literature in terms of the relationship between $\dot{Q}$ and measured oxygen consumption, $\dot{V}O_2$. The measurement error, evaluated as the deviation from linearity in this trend from participant to participant was on average lower than existing techniques of assessing $\dot{Q}$.

The final section of this chapter has described the future work in this field and the potential applications of this 5-gas analyser. The Lognormal Lung model requires development in order to provide simulation of expiratory tracer gas fraction profiles. This development includes the integration of a model of blood circulation around the body that is significantly more complex than that currently used. The potential benefits of assessing lung inhomogeneity using a CH_4 washin were described; patient comfort increased by a reduction in the period of each experimental procedure, and the avoidance of the physiological changes associated with hyperoxia. In order to fully assess the quality of $\dot{Q}$ measurements, a validation study is required, consisting of contemporaneous measurement of $\dot{Q}$ by the technique developed in this work and a well-established invasive technique that relies upon pulmonary artery catheterisation. Ultimately, employment of this open circuit washin technique in an intensive care setting will assess its potential to improve patient outcomes by monitoring $\dot{Q}$.

Chapter 6

Conclusions and Future Work

This thesis has demonstrated the potential of non-invasive techniques for evaluating lung inhomogeneity and cardiac output. The techniques rely on accurate measurement of respiratory gas fluxes by the compact molecular flow sensor (MFS). This device utilises direct laser absorption spectroscopy to evaluate CO_2 and H_2O concentrations every 10 ms, with off-axis cavity enhanced absorption spectroscopy enabling sensitive measurements of O_2 concentration to be made with the same time resolution. The spectroscopic systems are embedded within a pneumotachograph capable of making precise measurements of respiratory flows. To estimate lung inhomogeneity parameters the fluxes of O_2, CO_2, and N_2 are measured during a multiple breath N_2 washout, consisting of 10 min of normal breathing before the inspiratory gas is changed to medical O_2 for the final 5 min. These highly-precise measured profiles are then fit to a computational model of the lung that parameterises the underlying inhomogeneity of the lung's compliance, conductance and deadspace volume distributions.

This thesis has presented the first instances of this technique being utilised in clinical settings. Cross-sectional studies have been completed within the Oxford University Hospitals, evaluating the lung inhomogeneity in patients with COPD, with asthma, and having recently recovered from a primary spontaneous pneumothorax. In addition, a longitudinal study of patients with asthma was performed to determine the responses of the inhomogeneity indices to a range of therapeutic interventions. Finally, a study was undertaken at the University of California San Diego Radiology Imaging Laboratory comparing parameters quantifying lung ventilation and perfusion distributions from the gold-standard multiple gas elimination technique (MIGET) with derived parameters estimated from the Lognormal Lung model. Patients with a range of COPD disease severities were

evaluated during this study. In total, 200 N_2 washout experimental procedures were recorded during these clinical studies, with accepted parameter sets estimated in 181 (91 %) cases.

The inhomogeneity parameters were shown to be significantly different between patients with COPD and a healthy age-matched control group, even in patients for whom FEV_1 remained normal. Indeed, determined parameters were abnormally elevated even in smokers demonstrating non-obstructive spirometry. It was hypothesised that this technique could provide sensitive measures of inflammation or disease activity in the lung's smaller airways, even in the case of subtle smoking-related lung damage. Such a technique could enable earlier diagnosis of COPD, presenting opportunities for secondary interventions. To strengthen this hypothesis, studying further patients with early stage COPD is crucial.

The parameters derived from the Lognormal Lung model compared well with MIGET parameters describing the airways; ventilation inhomogeneity and deadspace ventilation. The agreement between the two methods was weaker for the parameters describing pulmonary circulation; perfusion inhomogeneity and shunt fraction. The information content within the recorded respiratory gas exchange profiles describing the circulatory system is subtle, so these results were not unexpected. Bimodal ventilation/perfusion distributions were measured by MIGET in all but one of the patients with COPD studied, whereas a significant assumption underlying the Lognormal Lung model is that both alveolar compliance and vascular conductance distributions are unimodal. Better agreement between the techniques would be predicted, therefore, in healthy individuals or those with early stage respiratory disease.

In the cross-sectional study of patients with asthma, inhomogeneity parameters were again found to be abnormally elevated when compared to an age-matched healthy group. Modest correlation of these parameters with measured spirometry was identified. The effects of bronchodilator administration on the inhomogeneity parameters were found to be independent of whether patients display spirometry measured reversibility; inhomogeneity is not a simple proxy of FEV_1. The inhomogeneity parameters show potential as objective measures of disease activity in asthma, reflecting disease control rather well.

Longitudinal evaluation of inhomogeneity in patients undertaking a range of therapeutic interventions established the capacity of these parameters to change in response to therapy. In the asthma treatment pathway, normal lung inhomogeneity was measured at baseline in the single patient who

responded to inhaled corticosteroid treatment, whereas each of the non-responders returned abnormally elevated parameters. Following three months of Mepolizumab treatment, a recently adopted injected biologic therapy, lung inhomogeneity was reduced in every patient despite mixed spirometric and biomarker responses. Recruitment to both arms of this study must be continued to ascertain whether lung inhomogeneity parameters prove capable of predicting symptom responses to different therapy types in patients with asthma, and/or providing an objective index that describes patient responses to biologic therapies. The identification of such an index is a priority from a medical economic perspective due to the high costs associated with the implementation of recently developed therapies.

These studies have demonstrated different aspects of the clinical potential of this technique of assessing lung inhomogeneity. To realise this potential, there is the requirement for future studies that are purpose designed trials driven by clinicians and/or elements of the healthcare industry. Given the high degree of regulation present across the medical landscape, enabling studies of this type will require development of an MFS that satisfies the relevant CE marking criteria. Ultimately, clinical adoption of this technique will depend on the demonstration of patient outcome improvements in trials investigating large numbers of patients.

In Chapter 5, the development of an MFS capable of contemporaneously evaluating the fluxes of five molecular species was presented. A compact Herriott cell was integrated into the pre-existing design, enabling the measurement of the fluxes of tracer gases CH_4 and C_2H_2 in addition to O_2, CO_2, and H_2O. Data recorded by this device during tracer gas washin procedures were fit to a model of tracer gas uptake by the body, to provide estimates of cardiovascular function in the form of cardiac output. A validation study was undertaken, evaluating cardiac output at rest and during moderate exercise on five consecutive days in eight healthy volunteers. The relationship between determined cardiac output and oxygen consumption was evaluated, and compared well with previously reported trends, although a degree of bias was present both at rest and during exercise. The average measurement error associated with cardiac output determination was lower than for existing techniques, $\pm 6\,\%$ and $\pm 3\,\%$ at rest and exercise, respectively. This study did demonstrate some limitations of the current implementation of this technique, for example the absence of any consideration of tracer gas recirculation in the model which led to low determined cardiac outputs in one volunteer.

The measurement apparatus developed in this thesis is capable of recording highly precise profiles of tracer gas washin procedures. To fully exploit the information encoded within these profiles, a more complex computational mechanistic model of cardiopulmonary function is required. Substantial development of the Lognormal Lung model is necessary, including detailed circulatory models capable of quantifying tracer gas recirculation and uptake by different tissue types in the body. Beyond improvements to the cardiac output determination, there are potential benefits to the parameterisation of lung inhomogeneity that might result from the implementation of a model offering a more holistic description of the cardiopulmonary system. First, the requirement to assume a cardiac output during fitting will be removed, with this becoming readily obtainable within the parameter estimation process, secondly, the requirement to utilise a medical O_2 breathing period will be removed, and lastly, the length of each experimental procedure can be shortened.

The benefits associated with direct measurements of cardiac output in intensive care settings, if achieved using an accurate, safe and non-invasive technique, are well established. Excitingly, this technique has the potential to provide clinicians with further potentially valuable diagnostic information. If determined cardiac output is combined with measured oxygen consumption and haemoglobin concentration, mixed venous oxygen saturations could readily be evaluated. Clinical measurement of this quantity by non-invasive methods has been limited to this point, although a technique described by Bush *et al.* has shown that non-invasive estimation of mixed venous oxygen saturation is achievable.[301] This quantity has been advocated as an index of global tissue hypoxia.[302] This index can provide clinicians with information about cardiocirculatory and/or metabolic impairment and thus the requirement for further diagnostics and appropriate action.[303] When measured perioperatively, mixed venous oxygen saturation has been found to be an indicator of both short and long term patient mortality.[304]

Bibliography

[1] M. R. Miller, J. Hankinson, V. Brusasco, F. Burgos, R. Casaburi, A. Coates, R. Crapo, P. Enright, C. P. M. van der Grinten, P. Gustafsson, R. Jensen, D. C. Johnson, N. MacIntyre, R. McKay, D. Navajas, O. F. Pedersen, R. Pellegrino, G. Viegi, and J. Wanger, "Standardisation of spirometry," *Eur. Resp. J.*, vol. 26, no. 2, pp. 319–338, 2005.

[2] A. Rhodes, M. Cecconi, M. Hamilton, J. Poloniecki, J. Woods, O. Boyd, D. Bennett, and R. Michael Grounds, "Goal-directed therapy in high-risk surgical patients: a 15-year follow-up study," *Intens. Care Med.*, vol. 36, pp. 1327–1332, 2010.

[3] J. B. West, *Ventilation/blood flow and gas exchange*. Blackwell Scientific Publications, fifth ed., 1990.

[4] C. Bauer and E. Schroder, "Carbamino compounds of haemoglobin in human adult and foetal blood," *J. Physiol.*, vol. 227, pp. 457–471, 1972.

[5] J. Wanger, J. Clausen, A. Coates, O. Pedersen, V. Brusasco, F. Burgos, R. Casaburi, R. Crapo, P. Enright, C. Grinten, P. Gustafsson, and J. Hankinson, "Standardisation of the measurement of lung volumes," *Eur. Resp. J.*, vol. 26, no. 3, pp. 511–522, 2005.

[6] M. C. Hart, M. M. Orzalesi, and C. D. Cook, "Relation between anatomic respiratory dead space and body size and lung volume," *J. Appl. Physiol.*, vol. 18, no. 3, pp. 519–522, 1963.

[7] J. Severinghaus and M. Stupfel, "Alveolar Dead Space as an Index of Distribution of Blood Flow in Pulmonary Capillaries," *J. Appl. Physiol.*, vol. 10, no. 3, pp. 335–358, 1957.

[8] WHO, "Global surveillance, prevention and control of chronic respiratory diseases: a comprehensive approach," *WHO Library*, 2007.

[9] S. L. Murphy, J. Xu, and K. D. Kochanek, "Deaths: Final Data for 2010.," *National vital statistics reports: from the Centers for Disease Control and Prevention, National Center for Health Statistics, National Vital Statistics System*, vol. 61, no. 4, pp. 1–117, 2013.

[10] N. S. Hopkinson, C. Englebretsen, N. Cooley, K. Kennie, M. Lim, T. Woodcock, A. A. Laverty, S. Wilson, S. L. Elkin, C. Caneja, C. Falzon, H. Burgess, D. Bell, and D. Lai, "Designing and implementing a COPD discharge care bundle," *Thorax*, vol. 67, no. 1, pp. 90–92, 2012.

[11] D. M. Mannino and B. J. Make, "Is it time to move beyond the "O" in early COPD?," *Eur. Resp. J.*, vol. 46, no. 6, pp. 1535–1537, 2015.

[12] J. R. Hurst, "Precision Medicine in Chronic Obstructive Pulmonary Disease," *Am. J. Respir. Crit. Care*, vol. 193, no. 6, pp. 593–4, 2016.

[13] J. McDonough, R. Yuan, M. Suzuki, N. Seyednejad, W. M. Elliot, P. G. Sanchez, A. C. Wright, W. B. Gefter, L. Litzky, H. O. Coxson, P. D. Pare, D. D. Sin, R. A. Pierce, J. C. Woods, A. M. McWilliams, J. R. Mayo, S. C. Lam, J. D. Cooper, and J. C. Hogg, "Small-Airway Obstruction and Emphysema in Chronic Obstructive Pulmonary Disease," *New Engl. J. Med.*, vol. 365, no. 17, pp. 1567–1575, 2011.

[14] J. C. Hogg, "Pathophysiology of airflow limitation in chronic obstructive pulmonary disease," *The Lancet*, vol. 364, no. 9435, pp. 709–721, 2004.

[15] Y. Oba and N. A. Lone, "Efficacy and safety of roflumilast in patients with chronic obstructive pulmonary disease: a systematic review and meta-analysis.," *Ther. Adv. Respir. Dis.*, vol. 7, no. 1, pp. 13–24, 2013.

[16] B. E. Miller, R. Tal-Singer, S. I. Rennard, A. Furtwaengler, N. Leidy, M. Lowings, U. J. Martin, T. R. Martin, D. D. Merrill, J. Snyder, J. Walsh, and D. M. Mannino, "Plasma Fibrinogen Qualification as a Drug Development Tool in Chronic Obstructive Pulmonary Disease. Perspective of the Chronic Obstructive Pulmonary Disease Biomarker Qualification Consortium.," *Am. J. Resp. Crit. Care*, vol. 193, no. 6, pp. 607–13, 2016.

[17] E. D. Bateman, S. S. Hurd, P. J. Barnes, J. Bousquet, J. M. Drazen, M. FitzGeralde, P. Gibson, K. Ohta, P. O'Byrne, S. E. Pedersen, E. Pizzichini, S. D. Sullivanee, S. E. Wenzel, and H. J.

Zar, "Global strategy for asthma management and prevention: GINA executive summary," *Eur. Respir. J.*, vol. 31, no. 1, pp. 143–178, 2008.

[18] H. Reddel, S. Ware, G. Marks, C. Salome, C. Jenkins, and A. Woolcock, "Differences between asthma exacerbations and poor asthma control," *Lancet*, vol. 353, no. 9150, pp. 364–369, 1999.

[19] D. Robinson, M. Humbert, R. Buhl, A. A. Cruz, H. Inoue, S. Korom, N. A. Hanania, and P. Nair, "Revisiting Type 2-high and Type 2-low airway inflammation in asthma: current knowledge and therapeutic implications," *Clin. Exp. Allergy*, vol. 47, no. 2, pp. 161–175, 2017.

[20] P. G. Woodruff, B. Modrek, D. F. Choy, G. Jia, A. R. Abbas, A. Ellwanger, J. R. Arron, L. L. Koth, and J. V. Fahy, "T-helper type 2-driven inflammation defines major subphenotypes of asthma," *Am. J. Respir. Crit. Care Med.*, vol. 180, no. 5, pp. 388–395, 2009.

[21] K. Samitas, E. Zervas, and M. Gaga, "T2-low asthma: Current approach to diagnosis and therapy," *Curr. Opin. Pulm. Med.*, vol. 23, no. 1, pp. 48–55, 2017.

[22] A. MacDuff, A. Arnold, and J. Harvey, "Management of spontaneous pneumothorax: British Thoracic Society pleural disease guideline 2010," *Thorax*, vol. 65, no. Suppl 2, pp. ii18–ii31, 2010.

[23] M. H. Baumann and M. Noppen, "Pneumothorax," *Respirology*, vol. 9, pp. 157–164, 2004.

[24] M. Noppen, S. Verbanck, J. Harvey, R. Van Herreweghe, M. Meysman, W. Vincken, and M. Paiva, "Music: A new cause of primary spontaneous pneumothorax," *Thorax*, vol. 59, no. 8, pp. 722–724, 2004.

[25] M. Alifano, S. N. Forti Parri, B. Bonfanti, W. A. Arab, A. Passini, M. Boaron, and N. Roche, "Atmospheric pressure influences the risk of pneumothorax: beware the storm!," *Chest*, vol. 131, no. 6, pp. 1877–1882, 2007.

[26] O. Lesur, N. Delorme, J. M. Fromaget, P. Bernadac, and J. M. Polu, "Computed tomography in the etiologic assessment of idiopathic spontaneous pneumothorax," *Chest*, vol. 98, no. 2, pp. 341–347, 1990.

[27] D. M. Donahue, C. D. Wright, G. Viale, and D. J. Mathisen, "Resection of pulmonary blebs and pleurodesis for spontaneous pneumothorax," *Chest*, vol. 104, no. 6, pp. 1767–1769, 1993.

[28] R. Hancox, I. Pavord, and M. Sears, "Associations between blood eosinophils and decline in lung function among adults with and without asthma," *Eur. Respir. J.*, vol. 51, no. 4, 2018.

[29] P. G. Woodruff, R. G. Barr, E. Bleecker, S. A. Christenson, D. Couper, J. L. Curtis, N. A. Gouskova, N. N. Hansel, E. A. Hoffman, R. E. Kanner, E. Kleerup, S. C. Lazarus, F. J. Martinez, R. Paine, S. Rennard, D. P. Tashkin, and M. K. Han, "Clinical significance of symptoms in smokers with preserved pulmonary function," *N. Engl. J. Med.*, vol. 374, no. 19, pp. 1811–1821, 2016.

[30] N. Petousi, N. P. Talbot, I. Pavord, and P. A. Robbins, "Measuring lung function in airways diseases: current and emerging techniques," *Thorax*, vol. 74, pp. 797–805, 2019.

[31] S. Stanojevic, P. Quanjer, M. R. Miller, and J. Stocks, "The Global Lung Function Initiative: dispelling some myths of lung function test interpretation," *Breathe*, vol. 9, no. 6, pp. 462–474, 2013.

[32] W. L. Eschenbacher, "Defining Airflow Obstruction," *Chronic Obstr. Pulm. Dis.*, vol. 3, no. 2, pp. 515–518, 2016.

[33] V. C. Moore, "Spirometry: step by step," *Breathe*, vol. 8, no. 3, pp. 232–240, 2012.

[34] B. G. Cooper, "An update on contraindications for lung function testing," *Thorax*, vol. 66, no. 8, pp. 714–723, 2011.

[35] C. P. Criée, S. Sorichter, H. J. Smith, P. Kardos, R. Merget, D. Heise, D. Berdel, D. Köhler, H. Magnussen, W. Marek, H. Mitfessel, K. Rasche, M. Rolke, H. Worth, and R. A. Jörres, "Body plethysmography - Its principles and clinical use," *Resp. Med.*, vol. 105, no. 7, pp. 959–971, 2011.

[36] T. Urbankowski and T. Przybyłowski, "Methods of airway resistance assessment," *Adv. Resp. Med.*, vol. 84, no. 4, pp. 134–141, 2016.

[37] J. B. West, "The birth of clinical body plethysmography: it was a good week," *J. Clin. Invest.*, vol. 114, no. 8, pp. 1043–1045, 2004.

[38] M. Goldman, H. Smith, and W. Ulmer, "Whole-body plethysmography," *Eur. Respir. Mon.*, vol. 31, pp. 15–43, 2005.

[39] T. R. Shin, Y. M. Oh, J. H. Park, K. S. Lee, S. Oh, D. R. Kang, S. Sheen, J. B. Seo, K. H. Yoo, J. H. Lee, T. H. Kim, S. Y. Lim, H. I. Yoon, C. K. Rhee, K. H. Choe, J. S. Lee, and S. D. Lee, "The Prognostic Value of Residual Volume/Total Lung Capacity in Patients with Chronic Obstructive Pulmonary Disease," *J. Korean Med. Sci.*, vol. 30, no. 10, pp. 1459–1465, 2015.

[40] Y. Tang, M. Zhang, Y. Feng, and B. Liang, "The measurement of lung volumes using body plethysmography and helium dilution methods in COPD patients: a correlation and diagnosis analysis," *Sci. Rep.*, vol. 6, pp. 1–7, 2016.

[41] D. C. Stanescu, D. Rodenstein, M. Cauberghs, and K. P. Van de Woestijne, "Failure of body plethysmography in bronchial asthma," *J. Appl. Physiol. Respir. Environ. Exerc. Physiol.*, vol. 52, no. 4, pp. 939–948, 1982.

[42] M. Kraft, J. Pak, R. J. Martin, D. Kaminsky, and C. G. Irvin, "Distal lung dysfunction at night in nocturnal asthma," *Am. J. Respir. Crit. Care Med.*, vol. 163, no. 7, pp. 1551–1556, 2001.

[43] M. R. Becklake, "A New Index of the Intrapulmonary Mixture of Inspired Air," *Thorax*, vol. 7, p. 111, 1952.

[44] W. D. Fowler, "Lung Function Studies. III. Uneven Pulmonary Ventilation in Normal Subjects and in Patients with Pulmonary Disease," *J. Appl. Physiol.*, vol. 2, no. 6, pp. 283–299, 1949.

[45] R. Rodríguez-Roisin, M. Drakulovic, D. A. Rodríguez, J. Roca, J. A. Barberà, and P. D. Wagner, "Ventilation-perfusion imbalance and chronic obstructive pulmonary disease staging severity.," *J. Appl. Physiol.*, vol. 106, no. 6, pp. 1902–8, 2009.

[46] M. P. Hlastala, "Multiple inert gas elimination technique.," *J. Appl. Physiol.*, vol. 56, no. 1, pp. 1–7, 1984.

[47] P. D. Wagner, "The multiple inert gas elimination technique (MIGET)," *Intens. Care Med.*, vol. 34, pp. 994–1001, 2008.

[48] P. D. Wagner, D. Dantzker, V. Iacovoni, W. Tomlin, and J. West, "Ventilation-perfusion inequality in asymptomatic asthma," *Am. Rev. Respir. Dis.*, vol. 118, no. 3, pp. 511–24, 1978.

[49] J. P. Whiteley, D. J. Gavaghan, and C. E. W. Hahn, "A Mathematical Evaluation of the Multiple Breath Nitrogen Washout (MBNW) Technique and the Multiple Inert Gas Elimination Technique," *Journal of Theoretical Biology*, vol. 194.4, pp. 517–539, 1998.

[50] J. E. Roos, H. McAdams, S. Kaushik, and B. Driehuys, "Hyperpolarized Gas MRI: Technique and Applications," *Magn. Reson. Imaging Clin. N. Am.*, vol. 23, no. 2, pp. 217–229, 2015.

[51] S. S. Kauczor, M. V. Knopp, E. W. Otten, D. Hofmann, K. F. Kreitner, H. Nilgens, R. Surkau, W. Heil, A. Potthast, and M. Thelen, "Normal and abnormal pulmonary ventilation: visualization at hyperpolarized He-3 MR Imaging," *Radiology*, vol. 201.2, pp. 564–568, 1996.

[52] J. P. Mugler and T. A. Altes, "Hyperpolarized 129Xe MRI of the human lung," *J. Magn. Reson. Imaging*, vol. 37, no. 2, pp. 313–331, 2013.

[53] L. A. Engel, "Gas mixing within the acinus of the lung.," *J. Appl. Physiol.*, vol. 54, no. 3, pp. 609–618, 1983.

[54] W. Fowler, E. Cornish, and S. Kety, "Lung function studies. VIII. Analysis of alveolar ventilation by pulmonary N2 clearance curves," *J. Clin. Invest.*, vol. 31, no. 1, pp. 40–50, 1952.

[55] P. D. Robinson, M. D. Goldman, and P. M. Gustafsson, "Inert gas washout: Theoretical background and clinical utility in respiratory disease," *Respiration*, vol. 78, no. 3, pp. 339–355, 2009.

[56] P. Subbarao, C. Milla, P. Aurora, J. C. Davies, S. D. Davis, G. L. Hall, S. Heltshe, P. Latzin, A. Lindblad, J. E. Pittman, P. D. Robinson, M. Rosenfeld, F. Singer, T. D. Starner, F. Ratjen, and W. Morgan, "Multiple-breath washout as a lung function test in cystic fibrosis: A cystic fibrosis foundation workshop report," *Ann. Am. Thorac. Soc.*, vol. 12, no. 6, pp. 932–939, 2015.

[57] A. Larsson, C. Jonmarker, and O. Werner, "Ventilation inhomogeneity during controlled ventilation. Which index should be used?," *J. Appl. Physiol.*, vol. 65, no. 5, pp. 2030–2039, 1988.

[58] P. D. Robinson, P. Latzin, S. Verbanck, G. L. Hall, A. Horsley, M. Gappa, C. Thamrin, H. G. M. Arets, P. Aurora, S. I. Fuchs, G. G. King, S. Lum, K. Macleod, M. Paiva, J. J. Pillow, S. Ranganathan, F. Ratjen, F. Singer, S. Sonnappa, J. Stocks, P. Subbarao, B. R.

Thompson, and P. M. Gustafsson, "Consensus statement for inert gas washout measurement using multiple- and singlebreath tests," *Eur. Respir. J.*, vol. 41, no. 3, pp. 507–522, 2013.

[59] A. R. Horsley, P. M. Gustafsson, K. A. Macleod, C. Saunders, A. P. Greening, D. J. Porteous, J. C. Davies, S. Cunningham, E. W. F. W. Alton, and J. A. Innes, "Lung clearance index is a sensitive, repeatable and practical measure of airways disease in adults with cystic fibrosis," *Thorax*, vol. 63, no. 2, pp. 135–140, 2008.

[60] P. Aurora, A. Bush, P. Gustafsson, C. Oliver, C. Wallis, J. Price, J. Stroobant, S. Carr, and J. Stocks, "Multiple-breath washout as a marker of lung disease in preschool children with cystic fibrosis," *Am. J. Respir. Crit. Care Med.*, vol. 171, no. 3, pp. 249–256, 2005.

[61] S. Verbanck, D. Schuermans, A. Van Muylem, M. Paiva, M. Noppen, and W. Vincken, "Ventilation distribution during histamine provocation," *J. Appl. Physiol.*, vol. 83, no. 6, pp. 1907–1916, 1997.

[62] S. Verbanck and M. Paiva, "Gas mixing in the airways and airspaces," *Compr. Physiol.*, vol. 1, no. 2, pp. 809–834, 2011.

[63] S. Verbanck, D. Schuermans, M. Meysman, M. Paiva, and W. Vincken, "Noninvasive assessment of airway alterations in smokers: The small airways revisited," *Am. J. Respir. Crit. Care Med.*, vol. 170, no. 4, pp. 414–419, 2004.

[64] S. Verbanck, D. Schuermans, and W. Vincken, "Inflammation and airway function in the lung periphery of patients with stable asthma," *J. Allergy Clin. Immunol.*, vol. 125, no. 3, pp. 611–616, 2010.

[65] B. R. Thompson, J. A. Douglass, M. J. Ellis, V. J. Kelly, R. E. O'Hehir, G. G. King, and S. Verbanck, "Peripheral lung function in patients with stable and unstable asthma," *J. Allergy Clin. Immunol.*, vol. 131, no. 5, pp. 1322–1328, 2013.

[66] P. Anagnostopoulou, S. Yammine, A. Schmidt, I. Korten, E. Kieninger, I. Mack, D. Trachsel, G. Hafen, A. Moeller, C. Casaulta, and P. Latzin, "False normal Lung Clearance Index in infants with cystic fibrosis due to software algorithms," *Pediatr. Pulmonol.*, vol. 50, no. 10, pp. 970–977, 2015.

[67] S. Summermatter, F. Singer, P. Latzin, and S. Yammine, "Impact of software settings on multiple-breath washout outcomes," *PLoS ONE*, vol. 10, no. 7, pp. 1–16, 2015.

[68] J.-L. Vincent, "Understanding cardiac output," *Emergen. Med.*, vol. 12, no. 4, p. 174, 2008.

[69] P. O. Åstrand, T. E. Cuddy, B. Saltin, and J. Stenberg, "Cardiac Output During Submaximal and Maximal Work.," *J. Appl. Physiol.*, vol. 19, pp. 268–274, 1964.

[70] J. S. Carey, P. A. Mohr, R. S. Brown, and W. C. Shoemaker, "Cardiovascular function in hemorrhage, trauma and sepsis: determinants of cardiac output and cardiac work.," *Annals of surgery*, vol. 170, no. 6, pp. 910–921, 1969.

[71] D. L. Dudgeon, P. A. Randall, R. B. Hill, and J. G. McAfee, "Mild Hypothermia: Its Effect on Cardiac Output and Regional Perfusion in the Neonatal Piglet.," *J. Pediatr. Surg.*, vol. 15, no. 6, pp. 805–810, 1980.

[72] S. Jhanji, J. Dawson, and R. M. Pearse, "Cardiac output monitoring: Basic science and clinical application," *Anaesthesia*, vol. 63, no. 2, pp. 172–181, 2008.

[73] M. M. Baum, S. Kumar, J. A. Moss, and P. D. Wagner, "Validation of a new spectrometer for noninvasive measurement of cardiac output," *Rev. Sci. Instrum.*, vol. 75, no. 7, pp. 2290–2299, 2004.

[74] J. Pugsley and A. B. Lerner, "Cardiac output monitoring: is there a gold standard and how do the newer technologies compare?," *Seminars in cardiothoracic and vascular anesthesia*, vol. 14, no. 4, pp. 274–282, 2010.

[75] S. H. Taylor, "Measurement of the Cardiac Output in Man," *Proc. R. Soc. Med.*, vol. 59(suppl), pp. 35–53, 1966.

[76] P. Lund-Johansen, "The dye dilution method for measurement of cardiac output.," *Eur. Heart J.*, vol. 11 Suppl I, pp. 6–12, 1990.

[77] K. L. Zierler, "Theoretical Basis of Indicator-Dilution Methods For Measuring Flow and Volume," *Circ. Res.*, vol. 10, no. 3, pp. 393–407, 1962.

[78] B. F. Geerts, L. P. Aarts, and J. R. Jansen, "Methods in pharmacology: Measurement of cardiac output," *Brit. J. Clin. Pharmaco.*, vol. 71, no. 3, pp. 316–330, 2011.

[79] J. Sandham, R. Hull, R. Brant, L. Knox, G. Pineo, C. Doig, D. Laporta, S. Viner, L. Passerini, H. Devitt, A. Kirby, and M. Jacka, "A Randomized, Controlled Trial of the Use of Pulmonary-Artery Catheters in High-Risk Surgical Patients," *New Engl. J. Med.*, vol. 348, no. 1, pp. 5–14, 2003.

[80] C. Richard, J. Warszawski, N. Anguel, N. Deye, A. Combes, D. Barnoud, T. Boulain, Y. Lefort, M. Fartoukh, F. Baud, A. Boyer, L. Brochard, and J. Teboul, "Early Use of the Pulmonary Artery Catheter and Outcomes in Patients with Shock and Acute Respiratory Distress Syndrome," *JAMA.*, vol. 290, no. 20, pp. 2713–2720, 2003.

[81] S. Harvey, D. A. Harrison, M. Singer, J. Ashcroft, C. M. Jones, D. Elbourne, W. Brampton, D. Williams, D. Young, and K. Rowan, "Assessment of the clinical effectiveness of pulmonary artery catheters in management of patients in intensive care (PAC-Man): A randomised controlled trial," *Lancet*, vol. 366, no. 9484, pp. 472–477, 2005.

[82] R. S. Wiener and H. G. Welch, "Trends in the use of the pulmonary artery catheter in the United States, 1993-2004," *JAMA.*, vol. 298, no. 4, pp. 423–429, 2007.

[83] L. R. Berthiaume, A. D. Peets, U. Schmidt, R. Shahpori, C. J. Doig, P. J. Boiteau, and H. T. Stelfox, "Time series analysis of use patterns for common invasive technologies in critically ill patients," *J. Crit. Care*, vol. 24, pp. 471.e9–471.e14, 2009.

[84] NICE Medical technologies guidance, "CardioQ-ODM oesophageal doppler monitor," *National Institute for Health and Clinical Excellence*, 2011.

[85] H. Møller-Sørensen, J. Cordtz, M. Østergaard, J. C. Nilsson, and K. L. Hansen, "Transesophageal Doppler reliably tracks changes in cardiac output in comparison with intermittent pulmonary artery thermodilution in cardiac surgery patients.," *Int. J. Clin. Monit. Com.*, vol. 31, no. 1, pp. 1–8, 2015.

[86] L. S. Nguyen and P. Squara, "Non-invasive monitoring of cardiac output in critical care medicine," *Front. Med.*, vol. 4, pp. 1–8, 2017.

[87] R. Newman, H. Pierre, and J. Scardo, "Thoracic-fluid conductivity in peripartum women with pulmonary edema," *Obstet. Gynecol.*, vol. 94, pp. 48–51, 1999.

[88] M. Imhoff, J. H. Lehner, and D. Lohlein, "Noninvasive whole-body electrical bioimpedance cardiac output and invasive thermodilution cardiac output in high-risk surgical patients," *Crit. Care Med.*, vol. 28, no. 8, pp. 2812–2818, 2000.

[89] H. Keren, D. Burkhoff, and P. Squara, "Evaluation of a noninvasive continuous cardiac output monitoring system based on thoracic bioreactance," *Am. J. Physiol. Heart Circ. Physiol.*, vol. 293, pp. 583–589, 2007.

[90] N. Y. Raval, P. Squara, M. Cleman, K. Yalamanchili, M. Winklmaier, and D. Burkhoff, "Multicenter evaluation of noninvasive cardiac output measurement by bioreactance technique," *J Clin. Monit. Comput.*, vol. 22, pp. 113–119, 2008.

[91] E. Kupersztych-Hagege, J. L. Teboul, A. Artigas, A. Talbot, C. Sabatier, C. Richard, and X. Monnet, "Bioreactance is not reliable for estimating cardiac output and the effects of passive leg raising in critically ill patients," *Brit. J. Anaesth.*, vol. 111, pp. 961–966, 2013.

[92] K. Tachibana, H. Imanaka, H. Miyano, M. Takeuchi, K. Kumon, and M. Nishimura, "Effect of ventilatory settings on accuracy of cardiac output measurement using partial CO2 rebreathing," *Anesthesiology*, vol. 96, no. 1, pp. 96–102, 2002.

[93] K. Tachibana, H. Imanaka, M. Takeuchi, Y. Takauchi, H. Miyano, and M. Nishimura, "Noninvasive cardiac output measurement using partial carbon dioxide rebreathing is less accurate at settings of reduced minute ventilation and when spontaneous breathing is present," *Anesthesiology*, vol. 98, no. 4, pp. 830–837, 2003.

[94] M. Rocco, G. Spadetta, A. Morelli, D. Dell'Utri, P. Porzi, G. Conti, and P. Pietropaoli, "A comparative evaluation of thermodilution and partial CO2 rebreathing techniques for cardiac output assessment in critically ill patients during assisted ventilation," *Intens. Care Med.*, vol. 30, no. 1, pp. 82–87, 2004.

[95] P. Palmers, W. Vidts, K. Ameloot, C. Cordemans, N. Van Regenmortel, I. De Laet, K. Schoonheydt, H. Dits, V. Eichhorn, D. Reuter, and M. Malbrain, "Assessment of three

minimally invasive continuous cardiac output measurement methods in critically ill patients and a review of the literature," *Anaesthesiol. Intensive Ther.*, vol. 44, no. 4, pp. 188–99, 2012.

[96] M. A. Sackner, D. Greeneltch, M. S. Heiman, S. Epstein, and N. Atkins, "Diffusing capacity, membrane diffusing capacity, capillary blood volume, pulmonary tissue volume, and cardiac output measured by a rebreathing technique," *Am. Rev. Respir. Dis.*, vol. 111, pp. 157–165, 1975.

[97] W. Barazanji, L. Johnson, and C. W. Hsia, "A modified rebreathing technique using an infrared gas analyzer," *J. Appl. Physiol.*, vol. 80, no. 4, pp. 1258–1262, 1996.

[98] E. M. Snyder, B. D. Johnson, and K. C. Beck, "An open-circuit method for determining lung diffusing capacity during exercise: comparison to rebreathe," *J. Appl. Physiol.*, vol. 99, no. 5, pp. 1985–1991, 2005.

[99] J. S. Sadeh, A. Miller, and M. L. Kukin, "Noninvasive measurement of cardiac output by an acetylene uptake technique and simultaneous comparison with thermodilution in ICU patients," *Chest*, vol. 111, no. 5, pp. 1295–1300, 1997.

[100] B. D. Johnson, K. C. Beck, D. N. Proctor, J. Miller, N. M. Dietz, and M. J. Joyner, "Cardiac output during exercise by the open circuit acetylene washin method: comparison with direct Fick," *J. Appl. Physiol.*, vol. 88, pp. 1650–1658, 2000.

[101] K. Gan, I. Nishi, I. Chin, and a. S. Slutsky, "On-line determination of pulmonary blood flow using respiratory inert gas analysis," *IEEE T. Bio-med. Eng.*, vol. 40, no. 12, pp. 1250–1259, 1993.

[102] M. B. Jaffe, "Mainstream or Sidestream Capnography?," *Respironics White Paper*, pp. 1–14, 2002.

[103] K. M. Downard, *Mass Spectrometry: A Foundation Course.* Royal Society of Chemistry, first ed., 2004.

[104] B. Buszewski, M. Kesy, T. Ligor, and A. Amann, "Human exhaled air analytics: biomarkers of diseases," *Biomed. Chromatogr.*, vol. 21, pp. 553–566, 2007.

[105] A. M. Ellis and C. A. Mayhew, *Proton Transfer Reaction Mass Spectrometry: Principles and Applications*. Wiley, first ed., 2013.

[106] A. Hansel, A. Jordan, R. Holzinger, P. Prazeller, W. Vogel, and W. Lindinger, "Proton transfer reaction mass spectrometry: on-line trace gas analysis at the ppb level," *Int. J. Mass Spectrom.*, vol. 149-150, pp. 609–619, 1995.

[107] P. Sulzer, A. Edtbauer, E. Hartungen, S. Jürschik, A. Jordan, G. Hanel, S. Feil, S. Jaksch, L. Märk, and T. D. Märk, "From conventional proton-transfer-reaction mass spectrometry (PTR-MS) to universal trace gas analysis," *Int. J. Mass Spectrom.*, vol. 321-322, pp. 66–70, 2012.

[108] J. A. Covington, M. P. van der Schee, A. S. Edge, B. Boyle, R. S. Savage, and R. P. Arasaradnam, "The application of FAIMS gas analysis in medical diagnostics," *Analyst*, vol. 140, no. 20, pp. 6775–6781, 2015.

[109] Y. Zrodnikov and C. E. Davis, "The highs and lows of FAIMS: Predictions and future trends for high field asymmetric waveform ion mobility spectrometry," *J. Nanomed. Nanotechnol.*, vol. 3, no. 5, 2012.

[110] M. Mazurenka, A. J. Orr-Ewing, R. Peverall, and G. A. Ritchie, "Cavity ring-down and cavity enhanced spectroscopy using diode lasers," *Annu. Rep. Prog. Chem., Sect. C*, vol. 101, pp. 100–142, 2005.

[111] B. Cummings, M. L. Hamilton, L. Ciaffoni, T. R. Pragnell, R. Peverall, G. A. D. Ritchie, G. Hancock, and P. A. Robbins, "Laser-based absorption spectroscopy as a technique for rapid in-line analysis of respired gas concentrations of O2 and CO2.," *J. Appl. Physiol.*, vol. 111, no. 1, pp. 303–307, 2011.

[112] J. M. Hollas, *Modern Spectroscopy*. Wiley, fourth ed., 2004.

[113] J. M. Hartmann, C. Boulet, and D. Robert, *Collisional Effects on Molecular Spectra*. Elsevier Science, first ed., 2008.

[114] V. Malathy Devi, D. Chris Benner, M. A. Smith, A. W. Mantz, K. Sung, L. R. Brown, and A. Predoi-Cross, "Spectral line parameters including temperature dependences of self- and

air-broadening in the 2 to 0 band of CO at 2.3 micron," *J. Quant. Spectrosc. Radiat. Transfer*, vol. 113, no. 11, pp. 1013–1033, 2012.

[115] F. Schreier, "Comments on "A Common Misunderstanding about the Voigt Line Profile"," *J. Atmos. Sci.*, vol. 66, no. 6, pp. 1860–1864, 2009.

[116] G. Berden and R. Engeln, *Cavity Ring-Down Spectroscopy Techniques and Applications*. Wiley-Blackwell, first ed., 2009.

[117] J. A. Silver, "Frequency-modulation spectroscopy for trace species detection: theory and comparison among experimental methods.," *Appl. Optics*, vol. 31, no. 6, pp. 707–717, 1992.

[118] L. S. Rothman, I. E. Gordon, Y. Babikov, A. Barbe, D. Chris Benner, P. F. Bernath, M. Birk, L. Bizzocchi, V. Boudon, L. R. Brown, A. Campargue, K. Chance, E. A. Cohen, L. H. Coudert, V. M. Devi, B. J. Drouin, A. Fayt, J. M. Flaud, R. R. Gamache, J. J. Harrison, J. M. Hartmann, C. Hill, J. T. Hodges, D. Jacquemart, A. Jolly, J. Lamouroux, R. J. Le Roy, G. Li, D. A. Long, O. M. Lyulin, C. J. Mackie, S. T. Massie, S. Mikhailenko, H. S. P. Müller, O. V. Naumenko, A. V. Nikitin, J. Orphal, V. Perevalov, A. Perrin, E. R. Polovtseva, C. Richard, M. A. H. Smith, E. Starikova, K. Sung, S. Tashkun, J. Tennyson, G. C. Toon, V. G. Tyuterev, and G. Wagner, "The HITRAN 2012 molecular spectroscopic database," *J. Quant. Spectrosc. Ra.*, vol. 130, pp. 4–50, 2013.

[119] L. Ciaffoni, D. P. O'Neill, J. H. Couper, G. A. D. Ritchie, G. Hancock, and P. A. Robbins, "In-airway molecular flow sensing: A new technology for continuous, noninvasive monitoring of oxygen consumption in critical care," *Sci. Adv.*, vol. 2:e1600560, 2016.

[120] K. Shibutani, T. Komatsu, K. Kubal, V. Sanchala, V. Kumar, and D. Bizzarri, "Critical level of oxygen delivery after cardiopulmonary bypass," *Crit. Care Med.*, vol. 11, no. 8, pp. 640–3, 1983.

[121] M. Bishop, W. Shoemaker, P. Appel, P. Meade, G. Ordog, J. Wasserberger, C. Wo, D. Rimle, H. Kram, and R. Umali, "Prospective, Randomized Trial of Survivor Values of Cardiac Index, Oxygen Delivery, and Oxygen Consumption as Resuscitation Endpoints in Severe Trauma," *J. Trauma*, vol. 38, no. 5, pp. 708–7, 1995.

[122] U. Frey, J. Stocks, A. Coates, P. Sly, and J. Bates, "Specifications for equipment used for infant pulmonary function testing," *Eur. Respir. J.*, vol. 16, no. 4, pp. 731–740, 2000.

[123] N. G. Mandal, "Respirometers including spirometer, pneumotachograph and peak flow meter," *Anaesth. Intens. Care. Med.*, vol. 7, no. 1, pp. 1–5, 2006.

[124] J. Humlíček, "Optimized computation of the voigt and complex probability functions," *J. Quant. Spectrosc. Radiat. Transfer*, vol. 27, no. 4, pp. 437–444, 1982.

[125] L. Galatry, "Simultaneous effect of doppler and foreign gas broadening on spectral lines," *Phys. Rev.*, vol. 122, no. 4, pp. 1218–1223, 1961.

[126] S. G. Rautian and I. I. Sobel'man, "The Effect of Collisions on the Doppler Broadening of Spectral Lines," *Sov. Phys. Usp.*, vol. 9, no. 5, pp. 701–716, 1967.

[127] R. K. Hanson, R. M. Spearrin, and C. S. Goldenstein, *Spectroscopy and Optical Diagnostics for Gases*. Springer International Publishing, first ed., 2016.

[128] R. M. Leach and D. F. Treacher, "The pulmonary physician in critical care · 2: Oxygen delivery and consumption in the critically ill," *Thorax*, vol. 57, no. 2, pp. 170–177, 2002.

[129] D. S. Martin, M. Khosravi, M. P. Grocott, and M. G. Mythen, "Concepts in hypoxia reborn," *Crit. Care*, vol. 14, no. 4, pp. 1–7, 2010.

[130] N. R. MacIntyre, "Tissue hypoxia: Implications for the respiratory clinician," *Resp. Care*, vol. 59, no. 10, pp. 1590–1596, 2014.

[131] F. Sebat, A. A. Musthafa, D. Johnson, A. A. Kramer, D. Shoffner, M. Eliason, K. Henry, and B. Spurlock, "Effect of a rapid response system for patients in shock on time to treatment and mortality during 5 years," *Crit. Care Med.*, vol. 35, no. 11, pp. 2568–2575, 2007.

[132] R. Daniels, T. Nutbeam, G. McNamara, and C. Galvin, "The sepsis six and the severe sepsis resuscitation bundle: a prospective observational cohort study," *Emerg. Med. J.*, vol. 28, no. 6, pp. 507–512, 2011.

[133] F. Sjöberg and M. Singer, "The medical use of oxygen: a time for critical reappraisal," *J. Intern. Med.*, vol. 274, no. 6, pp. 505–528, 2013.

[134] B. R. O'Driscoll, L. S. Howard, and A. G. Davison, "BTS guideline for emergency oxygen use in adult patients," *Thorax*, vol. 63, no. Suppl. 6, 2008.

[135] A. B. Christensen, J. H. Yee, R. L. Bishop, S. A. Budzien, J. H. Hecht, G. Sivjee, and A. W. Stephan, "Observations of molecular oxygen Atmospheric band emission in the thermosphere using the near infrared spectrometer on the ISS/RAIDS experiment," *J. Geophys. Res.*, vol. 117, no. 4, pp. 1–9, 2012.

[136] G. Gagliardi and H. Loock, *Cavity-Enhanced Spectroscopy and Sensing*. Springer-Verlag Berlin Heidelberg, first ed., 2014.

[137] S. Yang, M. R. Canagaratna, S. K. Witonsky, S. L. Coy, J. I. Steinfeld, R. W. Field, and A. A. Kachanov, "Intensity Measurements and Collision-Broadening Coefficients for the Oxygen A Band Measured by Intracavity Laser Absorption Spectroscopy," *J. Mol. Spectrosc.*, vol. 201, no. 2, pp. 188–197, 2000.

[138] M. D. Wheeler, S. M. Newman, A. J. Orr-ewing, and M. N. R. Ashfold, "Cavity ring-down spectroscopy," *J. Chem. Soc. Faraday Trans.*, vol. 94, no. 3, pp. 337–351, 1998.

[139] B. Bakowski, L. Corner, G. Hancock, R. Kotchie, R. Peverall, and G. Ritchie, "Cavity-enhanced absorption spectroscopy with a rapidly swept diode laser," *Appl. Phys. B*, vol. 75, pp. 745–750, 2002.

[140] A. Yariv and P. Yeh, *Photonics*. Oxford University Press, sixth ed., 2007.

[141] J. L. Jewell, J. P. Harbison, A. Scherer, Y. H. Lee, and L. T. Florez, "Vertical-Cavity Surface-Emitting Lasers: Design, Growth, Fabrication, Characterization," *IEEE J. Quantum Elect.*, vol. 27, no. 6, 1991.

[142] L. Ciaffoni, J. Couper, G. Hancock, R. Peverall, P. A. Robbins, and G. A. D. Ritchie, "RF noise induced laser perturbation for improving the performance of non-resonant cavity enhanced absorption spectroscopy," *Opt. Express*, vol. 22, no. 14, pp. 17030–8, 2014.

[143] P. D. Davis, G. D. Parbrook, and G. N. C. Kenny, *Basic Physics and Measurement in Anaesthesia*. Butterworth-Heinemann, fourth ed., 1995.

[144] B. Eckhardt, "Introduction. Turbulence transition in pipe flow: 125th anniversary of the publication of Reynolds' paper," *Phil. Trans. R. Soc. A*, vol. 367, no. 1888, pp. 449–455, 2009.

[145] S. Sutera and R. Skalak, "The history of Poiseuille's law," *Annu. Rev. Fluid Mech.*, vol. 25, pp. 1–19, 1993.

[146] E. Fried and I. Idel'chik, *Flow Resistance - A Design Guide for Engineers*. CRC Press, first ed., 1989.

[147] Engineering Toolbox, "Gases - Densities," *https://www.engineeringtoolbox.com/gas-density-d_158.html*, accessed 10 July 2018.

[148] Air Liquide, "Gas Encyclopedia," *https://encyclopedia.airliquide.com*, accessed 10 July 2018.

[149] W. Sutherland, "The viscosity of gases and molecular force," *Philosophical Magazine, Series 5*, vol. 36, no. 223, pp. 507–531, 1893.

[150] S. Chapman and T. Cowling, *The Mathematical Theory of Non-uniform Gases*. Cambridge University Press, third ed., 1970.

[151] V. Teske, E. Vogel, and E. Bich, "Viscosity measurements on water vapor and their evaluation," *J. Chem. Eng. Data*, vol. 50, no. 6, pp. 2082–2087, 2005.

[152] R. Brokaw, "Viscosity of gas mixtures," *NASA Technical Note*, vol. TN D-4496, 1968.

[153] G. Bellani, N. Patroniti, and A. Presenti, *Measurement of Functional Residual Capacity during Mechanical Ventilation. In: Yearbook of Intensive Care and Emergency Medicine 2010*. Springer, Berlin, Heidelberg, first ed., 2010.

[154] H. Richardson, "The respiratory quotient," *Physiol. Rev.*, vol. 9, pp. 61–125, 1929.

[155] J. F. Murray, "Oxygen cost of voluntary hyperventilation," *J. Appl. Physiol.*, vol. 14, no. 2, pp. 187–190, 1959.

[156] W. Larry Kenney, J. H. Wilmore, and D. L. Costill, *Physiology of Sport and Exercise*. Human Kinetics Australia P/L, sixth ed., 2015.

[157] E. P. Widmaier, H. Raff, and K. T. Strang, *Vander's Human Physiology: The Mechanisms of Body Function*. McGraw-Hill Education, fourteenth ed., 2016.

[158] J. E. Mountain, P. Santer, D. P. O'Neill, N. M. J. Smith, L. Ciaffoni, J. H. Couper, G. A. Ritchie, G. Hancock, J. P. Whiteley, and P. A. Robbins, "Potential for non-invasive assessment of lung inhomogeneity using highly precise, highly time-resolved, measurements of gas exchange," *J. Appl. Physiol.*, vol. 124, pp. 615–631, 2018.

[159] T. A. Wilson and K. C. Beck, "Contributions of ventilation and perfusion inhomogeneities to the VA/Q distribution.," *J. Appl. Physiol.*, vol. 72, no. 6, pp. 2298–2304, 1992.

[160] K. C. Beck, B. D. Johnson, T. P. Olson, and T. A. Wilson, "Ventilation-perfusion distribution in normal subjects.," *J. Appl. Physiol.*, vol. 113, no. 6, pp. 872–7, 2012.

[161] M. Sackner, K. Feisal, and A. Dubois, "Determination of Tissue Volume and Carbon Dioxide Dissociation Slope of the Lungs in Man," *J. Appl. Physiol.*, vol. 19, pp. 374–380, 1964.

[162] A. B. Baker and A. D. Farmery, "Inert gas transport in blood and tissues," *Compr. Physiol.*, vol. 1, no. 2, pp. 569–592, 2011.

[163] T. Kawashiro, R. S. Sikand, F. Adaro, H. Takahashi, and J. Piiper, "Study of intrapulmonary gas mixing in man by simultaneous wash-out of helium and sulfur hexafluoride," *Resp. Physiol.*, vol. 28, no. 2, pp. 261–275, 1976.

[164] R. Street, G. Watters, and J. Vennard, *Elementary fluid mechanics.* John Wiley & Sons, seventh ed., 1995.

[165] T. Ahrens and K. Ott, "Comparison of Three New Generation Pulse Oximeters in a Medical Intensive Care Unit," *Crit. Care Med.*, vol. 34, no. 12, p. A85, 2006.

[166] P. B. Batchelder and D. M. Raley, "Maximizing the laboratory setting for testing devices and understanding statistical output in pulse oximetry," *Anesth. Analg.*, vol. 105, no. Suppl. 6, 2007.

[167] P. H. Quanjer, G. J. Tammeling, J. E. Cotes, O. F. Pedersen, R. Peslin, and J. C. Yernault, "Lung volumes and forced ventilatory flows," *Eur. Respir. J.*, vol. 6, no. Suppl. 16, pp. 5–40, 1993.

[168] C. Zaher, R. Halbert, R. Dubois, D. George, and D. Nonikov, "Smoking-related diseases: The importance of COPD," *Int. J. Tuberc. Lung Dis.*, vol. 8, no. 12, pp. 1423–1428, 2004.

[169] B. Lundbäck, A. Lindberg, M. Lindström, E. Rönmark, A. C. Jonsson, E. Jönsson, L. G. Larsson, S. Andersson, T. Sandström, and K. Larsson, "Not 15 but 50% of smokers develop COPD? - Report from the Obstructive Lung Disease in Northern Sweden Studies," *Resp. Med.*, vol. 97, no. 2, pp. 115–122, 2003.

[170] R. J. Dennis, D. Maldonado, S. Norman, E. Baena, and G. Martinez, "Woodsmoke Exposure and Risk for Obstructive Airways Disease Among Women," *Chest*, vol. 109, no. 1, pp. 115–119, 1996.

[171] Global Strategy for the Diagnosis, Management, and Prevention of Chronic Obstructive Pulmonary Disease (2020 Report), *Global Initiative for Chronic Obstructive Lung Disease*. 2020.

[172] J. L. Hankinson, J. R. Odencrantz, and K. B. Fedan, "Spirometric reference values from a sample of the general U.S. Population," *Am. J. Resp. Crit. Care Med.*, vol. 159, no. 1, pp. 179–187, 1999.

[173] D. M. Mannino, A. S. Buist, and W. M. Vollmer, "Chronic obstructive pulmonary disease in the older adult: what defines abnormal lung function?," *Thorax*, vol. 62, no. 3, pp. 237–241, 2007.

[174] N. Anthonisen, E. Wright, and J. Hodgkin, "Prognosis in Chronic Obstructive Pulmonary Disease," *Am. Rev. Respir. Dis.*, vol. 133, pp. 14–20, 1986.

[175] P. Whiting, N. Singatullina, and J. H. Rosser, "Computed tomography of the chest: I. Basic principles," *BJA Education*, vol. 15, no. 6, pp. 299–304, 2015.

[176] N. L. Müller and H. Coxson, "Chronic obstructive pulmonary disease • 4: Imaging the lungs in patients with chronic obstructive pulmonary disease," *Thorax*, vol. 57, no. 11, pp. 982–985, 2002.

[177] W. Webb, M. Stein, W. Finkbeiner, J. Im, D. Lynch, and G. Gamsu, "Normal and Diseased Isolated Lungs: High-Resolution CT," *Radiology*, vol. 166, pp. 81–87, 1988.

[178] D. A. Lynch and M. L. Al-Qaisi, "Quantitative CT in COPD," *J. Thorac. Imaging*, vol. 28, no. 5, pp. 284–290, 2013.

[179] S. P. Bhatt, X. Soler, X. Wang, S. Murray, A. R. Anzueto, T. H. Beaty, A. M. Boriek, R. Casaburi, G. J. Criner, A. A. Diaz, M. T. Dransfield, D. Curran-Everett, C. J. Galban, E. A. Hoffman, J. C. Hogg, E. A. Kazerooni, V. Kim, G. L. Kinney, A. Lagstein, D. A. Lynch, B. J. Make, F. J. Martinez, J. W. Ramsdell, R. Reddy, B. D. Ross, H. B. Rossiter, R. M. Steiner, M. J. Strand, E. J. Van Beek, E. S. Wan, G. R. Washko, J. Michael Wells, C. H. Wendt, R. A. Wise, E. K. Silverman, J. D. Crapo, R. P. Bowler, and M. K. Han, "Association between functional small airway disease and FEV1 decline in chronic obstructive pulmonary disease," *Am. J. Resp. Crit. Care Med.*, vol. 194, no. 2, pp. 178–184, 2016.

[180] F. A. Mettler, W. Huda, T. T. Yoshizumi, and M. Mahesh, "Effective doses in radiology and diagnostic nuclear medicine," *Radiology*, vol. 248, no. 1, pp. 254–263, 2008.

[181] P. D. Wagner, D. R. Dantzker, R. Dueck, J. L. Clausen, and J. B. West, "Ventilation-Perfusion Inequality in Chronic Obstructive Pulmonary Disease," *J. Clin. Invest.*, vol. 59, pp. 203–216, 1977.

[182] S. Verbanck, D. Schuermans, A. Van Muylem, C. Melot, M. Noppen, W. Vincken, and M. Paiva, "Conductive and acinar lung-zone contributions to ventilation inhomogeneity in COPD," *Am. J. Resp. Crit. Care Med.*, vol. 157, no. 5, pp. 1573–1577, 1998.

[183] M. Delacre, D. Lakens, and C. Leys, "Why psychologists should by default use welch's t-Test instead of student's t-Test," *Int. Rev. Soc. Psychol.*, vol. 30, no. 1, pp. 92–101, 2017.

[184] Altman, D.G., *Practical Statistics for Medical Research.* Chapman & Hall, first ed., 1991.

[185] A. Agusti, P. Calverley, B. Celli, H. Coxson, L. Edwards, D. Lomas, W. MacNee, B. E. Miller, S. Rennard, E. K. Silverman, R. Tal-Singer, E. Wouters, J. Yates, and J. Vestbo, "Characterisation of COPD heterogeneity in the ECLIPSE cohort," *Resp. Res.*, vol. 11, no. 122, pp. 1–14, 2010.

[186] D. P. Johns, J. A. E. Walters, and E. Haydn Walters, "Diagnosis and early detection of COPD using spirometry," *J. Thorac. Dis.*, vol. 6, no. 11, pp. 1557–1569, 2014.

[187] A. Higham, A. M. Quinn, J. E. D. Cançado, and D. Singh, "The pathology of small airways disease in COPD: historical aspects and future directions," *Resp. Res.*, vol. 20, no. 1, pp. 1–11, 2019.

[188] D. E. O'Donnell and C. M. Parker, "COPD exacerbations • 3: Pathophysiology," *Thorax*, vol. 61, no. 4, pp. 354–361, 2006.

[189] I. Lichter and J. F. Gwynne, "Spontaneous pneumothorax in young subjects. A clinical and pathological study.," *Thorax*, vol. 26, no. 4, pp. 409–417, 1971.

[190] M. Ohata and H. Suzuki, "Pathogenesis of spontaneous pneumothorax," *Chest*, vol. 77, no. 6, pp. 771–776, 1980.

[191] V. Cottin, N. Streichenberger, J.-P. Gamondès, F. Thévenet, R. Loire, and J.-F. Cordier, "Respiratory bronchiolitis in smokers with spontaneous pneumothorax," *Eur. Respir. J.*, vol. 12, no. 3, pp. 702–704, 1998.

[192] M. Noppen, T. Dekeukeleire, S. Hanon, G. Stratakos, K. Amjadi, P. Madsen, M. Meysman, J. D'Haese, and W. Vincken, "Fluorescein-enhanced autofluorescence thoracoscopy in patients with primary spontaneous pneumothorax and normal subjects," *Am. J. Resp. Crit. Care Med.*, vol. 174, no. 1, pp. 26–30, 2006.

[193] P. M. Gustafsson, P. De Jong, H. Tiddens, and A. Lindblad, "Multiple-breath inert gas washout and spirometry versus structural lung disease in cystic fibrosis," *Thorax*, vol. 63, pp. 129–134, 2008.

[194] H. R. Omar, D. Mangar, S. Khetarpal, D. H. Shapiro, J. Kolla, R. Rashad, E. Helal, and E. M. Camporesi, "Anteroposterior chest radiograph vs. chest CT scan in early detection of pneumothorax in trauma patients," *Int. Arch. Med*, vol. 4, p. 30, 2011.

[195] R. Hallifax, N. M. J. Smith, N. Petousi, N. P. Talbot, G. A. Ritchie, N. Rahman, and P. A. Robbins, "Non-invasive measurement of lung inhomogeneity in patients who suffered a primary spontaneous pneumothorax," *Eur. Respir. J.*, vol. 52, no. 62, p. PA2414, 2018.

[196] B. Willemse, D. Postma, W. Timens, and N. ten Hacken, "The impact of smoking cessation on respiratory symptoms, lung function, airway hyperresponsiveness and inflammation," *Eur. Respir. J.*, vol. 23, pp. 464–476, 2004.

[197] N. Siafakas, P. Vermeire, N. Pride, P. Paoletti, J. Gibson, P. Howard, J. C. Yernault, M. Decramer, T. Higenbottam, D. Postma, and J. Rees, "ERS Consensus Statement: Optimal assessment and management of chronic obstructive pulmonary disease (COPD)," *Eur. Respir. J.*, vol. 8, pp. 1398–1420, 1995.

[198] D. Niewoehner, J. Kleinerman, and D. Rice, "Pathologic changes in the peripheral airways of young cigarette smokers," *New Engl. J. Med.*, vol. 291, no. 15, pp. 755–758, 1974.

[199] W. McNulty and O. S. Usmani, "Techniques of assessing small airways dysfunction," *Eur. Clin. Resp. J.*, vol. 1, p. 25898, 2014.

[200] F. J. Martinez, M. K. Han, J. P. Allinson, R. Graham Barr, R. C. Boucher, P. M. Calverley, B. R. Celli, S. A. Christenson, R. G. Crystal, M. Fageras, C. M. Freeman, L. Groenke, E. A. Hoffman, M. Kesimer, K. Kostikas, R. Paine, S. Rafii, S. I. Rennard, L. N. Segal, R. Shaykhiev, C. Stevenson, R. Tal-Singer, J. Vestbo, G. P. Woodruff, J. L. Curtis, and J. A. Wedzicha, "At the root: Defining and halting progression of early chronic obstructive pulmonary disease," *Am. J. Resp. Crit. Care Med.*, vol. 197, no. 12, pp. 1540–1551, 2018.

[201] J. Hogg, "Why does airway inflammation persist after smoking stops?," *Thorax*, vol. 61, pp. 96–97, 2006.

[202] D. H. Taylor, V. Hasselblad, S. J. Henley, M. J. Thun, and F. A. Sloan, "Benefits of smoking cessation for longevity," *Am. J. Public Health*, vol. 92, no. 6, pp. 990–996, 2002.

[203] R. T. Sadikot, T. Greene, K. Meadows, and A. G. Arnold, "Recurrence of primary spontaneous pneumothorax," *Thorax*, vol. 52, no. 9, pp. 805–809, 1997.

[204] H. L. Lippert, O. Lund, S. Blegvad, and H. V. Larsen, "Independent risk factors for cumulative recurrence rate after first spontaneous pneumothorax," *Eur. Respir. J.*, vol. 4, no. 3, pp. 324–331, 1991.

[205] J. Roca and P. D. Wagner, "Contribution of multiple inert gas elimination technique to pulmonary medicine 1. Principles and information content of the multiple inert gas elimination technique," *Thorax*, vol. 49, pp. 815–824, 1994.

[206] A. G. N. Agusti and J. A. Barbera, "Contribution of multiple inert gas elimination technique to pulmonary medicine 2. Chronic pulmonary diseases : chronic obstructive pulmonary disease and idiopathic pulmonary fibrosis," *Thorax*, vol. 49, pp. 924–932, 1994.

[207] G. Cremona, J. A. Barberà, T. Melgosa, L. Appendini, J. Roca, C. Casadio, C. F. Donner, R. Rodriguez-Roisin, and P. D. Wagner, "Mechanisms of gas exchange response to lung volume reduction surgery in severe emphysema," *J. Appl. Physiol.*, vol. 110, no. 4, pp. 1036–1045, 2011.

[208] J. A. Barberà, J. Ramirez, J. Roca, P. D. Wagner, J. Sanchez-Lloret, and R. Rodríguez-Roisin, "Lung Structure and Gas Exchange in Mild Chronic Obstructive Pulmonary Disease," *Am. Rev. Respir. Dis.*, vol. 141, pp. 895–901, 1990.

[209] J. A. Barberà, J. Roca, A. Ferrer, M. A. Félez, O. Díaz, N. Roger, and R. Rodriguez-Roisin, "Mechanisms of worsening gas exchange during acute exacerbations of chronic obstructive pulmonary disease," *Eur. Respir. J.*, vol. 10, pp. 1285–1291, 1997.

[210] N. W. Morrell, K. S. Nijran, T. Biggs, and W. A. Seed, "Magnitude and time course of acute hypoxic pulmonary vasoconstriction in man," *Resp. Physiol.*, vol. 100, no. 3, pp. 271–281, 1995.

[211] P. Wagner, G. Hedenstierna, G. Bylin, and L. Lagerstrand, "Reproducibility of the multiple inert gas elimination technique," *J. Appl. Physiol.*, vol. 62, no. 4, pp. 1740–1746, 1987.

[212] J. Cardús, F. Burgos, O. Diaz, J. Roca, J. A. Barberà, R. M. Marrades, R. Rodriguez-roisin, and P. D. Wagner, "Increase in Pulmonary Ventilation-Perfusion Inequality with Age in Healthy Individuals," *Am. J. Respir. Crit. Care Med.*, vol. 156, pp. 648–653, 1997.

[213] P. D. Wagner, H. Saltzman, and J. B. West, "Measurement of continuous distributions of ventilation-perfusion ratios: theory," *J. Appl. Physiol.*, vol. 36, no. 5, pp. 588–599, 1974.

[214] D. Altman and J. Bland, "Measurement in Medicine: the Analysis of Method Comparison Studies," *Statistician*, vol. 32, no. 3, pp. 307–317, 1983.

[215] D. Giavarina, "Understanding Bland Altman analysis," *Biochem. Medica*, vol. 25, no. 2, pp. 141–151, 2015.

[216] J. Bland and D. Altman, "Statistical methods for assessing agreement between two methods of clinical measurement," *Lancet*, vol. 327, pp. 307–310, 1986.

[217] I. Blumenthal, "Carbon monoxide poisoning," *J. R. Soc. Med.*, vol. 94, pp. 270–272, 2001.

[218] L. Melosini, F. L. Dente, E. Bacci, M. L. Bartoli, S. Cianchetti, F. Costa, A. D. Franco, L. Malagrin, F. Novelli, B. Vagaggini, and P. Paggiaro, "Asthma control test (ACT): Comparison with clinical, functional, and biological markers of asthma control," *J. Asthma*, vol. 49, no. 3, pp. 317–323, 2012.

[219] BTS/SIGN, *British guideline on the management of asthma.* 2019.

[220] E. F. Juniper, P. M. O'Byrne, G. H. Guyatt, P. J. Ferrie, and D. R. King, "Development and validation of a questionnaire to measure asthma control," *Eur. Respir. J.*, vol. 14, no. 4, pp. 902–907, 1999.

[221] E. O. Meltzer, W. W. Busse, S. E. Wenzel, V. Belozeroff, H. H. Weng, J. Feng, Y. Chon, C. F. Chiou, D. Globe, and S. L. Lin, "Use of the Asthma Control Questionnaire to predict future risk of asthma exacerbation," *J. Allergy Clin. Immunol.*, vol. 127, no. 1, pp. 167–172, 2011.

[222] J. M. Wraight, R. J. Hancox, G. P. Herbison, J. O. Cowan, E. M. Flannery, and D. R. Taylor, "Bronchodilator tolerance: The impact of increasing bronchoconstriction," *Eur. Respir. J.*, vol. 21, no. 5, pp. 810–815, 2003.

[223] N. Ullmann, S. Caggiano, and R. Cutrera, "Salbutamol and around," *Ital. J. Pediatr.*, vol. 41, no. Suppl 2, p. A74, 2015.

[224] D. W. Cockcroft and V. A. Swystun, "Asthma control versus asthma severity," *J. Allergy Clin. Immunol.*, vol. 98, pp. 1016–1018, 1996.

[225] R. H. Green, C. E. Brightling, S. McKenna, B. Hargadon, D. Parker, P. Bradding, A. J. Wardlaw, and I. D. Pavord, "Asthma exacerbations and sputum eosinophil counts: A randomised controlled trial," *Lancet*, vol. 360, no. 9347, pp. 1715–1721, 2002.

[226] K. Ashutosh, "Nitric oxide and asthma: a review," *Curr. Opin. Pulm. Med.*, vol. 6, no. 1, pp. 21–25, 2000.

[227] K. Alving, E. Weitzberg, and J. M. Lundberg, "Increased amount of nitric oxide in exhaled air of asthmatics," *Eur. Respir. J.*, vol. 6, no. 9, pp. 1368–1370, 1993.

[228] B. Horn, E. Robin, J. Theodore, and A. Van Kessel, "Total eosinophil counts in the management of bronchial asthma," *New Engl. J. Med.*, vol. 292, no. 22, pp. 1152–1155, 1975.

[229] D. N. Payne, I. M. Adcock, N. M. Wilson, T. Oates, M. Scallan, and A. Bush, "Relationship between exhaled nitric oxide and mucosal eosinophilic inflammation in children with difficult asthma, after treatment with oral prednisolone," *Am. J. Respir. Crit. Care Med.*, vol. 164, no. 8, pp. 1376–1381, 2001.

[230] I. D. Pavord, S. Korn, P. Howarth, E. R. Bleecker, R. Buhl, O. N. Keene, H. Ortega, and P. Chanez, "Mepolizumab for severe eosinophilic asthma (DREAM): A multicentre, double-blind, placebo-controlled trial," *Lancet*, vol. 380, pp. 651–659, 2012.

[231] D. M. McNicholl, M. Stevenson, L. P. McGarvey, and L. G. Heaney, "The utility of fractional exhaled nitric oxide suppression in the identification of nonadherence in difficult asthma," *Am. J. Respir. Crit. Care Med.*, vol. 186, no. 11, pp. 1102–1108, 2012.

[232] P. J. Barnes, "Inhaled corticosteroids," *Pharmaceuticals*, vol. 3, pp. 514–540, 2010.

[233] D. S. Postma and H. A. Kerstjens, "Characteristics of airway hyperresponsiveness in asthma and chronic obstructive pulmonary disease," *Am. J. Resp. Crit. Care Med.*, vol. 158, pp. S187–S192, 1998.

[234] A. Ullman and N. Svedmyr, "Salmeterol, a new long acting inhaled β2 adrenoceptor agonist: comparison with salbutamol in adult asthmatic patients," *Thorax*, vol. 43, no. 9, pp. 674–678, 1988.

[235] M. Aubier, W. R. Pieters, N. J. Schlösser, and K. O. Steinmetz, "Salmeterol/fluticasone propionate (50/500 μg) in combination in a Diskus inhaler (Seretide) is effective and safe in the treatment of steroid-dependent asthma," *Resp. Med.*, vol. 93, no. 12, pp. 876–884, 1999.

[236] M. Berry, B. Hargadon, A. Morgan, M. Shelley, J. Richter, D. Shaw, R. H. Green, C. Brightling, A. J. Wardlaw, and I. D. Pavord, "Alveolar nitric oxide in adults with asthma: evidence of distal lung inflammation in refractory asthma," *Eur. Respir. J.*, vol. 25, no. 6, pp. 986–991, 2005.

[237] D. Hodgson, J. Anderson, C. Reynolds, G. Meakin, H. Bailey, I. Pavord, D. Shaw, and T. Harrison, "A randomised controlled trial of small particle inhaled steroids in refractory eosinophilic asthma (SPIRA)," *Thorax*, vol. 70, no. 6, pp. 559–565, 2015.

[238] D. T. McLeod, S. J. Capewell, J. Law, W. MacLaren, and A. Seaton, "Intramuscular triamcinolone acetonide in chronic severe asthma," *Thorax*, vol. 40, no. 11, pp. 840–845, 1985.

[239] J. R. Panickar, P. Kenia, M. Silverman, and J. Grigg, "Intramuscular triamcinolone for difficult asthma," *Pediatr. Pulm.*, vol. 39, no. 5, pp. 421–425, 2005.

[240] H. Arnold, "Systemic Steroid Therapy with Intramuscularly Injected Triamcinolone," *South. Med. J.*, vol. 71, no. 2, pp. 102–107, 1978.

[241] M. J. Leckie, A. Ten Brinke, J. Khan, Z. Diamant, B. J. O'Connor, C. M. Walls, A. K. Mathur, H. C. Cowley, K. F. Chung, R. Djukanovic, T. T. Hansel, S. T. Holgate, P. J. Sterk, and P. J. Barnes, "Effects of an interleukin-5 blocking monoclonal antibody on eosinophils, airway hyper-responsiveness, and the late asthmatic response," *Lancet*, vol. 356, pp. 2144–2148, 2000.

[242] A. Menzies-Gow, P. Flood-Page, R. Sehmi, J. Burman, Q. Hamid, D. S. Robinson, A. B. Kay, and J. Denburg, "Anti-IL-5 (mepolizumab) therapy induces bone marrow eosinophil maturational arrest and decreases eosinophil progenitors in the bronchial mucosa of atopic asthmatics," *J. Allergy Clin. Immunol.*, vol. 111, pp. 714–719, 2003.

[243] P. Haldar, C. E. Brightling, B. Hargadon, S. Gupta, W. Monteiro, A. Sousa, R. P. Marshall, P. Bradding, R. H. Green, A. J. WardIaw, and I. D. Pavord, "Mepolizumab and exacerbations of refractory eosinophilic asthma," *New Engl. J. Med.*, vol. 360, no. 10, pp. 973–984, 2009.

[244] H. G. Ortega, M. C. Liu, I. D. Pavord, G. G. Brusselle, J. M. FitzGerald, A. Chetta, M. Humbert, L. E. Katz, O. N. Keene, S. W. Yancey, and P. Chanez, "Mepolizumab treatment in

patients with severe eosinophilic asthma," *New Engl. J. Med.*, vol. 371, no. 13, pp. 1198–1207, 2014.

[245] C. S. Farah, T. Badal, N. Reed, P. G. Rogers, G. G. King, C. Thamrin, M. J. Peters, and L. M. Seccombe, "Mepolizumab improves small airway function in severe eosinophilic asthma," *Resp. Med.*, vol. 148, no. February, pp. 49–53, 2019.

[246] National Institute for Health and Care Excellence, "Single technology appraisal: Mepolizumab for treating severe refractory eosinophilic asthma," *Committee Papers*, no. 798, 2016.

[247] O. Allen, "Slipping through the net: The reality facing patients with difficult and severe asthma," *Asthma UK Report*, pp. 1–20, 2018.

[248] H. Ortega, H. Li, R. Suruki, F. Albers, D. Gordon, and S. Yancey, "Cluster Analysis and Characterization of Response to Mepolizumab: A Step Closer to Personalized Medicine for Patients with Severe Asthma," *Ann. Am. Thorac. Soc.*, vol. 11, no. 7, pp. 1011–1017, 2014.

[249] T. Numata, K. Nakayama, H. Utsumi, K. Kobayashi, H. Yanagisawa, M. Hashimoto, S. Minagawa, T. Ishikawa, H. Hara, J. Araya, and K. Kuwano, "Efficacy of mepolizumab for patients with severe asthma and eosinophilic chronic rhinosinusitis," *BMC Pulm. Med.*, vol. 19, no. 176, pp. 1–9, 2019.

[250] S. S. Shapiro and M. B. Wilk, "An analysis of variance test for normality (complete samples)," *Biometrika*, vol. 52, no. 3/4, pp. 591–611, 1965.

[251] L. Lyons, *A Practical Guide to Data Analysis for Physical Science Students.* Cambridge University Press, first ed., 1991.

[252] J. Tolles and W. J. Meurer, "Logistic regression: Relating patient characteristics to outcomes," *JAMA.*, vol. 316, no. 5, pp. 533–534, 2016.

[253] T. Fawcett, "An introduction to ROC analysis," *Pattern Recogn. Lett.*, vol. 27, no. 8, pp. 861–874, 2006.

[254] T. Perez, P. Chanez, D. Dusser, and P. Devillier, "Small airway impairment in moderate to severe asthmatics without significant proximal airway obstruction," *Respir. Med.*, vol. 107, no. 11, pp. 1667–1674, 2013.

[255] B. Lipworth, A. Manoharan, and W. Anderson, "Unlocking the quiet zone: the small airway asthma phenotype," *Lancet Respir. Med.*, vol. 2, no. 6, pp. 497–506, 2014.

[256] L. G. Heaney, J. Busby, P. Bradding, R. Chaudhuri, A. H. Mansur, R. Niven, I. D. Pavord, J. T. Lindsay, and R. W. Costello, "Remotely monitored therapy and nitric oxide suppression identifies nonadherence in severe asthma," *Am. J. Respir. Crit. Care Med.*, vol. 199, no. 4, pp. 454–464, 2019.

[257] A. ten Brinke, A. H. Zwinderman, P. J. Sterk, K. F. Rabe, and E. H. Bel, ""Refractory" eosinophilic airway inflammation in severe asthma: Effect of parenteral corticosteroids," *Am. J. Respir. Crit. Care Med.*, vol. 170, no. 6, pp. 601–605, 2004.

[258] F. C. Albers, H. G. Ortega, E. S. Bradford, M. J. Gilson, R. G. Price, S. W. Yancey, and W. C. Moore, "Durability of Clinical Response Following Long-Term Treatment with Mepolizumab in Patients with Severe Eosinophilic Asthma: The COLUMBA Study," *Am. J. Respir. Crit. Care Med.*, vol. 197, p. A1372, 2018.

[259] M. Cormier, S. Chaboillez, and C. Lemiere, "Secondary loss of response to mepolizumab in severe eosinophilic asthma," *J. Allergy Clin. Immunol. Pract.*, vol. Epub ahead of print, 2019.

[260] T. F. Carr, A. A. Zeki, and M. Kraft, "Eosinophilic and Noneosinophilic Asthma," *Am. J. Respir. Crit. Care Med.*, vol. 197, no. 1, pp. 22–37, 2018.

[261] G. Plant, M. Nikodem, P. Mulhall, R. K. Varner, D. Sonnenfroh, and G. Wysocki, "Field test of a remote multi-path CLaDS methane sensor," *Sensors*, vol. 15, no. 9, pp. 21315–21326, 2015.

[262] D. Thomazy, S. So, A. Kosterev, R. Lewicki, L. Dong, A. A. Sani, and F. K. Tittel, "Low-power laser-based carbon monoxide sensor for fire and post-fire detection using a compact Herriott multipass cell," *Proc. SPIE.*, vol. 7608, 2010.

[263] D. R. Herriott and H. J. Schulte, "Folded Optical Delay Lines," *Appl. Optics*, vol. 4, no. 8, p. 883, 1965.

[264] C. G. Tarsitano and C. R. Webster, "Multilaser Herriott cell for planetary tunable laser spectrometers," *Appl. Optics*, vol. 46, no. 28, pp. 6923–6935, 2007.

[265] J. E. Greivenkamp, *Field Guide to Geometrical Optics*. SPIE. Field Guide, 2004.

[266] O. Svelto, *Principles of Lasers*. Plenum Press, fourth ed., 1998.

[267] D. Cramer, J. E. Cotes, D. J. Chinn, L. E. Fabbri, H. Matthys, O. F. Pedersen, R. Peslin, P. H. Quanjer, J. Roca, G. J. Tameling, and J. C. Yernault, "Standardization of the measurement of transfer factor (diffusing capacity)," *Eur. Respir. J.*, vol. 6, no. 16, pp. 1577–1578, 1993.

[268] B. L. Graham, V. Brusasco, F. Burgos, B. G. Cooper, R. Jensen, A. Kendrick, N. R. Macintyre, B. R. Thompson, and J. Wanger, "2017 ERS/ATS standards for single-breath carbon monoxide uptake in the lung," *Eur. Respir. J.*, vol. 49, no. 1, pp. 1–31, 2017.

[269] J. M. Bennett and E. J. Ashley, "Infrared Reflectance and Emittance of Silver and Gold Evaporated in Ultrahigh Vacuum," *Appl. Optics*, vol. 4, no. 2, p. 221, 1965.

[270] P. K. Weathersby and L. D. Homer, "Solubility of inert gases in biological fluids and tissues: a review," *Undersea Biomed. Res.*, vol. 7, no. 4, pp. 277–96, 1980.

[271] P. D. Wagner, P. F. Naumann, and R. B. Laravuso, "Simultaneous measurement of eight foreign gases in blood by gas chromatography," *J. Appl. Physiol.*, vol. 36, no. 5, pp. 600–605, 1974.

[272] E. Wilhelm, R. Battino, and R. J. Wilcock, "Low-Pressure Solubility of Gases in Liquid Water," *Chem. Rev.*, vol. 77, no. 2, pp. 219–262, 1977.

[273] Y. Ohta, A. Ar, and L. E. Farhi, "Solubility and partition coefficients for gases in rabbit brain and blood," *J. Appl. Physiol.*, vol. 46, no. 6, pp. 1169–1170, 1979.

[274] M. Meyer, U. Tebbe, and J. Piiper, "Solubility of inert gases in dog blood and skeletal muscle," *Pflug. Arch. Eur. J. Phy.*, vol. 384, no. 2, pp. 131–134, 1980.

[275] M. D. Levitt and D. G. Levitt, "Use of inert gases to study the interaction of blood flow and diffusion during passive absorption from the gastrointestinal tract of the rat," *J. Clin. Invest.*, vol. 52, no. 8, pp. 1852–1862, 1963.

[276] J. G. Priestley and H. Schwarz, "The solubility of acetylene in blood: 1. Determination of acetylene dissolved in blood or other liquids," *The Journal of Physiology*, vol. 99, no. 1, pp. 49–56, 1940.

[277] A. Grollman, "The solubility of gases in blood and blood fluids," *J. Biol. Chem.*, vol. 82, pp. 317–325, 1929.

[278] M. Meyer and P. Scheid, "Solubility of acetylene in human blood determined by mass spectrometry," *J. Appl. Physiol.*, vol. 48, no. 6, pp. 1035–1037, 1980.

[279] C. B. Chapman, H. L. Taylor, C. Borden, R. V. Ebert, and A. Keys, "Simultaneous determinations of the resting arteriovenous oxygen difference by the acetylene and direct Fick methods," *J. Clin. Invest.*, vol. 29, no. 6, pp. 651–659, 1950.

[280] M. McGregor, R. E. Donevan, and N. M. Anderson, "Influence of carbon dioxide and hyperventilation on cardiac output in man," *J. Appl. Physiol.*, vol. 17, no. 6, pp. 933–937, 1962.

[281] R. E. Donevan, N. M. Anderson, P. Sekelj, O. Papp, and M. McGregor, "Influence of voluntary hyperventilation on cardiac output," *J. Appl. Physiol.*, vol. 17, pp. 487–491, 1962.

[282] A. Kiers, T. H. W. Van Der Mark, M. G. Woldring, and R. Peset, "Determination of the functional residual capacity during exercise," *Ergonomics*, vol. 23, no. 10, pp. 955–959, 1980.

[283] D. Y. Sue, "Measurement of lung volumes in patients with obstructive lung disease," *Annals of the American Thoracic Society*, vol. 10, no. 5, pp. 525–530, 2013.

[284] L. A. Critchley and J. A. Critchley, "A meta-analysis of studies using bias and precision statistics to compare cardiac output measurement techniques," *J. Clin. Monit. Comput.*, vol. 15, no. 2, pp. 85–91, 1999.

[285] K. Mizuno, Y. Ichinose, H. Ishii, and I. Nishi, "Pulmonary tissue volume measured by acetylene rebreathing under artificial ventilation," *Respirology*, vol. 5, no. 2, pp. 147–152, 2000.

[286] M. A. Sackner, G. Markwell, N. Atkins, S. J. Birch, and R. J. Fernandez, "Rebreathing techniques for pulmonary capillary blood flow and tissue volume," *J. Appl. Physiol. Respir. Environ. Exerc. Physiol.*, vol. 49, no. 5, pp. 910–915, 1980.

[287] L. Cander and R. E. Forster, "Determination of pulmonary parenchymal tissue volume and pulmonary capillary blood flow in man," *J. Appl. Physiol.*, vol. 14, no. 4, pp. 541–551, 1959.

[288] R. J. Farney, A. H. Morris, R. M. Gardner, and J. D. Armstrong, "Rebreathing pulmonary capillary and tissue volume in normals after saline infusion," *J. Appl. Physiol. Respir. Environ. Exerc. Physiol.*, vol. 43, no. 2, pp. 246–253, 1977.

[289] C. Wolff, "Normal cardiac output, oxygen delivery and oxygen extraction," *Adv. Exp. Med. Biol.*, vol. 599, pp. 169–182, 2008.

[290] J. O. Dunn, M. G. Mythen, and M. P. Grocott, "Physiology of oxygen transport," *BJA Education*, vol. 16, no. 10, pp. 341–348, 2016.

[291] B. Y. A. Brown and A. L. Goodall, "Normal variations in blood haemoglobin concentration," *J. Physiol.*, vol. 104, pp. 404–407, 1946.

[292] M. R. Piano, "Alcohol's Effects on the Cardiovascular System," *Alcohol Res-Curr. Rev.*, vol. 38, no. 2, pp. 219–241, 2017.

[293] M. Kupari, "Drunkenness, Hangover, and the Heart," *Acta Med. Scand.*, vol. 213, no. 2, pp. 84–90, 1983.

[294] H. Kelbaek, S. Floistrup, T. Gjorup, N. Christensen, O. Hartling, and J. Godtfredsen, "Central and Peripheral Haemodynamic Changes After Alcohol Ingestion," *Alcohol Alcohol.*, vol. 23, no. 3, pp. 211–216, 1988.

[295] S. Hafner, F. Beloncle, A. Koch, P. Radermacher, and P. Asfar, "Hyperoxia in intensive care, emergency, and peri-operative medicine: Dr. Jekyll or Mr. Hyde? A 2015 update," *Ann. Intens. Care*, vol. 5, no. 42, pp. 1–14, 2015.

[296] P. Asfar, M. Singer, and P. Radermacher, "Understanding the benefits and harms of oxygen therapy," *Intens. Care Med.*, vol. 41, no. 6, pp. 1118–1121, 2015.

[297] M. Kleen, O. Habler, J. Hutter, G. Kemming, A. Podtschaske, M. Tiede, M. Welte, P. E. Keipert, S. Batra, N. S. Faithfull, C. Corso, B. Zwissler, and K. Messmer, "Hemodilution and hyperoxia locally change distribution of regional pulmonary perfusion in dogs," *Am. J. Physiol. Heart Circ. Physiol.*, vol. 274, no. 43, pp. 520–528, 1998.

[298] M. N. Melsom, T. Flatebø, and G. Nicolaysen, "Hypoxia and hyperoxia both transiently affect distribution of pulmonary perfusion but not ventilation in awake sheep," *Acta Physiol. Scand.*, vol. 166, no. 2, pp. 151–158, 1999.

[299] J. Huygh, Y. Peeters, J. Bernards, and M. L. Malbrain, "Hemodynamic monitoring in the critically ill: an overview of current cardiac output monitoring methods," *F1000Research*, vol. 5, pp. 1–9, 2016.

[300] J. Teboul, B. Saugel, M. Cecconi, D. De Backer, C. K. Hofer, X. Monnet, A. Perel, M. R. Pinsky, D. A. Reuter, A. Rhodes, P. Squara, J. L. Vincent, and T. W. Scheeren, "Less invasive hemodynamic monitoring in critically ill patients," *Intens. Care Med.*, vol. 42, no. 9, pp. 1350–1359, 2016.

[301] A. Bush and C. M. Busst, "Cardiovascular function at rest and on exercise in patients with cryptogenic fibrosing alveolitis," *Thorax*, vol. 43, no. 4, pp. 276–283, 1988.

[302] G. Kandel and A. Aberman, "Mixed Venous Oxygen Saturation: Its Role in the Assessment of the Critically Ill Patient," *Arch. Intern. Med.*, vol. 143, pp. 1400–1402, 1983.

[303] P. V. Beest, G. Wietasch, T. Scheeren, P. Spronk, and M. Kuiper, "Clinical review: use of venous oxygen saturations as a goal - a yet unfinished puzzle," *Crit. Care*, vol. 15, no. 232, pp. 1–9, 2011.

[304] J. Holm, E. Håkanson, F. Vánky, and R. Svedjeholm, "Mixed venous oxygen saturation predicts short- and long-term outcome after coronary artery bypass grafting surgery: a retrospective cohort analysis," *Brit. J. Anaesth.*, vol. 107, no. 3, pp. 344–350, 2011.